Nanoscale measurements of the mechanical properties of lipid bilayers

Paul Köcher

St Cross College

University of Oxford

Thesis submitted in fulfilment of the requirements for the degree of

Doctor of Philosophy

Trinity Term 2014

Abstract

Nanoscale measurements of the mechanical properties of lipid bilayers

Paul Köcher, St Cross College, DPhil, Trinity Term 2014

Lipid bilayers form the basis of the membranes that serve as a barrier between a cell and its physiological environment. Their physical properties make them ideally suited for this role: they are extremely soft with respect to bending but essentially incompressible under lateral tension, and they are quite permeable to water but essentially impermeable to ions which allows the rapid establishment of the osmotic gradients. The function of membrane proteins, which are vital for tasks ranging from signal transduction to energy conversion, depends on their interactions with the lipid environment. Because of the complexity of natural membranes, model systems consisting of simpler lipid mixtures have become indispensable tools in the study of membrane biophysics. The objective of the work reported here is to develop a deeper understanding of the underlying physics of lipid bilayers through nanoscale measurements of the mechanical properties of mixed lipid systems including cholesterol, a key ingredient of cell membranes.

Atomic force microscopy (AFM) has been used extensively to measure the topographical and elastic properties of supported lipid bilayers displaying complex phase behaviour and containing mixtures of important PC, PE lipids and cholesterol. Phase transformations have been investigated varying the membrane temperature, and the effects of cholesterol in controlling membrane fluidity, phase, and energetics have been studied. Elastic modulus measurements were correlated with phase behaviour observations.

To aid in the nanoscale probing of lipid bilayers, AFM probes with a high aspect ratio and tip radii of $\sim$4 nm were fabricated and characterised. These probes were used to investigate the phase boundary in binary and ternary lipid systems, leading to the discovery of a raised region at the boundary which has implications for the localisation of reconstituted proteins as well as the role of natural domains or lipid rafts. The electrical properties of the probes were examined to assess their potential application for combined structural and electrical measurements in liquid.

A novel technique was developed to aid in the study of the physical properties of lipid bilayers. Membrane budding was induced above microfabricated substrates through osmotic pressure. Modification of the adhesion energy of the bilayer through biotin-avidin linking was successful in modulating budding behaviour of liquid disordered bilayers. The free energy of the system was modelled to allow quantitative information to be extracted from the data.

This thesis is dedicated to my friend and mentor
Prof. Dr. Heinz Allekotte
for giving me the life-changing opportunity that has led me here.

Acknowledgements

I would like to thank:

- My supervisor, John F. Ryan, for continuous support, guidance, and encouragement. I am grateful for the opportunity to learn so much as part of an international team of researchers.
- Nahoko Kasai and all the members of Shitsubun group at NTT BRL for their incredible hospitality and for the inspiration they provided.
- Chandra S. Ramanujan for introducing me to the project, teaching me atomic force microscopy, and for always being a voice of encouragement and support.
- Jason Brown for his hard work modifying and imaging AFM probes, and for teaching me scanning electron microscopy, and for always being good banter.
- The members of the Ryan group, for their camaraderie, their assistance, and their input.
- The board of the Erlin und Heinz Allekotte Stiftung zur Förderung der Ausbildung besonders begabter Kinder for the opportunity to study abroad.
- Elspeth Garman for her encouragement and support in dark times.
- My friends. In particular Cal for keeping me sane and revealing to me the merits of Scottish Zen.
- My family for their love and support. Good work, team.

Contents

Chapter 1

Introduction

Nanoscale measurement techniques have many potential applications in biology and medicine, ranging from molecular diagnostics and early stage detection of disease to targeted drug delivery. Furthermore, they permit the detection and measurement of biophysical properties – mechanical and electrical – at the molecular level. And they have the ability to image and manipulate individual molecules and to measure molecular interactions in real time with sub-molecular resolution. However, biological processes are extremely complex in general, often involving multiple competing and/or complementary biochemical pathways. Consequently, it is invariably the case that simplified "model" systems need to be devised in order to permit the underlying physical properties to be investigated. An important example of this approach is the use of model membranes to mimic the behaviour of cell membranes.

Cell membranes are the barriers that separate cells from their environment as well as certain cellular sub-compartments from the rest of the cell and as such constitute an essential component of living systems as we know them. Without such a barrier, cells could not function, as the proteins and organelles that they are composed of would simply diffuse away. More than just providing a compartment, the cell membrane houses a host of proteins – approximately 30% of all the proteins encoded in eukaryotic organisms are transmembrane proteins [1]. In many respects these molecules are the basic information processing devices in biology: they are responsible for sensory signal input and transduction, and they control and regulate numerous processes including energy conversion, secretion, food uptake, osmoregulation etc. As such, it comes as no surprise that their failure to function properly often results in pathology. Two thirds or more of all available drugs target transmembrane proteins [2].

The primary structural components of cell membranes are phospholipids, glycolipids, and sterols, collectively known as lipids. These amphiphilic molecules, composed of a hydrophilic head group and (as a rule) two hydrophobic hydrocarbon tails, spontaneously organise in an aqueous environment. The molecular structures of sev-

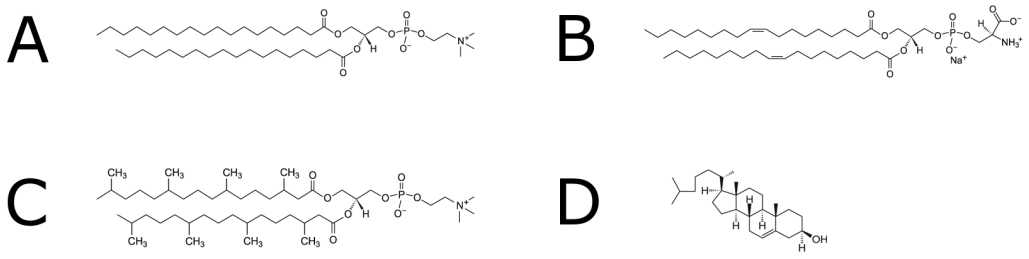

Figure 1.1: Molecular structure of selected lipids. A: 1,2-distearoyl-sn-glycero-3-phosphocholine (DSPC; 18:0 PC), with a choline headgroup and fully saturated hydrocarbon tails. B: 1,2-dioleoyl-sn-glycero-3-phospho-L-serine (DOPS; 18:1 PS), with a serine headgroup and mono-unsaturated hydrocarbon tails. C: 1,2-diphytanoyl-sn-glycero-3-phosphocholine (DPhPC; 4ME 16:0 PC), with methyl side groups on its hydrocarbon tails. D: Cholesterol.

eral lipids used in this thesis is given in fig. 1.1. The driving forces of this organisation are the energetic cost of exposing the hydrocarbon tails to the aqueous solution, the shape of the lipid molecules and the resulting steric considerations, and entropic effects. Depending on concentration, ionic conditions, lipid type, and temperature lipids in water can form micelles, multilamellar and unilamellar vesicles of various sizes, or bilayer sheets (as well as other more exotic and less biologically relevant arrangements).

Bilayers are composed of two leaflets facing one another, such that the hydrophobic tails are on the inside and shielded from the water molecules by the head groups. There are many different types of naturally occurring lipids with varying head groups, tail lengths, and degree of tail saturation. All of these factors affect the behaviour of these lipids, the bilayers they form, and how these bilayers interact with their non-lipid constituents. Indeed, an understanding of lipids has proven essential for the successful crystallisation of many membrane proteins [3], giving an indication of the importance of foundational research in this area. This thesis is chiefly concerned with the behaviour and biophysics of lipid bilayers.

Native cellular membranes contain a rich mixture of lipids and proteins. The lipid content ranges from ∼20% by weight in the mitochondrial inner membrane to 80% in

Table 1.1: Lipid classes in rat synaptic membrane, adapted from Cotman 1969 [4].

Lipid class	% weight
cholesterol	18.6 ± 1.2
ceramide	1.6 ± 0.3
glycolipid	0.9 ± 0.15
phosphoethanolamine (PE)	28.2 ± 1.3
phosphatidylserine (PS) + phosphatidylinositol (PI)	11.8 ± 0.6
phosphocholine (PC)	33.9 ± 0.6
sphingomyelin	3.0 ± 0.3
lyso PC	1.0 ± 0.7

the myelin sheath of nerve axons. The lipid composition of a membrane also depends very much on the cell type: Table 1.1 lists the lipids present in rat synaptic membrane. In this case approximately one third of the lipid content has a phosphocholine (PC) headgroup. But even within this category there are many different molecular species, a fact revealed in table 1.2. These lipids can have quite different structures at ambient temperatures and consequently their mixtures display complex phase behaviour with characteristically differing physical properties. This example serves to illustrate the need for simplifying the model system in order to investigate the underlying physical properties of membranes, but hopefully without significantly reducing its biological relevance.

Cell membranes typically contain up to 20% cholesterol, but this can increase locally to as much as 50% in specific "lipid rafts". These cholesterol-rich regions of the membrane promote the concentration of particular proteins, e.g. α-amino-3-hydroxy-5-methyl-4-isoxazolepropionic acid (AMPA) receptors in the post-synaptic membrane, which enhance signaling. The underlying biophysics of these lipid domains or rafts is therefore of considerable fundamental interest and biological relevance.

When reconstituted into certain multi-phase model membranes, receptors such as AMPAR are observed to localise preferentially at the boundary between the phases [6]. To understand this behaviour and its implications for protein localisation in cell

Table 1.2: Prevalence and main transition temperature of different PC lipids in rat synaptic membrane, adapted from references [4] and [5].

PC side chain designation (length:unsaturation)	% weight	T_m (° C)
16:0	50.7	41
16:1	1.0	-36
17:0	0.2	48
18:0	12.6	55
18:1	24.2	-20
18:2	0.6	-53
20:0	trace	66
18:3	1.0	-60
20:3	0.1	-55
20:4	5.6	-70
22:6	3.4	-68

membranes, it is crucial to develop a deeper understanding of the lipid boundary itself – an aspect of bilayer structure that has been given surprisingly little attention in the past. The study of cholesterol-rich membranes and their phase behaviour forms an important part of this thesis.

More generally, the behaviour of all membrane proteins depends to some degree on their interactions with the lipid molecules they are surrounded by. An understanding of the biophysics of lipid membranes is therefore indispensable in the effort to shed light on a wide range of biological processes. This thesis is a record of work done in an effort to further the biophysical understanding of lipid bilayers and to develop novel techniques to accomplish this goal.

1.1 AFM

The atomic force microscope (AFM) is a form of scanning probe microscope introduced by Binnig et al [7]. Its development was preceeded by the invention of the scanning tunneling microscope (STM) in 1981, by Binnig and Rohrer [8, 9]. Both

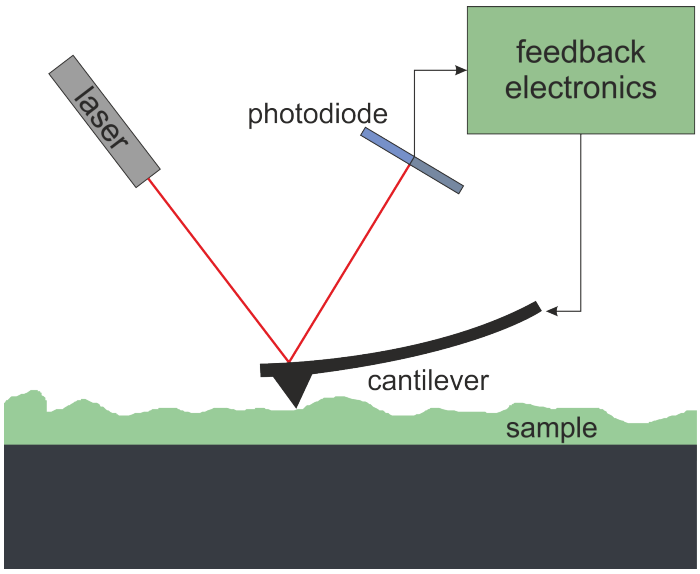

Figure 1.2: Schematic illustration of an AFM tip scanning a surface. Deflection is being monitored with an optical lever detection system.

techniques are characterised by their use of an extremely sharp probe, brought into close proximity to the sample to be investigated, and then laterally scanned across it. A feedback loop is employed to keep the distance between the microscope and the sample constant. In STM it is the tunneling current that is used in the feedback, while AFM uses the deflection of the cantilever onto which the tip is fixed. This deflection is also a measure of the force applied to the sample by the tip, once the spring constant and the inverse optical lever sensitivity (invOLS) are calibrated. There are several ways in which the deflection of the cantilever may be measured, but by far the most common method is to measure the deflection of a laser beam reflected from the back surface of the cantilever [10]. In principle, only two closely spaced photodiodes are necessary to measure vertical displacement, but the use of four diodes allows measurement of torque applied to the cantilever, for instance through friction on the sample surface, and this has become the standard for commercial AFMs. Less common methods to detect deflection include piezoresistive detection [11], piezoelectric detection [12], optical interferometry [13], and capacitive detection [14], among others. The concept and operation of an AFM was reviewed in depth by Giessibl [15].

A schematic representation of the basic AFM setup using an optical lever detection system is given in fig. 1.2.

AFM boasts similar capabilities as STM in terms of resolution and versatility, but adds the big advantage of not depending on conductive tips and samples [7]. Its ability to image samples submerged in an aqueous environment [16] made it an important addition to the toolbox of the biological sciences. Comprehensive reviews of AFM imaging techniques applied to biological structures were published by Fotiadis et al [17], Engel and Müller [18], and Müller and Dufrêne [19], among others.

Numerous distinct AFM operating modes were developed in the years following its inception. The most straightforward of these is the so-called contact mode. Here, a constant deflection (and hence a constant force) is maintained by the feedback loop as the tip is scanned over the surface [20]. The forces applied tend to be in the range of 10^{-6} - 10^{-11} N, depending on the cantilever used and the sample to be investigated [21]. Several so-called dynamic modes of AFM rely on oscillating the cantilever, generally at or near its first resonance frequency. The diversity of dynamic AFM modes stems from the existence of several parameters sensitive to the tip-sample interactions – oscillation amplitude, frequency, and phase shift being the main ones [22]. Two major dynamic modes are amplitude modulation atomic force microscopy (AM-AFM, also known as tapping mode AFM) [21, 23] and frequency modulation atomic force microscopy (FM-AFM, also known as non-contact AFM) [24]. Garcìa and Peréz [22] detail the principles of each of these techniques and outline their respective advantages and disadvantages. In brief, AM-AFM is more suited to imaging in air and in liquid, while FM-AFM tends to be used in vacuum (although it can be used for biological samples as well).

1.1.1 Measuring mechanical properties with AFM

Besides allowing the collection of information such as sample height, friction, phase shift, etc. in scans across the surface, AFM is also suited as a nano-indentation tool [25–28]. Indentation measurements of surfaces with AFM tips yield force curves and are of particular interest for biological applications thanks to their high sensitivity and positional accuracy [29]. The technique is suited to the investigation of both elastic and plastic materials [25, 30–32], and the ability to conduct measurements in aqueous conditions makes AFM indentation viable for the study of biological samples. Early force curve measurements were carried out on bone marrow [33] and cartilage [34, 35]. As the technique matured, it was applied to smaller and smaller biological systems, ranging from individual cells [36–42], to individual cell components such as the cytoskeleton [43–45], down to single proteins [46–48] and indeed single lipids[49]. Its excellent resolution in terms of both the indentation distance and the force applied makes AFM a uniquely suitable technique to study thin layers, such as polymer films [25, 50–53] and lipid bilayers [54–58].

There are a number of models available to aid in the quantitative interpretation of force curve data. Some of the more notable examples for modelling indentation on soft materials will be summarised here. The problem of contact between isotropic elastic bodies was formalised in the works of Hertz [59] and Boussinesq [60] in the 1880s. To this day, a large portion of the work found in the literature employs a Hertzian contact model to estimate material properties of samples. The model assumes linear elasticity and infinite sample thickness. It has been noted that in many experiments, these assumptions are not adequately met and can lead to significant errors [51, 61, 62].

Improvements upon the work of Boussinesq and Hertz were made in the second half of the last century by Sneddon, who derived solutions for a number of axisymmetric indenter geometries [63]. His work represents an important improvement as far as AFM indentation is concerned (where the indenter shape is generally not spherical),

but it still applied only to samples of infinite thickness. Predating its invention by decades, it also did not anticipate the near-atomic resolution that AFM would bring: It is a continuum model which assumes length scales at which the atomic nature of materials becomes irrelevant (i.e. an elastic continuum). The author is not aware of any contact mechanics models that take into account the atomic/molecular structure of materials.

Initial attempts to solve contact problems involving finite layer thickness required extensive numerical computations [64–66], making them impractical for routine AFM data analysis. Subsequent results provided an approximate analysis for very thin layers of soft material bonded to an incompressible substrate [67]. It has since been shown that the relation between force and indentation is strongly dependent on whether the sample layer is free to slide or bonded to the substrate, leading to the development of indentation models that account for bonded and unbonded layers [68, 69].

A review of the techniques and pitfalls associated with the indentation of soft, thin layers and the modelling of the resulting data was published by Dimitriadis et al [70].

1.1.2 AFM tip modification

At the heart of all scanning probe microscopy methods lies the cantilever tip with which the sample surface is interrogated. The size of this tip apex is the predominant determining factor in the maximum obtainable resolution in the lateral plane. Similarly, tips with higher aspect ratios are able to probe steeper features and deeper recesses on the sample surface with fewer artifactual features. For this reason, there have been numerous attempts at fabricating tips of ever smaller sizes, and higher aspect ratios, as well as modifying existing tips to improve their performance.

The majority of physical tip modification methods focus on the attachment of carbon nanotubes (CNTs) to AFM probes [71]. CNTs have properties that make them

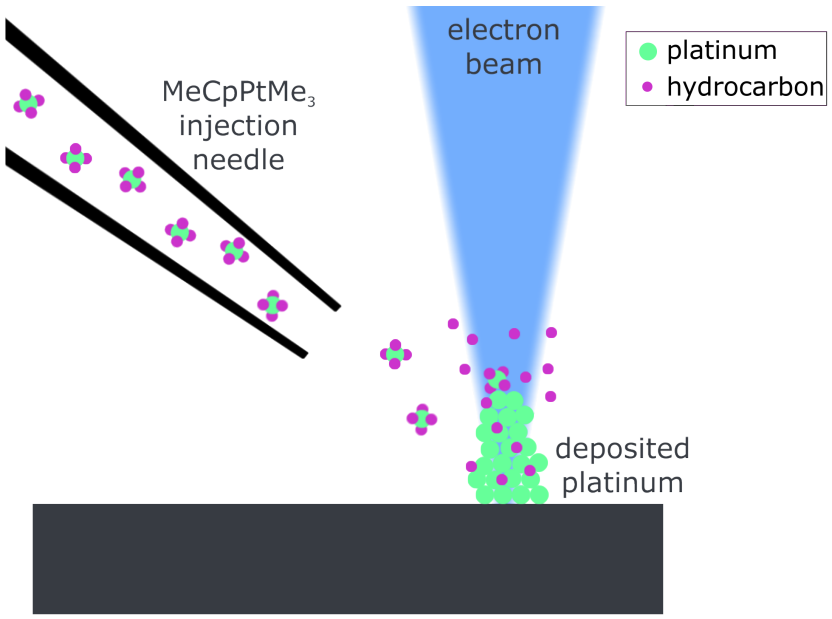

Figure 1.3: A schematic diagram of the process of electron beam induced deposition. A precursor gas – in this case methylcyclopentadienyl (trimethyl) platinum IV – is injected into the chamber in the region of the electron beam, which is used to "crack" the precursor molecules and deposit the material onto the sample surface.

well suited to the role of an AFM probe tip: They have outstanding hardness and durability [72–76], can be extremely small, and have an essentially cylindrical shape (meaning their aspect ratio is extremely high). The advantages and disadvantages of such tips are covered in more detail in chapter 2.

Another common way to modify AFM probes is by depositing material locally at the apex of an existing probe. This can be done by means of ion beam induced deposition (IBID) [77] or electron beam induced deposition (EBID). These two techniques are inherently similar: Both are executed in high vacuum – usually inside a scanning electron microscope (SEM) – and rely on the "cracking" of precursor gas molecules to deposit the constituent material on the surface of the sample (see fig. 1.3). It is also possible to deposit carbon from residual hydrocarbons in the chamber when using EBID, obviating the need for a precursor gas [78]. While the deposition rate and

purity of the deposit is higher using IBID [79], it suffers from higher angular spread of secondary electrons, resulting in a lower spatial resolution. As a result, EBID is generally the preferred method for modification of AFM probes, where minimising the size of the deposit is of paramount importance. EBID deposition of metals has been used to improve STM probes as early as 1988 and resulted in tip radii of 15 nm [80]. The same modifications obviously lend themselves to AFM probes, and were first applied by Hübner et al in 1992 [81]. Since then, there have been a number of successful attempts to improve and build upon this work, which is also covered in chapter 2.

The use of conductive materials in AFM probes is a promising innovation as it allows the simultaneous recording of electrical and mechanical properties of a sample. This has obvious implications for the observation of electronic devices and the study of semiconductors, but it has also proven useful in the study of biological systems. Examples include studies performed on metalloproteins such as cytochrome C [82, 83], lipid membranes [84], and bacterial protein layers such as bacteriorhodopsin from *H. salinaria* [85], the hexagonally packed intermediate layer of *D. radiodurans* [86], and outer membrane protein F from *E. coli* [87].

Where conductive probes are to be used in liquid – as is generally desirable for biological applications – they have to be insulated everywhere except at the tip to reduce background current and capacitance from the solution. Several approaches to achieving this have been reported. Insulated AFM probes may be broadly classified into two types: ones where the tip itself is conducting and constitutes the electrode [86, 88–96] and ones which have an electrode near or surrounding a non-conducting tip [97–100].

Each of these types of probes has been fabricated in a variety of ways. Some attempts involve fabrication at the wafer level, either using conventional lithography [92, 100–102], or electron beam lithography [94, 103]. Such an approach is economical due to its high throughput, but can suffer from yields as low as 50% [86]. Another method

for fabrication involves focussed ion beam (FIB) milling, whereby the previously applied insulating coating is ablated to expose the underlying conductive layer. Both recessed electrode probes [97, 98] and tip electrode probes [89, 93, 95, 96, 104] have been fashioned in this way. In some instances, EBID was used to fashion a tip out of tungsten [89] or cobalt [104] after FIB milling. While such techniques are more time-consuming than batch fabrication, they have higher yields and better control thanks to in situ SEM imaging.

1.2 Lipid bilayers

Due to the complex nature of cell membranes, which consist of mixtures of many lipids often with asymmetric distributions between leaflets anchored into cytoskeletal support structures and containing a host of transmembrane and membrane-bound proteins, it is often instructive to study so-called model membranes instead. These simplified versions of cellular membranes usually consist of several species of lipid allowing conclusions to be drawn about the interaction of these lipids with one another and proteins reconstituted into them. Study of model membranes has led to the discovery of a number of different phases in which bilayers can exist. Most notable among these are:

- The gel phase (L_β), in which the hydrocarbon chains in each leaflet are in a well-ordered state and lateral motion of lipids is restricted.

- The liquid disordered phase (L_α, also known as the liquid crystalline phase, fluid phase, or simply liquid phase), characterised by relatively free lateral diffusion of lipids and little ordering of the hydrocarbon chains.

- The liquid ordered phase (L_o), in which there is an ordering of the hydrocarbon chains, but little restriction of lateral lipid motion.

There are also more exotic phases such as the "subgel" phase and the "ripple" phase. An early review of characterisations of lipid film phases was published by Dufrêne and Lee in 2000 [105], which is concerned with the applications of AFM for characterising both the structural and physical properties of lipid films. For a review on lipid phase structure and thermodynamics see Tristram-Nagle and Nagle 2004 [106], which summarises experimental work using dilatometry, density centrifugation, differential scanning calorimetry, and X-ray scattering techniques to shed light on lipid bilayer structure as a function of temperature. A more recent review of phase separation in membranes was published by Heberle and Feigenson [107]. This paper focuses on compositional heterogeneities at length scales from a few nanometres to micrometres, paying special attention to the range associated with cell membrane rafts. Zumbuehl et al [108] reviewed selected artificial lipids, highlighting the impact of the hydrophobic tails and the interfacial backbone connecting them to the head group on phase behaviour (including interdigitated phases). For reviews of phase behaviour of natural membranes, focusing on the formation of cholesterol-containing rafts, see Simons and Ikonen [109] and Jacobson et al [110]. The former introduces the concept of lipid rafts in cell membranes and proposes their function as protein recruitment platforms during signal transduction. The latter compares naturally occurring lateral heterogeneity with the concept of lipid rafts as it has emerged from the study of model membrane systems, cautioning that the differences are significant. It also provides a review of the physical tools used to study biological membranes as a liquid that is ordered in space and time. A review of particular interest to this thesis was published recently by Alessandrini and Facci [111]. It is concerned with the use of AFM to elucidate the phase behaviour of supported bilayers (see also section 1.2.1).

Cholesterol (see fig. 1.1D) in particular has profound and complicated effects on lipid bilayers and their phase behaviour. Although it is a lipid, the structure of cholesterol is very different from that of a phospholipid. Its hydrophilic domain is compar-

atively small, consisting of a single alcohol group. Meanwhile, its hydrophobic part takes the form of a planar structure composed of several fused hydrocarbon rings, terminated in a short single chain tail. Cholesterol intercalates between lipid molecules, filling free spaces and reducing the mobility of the surrounding hydrocarbon tails [112]. This has the effect of increasing the mechanical rigidity of liquid phase bilayers [113], while reducing the rigidity of gel phase bilayers [114] (and inducing the transition to the liquid ordered phase). Due to its central role in modulating membrane fluidity in vivo, cholesterol has been the focus of numerous studies, both experimental and theoretical.

Over the years, numerous experimental techniques have been used to investigate lipid bilayers and their structural and functional properties. Different methods are more suited to different aspects of lipid behaviour, and no single technique is able to probe the entire range of phenomena exhibited by lipid bilayers. This point is illustrated in fig. 1.4. The figure shows a logarithmic plot of the time and length scales over which some bilayer events occur. These events range from the molecular scale of rotational diffusion and gauche effects (not accessible by current experimental techniques), over raft nucleation and growth at intermediate scales (potentially accessible via high-speed AFM), to the presence of stable macrodomains spanning many micrometres (in the domain of optical techniques).

Optical microscopy techniques appeal through their relative simplicity and high throughput, but tend to lack both spatial and temporal resolution. Techniques such as fluorescence resonance energy transfer (FRET) [116], near-field scanning optical microscopy (NSOM) [117, 118], fluorescence correlation spectroscopy (FCS) [119, 120], and fluorescence recovery after photobleaching (FRAP) [121] substantially extend the ability of optical techniques to provide quantitative information. Super-resolution microscopy extended the reach of optical techniques in terms of spatial resolution. The inception of stimulated-emission-depletion (STED) microscopy allowed the observa-

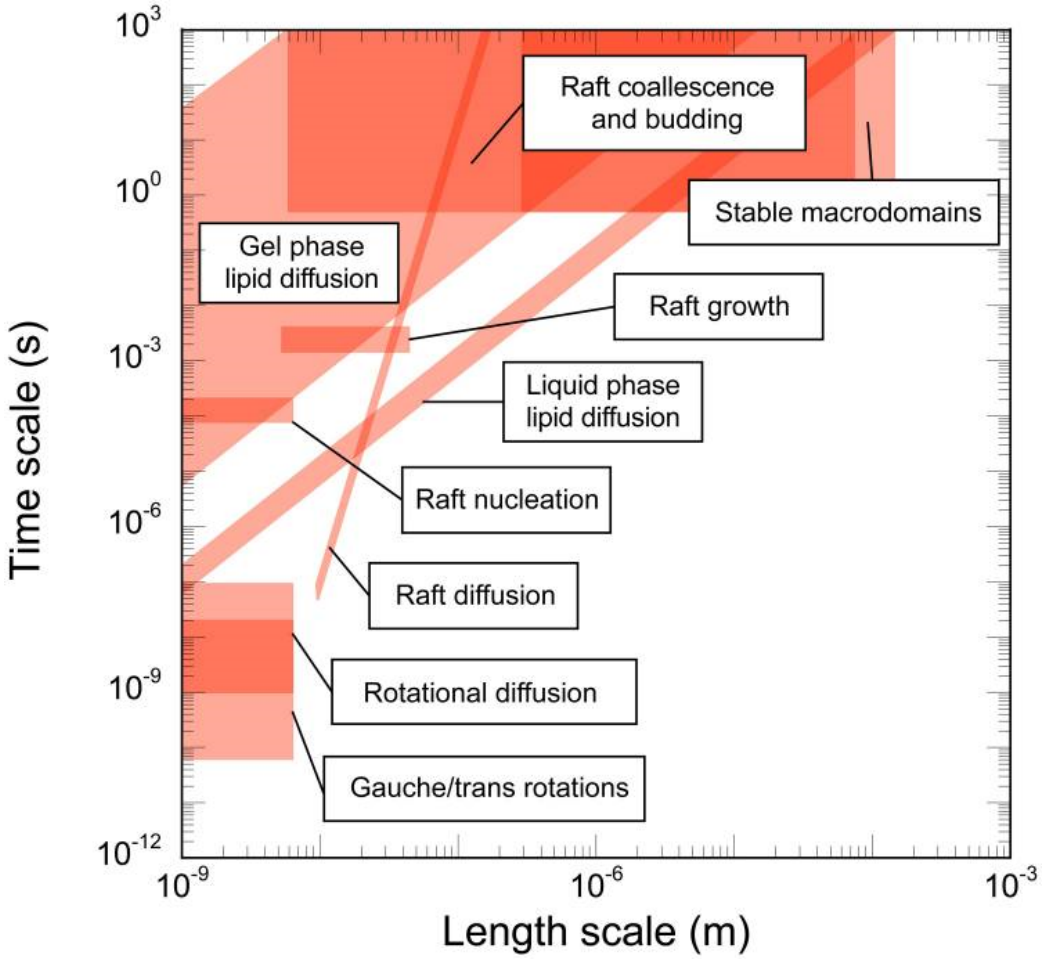

Figure 1.4: An illustration of the range of times and lengths over which membrane phenomena occur. It is clear that no single technique is able to adequately probe the entire regime, necessitating a multi-pronged approach to the experimental study of lipids and bilayers. Reprinted from Elson et al [115].

tion of fluorescent probes with a resolution an order of magnitude below the diffraction limit [122]. More recently, stochastic methods have been employed to achieve super-resolution: Stochastic optical reconstruction microscopy (STORM) [123] and photoactivated localization microscopy (PALM) [124] are the most well-established of these and are able to localise particles with, in principle, molecular-scale resolution. In practice, resolutions down to 6 nm has been reported [125]. Nevertheless, techniques not relying on optics remain the methods of choice when spatial resolution is paramount.

Nuclear magnetic resonance (NMR) spectroscopy [126, 127] has been used since the 1960s to study lipid bilayers [128–130]. In this technique, the absorption of electromagnetic radiation by certain nuclei in a magnetic field is exploited to determine the structure, dynamics, reaction state, and chemical environment they are in. Electron paramagnetic resonance (EPR) is analogous in its basic concept to NMR, but it is less widely used due to the prerequisite of unpaired electrons in the sample. This requirement is an impediment in that most stable molecules have all their electrons paired, but it also grants EPR great specificity.

Structural analyses of lipid bilayers by means of neutron [131], electron, or X-ray [132, 133] diffraction boast superb resolution, but to achieve this requires lipids to be in conditions dissimilar to physiological ones. In particular the low level of hydration required in such experiments leads to difficulties in generalising the conclusions drawn from them to biologically relevant cases.

Scanning probe techniques are another popular non-optical technique for the study of bilayers. Of these, AFM is by far the most common, although other techniques have been pioneered. NSOM may be combined with AFM to provide combined fluorescence and topographical information. Scanning electrochemical microscopy (SECM) [134, 135] and scanning ion conductance microscopy (SICM) [136] are used to detect electroactive species in liquid and have both been used to study bilayers.

Kelvin probe force microscopy (KPFM) [137] provides a way to measure the contact potential. An example of its application is the detection of nanoscale electrostatic domains in lipid membranes which have implications for understanding the amyloid toxicity of Alzheimer's disease [138, 139].

A review of the most common experimental techniques used for the structural study of bilayers to date can be found in Elson et al [115]. It covers a wide range of techniques, including AFM, NSOM, FRET, FRAP, STORM, PALM, FCS, STED, and NMR, and their applications in the study of the phase behaviour of bilayers.

Molecular dynamics (MD) simulations have also been widely used to study lipid bilayers [140–142]. Virtually all aspects of lipid bilayer behaviour have been studied in this way, including the effect of cholesterol [143] and bilayer permeability to a variety of molecules, such as water [144, 145], small organic molecules [146], and carbon nanotubes [147]. Of particular interest to this thesis is recent work investigating the Poisson's ratio, ν, and Young's modulus of lipid bilayers in different phases by means of MD simulation [148]. The study concludes that in general the assumption of incompressibility ($\nu = 0.5$) is valid for bilayers in the liquid disordered and gel phases (liquid ordered systems were not investigated). Values of Young's modulus derived for liquid disordered bilayers is $\sim$5 MPa (no value given for gel phase).

1.2.1 Supported lipid bilayers

When studying lipid bilayers with scanning probe microscopy techniques, it is generally necessary to place them on a solid support to localise them. Supported lipid bilayers (SLBs) are the system of choice when studying single or mixed lipid systems as well as lipid-protein systems with AFM. The most commonly used support surface used is muscovite mica, which is inexpensive and may readily be cleaved into atomically flat crystal planes. Freshly cleaved mica is relatively hydrophilic and negatively charged. As a result, lipid vesicles in ionic buffer solution spontaneously rupture on

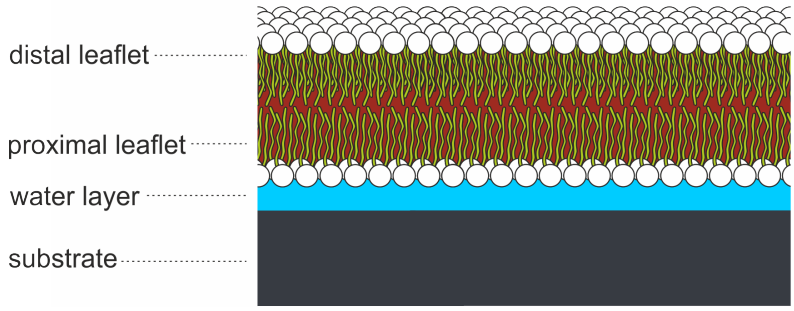

Figure 1.5: A schematic diagram showing a supported lipid bilayer, composed of two leaflets (proximal and distal with respect to the substrate) separated from a flat substrate by a thin water layer.

its surface to form bilayers adhered to it. The rupture process has been studied using quartz crystal microbalance (QCM) studies [149–151], as well as being observed with AFM [152–155]. Sometimes the two techniques are combined [156–159]. A schematic illustration of a suspended bilayer is shown in fig. 1.5.

As mentioned, SLBs are commonly used in the study of lipid behaviour and protein structure via SPM techniques. They have been used to study the effects of pH [160], ionic strength [160, 161], temperature [157, 162–165], phospholipid structure [57, 161], lipid charge [166], and lipid-protein interactions [153, 167, 168] on bilayer properties, among many other factors. Beyond this, there are numerous applications for supported bilayers in diverse fields. Examples include advances in novel water purification and desalination techniques [169], pollutant sensing and monitoring [170], neuroreceptor detection [171], and amperometric sensing devices [172]. A deeper understanding of lipid biophysics is indispensable in the development of both novel devices and in research into living systems. Many questions about the behaviour of lipids and lipid-protein systems remain unanswered, due to a lack of the tools to study bilayers in the required detail.

When employing SLBs for the study of lipids and proteins, it is important to be aware of the effect of the support on the system. It is known that a water layer of several nanometers forms between a lipid bilayer and its support [173, 174], so the

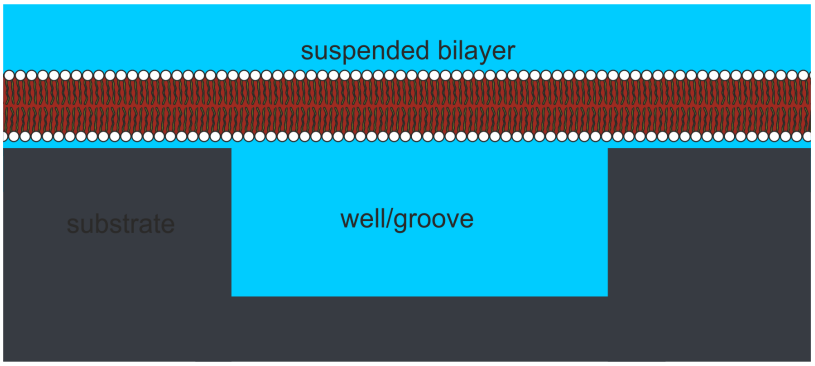

Figure 1.6: Schematic of a bilayer spanning a recessed groove or well in a microfabricated substrate, forming a suspended bilayer surrounded by aqueous environment on either side.

bilayer is not resting directly on the support. Still, caution should be employed in generalising conclusions from SLB experiments, as the nature of the support has been shown to affect lipid nanomechanics [160].

1.2.2 Suspended bilayers

Some of the issues caused by the use of SLBs can be addressed by using microfabricated substrates with wells or other recesses in them. When lipid bilayers are placed on such substrates, some of the bilayer spans the recessed regions, forming a suspended bilayer, as can be seen in fig. 1.6. This removes the effects of a hard substrate in the proximity of the bilayer. There are numerous potential applications for incorporation of suspended bilayers in devices, ranging from sensors [175], to DNA sequencing [176], to the development of an interface between neurons and silicon chips (Nahoko Kasai, personal communication, December 2012). Confining solution inside cavities allows the two leaflets of a bilayer to be placed in distinct aqueous environments, as well as enabling convenient fluorescent detection of suspended bilayers [177, 178].

AFM imaging of suspended bilayers is less straightforward than imaging SLBs, but it is nevertheless possible [84]. The mechanical properties of membranes may be assessed by comparing the data to a suitable model. The elastic modulus [179] and

structural changes upon stretching [180] have been measured in the case of purple membrane of *H. salinaria*. Stability may be improved by depositing a mesh of CNTs on the substrate which lends some support to the suspended part of the bilayer. This has also been demonstrated with purple membrane [181].

1.3 Overview

Chapter 2 describes the fabrication process and subsequent characterisation of AFM probes modified by electron beam induced deposition of platinum. These tips are significantly sharper than the commercial probes before modification, and have a much improved aspect ratio. Their ability to withstand the stresses of contact and tapping mode AFM imaging is investigated and their performance is compared to unmodified probes in a variety of ways. Their electrical properties were also characterised.

Chapter 3 is concerned with the use of force curves (aided by imaging) to assess the mechanical properties of supported lipid bilayers. Several lipid systems are studied and the effect of cholesterol content and temperature on their mechanical properties is investigated. The modified probes introduced in chapter 2 are used to probe the boundary region between different lipid phases with unprecedented resolution.

In chapter 4 a new technique for the study of lipid bilayers is introduced and explored. Giant unilamellar vesicles are ruptured across microfabricated well substrates. By applying osmotic pressure, membrane budding is induced and observed using confocal microscopy. Lipid bilayers of varying compositions and phases are studied and compared. A mathematical model designed to explain the energetics of membrane budding in the experiments is used to obtain quantitative information about the mechanical properties of the membranes.

In chapter 5 the use of modified probes for the simultaneous study of membrane channels in terms of topography and electrical conductivity is discussed. The design

and construction of a prototype cantilever holder and AFM stage are detailed, and preliminary measurements to characterise noise levels and investigate the feasibility of the proposed simultaneous measurements are presented.

Chapter 6 offers concluding remarks about the work presented in the thesis, as well as presenting an outlook on potentially fruitful directions for future work.

Appendix A contains the code for the MatLab program used to analyse the force curve data presented in chapter 3.

Chapter 2

EBID modification of AFM probes

2.1 Introduction

Atomic Force Microscopy (AFM) is a well-established technique for high-resolution spatial imaging and surface characterization. In addition to enabling routine sub-nm topographical measurements on conducting and insulating materials, such as quantification of surface roughness, AFM has become a tool of choice for high-resolution imaging of biological materials. Sub-cellular structures, such as membranes, DNA and individual proteins can be investigated under near-physiological conditions, not only in terms of topography, but information can also be obtained on mechanical, chemical and functional properties.

At the heart of AFM, and every scanning-probe microscopy technique, is the carefully constructed probe tip which is used to interrogate the sample surface. AFM cantilevers are most commonly microfabricated silicon-nitride chips with a sharp pyramid-shaped tip apex forming the probe [182]; metal-coated tips can enable electrical measurements [183] or they can be functionalised to provide chemical sensitivity [184]. At a simplistic level, the interaction responsible for AFM image formation may be described as the direct contact between the area of the probe tip and the sample surface. Although the true interactions are more complicated, and long-range forces can play a significant role, the size of the probe is critical in determining the spatial resolution. To this end, there have been many efforts to fabricate smaller and sharper probes, with the majority of recent work concentrating on using carbon nanotubes (CNTs) as AFM probes [71].

CNTs have material properties that make them well suited for AFM and the high resolution possible with CNT AFM probes has been demonstrated on a variety of samples. Their advantages in terms of high aspect-ratio, mechanical properties and well-defined chemistry are documented. The first multi-walled CNT probes for AFM were presented by Dai et al in 1996 [185]. Single-walled nanotubes followed shortly after [186]. The latter have the advantage in terms of probe radius, but are more

difficult to work with and are more prone to buckling [147]. Although there are reports of successful CNT preparation and cantilever attachment techniques, including electrostatic pick-up with an AFM cantilever and mechanical micromanipulation in a scanning electron microscope (SEM), these methods are complex, multi-stage processes; it has proven very difficult to consistently produce CNT probes of a specified length, diameter and orientation, all of which are essential for reproducible high-quality imaging. CNT probes are also liable to cause imaging artefacts when scanning steep steps and other high aspect ratio features [187]. Reviews on fabrication of CNT probe tips and their application can be found in Wilson and Macpherson [71], Nguyen et al [188], and Hafner et al [189].

In this work we use a rapid and more direct route to the fabrication of ultra-sharp, high aspect-ratio probes for AFM: Electron-Beam-Induced Deposition (EBID) [190]. Although it is a well-established nanofabrication technique, there are surprisingly few reports on the use of EBID to produce ultra-high resolution AFM probes. Efforts in this area normally rely on volatile hydrocarbons, present in the SEM chamber through contamination, to grow carbonaceous deposits [191–198]. The reproducibility, composition and chemical nature of the deposited material therefore strongly depends on the level and type of contaminant in the microscope. Deposition times also depend upon the degree of contamination but are typically long, which means that the geometry of the deposit may be compromised by instrument stability and sample drift. The resulting probes are highly insulating, precluding their use for sensitive electrical measurements. Other materials, such as tungsten [89] and cobalt [104], have been deposited with EBID to modify AFM cantilevers for the purposes of electrical and magnetic studies.

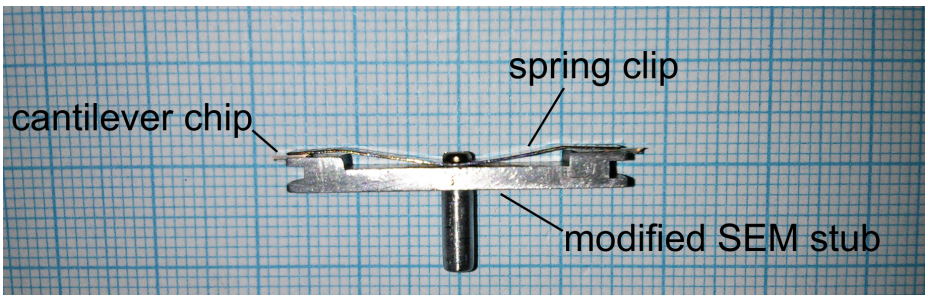

Figure 2.1: Photograph of the holder used for EBID modification of up to two cantilevers at a time. The holder was made from a standard circular SEM stub by removing the sides of the disk (allowing for greater rotational freedom) and milling down into the centre to allow for the attachment of the spring clip by means of a screw. Grooves were milled in the ends to localise the cantilever chip in place.

2.2 Experimental

2.2.1 Microfabrication

The probes described here are fabricated by EBID of platinum on the tip of commercial AFM cantilevers. Platinum is highly inert and has good biocompatibility; it is also a well-established electrode material, making it potentially suitable to electrical modes of AFM. The EBID process and subsequent SEM imaging was performed in an FEI Nova 600 NanoLab (FEI, The Netherlands). AFM cantilevers (OMCL-TR800PB-1 and OMCL-RC800PB-1, Olympus, Japan) were positioned in a custom holder made from a modified SEM stub. The holder incorporated a conducting spring-clip to hold the cantilever chip in place and enabled the cantilever to be held and imaged at a large range of angles for modification and subsequent inspection (see fig. 2.1). Due to the short working distance of the electron microscope it was necessary to recess the spring clip to avoid possible contact with the scan head.

For modification, the cantilever chips were aligned so that the tip axis was collinear with the electron beam. The choice of the electron beam voltage, current and patterning parameters for EBID is critical in determining the geometry, dimensions and composition of the resulting deposit, whilst optimal focus and astigmatism

correction are crucial for production of the smallest features. Through a series of systematic experiments, probes with the smallest radius of curvature were grown with the microscope in "Immersion-lens mode", set at an electron beam voltage of 18 kV and a nominal beam current of 39 pA. To help obtain highly reproducible deposits of known composition, the SEM chamber and the cantilever were subjected to a brief RF-plasma clean with an Evactron 25 De-Contaminator (XEI Scientific, USA) immediately prior to EBID. This removes organic contaminants that would otherwise be incorporated into the deposited material. The platinum-containing precursor, methylcyclopentadienyl (trimethyl) platinum IV (FEI, The Netherlands) is introduced through a gas-injection needle positioned ∼100 µm from the sample surface. Platinum deposition is initiated by the interaction of the electron beam and surface-adsorbed precursor molecules; by localising the beam at a point on the tip apex of the cantilever, an ultra-sharp, high aspect-ratio probe is grown, whose height is controlled by the duration of the irradiation.

Sputtered gold films for characterisation of the lateral resolution of AFM probes were deposited in an Emitech K675XD sputter coater (Quorum Technologies Ltd., UK). Polystyrene latex nanospheres for assessment of aspect ratio of probes and multi-walled carbon nanotubes used for tip reconstruction calculations were obtained from Sigma-Aldrich Corporation, USA.

2.2.2 Mechanical Characterisation

After EBID deposition the probes were characterised both mechanically and electrically using a Dimension 3100 AFM (Bruker Corporation, USA). For the mechanical characterisation, a number of samples were assessed for their suitability, including test gratings – TGT1 spikes and TGQ1 square gratings (NT-MDT, Russia), as well as a NioProbe film sample for tip sharpness assessment (Aurora NanoDevices Inc., Canada) – carbon nanotubes (CNTs) on mica, DNA on mica, and gold nanoparticles

on mica, among others. A chromium-coated glass cover slip sputtered with 20 nm of gold in an Emitech K675XD coater (Quorum Technologies, UK) was found to be the most suitable sample to compare the performance of modified and commercial probes in terms of lateral resolution. This sample, however, yields almost no information on the impact of the high aspect ratio of the modified probes. Polystyrene latex nanospheres (Thermo Scientific, USA) arranged in a hexagonally close packed monolayer on mica were found to give a suitable topography to examine effects of aspect ratio on probe performance.

2.2.3 Electrical Characterisation

The characterisation of the electrical properties of the modified probes was performed using the tunnelling AFM (TUNA) attachment for the Dimension 3100 AFM and the corresponding AFM holder. Gold and platinum coated glass samples were electrically connected to the sample stage by means of a spring clip on a polished aluminium block. Modified and commercial probes were brought into contact with the gold or platinum film, completing the circuit. Calibration of the TUNA module is discussed in section 2.3.3. Desktop multimeter readings were used as a secondary source of data to confirm the validity of the measurements.

2.3 Results

2.3.1 SEM imaging

SEM images of the pyramidal tip of a commercial OMCL-TR800PB-1 cantilever before and after EBID modification are shown in fig. 2.2. The commercial probe dimensions are typical of this model of cantilever, with a measured radius of curvature of $\sim$21 nm, compared with $\sim$4 nm for the EBID-modified probe (see insets in fig. 2.2); in this case (exposure duration of 500 ms) the platinum probe tip has a length of

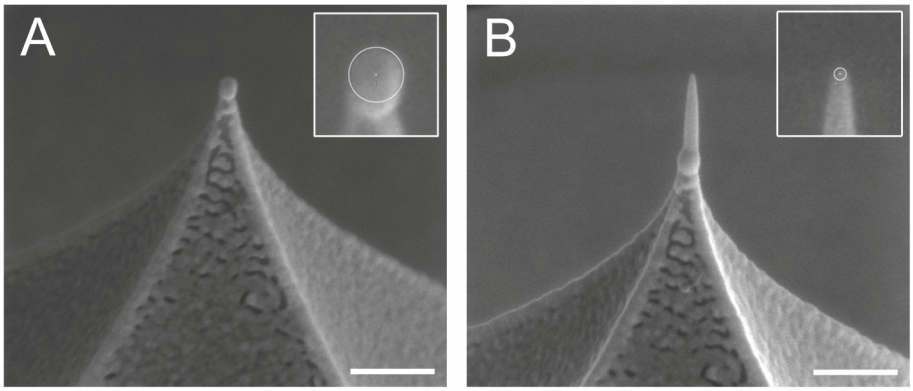

Figure 2.2: SEM images of (A) a commercial OMCL-TR800PB-1 cantilever and (B) the same cantilever following modification by EBID of platinum; scale bars: 200 nm. In both images the axis of the probe is tilted at 52° to the electron beam. The magnified probe tips (shown inset) show calibrated circles drawn in the SEM software to measure radius-of-curvature; circles of radius ∼21 nm and ∼4 nm for the commercial and modified probe, respectively. Figure adapted from reference [190].

∼225 nm and is ∼35 nm wide at its base. SEM imaging of the probes confirmed that the results were highly repeatable (a total of more than 100 probes were produced with radius 4.0 ± 1.0 nm) and the length of the probes finely tunable by varying the duration of the deposition. It was found that increasing the deposition time produces a longer probe but does not increase its radius of curvature at the tip. The probes were also imaged after use to determine their ability to withstand the interaction with hard samples in routine AFM imaging.

2.3.2 Characterisation of mechanical properties

Radius of curvature is generally considered to be the most important aspect of an AFM probe in determining its performance. This is generally true when the goal is to maximise lateral resolution on samples with only small height variations. When imaging samples with large, sudden height variations, such as steps, protrusions, or recesses, on the other hand, aspect ratio of the probe becomes important. To characterise each of these aspects of probe geometry, different samples as well as different imaging parameters are required. Consequently, the mechanical characterisations was

performed in two steps, the first to determine lateral resolution, and the second to assess the effect of aspect ratio on probe performance.

2.3.2.1 AFM of gold grains

Sputtered gold films with a characteristic grain size in the region of the probe radii were imaged with modified and unmodified probes. The surface was imaged in contact mode, and scan parameters were optimised in each case. Generally, no significant differences in imaging parameters (free amplitude, amplitude setpoint, integral/proportional gain, scan speed) were required between the two types of probe to obtain optimal imaging. The resulting images were compared visually and analysed for information pertaining to the resolution. Typical AFM scans and sample line sections are shown in fig. 2.3. The images are unmodified apart from routine first-order flattening to remove overall tilt and line to line offsets. The enhanced level of detail obtained with the modified probe (fig. 2.3 B) is clear in a comparison of the two images and their line scans. Since the image obtained in AFM is the result of a convolution of the probe tip with the surface features, a probe with a radius of curvature larger than the features on the surface of the sample will give little information of the actual topography. Instead, the image will effectively be an image of the probe itself, repeated at all the highest features of the surface. This effect can be seen in fig. 2.3 A, taken with a $\sim$21 nm radius probe, where there is little feature–to–feature variation. In fig. 2.3 B, captured using a $\sim$4 nm radius modified probe, many of the smaller features are resolved and the image is more representative of the actual topology of the surface.

The probes were subsequently imaged using SEM to assess any damage caused by scanning. No significant probe wear or contamination was observed, confirming that the images were not affected by either of these extraneous factors. The radius of

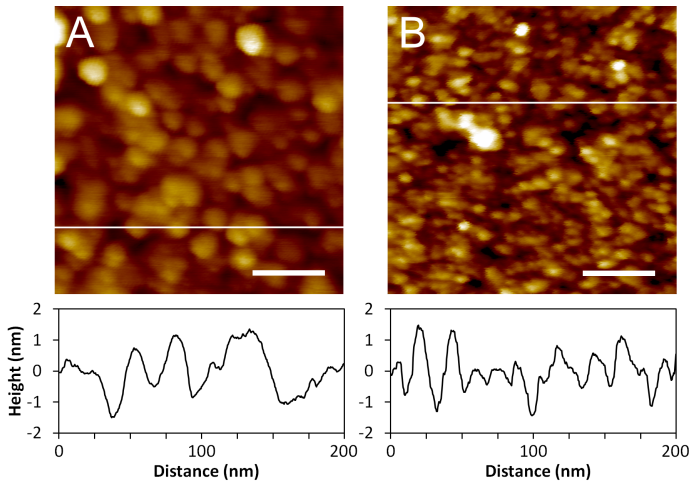

Figure 2.3: AFM height images captured with commercial (A) and modified (B) probes on a 20 nm layer of sputtered gold on glass. Cross sections along the white lines are given below each scan and highlight the differences in feature-to-feature variation. Scale bars: 50 nm. Figure adapted from reference [190].

curvature of the modified probe was unchanged to within the tolerance of the SEM measurement (∼0.5 nm).

To provide a quantitative measure of the improved performance of the modified probe, power spectral density (PSD) curves were calculated for each probe and compared. PSDs describe the topographical data as a function of spatial frequency and enable a more thorough comparison of probe performance than simple statistical parameters, such as surface roughness, which ignore the lateral length-scale of the topography [199–201]. Shown in fig. 2.4 are PSDs calculated from the images in fig. 2.3 over the range of spatial frequencies corresponding to feature sizes from 200 nm (the image size) down to 0.8 nm, which is considerably smaller than the radius of either probe. A higher PSD at a certain spatial frequency indicates a higher sensitivity of the probe to features corresponding to that frequency. The figure shows that the modified probe produces a higher spectral density over most of the spatial frequency range. This can be seen more clearly in the ratio of the PSD curves, shown in the inset of fig. 2.4. At the lowest spatial frequencies, corresponding to the very largest feature sizes, the PSD ratio approaches one, confirming as expected that both probes

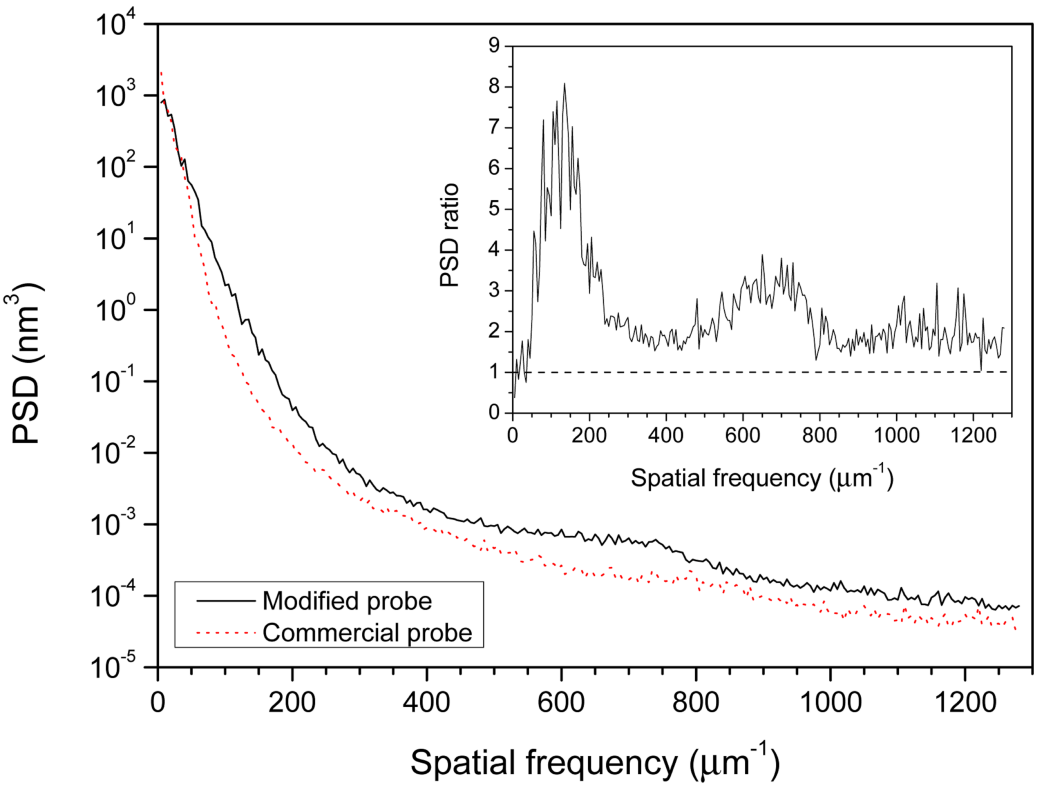

Figure 2.4: Power spectral densities corresponding to the AFM images in fig. 2.3. The ratio of power spectral densities of the modified probe to the commercial probe is shown in the inset. A ratio greater than one indicates improved performance with the modified probe. Figure adapted from reference [190].

perform in the same way. At 50 μm^{-1}, which corresponds to a feature size of 20 nm, the PSD ratio is already greater than two. It further improves up to a maximum of $\sim$8 as the feature size diminishes. The degree of enhancement decreases at spatial frequencies close to 250 μm^{-1}, corresponding to the 4 nm radius of curvature of the modified probe.

The small increase in the PSD ratio centred on $\sim$650 μm^{-1} is unexpected and may be the result of a real increase of features on the surface in the size range 1.25 - 2 nm, which the modified probe would likely be better at recording. Alternately, it is possible that the modified probe, due to its high aspect ratio, causes a slight increase in noise that corresponds to these spatial frequencies.

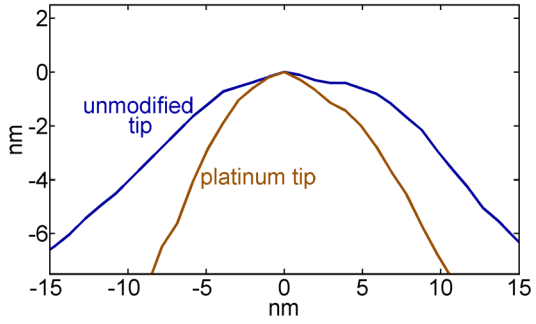

Figure 2.5: Blind reconstruction profiles of modified (red) and commercial (blue) probes from images of multiwalled carbon nanotubes on mica.

2.3.2.2 AFM of carbon nanotubes

Single multiwalled carbon nanotubes on mica were imaged such that each scan line crossed the nanotube at right angles. The resulting images were used to estimate the tip shape with the blind reconstruction algorithm of the scanning probe analysis software SPIP^{TM}. An example of a blind reconstruction of a commercial and modified probe is shown in fig. 2.5. The reconstruction of the modified probe (red curve) has a radius of curvature of between 5 and 7 nm, while the one of the radius of curvature of the commercial probe (blue curve) is between 18 and 22 nm. These values are in good agreement with the values obtained from SEM measurements for these probes. Blind reconstructions of the tip shape offer a crude measure of tip performance. The smaller the reconstructed tip, the smaller the distortion of the topography image by the convolution of tip and surface features.

2.3.2.3 AFM of polystyrene nanospheres

The radius of an AFM probe tip is of primary importance for better resolution on a relatively flat surface, however probe aspect ratio is the determining factor when imaging steep slopes and recesses. A close-packed monolayer of nanospheres forms high aspect ratio surface features, with the interstices between spheres being particularly suitable for probe evaluation.

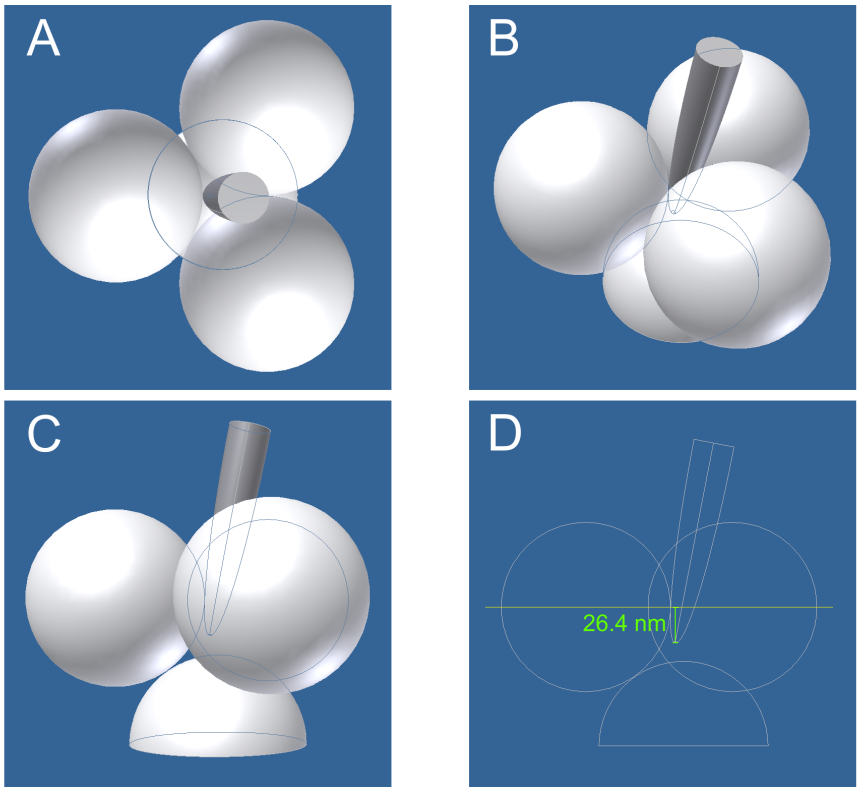

Figure 2.6: Collision detection modelling of a modified probe tip being inserted into the interstitial space between three 125 nm diameter nanospheres. A, B, and C show top, angled, and side views, respectively, of the sphere array with the platinum pillar probe tip inserted to its maximal depth. D shows a wire side view with the measurement of the insertion distance past the equatorial plane (in this case 26.4 nm) marked.

Polystyrene nanospheres suspended in solution spontaneously arrange in a hexagonally close packed arrangement on a flat surface when left to dry. The size of the sphere dictates the size of the interstitial gap, with the relation of the radius of diameter of the largest cylinder that can be fit between three adjacent spheres given by

$$r = (\frac{2}{\sqrt{3}} - 1)R$$

where r is the radius of the hypothetical cylinder (the interstitial radius), and R is the radius of the spheres. Initially, 125 nm diameter spheres (deposited on freshly cleaved mica) were selected for their interstitial radius of just over 9 nm, which we expected would exclude the unmodified probe but admit the modified ones. In practice it was found that the depth to which the modified probes penetrated the layer was incommensurate with the results expected from collision detection modelling. In the modelling a computer aided design program was used to model the tip (using SEM images as a reference) and a unit cell of the sphere array. The tip was then inserted into the interstitial space (angled by 11°, which is the angle at which the cantilever chip is held in the AFM holder) and its maximal penetration depth recorded. Images of the collision modelling process are given in fig. 2.6. The expected penetration depth of a typical 4 nm radius of curvature tip into an array of 125 nm nanospheres was found to be ∼85 nm by this method, measured as the distance from the tops of the spheres in the layer. The experimental value was found to be around 55 nm, when the nanospheres were imaged in air in tapping mode. This discrepancy was likely due to the dispersant compound included at low concentration in the solution of the nanospheres to stop aggregation, which was deposited in the interstitial spaces as the water evaporated and was visible in SEM imaging. Even with this contamination issue, the 125 nm sphere samples highlighted advantages to using the modified probes over the commercial ones (fig. 2.7).

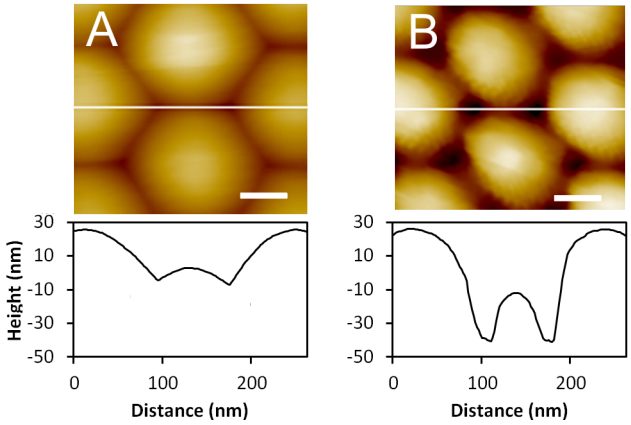

Figure 2.7: AFM height images captured with commercial (A) and modified (B) probes on 125 nm polystyrene spheres. Cross sections along the white lines are given below each scan and show the improved detail retrieval of the modified probe, especially in the recessed regions in between spheres. Scale bars: 100 nm.

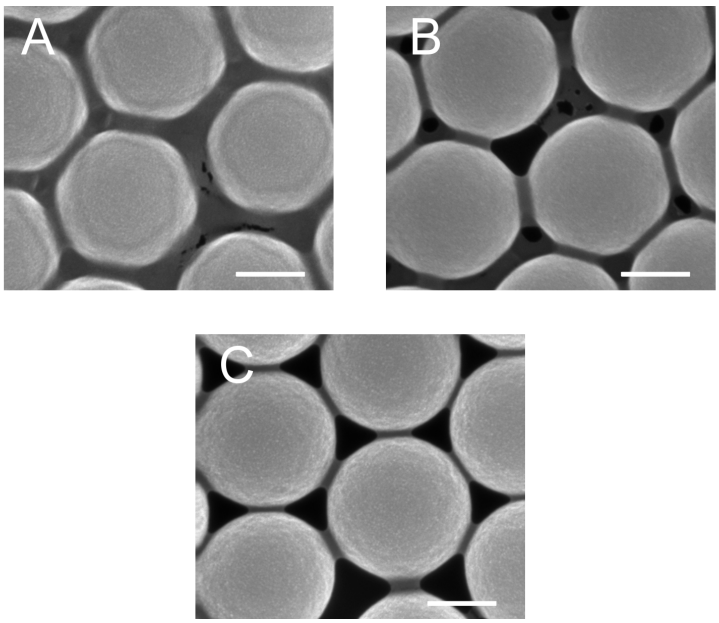

Figure 2.8: SEM images of 400 nm polystyrene beads. A: Nanosphere layer on mica near the edge of the sample, coated with 5 nm of titanium. The interstitial regions between spheres are almost completely blocked by deposited dispersant. B: Nanosphere layer near the centre of the same sample. Dispersant contamination is noticeably reduced. C: Nanosphere layer deposited on mica, then placed in excess water for two hours, dried once more, and finally coated with 5 nm of ITO. Interstitial regions seem essentially free of contamination. Scale bars: 200 nm.

400 nm diameter nanospheres were imaged as well, but the problem of the dispersant contamination persisted. Imaging of these nanospheres with SEM led to the discovery that the contamination was less pronounced in the centre of the sample (which dried out last) than near the edges (see fig. 2.8 A and B). AFM measurements bore this out: The height difference from the top of the spheres to the lowest point reached in the interstitial space was ∼15% higher in the centre than near the edges. Leaving the deposited nanospheres in pure water for two hours was found to further reduce the amount of contaminant present, as evidenced by SEM imaging (see fig. 2.8 C). Unfortunately, these measures also left the nanospheres very weakly bound to each other, resulting in them moving under the influence of the AFM tip, especially when imaging near an edge of the monolayer or near defects. A thin coating of ITO or titanium was found to resolve this problem satisfactorily without blocking the interstitial spaces.

AFM topography images of nanospheres soaked for two hours in pure water and coated with 10 nm of ITO captured with modified and commercial probes are shown in fig. 2.9. Even though the interstitial radius between three of these spheres is almost 31 nm (not accounting for residual contaminant or the ITO film), the commercial probes do not penetrate past the equatorial plane of the spheres (fig. 2.9 A). In contrast, the modified probes are able to penetrate all the way down to the mica surface beneath the spheres, as can be seen in the cross sections of fig. 2.9 B, where the total height between the bottom of the scan and the top of the sphere is 400 nm – the diameter of the spheres.

The intricacies of the AFM probe/holder ensemble, resulted in some scanning artefacts in the images in fig. 2.9 B. Peculiarly, some of these artefacts were visible in only one scan direction, but not in the other. The line scans in fig. 2.10 show distinctive spikes at the leading edge of the spheres in the trace scan direction (cantilever being pulled along surface), but not in the retrace direction (cantilever being pushed

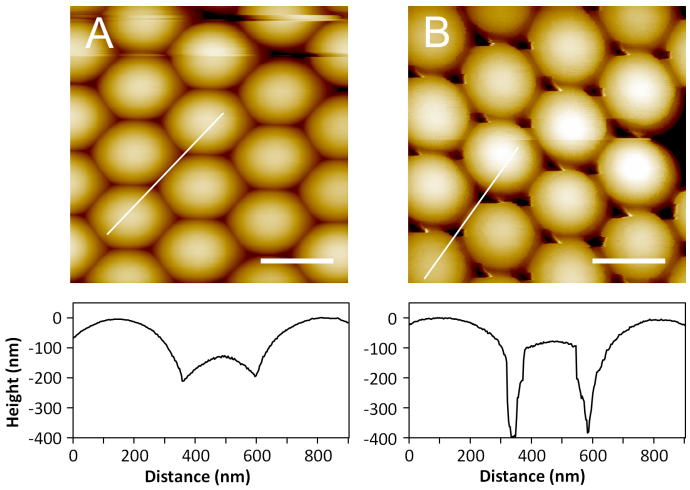

Figure 2.9: AFM height images captured with commercial (A) and modified (B) probes on 400 nm polystyrene spheres. Cross sections along the white lines are given below each and show clearly that the high aspect ratio modified probe is able to penetrate. Scale bars: 400 nm. Figure adapted from reference [190].

along surface). The reason for these spikes is that when the cantilever is being pulled along the surface, the edges of the spheres apply a torque to the tip that results in a deflection of the laser spot that triggers the feedback mechanism to pull the cantilever up. This, in combination with the high gains necessary to image samples with such a large z-range, resulted in a momentary overshooting of the tip, i.e. a spike. The same thing does not occur in the retrace direction, where the tip is being pushed along the surface, as the torque applied by the edges of the spheres acts in the opposite sense.

2.3.3 Characterisation of electrical properties

One of the significant advantages of using EBID platinum as opposed to, for instance, carbon, is that the deposited material is electrically conductive. This means that the modified AFM probes can be used for electrical modes of AFM, such as conductive AFM or Kelvin probe force microscopy. EBID platinum, however, does not have the same electrical properties as the bulk material, due to the inclusion of hydrocarbon impurities from the precursor gas.

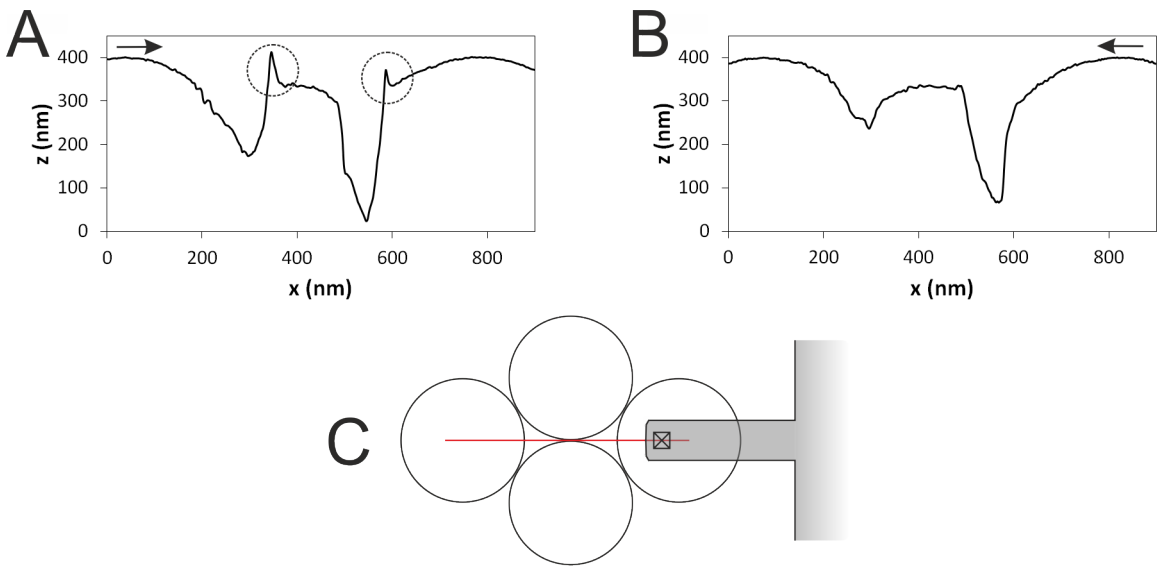

Figure 2.10: AFM line scans taken from the trace (A) and retrace (B) data of the same scan on 400 nm nanospheres. Scan direction is indicated by black arrows. The spikes in the trace scan (dashed circles) are the result of the side of the platinum pillar of the modified probe hitting the edge of a sphere, causing a torque on the cantilever that mimics deflection. This in turn triggers the feedback to momentarily pull the cantilever up further than is required, resulting in a spike. The schematic diagram (C) is a top down view showing the location of the profiles with respect to the sphere array as well as the cantilever orientation (cantilever not to scale).

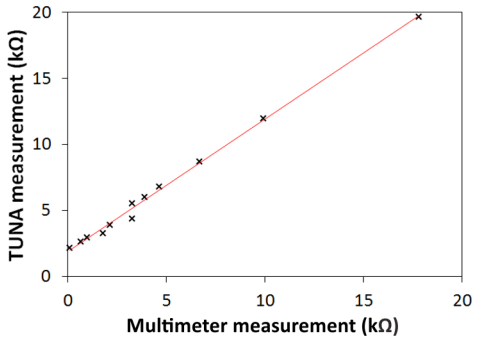

Figure 2.11: Graph showing the calibration measurements (measurements >20 kΩ omitted) and the best fit line. The offset introduced by the TUNA module is the y-intersect of the fit: 1950 ± 88 Ω.

For the electrical characterisation, samples of sputtered gold and platinum were connected electrically to the sample stage by means of a machined aluminium slide with a conductive spring clip to complete the circuit with the TUNA module on the AFM. Measurements with a desktop multimeter indicated that the resistance introduced by this setup was in the range of a few ohms, which is negligible compared to the resistances of both types of probes. The resistance of the TUNA module itself, however, was found to be significant. To eliminate this offset, a calibration was carried out using known resistances ranging from 100 Ω to 1 MΩ to determine the value of the intrinsic resistance of the TUNA module. The calibration data were analysed using MatLab and are shown in fig. 2.11. The offset was found to be 1950 ± 88 Ω.

The measurements were carried out by performing an indentation (i.e. force curve) on the surface while recording both deflection and current (fig. 2.12). This gave an indication of the approximate deflection at which to do current-voltage sweeps. Due to the granular nature of the conductive films used, it was impossible to reliably predict at what deflection good electrical contact would be made. Sometimes it was necessary to indent in several locations to find optimal conductivity. Once a good location and the right pressure (i.e. deflection) was found, the voltage was swept across a few millivolts and current was measured. Due to the stochastic nature of the contact and the inherent variability between probes, this process was repeated

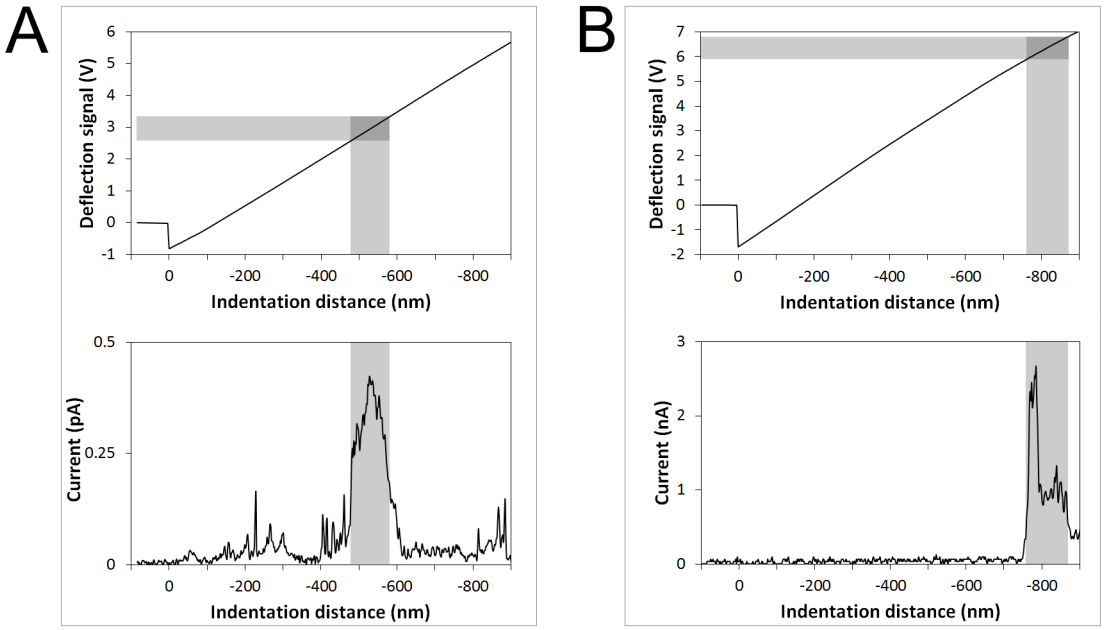

Figure 2.12: Examples of force curves (top row) and corresponding current measurements (bottom row) for a modified probe (A) and a commercial cantilever (B). The shaded regions show how the approximate deflection for the subsequent current-voltage sweeps was determined. Due to the stochastic nature of the contact between tip and sample the deflection values were individually determined for each probe measured.

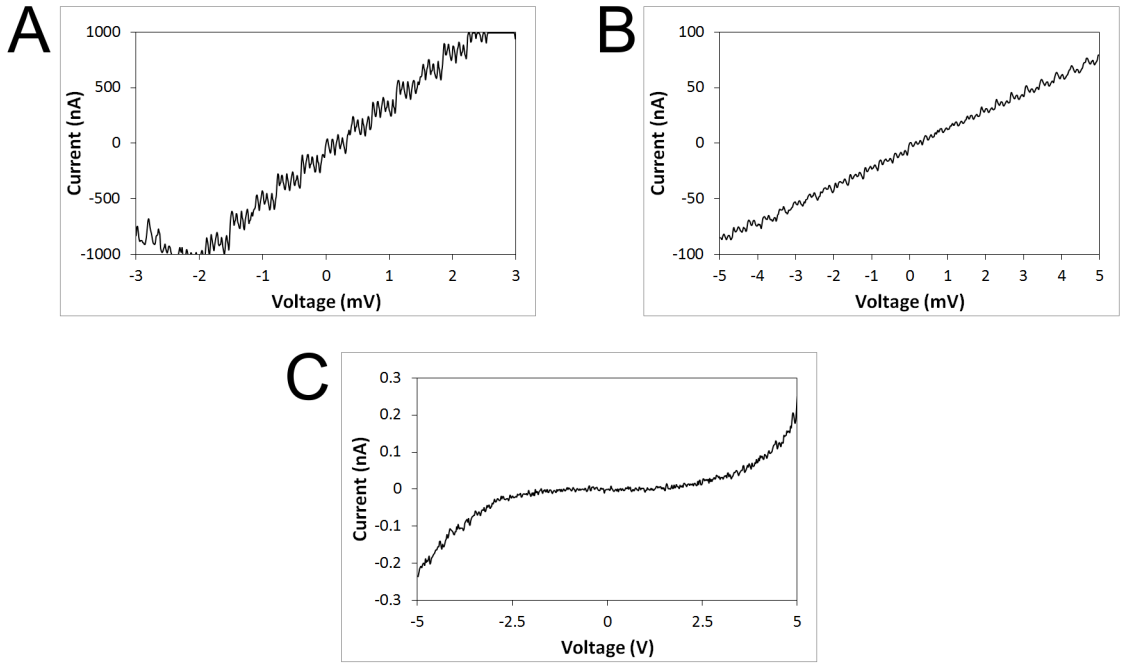

Figure 2.13: Characteristic examples of current-voltage sweeps of AFM probes captured using the TUNA module. A: Commercial cantilever. The non-linear effects at the lower left corner are the result of clipping due to the maximum current range of the TUNA module (1 μA). B: Modified probe (EBID after plasma cleaning). C: Modified probe (no plasma cleaning).

numerous times for each probe until it was clear that no better conductivity could reasonably be expected to be found. Where possible, the highest sensitivity setting of the TUNA module was used in combination with small sweep voltages, in order to prevent damage to the probes. Possible effects of high currents include delamination of the gold coating of the cantilevers, spot welding of the tip to the sample, and warping/bending of the tip in the case of modified probes.

Commercial OMCL-RC800PB cantilevers measured in this way gave an average resistance value of 0.55 ± 0.13 kΩ from a sample of ten probes. A representative example of the current-voltage sweep measurement for one commercial probe is given in fig. 2.13 A. The initial generation of modified probes measured gave a rather large resistance of 123 ± 82 MΩ ($N = 8$). Some of these probes also exhibited pronounced non-Ohmic behaviour (see fig. 2.13 C). This behaviour resembles the

behaviour of a thermistor, indicating that there may be a non-metallic component in the circuit. This suspicion is corroborated by the finding that the resistance of modified probes that were subjected to an RF-plasma clean immediately prior to EBID displayed a markedly lower resistance at 148 ± 35 kΩ ($N = 4$) and did not display non-Ohmic behaviour (fig. 2.13 B). It seems likely that the probes fabricated without plasma cleaning had a thin layer of carbonaceous material separating the deposited platinum from the gold coated cantilever, causing high resistances (that were also highly variable) and non-Ohmic behaviour.

The resistance of the platinum pillar is given by the integral

$$R = \int_0^L \frac{\rho}{\pi r(x)^2}\,\mathrm{d}x$$

where L is the length of the platinum pillar, ρ is the resistivity of EBID platinum, $r(x)$ is the radial dimension of the pillar as a function of the distance along the pillar's axis, x. Modelling the tip as a tapered wire (i.e. a section of a cone), the resistance may be estimated as

$$R = \frac{\rho L}{\pi r_{min} r_{max}}$$

where r_{min} and r_{max} are the radii at the thin and thick end of the wire/pillar, respectively. Using the dimensions of the tip in fig. 2.2 as an example and using a typical resistivity of EBID deposited platinum of 10^5 μΩcm [202] yields an estimated resistance of approximately 500 kΩ. The resistance of the rest of the circuit (commercial probe, AFM stage, wire connectors, etc.) is only of the order of a few tens of Ohms and can be ignored for this calculation. The fact that the measured resistance is significantly lower than the estimated value may be an indication that the EBID platinum was annealed by the relatively large currents passing through it during measurement. Annealing by heating EBID deposited platinum has been shown to decrease resistivity by driving off contaminant particles [203]. The idea

that annealing may be occurring is further corroborated by SEM images captured after electrical characterisation, which showed that some of the probes were slightly bent – a phenomenon that was not observed after just imaging in the AFM. SEM imaging also confirmed that the modified probes were not significantly deformed or damaged by force curve indentation on gold films.

2.4 Discussion

In this chapter, the fabrication and characterisation of high aspect-ratio AFM probes of 4.0 ± 1.0 nm radius of curvature by EBID of platinum was presented. Contact-mode topographical imaging of a sputtered gold surface was used to illustrate the improved imaging performance of the modified probes over the commercial cantilevers, while power spectral density plots were used to quantify the enhanced sensitivity as a function of spatial frequency. The ability of the modified cantilevers to probe high aspect-ratio features was illustrated by imaging a close-packed array of nanospheres. In both cases the modified probes significantly outperformed their commercial counterparts.

The probes were also characterised electrically by bringing them into contact with a conducting surface using the AFM and carrying out voltage sweeps while measuring the current. The expected resistance of the deposited pillar proved larger than the measured value by almost a factor of ∼3, which indicates that the current passed through the probes during measurement may be annealing the EBID platinum, driving off some of the carbonaceous inclusions and increasing the atomic fraction of platinum in the pillar. This is not anticipated to be an issue in the utilisation of the probes, as the currents passed in the proposed applications (electrical measurements on ion-channels in biological membranes – see chapter 5) would be in the pA range instead of the nA range. Similarly, the high resistance of the probes compared to

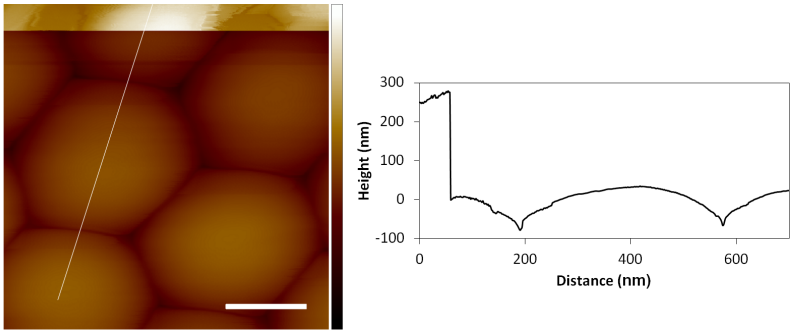

Figure 2.14: An AFM scan during which the platinum pillar was severed from the AFM probe. The slow scan direction was top to bottom and the tip snapped approximately one tenth of the way down. The colour scale represents 600 nm, scale bar is 200 nm. The cross section shows a step height of ∼275 nm. This value is in agreement with measurements made on SEM images of the same probe before use (which place its length at ∼280 nm).

their commercial counterparts ought not to be an impediment to their use, since the typical resistance of ion channels is in the tens of MΩ. This means that the voltage drop across the platinum pillar, although higher than in commercial probes, would still be insignificant in an experiment.

While the probes were shown to be able to withstand routine AFM work, there were instances where the platinum pillar was snapped off during AFM use. In some instances, this resulted in images with an apparent height step in them, caused by the sudden shortening of the AFM probe. An example of such an event is given in fig. 2.14. The step height in these images corresponds to the length by which the tip was shortened. Comparisons with SEM images of the probes after formation (before use) indicated that the entire platinum pillar was severed from the AFM probe. This leads to the conclusion that the weakest part of the probe is the contact region between the gold and the platinum – perhaps due to residual impurities adsorbed to the gold surface prior to EBID. This is further supported by SEM imaging of broken probes, which showed that the platinum pillar was removed completely as opposed to breaking part way down its length. A potential solution to this problem which would not complicate the fabrication procedure significantly, would be to image

the base of the pillar in the SEM immediately after deposition. Due to residual precursor gas remaining in the chamber, additional beam exposure results in further platinum deposition. The result would be a larger contact region between the pillar and the pyramidal probe tip, at the expense of a slightly thicker pillar near the base. Depending on the planned application, sacrificing some of the aspect-ratio of the probe would be worth the improved resilience.

Chapter 3

Force curves measurements of lipid bilayers

3.1 Introduction

3.1.1 AFM and biological membranes

Biological membranes serve as barriers separating both compartments within a cell as well as the cell itself from its environment. Plasma membranes are complex structures with many constituent parts. The basic structure is that of a liquid disordered bilayer composed of various types of phospholipids, glycolipids, sphingolipids, and sterols. It also contains a large array of proteins, many of which play pivotal roles in cellular processes. Other proteins link the membrane to its cytoskeletal support, giving the cell its shape and facilitating motility and changes in cell shape, for instance during mitosis.

Supported lipid bilayers (SLBs) have taken on a pivotal role in the study of a variety of biological systems. Their ability to serve as models for cellular membranes [204–211] has made them important tools in structural and molecular biology. They are particularly helpful in studying e.g. transmembrane transport, establishing differences between lipids, and determining properties of membrane proteins via reconstitution. The simplicity and reproducibility of their formation by vesicle fusion on hydrophilic supports [204, 206] further encourages the widespread use of SLBs. Their properties show potential for use in biotechnological applications such as biosensors and diagnostic and biomimetic devices [207, 212–218].

AFM techniques have become an essential part of the experimental toolbox in the study of the structure and function of biological membranes [105, 219–224]. Advantages for investigation of biomembranes include a lateral resolution on the order of 1 nm, height resolution of 0.1 nm, image capture time on the order of a few minutes (or on the order of 10s of ms in the case of high-speed AFM [225]) and the ability to collect data in a wide range of biologically relevant conditions. The structure of biological membranes cannot be adequately probed by averaging techniques such as

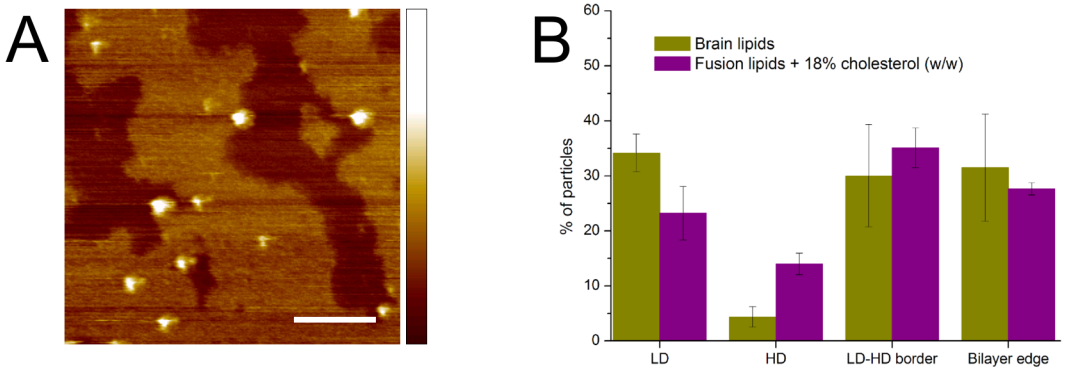

Figure 3.1: A: AFM height image of glutamate receptors (GluA2) reconstituted into fusion lipids composed of POPE, POPS, POPC, and cholesterol. The receptors preferentially localise at the phase boundary between the high and low domains of the bilayer. Scale bar is 200 nm, colour scale represents 6 nm. B: Chart indicating the preferential localisation of GluA2 at the boundary between phases when reconstituted into porcine brain lipid (green bars) or fusion lipids (purple bars). The data shows that a significant proportion of the reconstituted receptors are drawn to the phase boundary, as well as the edges of the lipid bilayer. Figure adapted from reference [6].

x-ray diffraction, whereas AFM is ideally suited to exposing the local structure of a sample. A further advantage is that only miniscule quantities of material are required to prepare a sample. While AFM has been widely used to study real cells and their membranes [226–229], native membranes are rather difficult to study at the nm - µm length scales because of their complexity. Model systems, such as SLBs, are especially well-suited to investigation with AFM, since they are essentially atomically flat and the features of interest they exhibit are generally on length scales accessible to AFM technology.

3.1.2 Force curves

Understanding the mechanical properties of lipid bilayers is an essential step in the study of biological membranes and the proteins they harbour. In some cases lipid mechanics is directly linked to protein activity, as in the case of mechanosensitive ion channels for example [230]. It has been proposed that any ion channel that changes its hydrophobic thickness or areal footprint during a conformational change is affected to

some degree by its local environment [231–234]. Protein localisation is also dependent on lipid environment. Hydrophobic matching drives proteins to segregate into bilayer domains that minimise the energetic penalty of exposing hydrophobic areas of the protein to water and hydrophilic areas to the hydrocarbon domain of the membrane. This is observed in model membranes, where proteins can be observed to preferentially segregate into one phase over another [235] or to "dress" the boundary between phases (see fig. 3.1). In native membranes, similar phenomena are proposed to occur in lipid rafts, physically distinct domains proposed to be involved in recruiting certain classes of membrane proteins to establish and fortify signalling chains across the membrane.

The work presented in this chapter aims to shed light on the mechanical properties of specific model membrane systems, in particular focusing on the effect of temperature and cholesterol on their phase behaviour. The physical properties of the lipid phase boundary is investigated in the hope of revealing the reasons why certain proteins tend to be attracted to this region in model systems.

3.2 Experimental

3.2.1 Materials and sample preparation

1,2-distearoyl-sn-glycero-3-phosphocholine (DSPC, 18:0), 1,2-dioleoyl-sn-glycero-3-phosphocholine (DOPC, 18:1), 1-palmitoyl-2-oleoyl-sn-glycero-3-phosphoethanolamine (POPE, 16:0-18:1) and cholesterol were procured from Avanti Polar Lipids, Inc., USA. A summary of the lipids and their properties is found in table 3.1. The gel transition temperature (T_m) varies greatly with the lipid tail structure (especially degree of unsaturation). Lipid samples were prepared using the vesicle fusion method: A suspension of lipid vesicles is prepared by mixing lipids in chloroform to the desired composition (e.g. DSPC:DOPC at a ratio of 1:1, with varying mole fractions of cholesterol), drying them under a stream of argon, desiccating them for two hours in

a vacuum chamber, adding de-ionised water, and sonication with a probe sonicator (VCX750, Sonics & Materials, Inc., USA) with a stepped microtip. The resulting solution is added to freshly cleaved mica with the desired imaging buffer (typically 150 mM KCl and 10 mM TRIS-HCl at pH 7.4) to form a supported lipid bilayer. After an incubation time of approximately fifteen minutes, the buffer is exchanged multiple times to remove excess lipid material. Imaging over the course of twelve hours show little change in the system indicating that it is at equilibrium.

Table 3.1: Properties of the lipids used in this chapter obtained from [5].

Lipid	Tail structure (length:unsaturated[position])	T_m (°C)	Bilayer thickness (nm) (from X-ray diff.)
DSPC	18:0/18:0	55	5.2
DOPC	18:1[9]/18:1[9]	-17	3.9
POPE	16:0/18:1[9]	26	4.2

Force curve measurements and imaging of DSPC/DOPC/cholesterol bilayers were carried out using gold coated triangular OMCL-TR800PB or rectangular OMCL-RC800PB pyramidal-tipped silicon nitride cantilevers (Olympus, Japan) with nominal spring constants in the range 0.39 - 0.76 N/m. The boundary region of DSPC/-DOPC/cholesterol bilayers was examined with modified cantilevers (see chapter 2). POPE bilayers were studied using OMCL-TR800PSA and OMCL-RC800PSA cantilevers, which are identical to the above except that they lack the conductive gold coating on the tip side. All AFM experiments detailed in this chapter were carried out using an Asylum MFP-3D AFM (Asylum Research, USA).

3.2.2 Force curve experiments

Each cantilever was calibrated prior to experiment. The sensitivity of the lever (the invOLS, or "inverse optical lever sensitivity") was measured by performing a force curve measurement on mica. The thermal spectrum was used to fit a simple har-

monic oscillator model to and determine the value of the spring constant [236]. In experiments using modified probes, this approach was deemed too risky due to the potentially fragile nature of the platinum pillars. In these cases, calibration was performed using the GetReal^{TM}method. This relies on a thermal spectrum captured in air and applies a model of the cantilever's harmonic properties (which depends on the length, width, and shape of the cantilever) to determine both the invOLS and the spring constant. The calibration was performed multiple times and an average value was used for the spring constant. The invOLS was subsequently re-measured in liquid, since its value changes in different media.

The sample was initially imaged in tapping mode, using a setpoint as close as possible to the free amplitude while still obtaining a good image. Feedback was increased as far as possible without causing increased noise and oscillation, so as to further minimise the likelihood of tip-sample interactions causing strong perturbations to the soft lipid bilayer. A suitable area of the bilayer was selected and scanned, and the resulting image served as a map for the subsequent indentations.

Force curve measurements were carried out in contact mode (which is to say no oscillation was imposed on the tip) at an approach speed of 120 nm/s along the z-axis. Due to the small thickness of lipid bilayers, the sampling rate was increased from 2 kHz to 5 kHz. While this increased the volume of data, making it more computationally intensive to analyse, it was made worthwhile by the increased number of data points that could be used to fit the indentation model. The "extend" portion of the force curve was terminated once the deflection reached a predetermined trigger point relative to the initial deflection. The magnitude of the triggering deflection was determined individually for each cantilever, as the force (and hence deflection) necessary to penetrate to the underlying mica substrate depends on the radius of curvature and shape of the probe tip. In each case, the lowest possible trigger point that encompassed the entire region of interest was used, in order to avoid unnecessary wear

to the tip. Measurements were carried out with modified probes (see chapter 2) to investigate the boundary between lipid domains. SEM imaging after the experiments confirmed that the modified probes were able to withstand the stresses of force curve measurement.

3.2.3 Temperature variation

In experiments where the temperature was the variable of interest, the MFP-3D CoolerHeater^{TM}accessory was used (Asylum Research, USA). A Peltier element that is thermally coupled to the sample stage varies the temperature of the sample in the range -25°C - 120°C. To avoid excessive evaporation of the sample buffer at higher temperatures, the stage is equipped with a membrane that forms an airtight seal around the sample. In practice, the use of this membrane seal was found to affect both imaging quality and force curve acquisition negatively, so its use was avoided. The temperatures at which the data for this chapter were recorded (up to ∼30°C) where not so high as to cause significant evaporation of the sample buffer.

The CoolerHeater accessory was used in the "low noise" mode, as it was found that this created less interference when taking the measurements. Nevertheless, significant noise was caused by the switching from positive to negative voltage in the Peltier element. This only occurred at temperatures near ambient temperature, where the feedback loop would cause the Peltier element to switch between heating and cooling operation. For this reason, it was necessary to disable the feedback and run the Peltier element at a fixed voltage, while recording the equilibrium temperature using the inbuilt thermometer for measurements between $\sim 23-27$°C. This meant that the temperature could not be as finely controlled in this region.

3.2.4 Software analysis

The AFM software used to capture the force curves contains a program for force curve analysis, but it was found that the manual selection of the contact point implemented in this program led to significant variations in the resulting elastic modulus values. This was in addition to the problem of analysing many hundreds of force curves individually. It was therefore deemed necessary to automate the process of contact point selection so as to reduce experimenter influence as much as possible. The recorded force curves were exported to text files and analysed using software written in MatLab. The analysis procedure used as well as the code of the program are found in Appendix A.

3.3 Imaging results

AFM imaging provides information about bilayer phase, leaflet conformation and thickness, as well as providing a necessary topography map that allows the collection of force curve data. Bilayers composed of mixtures of DSPC and DOPC form a mixed-phase system composed of a DSPC-rich high domain in the gel (L_β) phase and a DOPC-rich low domain in the liquid crystalline, or liquid disordered, (L_α) phase. As cholesterol concentration is increased the high domain transitions from the gel phase to the liquid ordered (L_o) phase, and there is a brief window in which L_o and L_β coexist. In a system with two phases, four different leaflet conformations are possible: two symmetric conformations with each leaflet in the same phase, and two asymmetric conformations with proximal and distal leaflets in different phases. In practice, only symmetric conformations are seen, indicating that there is an energy penalty associated with the asymmetric conformations. An example of an AFM topography image of the DOPC/DSPC system is shown in fig. 3.2. Also shown is a cross section illustrating the height profile of the different phases, and a histogram showing

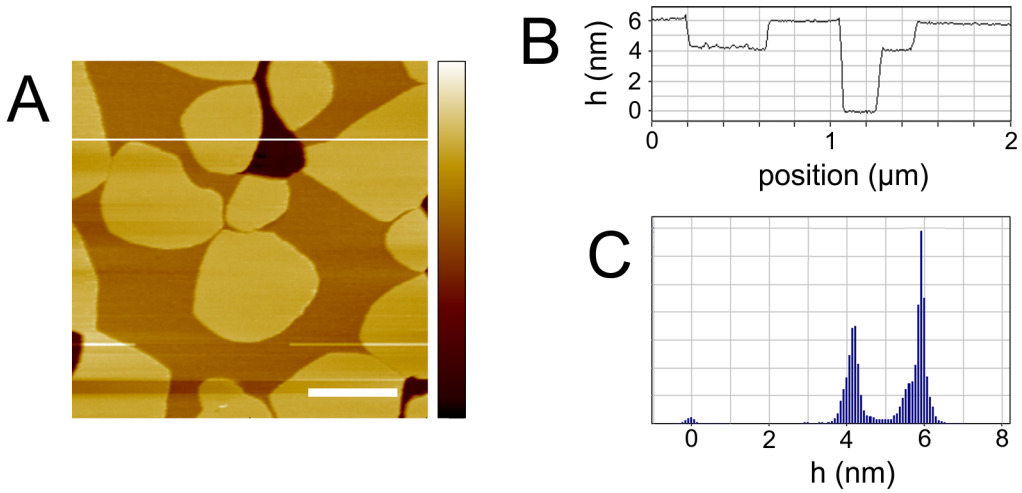

Figure 3.2: A: AFM topography image of a 1:1 mixture of DOPC and DSPC at room temperature. Scale bar is 500 nm and colour scale represents 9 nm. B: Line section (white line in A) illustrates the domain structure and the differences in height (h) – defined as the vertical distance to the mica surface (darkest regions in A) – across domains. C: Histograms provide an accurate way to determine the height difference over the whole image.

the height distribution over the whole image. Using a histogram to determine height is more reliable than simply measuring the height differences in cross sections or line scans, due to the larger volume of data included. Frequently an image requires some post-capture flattening before being amenable to histogram height measurements. Line subtraction, plane subtraction, or revolving an arc (where a virtual arc of a fixed radius is revolved horizontally over or under the data and the resulting envelope is subtracted as a background) were used as needed to flatten images. Depending on the image, it can be difficult to flatten the entire image properly. In these cases the image was subdivided into regions that could be adequately flattened, and a separate histogram was plotted for each region.

Increasing cholesterol concentration leads to visible changes in the lipid bilayer patches. AFM height images showcasing these changes are given in fig. 3.3. With little or no cholesterol, the bilayer appears as a “bulk” low domain with “islands” of high domain. These high domain islands tend to be between 200 and 3000 nm

across and appear relatively rounded in shape (fig. 3.3A). At 5 mol% cholesterol, the picture appears similar, although the sizes of the high domain islands appear to be somewhat smaller ranging from 100 to 2000 nm (fig. 3.3B). Increasing the amount of cholesterol to 10 mol% seems to cause the high domain islands to spread themselves along the edges of bilayer patches and hints of a high domain "rim" can be seen around some patches (fig. 3.3C). This trend is borne out further at 15 mol%, where the initial picture is reversed: There now seem to be low domain islands enclosed by high domain (fig. 3.3D and E). At 20 mol% cholesterol, there is once again a shift in appearance, and the high domain now takes the form of small islands ranging in size from about 10 to 300 nm. These small islands seem to have a somewhat less rounded and regular shape than those found at low cholesterol concentration (fig. 3.3F). 25 mol% cholesterol seems to result in a similar structure as 20 mol%, albeit with significantly enlarged high domain islands. These seem to fall in the range from 50 to 800 nm. The high domain also seems to be more susceptible to deformation by the tip during scanning, as evidenced by the "streaks" visible in fig. 3.3G. The highest cholesterol concentration for which useful imaging data was obtainable was 30 mol%. At this concentration the high domain regions take on distinctly irregular shapes with jagged boundaries.

From height images such as the ones in fig. 3.3 it is possible to measure the height difference between the high and low domains. The measurements are presented as a function of cholesterol concentration in fig. 3.4. The graph shows that there is a height difference between the two domains of $\sim$1.3 nm when no cholesterol is present. This value increases to over 2 nm at 15 mol% cholesterol, before once again decreasing as cholesterol concentration is further increased. The height difference at 30 mol% cholesterol is close to 1 nm.

The vertical error bars on the data points in fig. 3.4 were calculated from an estimation of the errors in the measurement of each height difference using the histogram

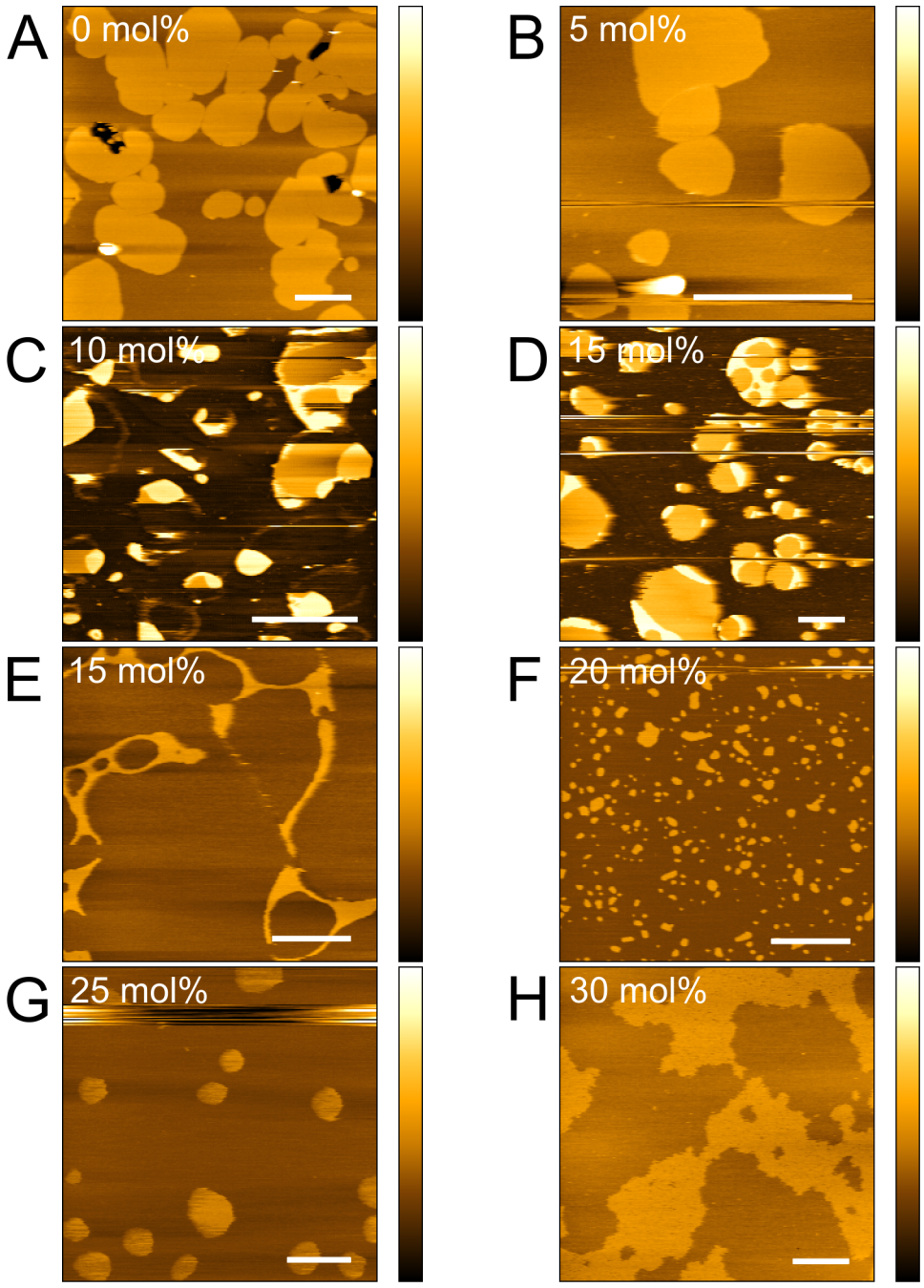

Figure 3.3: Representative AFM height images depicting the domain structures found in DOPC/DSPC bilayers on mica at room temperature with varying cholesterol concentration. Cholesterol content given in top left of each image. A: large, rounded islands of HD; B: similar to A, but high domains are slightly smaller; C: HD islands still present but now preferentially located at the edges of patches. Some patches display a thin "rim" of HD around them; D: HD forms mostly as a rim around edges of patches, and encloses LD areas; E: another example more clearly showing how thin strands of HD surround islands of LD; F: HD forms small, rounded islands; G: similar to 20% cholesterol, although HD islands seem somewhat larger in size; H: HD forms large, interconnected, irregularly-shaped islands with jagged/rough edges. All scale bars are 1 µm, all colour scales represent 8 nm.

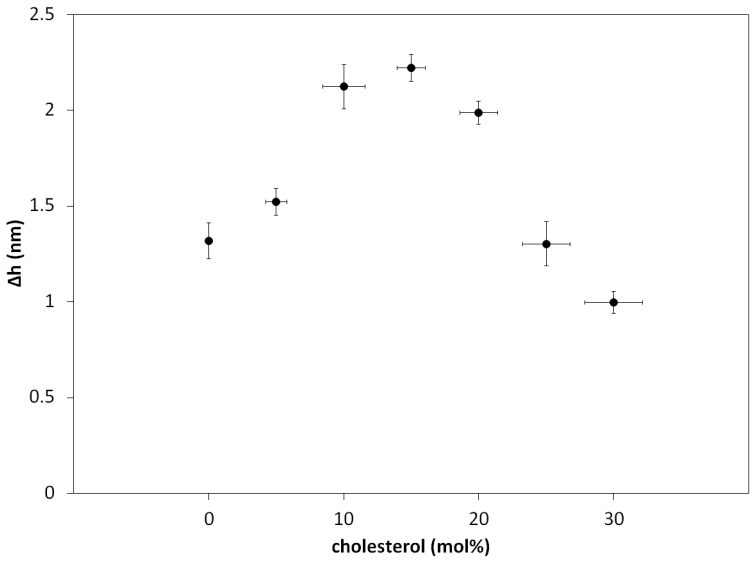

Figure 3.4: This graph shows the height difference between the low and high domains (Δh) in 1:1 DOPC/DSPC as a function of cholesterol concentration. The height difference reaches its maximum at around 15 mol% cholesterol. The lowest difference is recorded at high cholesterol concentrations, while low cholesterol bilayers seem to exhibit an intermediate Δh.

method described above and the standard error on the mean calculated from the variation between different histogram measurements. The error in the AFM z-piezo is of the order of a few picometres and thus not significant. The effect of ambient noise on the AFM height data, which gives rise to variations on the order of approximately 0.1 nm, are averaged out due to the large volume of data used in the histogram measurement method. The horizontal error bars give an indication of the uncertainty in the cholesterol concentration due to pipetting errors. The magnitude of these error bars was estimated by pipetting volumes of pure water and measuring their weight using a microgram scale.

Images such as the ones shown in fig. 3.3 also serve as a measure of the total area fraction of the individual domains at varying cholesterol concentration. To obtain this data, the images were flattened where necessary, and then a threshold selection of one domain was performed and the area measured. Where the coverage of the lipid was incomplete, another threshold selection was performed to measure the total area of

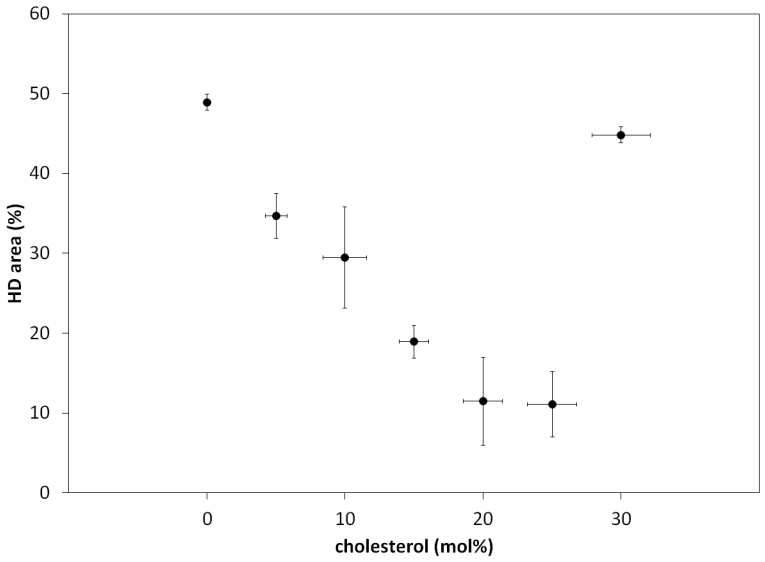

Figure 3.5: This graph shows how much of the total bilayer area of 1:1 DOPC/DSPC consists of high domain at various concentrations of cholesterol. The fractional area of the high domain starts out at close to 50% and then decreases relatively steadily as cholesterol concentration is increased until about 20 mol%, after which it briefly plateaus before abruptly jumping back up to nearly 50% of the total area.

lipid present in the image. The data of the fractional area of the high domain is given in fig. 3.5. The bilayer seems to consist of nearly equal areas of high and low domain when no cholesterol is present. As soon as cholesterol is introduced, there appears to be a marked decrease in the relative area of high domain bilayer – a trend that continues up to a cholesterol content of 20 mol%, where the fractional high domain area stabilises at around 10%. Further increasing the cholesterol concentration from 25 to 30 mol% gives rise to a sharp increase in the fractional area of the high domain, almost back up to the initial 50%.

The vertical error bars in fig. 3.5 were obtained by estimating the error in the threshold selection technique and scaling it using the total area of lipid considered for the individual data points. The horizontal error bars are identical to the ones in fig. 3.4.

3.4 Force curve results

3.4.1 Force curves on DSPC/DOPC bilayers

Force curve measurements were carried out on both the high and low domains at various cholesterol mole fractions. Qualitative differences between the two domains are clear and pronounced: Breakthrough seems to occur in two distinct steps, or "kinks", on the high domain with an initial, partial event followed by a second breakthrough to the mica surface. The high domain also withstands a significantly higher force until breakthrough occurs. It appears that the high domain is compressed into a putative "thin layer" before being fully penetrated by the tip. The schematic diagram of a high domain force curve given in fig. 3.8 showcases the two-step breakthrough, as well as highlighting the quantitative measurements that can be extracted from the force curves. The low domain force curves only exhibit a single breakthrough event. As cholesterol concentration is increased, there is a noticeable change in the shape of the high domain force curves, while the low domain curves remain qualitatively and quantitatively similar to their low-cholesterol counterparts (fig. 3.6).

AFM scanning after execution of force curves on the high domain at low cholesterol concentrations ($\leq$5 mol%) revealed that in some cases (and especially after repeated force curves in the same location) lasting depressions persisted, indicating that the thin layer suggested above is relatively stable. Examples of these depressions, which were of sizes on the order of the tip size, are shown in fig. 3.7. No such marks were visible on the low domain, nor on the high domain when the cholesterol concentration exceeded 5 mol%. Due to this phenomenon, no force curves on the high domain used for analysis of the elastic modulus were repeated at the same point on the bilayer. Low domain force curves did not seem to change significantly upon repeat indentations, but the locations were nonetheless changed frequently.

The force curves were analysed using the theory developed by Chadwick [69]. The

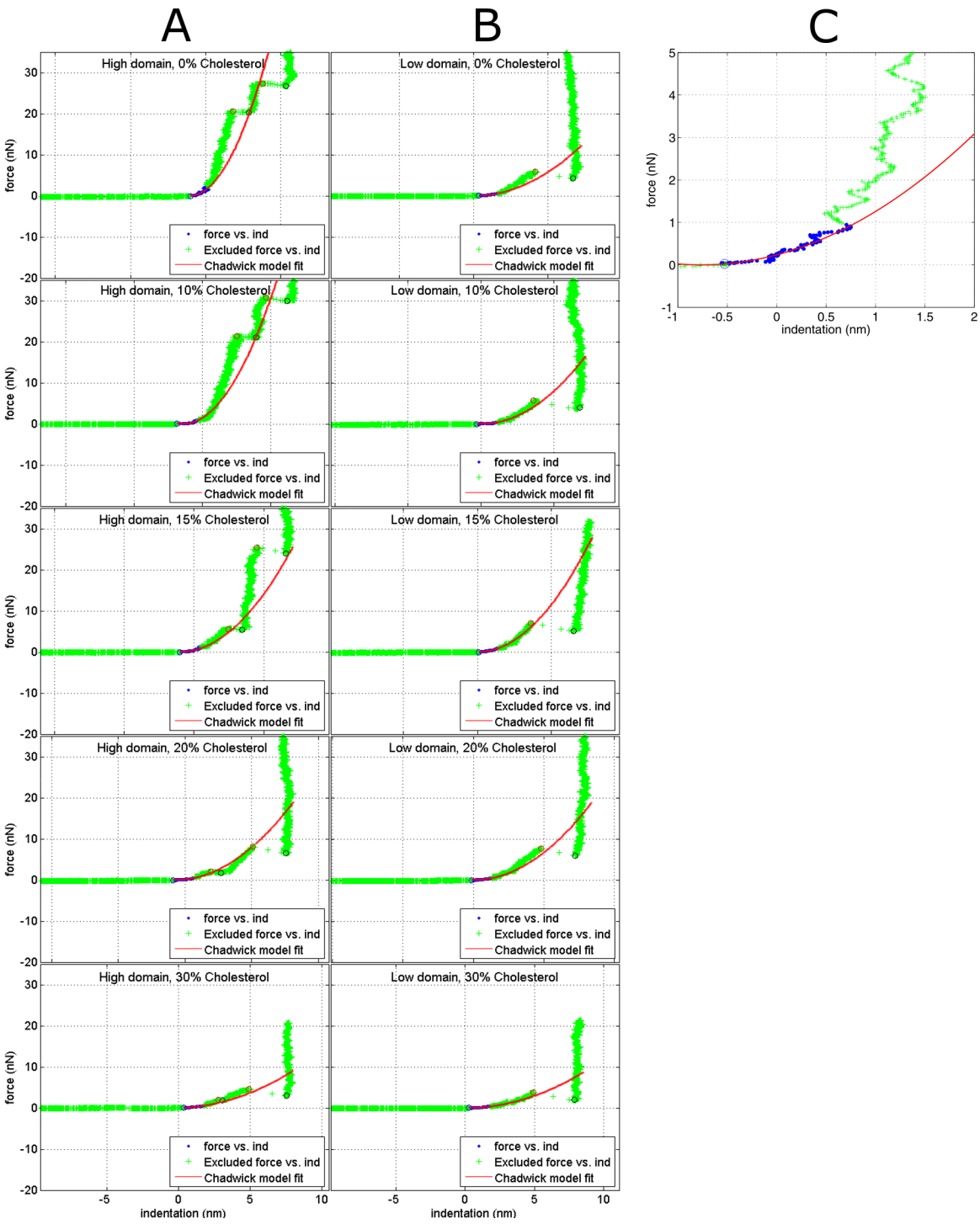

Figure 3.6: These are typical force curves on the high domain (column A) and the low domain (column B) of the DSPC/DOPC/cholesterol system, including the parabolic fit computed from the first 20% of the indentation (blue points) by the fitting software in MatLab. A magnified example of the fit region is shown in C (0 mol% cholesterol HD). The blue circle in each graph represents the contact point determined by the fitting algorithm. The red and black circles show where the program has determined the beginning and end of the breakthrough events. The high domain exhibits two breakthrough events that become less pronounced with increasing cholesterol, while the low domain has only a single event. The force at which the final breakthrough occurs is reduced significantly at higher cholesterol concentrations for the high domain, but remains unchanged for the low domain.

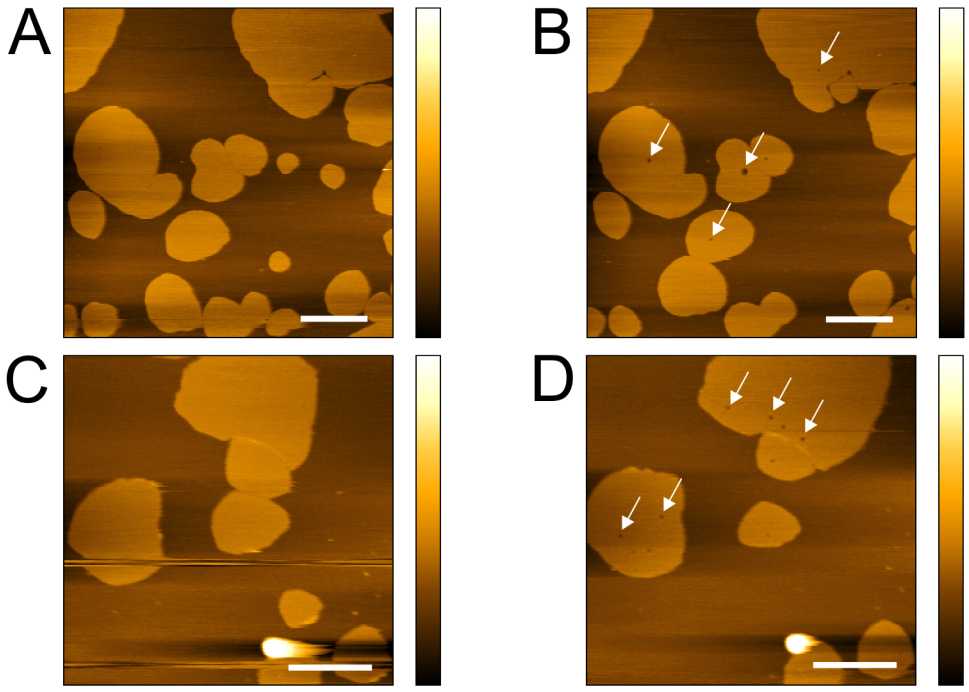

Figure 3.7: Examples of indentations left by the tip during force curve capture. A and B: The same area of 0 mol% cholesterol DOPC/DSPC bilayer before (A) and after (B) force curve capture. Several small indentations mark points where multiple force curves were performed at the same location. Scale bars represent 1 µm and colour scales represent 8 nm. C and D: As above, but with a DOPC/DSPC bilayer containing 5 mol% cholesterol. White arrows in B and D indicate locations of some puncture marks. Scale bars represent 500 nm and colour scales represent 8 nm.

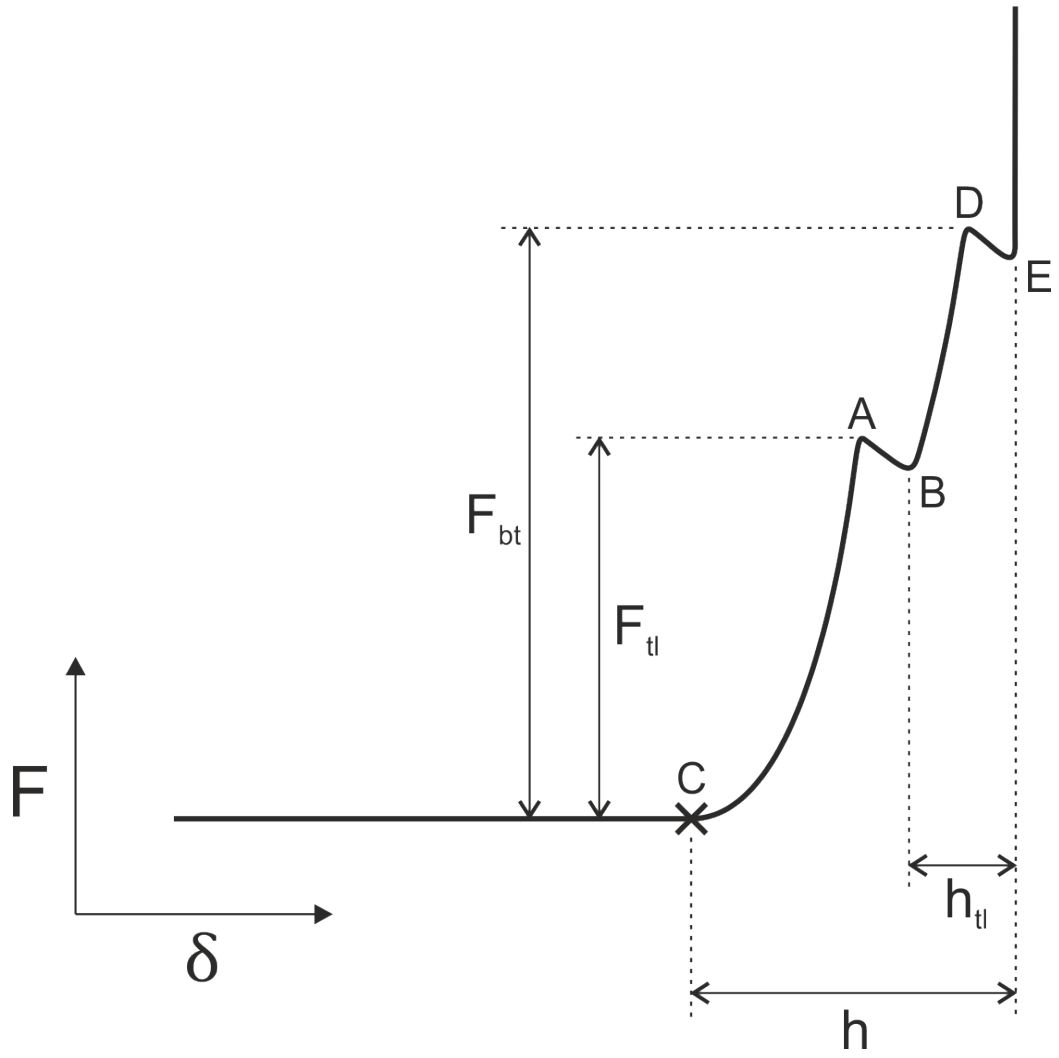

Figure 3.8: A schematic diagram of a force curve on the DSPC-rich domain at low cholesterol concentration, exhibiting two distinct breakthrough events, or "kinks". The contact point (C) is where the tip makes contact with the bilayer. As more force is applied the tip indentation into the bilayer (δ) increases (C→A). When the force reaches F_{tl}, the force required to compress the bilayer into the hypothesized "thin layer", a sudden increase in indentation and a concomitant decrease in force – the first kink (A→B) – occurs. Once the thin layer has formed underneath the tip, it in turn is indented under the increasing force exerted by the tip (B→D). At the critical force F_{bt}, the force required to break through the bilayer, a second kink occurs (D→E), after which the tip is in contact with the hard mica surface used as a support for the bilayer. This is essentially incompressible at the forces applied, and no further indentation occurs.

model assumes a spherical indenter being pushed against a thin film atop a harder material. For a membrane that is able to slide across the substrate, the force F is related to the indentation δ by the formula

$$F = \frac{2\pi ER}{3h}\delta^2$$

where h is the thickness of the membrane (i.e. total indentation from point of contact to mica), E is the Young's modulus, and R is the radius of the spherical indenter. The membrane is considered to be incompressible (Poisson's ratio $\nu = 0.5$).

For comparison, the corresponding expression in the Hertz model for the indentation of a semi-infinite half-space with a spherical punch is

$$F = \frac{4ER^{\frac{1}{2}}}{1-\nu^2}\delta^{\frac{3}{2}}.$$

The trends in the elastic modulus of the high and low domains of this lipid mixture are shown in fig. 3.9. It appears that the elastic modulus of the low domain decreases upon inclusion of cholesterol up to 10 mol%. It then increases again slightly at 15 mol% cholesterol. In the high domain it seems that adding cholesterol initially increases the modulus (up to around 5 mol% cholesterol), before significantly reducing it in the range between 10 and 20 mol%. Beyond this the modulus remains the same to within the experimental error for both high and low domain.

Breakthrough force (F_{bt}) on the high domain seems to correlate strongly with modulus, as expected (see fig. 3.10). The initial increase in breakthrough force at low cholesterol concentrations seems to mirror the increase in modulus in this regime. Again, the graph shows a precipitous decrease followed by a plateau above 20 mol% cholesterol. The breakthrough force in the low domain seems to remain almost constant throughout the measured range.

The vertical error bars in both fig. 3.9 and fig. 3.10 arise from a combination of

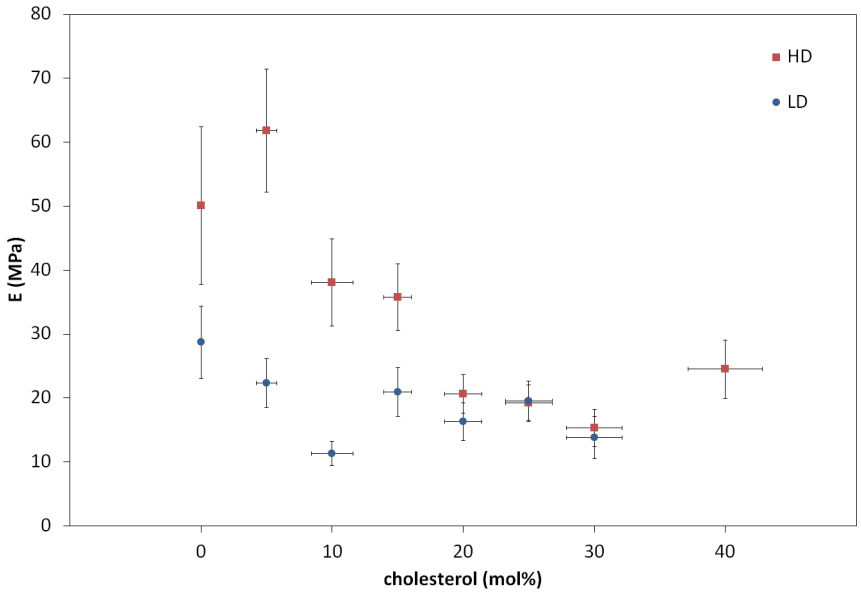

Figure 3.9: Graph depicting the elastic modulus of a DOPC/DSPC bilayer as a function of cholesterol content. Red squares correspond to high domain modulus values, while blue circles show low domain modulus values. The modulus values were calculated using the Chadwick model [69] for multiple force curves (mean $N = 36$) and averaged.

the statistical error on the mean, and the error in the spring constant calibration. For the estimation of the error in modulus measurements it is important to take into account the variability of the tip radius as well. The error in the spring constant calibration was estimated by comparing multiple calibrations of the same cantilever. The fractional error in the calibration of the spring constant was found to be less than 1.5% from a sample size of nine measurements.

The height of the bilayer is recorded in each force curve as the indentation distance between the contact point and the final point of the final kink (which is where the tip contacts the mica surface). Overall, the heights measured in this way seem to be ∼2 - 3 nm higher than those obtained from AFM images (such as fig. 3.2 A). The reason for this is that even when imaging in tapping mode and taking care to maximise the amplitude setpoint (i.e. minimise the force exerted on the sample), there is a residual average pressure applied to the bilayer. Values quoted in the literature range

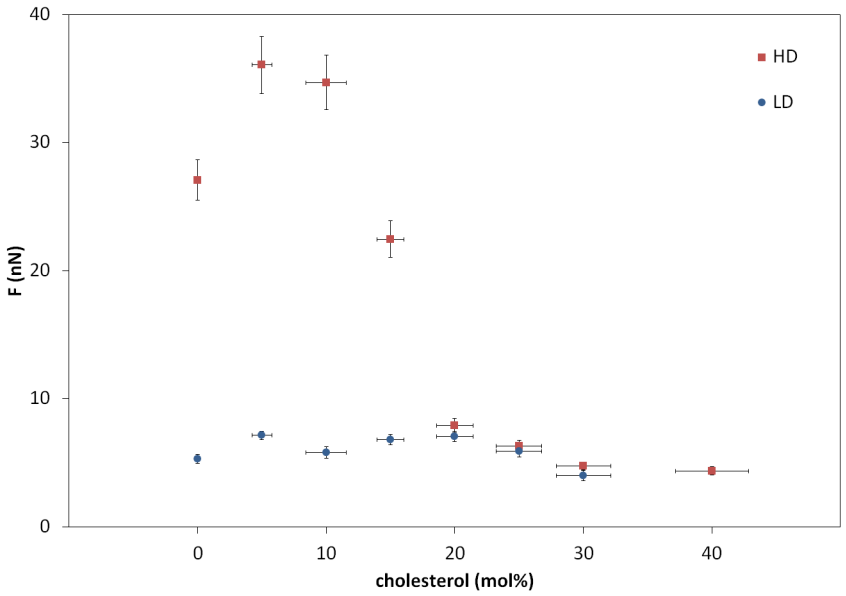

Figure 3.10: Graph showing the dependence of the breakthrough force of a DOPC/D-SPC bilayer on the cholesterol content. Red squares are values for the high domain; blue circles are low domain values. The breakthrough force of each force curve is measured as the difference in force between the highest point of the last detected kink and the contact point. The data shown are averages over many force curves at each cholesterol concentration.

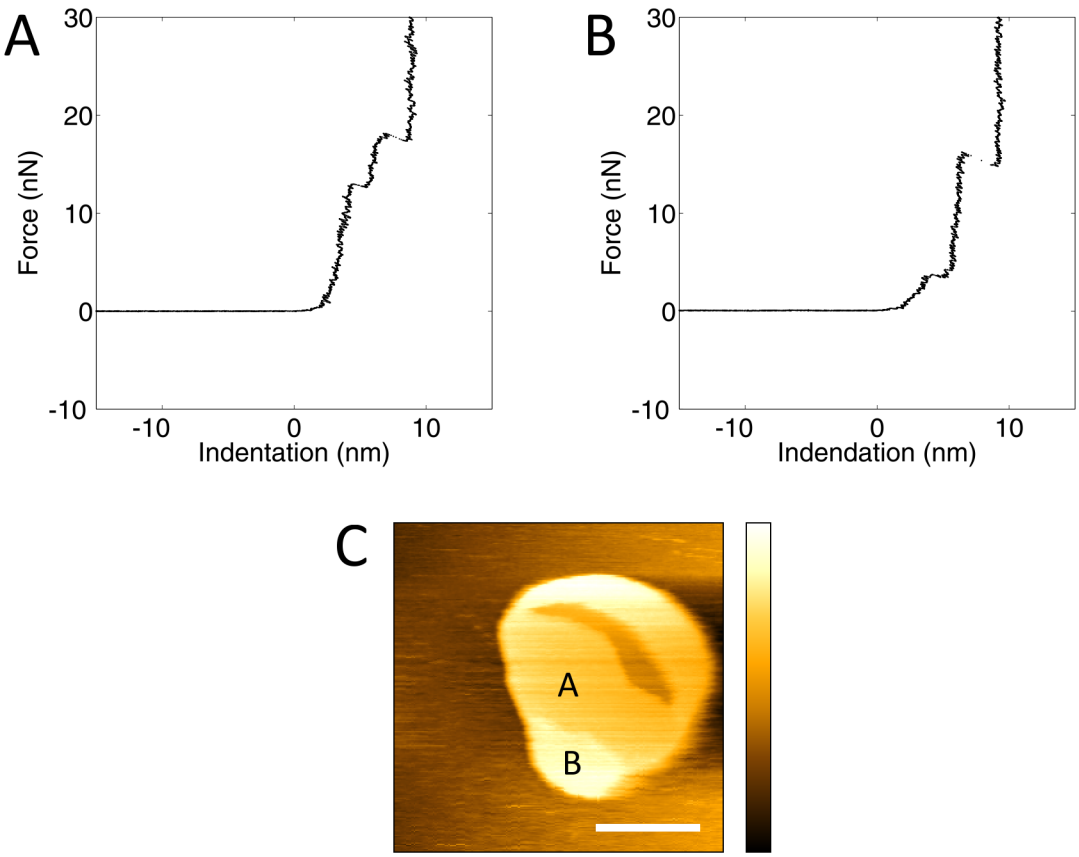

Figure 3.11: Force curves captured on a small patch containing nominally 10 mol% cholesterol with three distinct domains. A: Force curve resembling those of bulk HD at 0 - 10 mol% cholesterol. B: Force curve resembling those at ∼15 mol% cholesterol. C: AFM height image of the small patch showing the locations of force curves A and B. The force curve showing behaviour indicative of higher cholesterol content was captured on the highest domain of the patch. Scale bar is 200 nm, colour scale represents 10 nm.

from several nano-Newtons [237, 238] to tens of nano-Newtons [239–241]. The height derived from the force curves is larger because it is measured from the contact point, where the force applied to the sample is equal to or at least close to zero. It is possible to derive the average force exerted on the sample during imaging by extracting the force measured in the force curve at the point where the distance between the tip and the mica surface is equal to the height derived from the images. Such an analysis reveals that the average forces exerted during imaging are in the range 3.5 - 5.5 nN.

In a few cases the coexistence of liquid ordered and gel phase was observed in

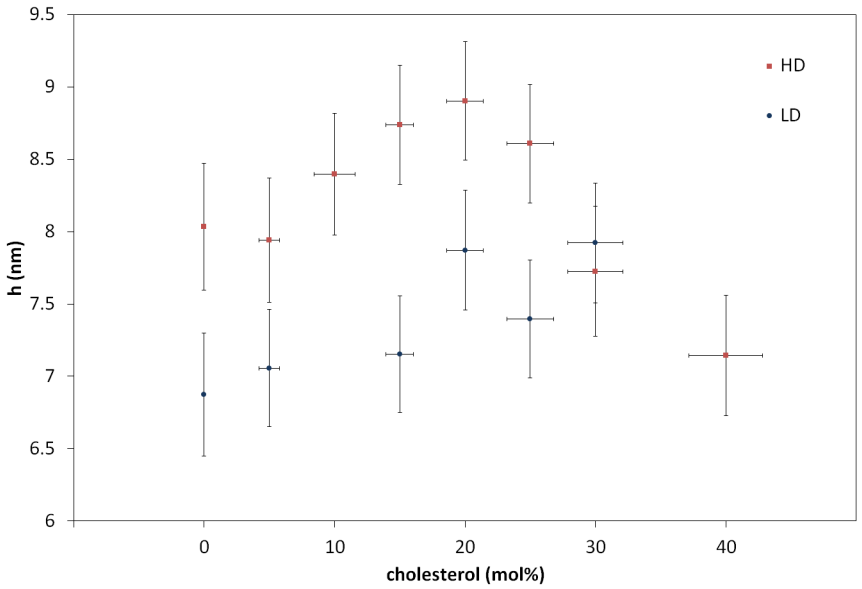

Figure 3.12: Graph showing the dependence of the height of the high and low domains of a DOPC/DSPC bilayer as a function of cholesterol content. The heights are derived from the force curves by taking the average of the indentation distance between the contact point and the point at which the tip comes into contact with the underlying mica surface.

small patches. Fig. 3.11 C depicts an example of small patch of bilayer nominally containing 10 mol% cholesterol showing domains with three heights. Typical force curves on the highest and second highest domain are shown in fig. 3.11 A and B. The highest domain seems to exhibit behaviour similar to high domain bilayers at ∼15 mol% cholesterol, while the second highest domain behaves more like the high domain of 0 - 10 mol% cholesterol bilayers. The modulus of the highest domain was found to be ∼18 MPa.

Plotting bilayer height against cholesterol concentration yields an interesting result: the height of the high domain (fig. 3.12) seems to resemble very closely the graph of the height difference between the domains (fig. 3.4). Both the shape as well as the height differences between the central maximum and the beginning and end points match up well. It seems likely that changes in the height of the high domain are chiefly responsible for the changes in the height difference between the domains.

A more detailed analysis of the force curves obtained on the high domain include

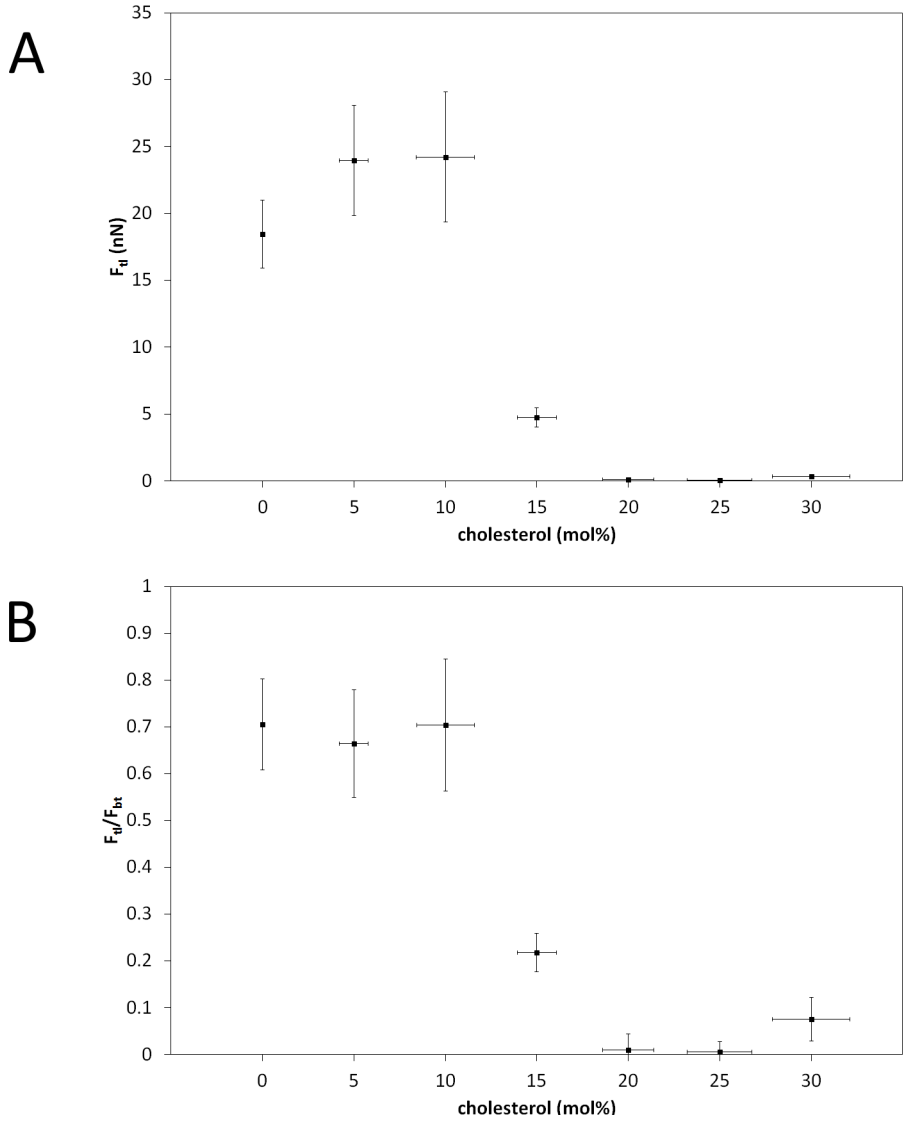

Figure 3.13: Graphs showing the force at which the high domain is compressed into the posited thin layer (F_{tl}) and its dependence on cholesterol concentration. A: Absolute values of F_{tl}. B: Fractional values of F_{tl}/F_{bt} (F_{bt} is the breakthrough force).

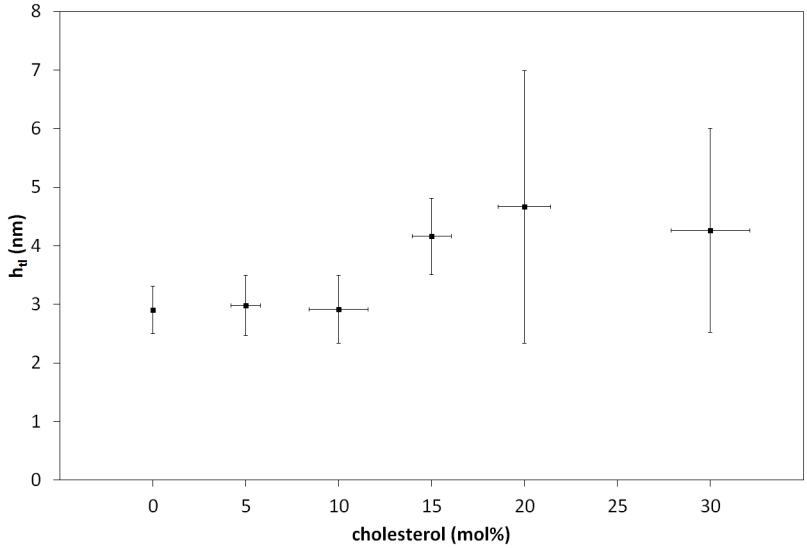

Figure 3.14: Graph displaying the effect of cholesterol on the height of the thin layer (h_{tl}) formed upon compression of the high domain in the DOPC/DSPC system.

the force required to compress the bilayer into the intermediate thin layer, F_{tl}, i.e. the force difference between the contact point and the highest point of the first kink. Graphs showing the absolute value of F_{tl} and the ratio of F_{tl}/F_{bt} are given in fig. 3.13A and B, respectively. It appears as though the high domain is compressed into the posited thin layer at a force equal to 70% of the breakthrough force at cholesterol concentrations up to 10 mol%. At 15 mol% it is only 20%, and above this the majority of force curves do not show two distinct breakthrough events anymore.

The height of the thin layer (h_{tl}) can be measured as the indentation difference between the minimum of the first kink and the minimum of the second kink. It should be noted that this is a measure of the height of the thin layer under compression, and that this compression is dependent on F_{tl}. The graph in fig. 3.14 shows that the height of the thin layer is constant at ∼3 nm up to a 10 mol% cholesterol content, even though the compression of the layer is 30% higher at 5 and 10 mol% than it is at 0 mol% cholesterol. The thin layer increases in height to ∼4 nm at 15 mol% cholesterol and further increases to ∼4.7 nm at 20 mol%. It is unclear whether this is due to a change in composition or simply because the force exerted by the cantilever

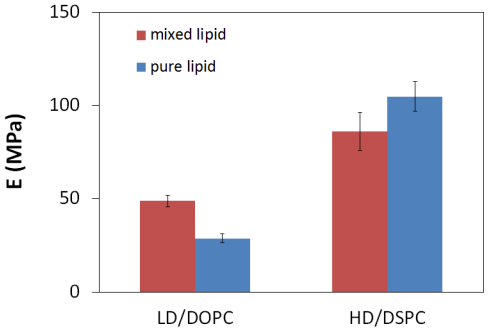

Figure 3.15: Column chart showing how the elastic modulus of pure DOPC and DSPC (blue columns) compares to that of their respective phases in the 1:1 mixed system (red columns). The modulus of pure DOPC is lower than that of the low domain, while the modulus of pure DSPC is greater than that of the high domain.

is lower at these concentrations (owing to the fact that less force is required to cause the transition from high domain to thin layer). Data beyond 15 mol% cholesterol should be considered unreliable, as mentioned above.

In order to compare the lipid mixture to its pure components, force curves on pure DSPC and pure DOPC bilayers, as well as on a 1:1 mixture of the two were captured with the same cantilever. They were analysed in the same way as the experiments with varying cholesterol content were. The results, summarised in fig. 3.15, indicate that pure DSPC has a higher modulus than the high domain in the mixture, while pure DOPC has a lower modulus than the low domain in the mixture. The increase in modulus of pure DSPC over the mixed HD is ∼25%, while the reduction in modulus of pure DOPC from the mixed LD was ∼40%. Intuitively, this result is just as one might expect: In the mixed system, the high and low domains are DSPC-rich and DOPC-rich phases. That is to say, each phase contains some amount of the other type of lipid, bestowing its properties on that phase in some measure.

3.5 Effect of temperature on POPE bilayers

The lipid POPE is a common component in lipid mixtures used for protein reconstitution, especially when it is desired to fuse protein-containing liposomes with painted bilayers, e.g. for electrophysiology [242]. It has been noted in AFM studies that membrane proteins such as AMPAR and KcsA reconstituted into mixtures of POPE:POPC:POPS (at 2:1:1) tend to localise at the phase boundary between the high and low domains [6, 235]. Of the lipids in this mixture, POPE is the only one with a gel transition temperature higher than room temperature at 26° [243, 244]. At $T < T_m$ it is expected therefore that gel phase domains begin to nucleate, giving rise to mixed phase LD/HD behaviour at ambient temperatures. As such, this lipid is key in the two-domain-structure of the lipid mixture, and understanding POPE underlies any understanding of the phase-related behaviour of proteins incorporated in the mixture.

3.5.1 Imaging of POPE bilayers at various temperatures

AFM imaging using the CoolerHeater^{TM}temperature control stage reveal that bilayers composed of POPE exhibit a topography that is highly variable at temperatures near room temperature. Figure 3.16 shows the changes a POPE bilayer undergoes as temperature is varied. The first sequence show the effect of decreasing the temperature from 20°C to 14°C. In the run up to the sequence, the temperature was gradually lowered from 30°C over the course of several hours. The high domain regions that have nucleated and grown in the low domain can be seen to increase in size as the temperature is lowered. The second sequence in fig. 3.16 shows the response of the bilayer to an increase in temperature from 20°C to 27.7°C. Just before the sequence, the temperature was abruptly increased from 10°C to 20°C. This is likely the reason for the large number nucleation sites at which low domain has begun to form. These

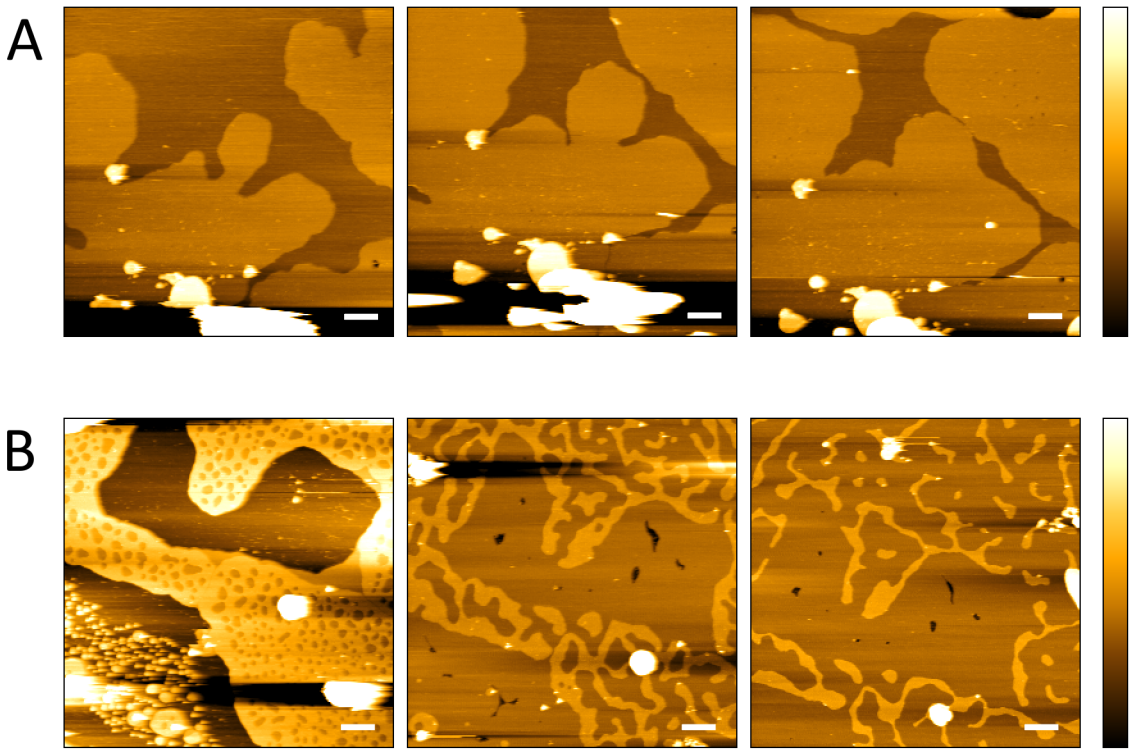

Figure 3.16: Sequences of AFM height images of a POPE bilayer on mica support at various temperatures. A, from left to right: Bilayer imaged at 20°C, 17°C, and 14°C. The high domain area increases as the bilayer is cooled. B, from left to right: Bilayer imaged at 20°C, 23.9°C, and 27.7°C. Low domain regions nucleate in the high domain regions and grow as the bilayer is heated. The mica visible in the first image of sequence B was covered by bilayer in the subsequent images. All scale bars are 1 µm, and the colour scales represent 10 nm.

low domains can be seen to increase in size as the temperature is increased. The bare mica areas visible in the first scan have been filled in by lipid bilayer in subsequent scans – a phenomenon that was observed frequently, and especially at higher temperatures.

From images such as the ones in fig. 3.16, it is possible to measure the area fraction occupied by each domain as a function of temperature. This was done using the same method described in section 3.3. The results of this analysis are given in fig. 3.17. It can be seen that while there is a marked decline in the area of the high domain as temperature is increased from 20 to 25°C, there is still an appreciable amount of high domain left at temperatures significantly higher than the transition temperature.

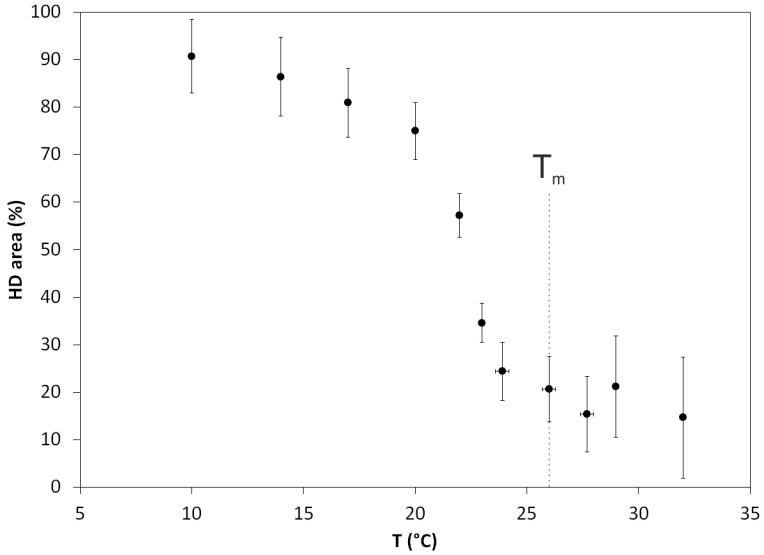

Figure 3.17: Graph of the percentage of the total area of AFM images such as the ones in fig. 3.16 that consists of high domain. The shape of the graph is sigmoidal, with a sharp decline in the amount of high domain at temperatures between 20 and 25°C. There are three data points with horizontal error bars – these are data points for which the temperature feedback had to be switched off due to the noise created by changes in the polarity of the voltage across the Peltier element (see section 3.2.3).

Similarly, there are still some low domain areas in evidence at temperatures much lower than the transition temperature.

3.5.2 Force curves on POPE bilayers.

Examples of POPE force curves are shown in fig. 3.18. The shapes of the force curves on the low domain bore a lot of similarity to their counterparts in the DOPC/DSPC system, and were qualitatively unaffected by changes in temperature. The high domain force curves, by and large, were qualitatively different from DOPC/DSPC high domain force curves. While in a few instances the high domain of POPE exhibited two kinks, most of the force curves only had a slight "hump" where the first kink might have been. Das et al proposed a mechanism for a similar phenomenon in sphingomyelin-rich domains involving the breaking of inter-lipid hydrogen bonds [245]. PE head groups, like sphingomyelin, have hydrogen bonding sites, so it appears likely

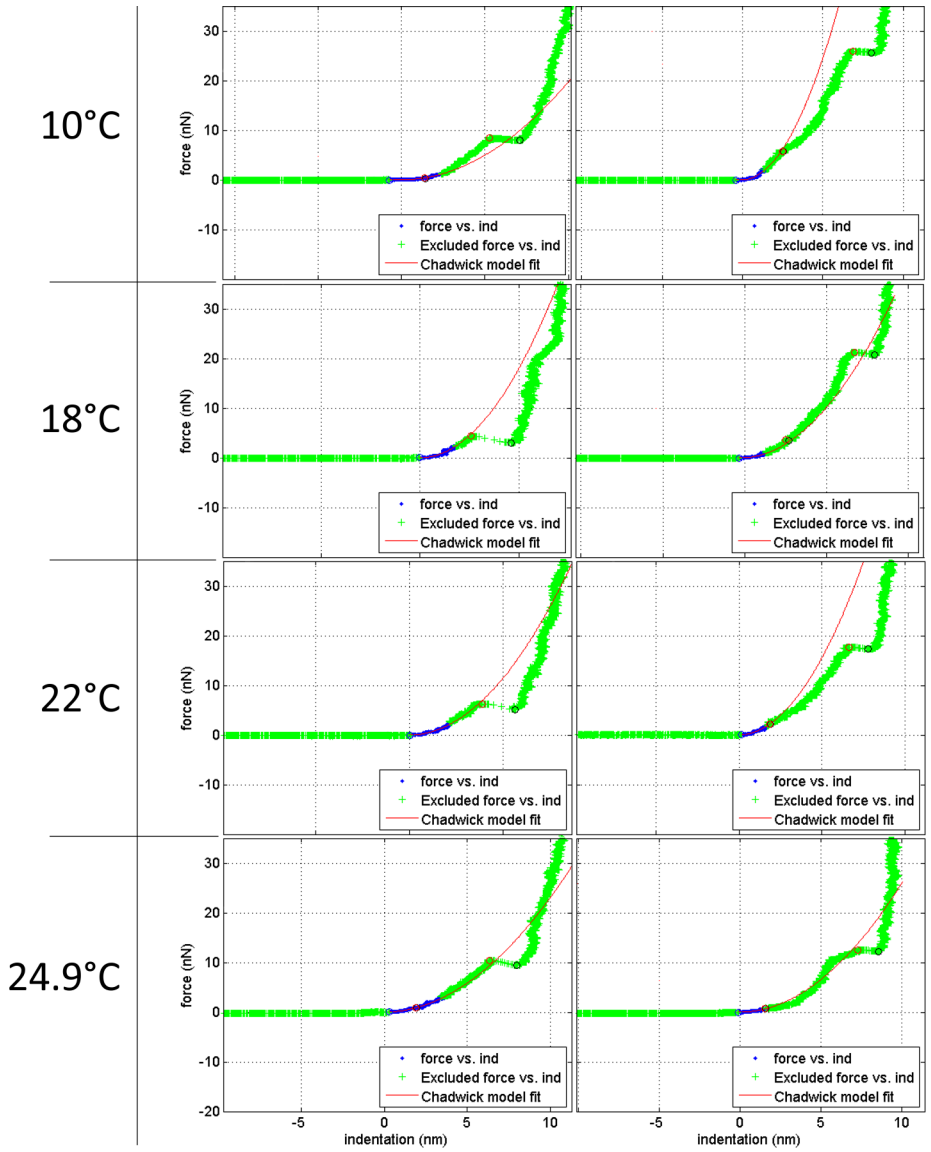

Figure 3.18: These are typical force curves on the low domain (left column) and the high domain (right column) of a pure POPE bilayer at various temperatures, including the parabolic fit computed from the first 20% of the indentation (blue points) by the fitting software. The blue circle in each graph represents the contact point determined by the fitting algorithm. The red and black circles show where the program has determined the beginning and end of the breakthrough events. Low domain force curves remain qualitatively similar as temperature is increased. Most high domain force curves, while not exhibiting the dual kink shape seen in DSPC and DSPC-rich bilayers, do exhibit an initial "hump" that is reminiscent of the first kink in DSPC gel bilayers. This hump becomes less and less pronounced as temperature is increased. The force at which breakthrough occurs is also reduced with increasing temperature.

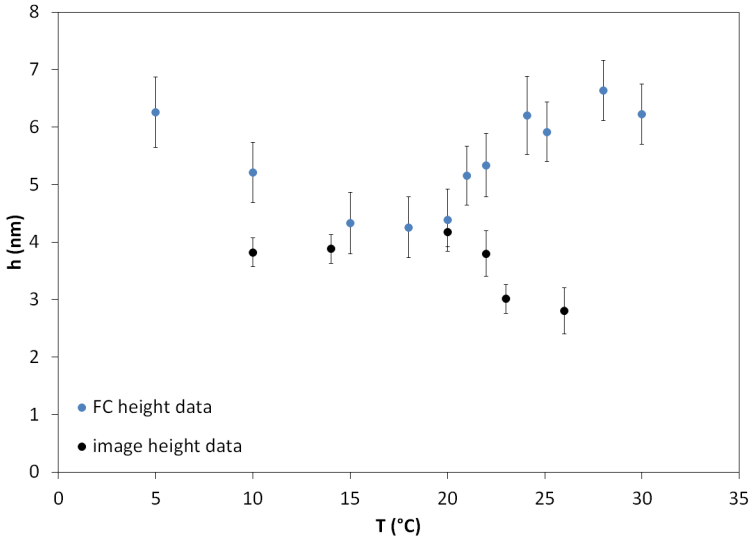

Figure 3.19: Graph showing the height of the low domain of a POPE bilayer on mica at different temperatures, as determined from AFM height images (black circles) and from force curve data (blue circles). The height as determined by AFM imaging seems to be constant at ∼4 nm at temperatures up to 20°C, after which it declines to ∼3 nm over a span of 6°C. The force curve derived height on the other hand seems initially decrease from ∼6 nm at 5°C to ∼4.5 nm at 15°C, after which it increases once again to ∼6 nm as temperature is further increased.

that the cause of this hump shape is also the breaking of hydrogen bonds. The hump shape became less pronounced as temperature was increased.

Height information gathered from force curves in the same way described in section 3.4.1 yields an interesting comparison to the corresponding data obtained from AFM height images. Shown in the graph in fig. 3.19 is the height of the low domain of POPE as measured from force curves (blue circles) and images (black circles). As for the DOPC/DSPC system, the heights obtained from force curves are consistently higher than those obtained from imaging. More interestingly, there seems to be opposite trends in the height above temperatures of ∼ 20°C: here the height of the bilayer appears to increase with temperature when measured using force curves, while heights obtained from images decrease with increasing temperature.

The elastic modulus of the high and low domains of a POPE bilayer as a function of temperature is shown in fig. 3.20. There is a clear decreasing trend in the modulus of

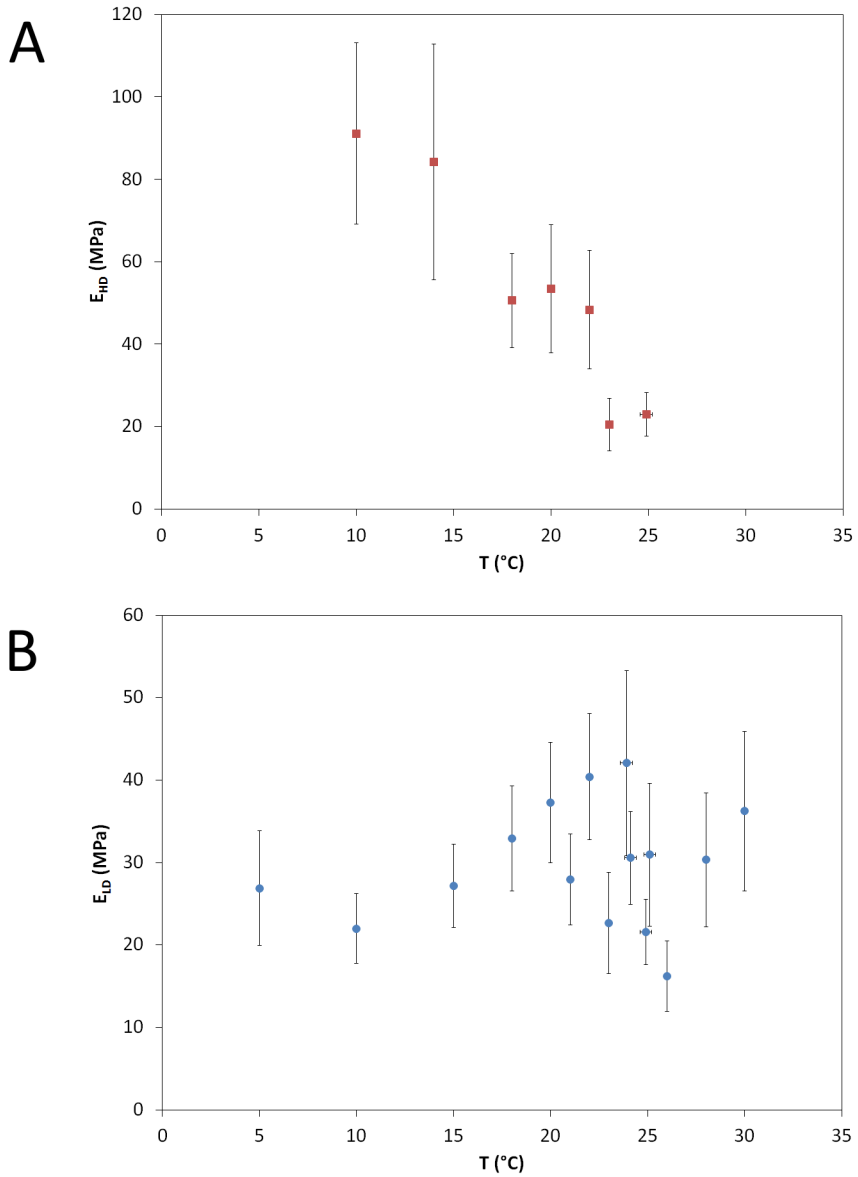

Figure 3.20: Graphs showing the elastic modulus of the high domain (A) and low domain (B) of a POPE bilayer on mica at different temperatures, determined by fitting the Chadwick model to force curves. The modulus of the high domain seems to decrease with increasing temperature. The low domain modulus shows no clear temperature dependence over the measured range, although fluctuations in modulus measurements increase at higher temperatures.

the high domain as temperature is increased. From 10 to 25°C its modulus decreases by a factor of >4. The low domain, on the other hand, shows no clear upward or downward trend. It seems that the fluctuations in the measurement increase at higher temperatures.

Vertical error bars in the figures referenced above were obtained in the same way as for the DOPC/DSPC graphs. Horizontal error bars, where present, stem from slight variations in temperature that occur when the temperature feedback was turned off (see section 3.2.3 for details).

Landau theory of phase transition may be brought to bear on the gel to liquid phase transition of lipid bilayers as demonstrated by Sackmann and Lipowsky [246]. The free energy difference between the L_α and L_β phases can be divided into the two following parts. The power expansion of the free energy in terms of $\rho = \rho_\alpha - \rho_\beta$, the difference in lateral packing density of the phases is given by

$$\Delta G_\rho = \frac{1}{2}a(T - T_m)\rho^2 + \frac{1}{4}A_4\rho^4 + \frac{1}{6}A_6\rho^6$$

where T is temperature, T_m is the transition temperature, and a, A_4, and A_6 are parameters dependent on temperature and lateral pressure. The change in tilt angle, θ, and the coupling between chain tilting and lateral packing density contributes a term to the free energy given by

$$\Delta G_\theta = \frac{1}{2}K_{11}(\theta_\beta - \theta_\alpha)^2 + t\rho^2(\theta_\beta - \theta_\alpha)$$

where K_{11} is the orientational elastic constant of the bilayer (related to the bending modulus κ and the membrane thicknes d by the equation $K_{11} = \kappa/d$), and t is a further parameter dependent on temperature and lateral pressure.

Minimising the total free energy of the bilayer with respect to θ_β yields the ex-

pression

$$(\theta_\beta - \theta_\alpha) = -\frac{t\rho^2}{K_{11}}$$

which can be substituted into the equation for the total free energy to give

$$\Delta G_{tot} = \frac{1}{2}a(T - T_m)\rho^2 + \frac{1}{4}(A_4 - \frac{2t^2}{K_{11}})\rho^4 + \frac{1}{6}A_6\rho^6.$$

Minimising this expression with respect to ρ and solving it leads to the expression for the difference in lateral density between gel and liquid phases

$$\rho = \left(\frac{a(T_m - T)}{A_4 - 2t^2/K_{11}}\right)^{\frac{1}{2}}$$

which, for the purposes of this analysis can be simplified to

$$\rho = \rho_0(T_m - T)^{\frac{1}{2}}.$$

A relation between Young's modulus E and lateral packing density ρ can be found by noting that the bulk modulus B is given by

$$B = \frac{E}{3(1 - 2\nu)},$$

and for a system obeying a Lennard-Jones potential, $B \propto \rho$ [247]. Assuming the other terms in the above expression only depend weakly on temperature, this shows that $E \propto \rho$. Prior work using AFM has examined the relation between temperature and breakthrough force for POPE (see Alessandrini and Facci [111]), but none have related elastic modulus to temperature. The advantages of the latter approach is that the modulus values are derived from the early parts of the force curves, where the system is less perturbed by the AFM tip.

Fitting the data in fig. 3.20 A to the equation $E = E_0 + E_1(T_m - T)^n$, where T_m is

obtained from fig. 3.17 (23°C). The fit results in $n = 0.49$, indicating the mean field approach is appropriate for this data set. E_0 is computed as 21.8 MPa, which is in good agreement with the modulus value of the fluid phase in that temperature range. The adjusted R^2 value for the fit is 0.92.

The L_β - L_α transition in lipid bilayers has been studied extensively using deuterium NMR in which the time-averaged electric field gradient tensor of the deuterium quadrupole interaction is measured. Hawton and Doane [248] observed this splitting in DPPC and DMPC bilayers to vary with temperature as $\sim (T_m - T)^{\frac{1}{2}}$ in the neighbourhood of T_m . The phase transition is regarded as being first order, but order parameter fluctuations – essentially lipid areal density fluctuations – give the appearance of mean-field behaviour in the mixed phase region. Interestingly, NMR experiments on PE lipid bilayers (dimyristoylphosphatidylethanolamine [248] and POPE [249]) failed to detect this splitting in the region $T < T_m$, which was attributed to PE lipids being only weakly hydrated in the L_β phase. The AFM experiments presented here measure the membrane elastic modulus which is proportional to the (areal) lipid density and so circumvent the requirement in NMR for fluctuation-driven motional narrowing: the mean field behaviour observed at $T < T_m$ is in excellent agreement with the NMR measurements of transitions in PC lipid bilayers.

3.6 Modified probes and the HD/LD boundary

The boundary between lipid phases presents an opportunity to study the kinetics and energetics of phase transitions. Little is known about the physical structure of the bilayer in this region. Hydrophobic interactions likely cause tilting of the lipids at the boundary between domains of differing thickness. This may also lead to an increased incidence of defects as compared to flat regions of the bilayer. An example of the biological significance of the phase boundary is found in the preferential localisation

of AMPA receptors in this region upon reconstitution into DSPC/DOPC/cholesterol bilayers [6] (see also fig. 3.1). In an attempt to shed light on this phenomenon, the boundary region was probed using EBID modified AFM tips. The data was collected by first imaging an area containing a boundary at high magnification, and then carrying out force curves in a line across the boundary. The same area was subsequently rescanned to assess the extent of drift and diffusion/deformation of the sample. It is not practical to use commercial probes for this purpose, since the transition from HD to LD occurs on a scale smaller than the radius of commercial probes. A further issue results from the fact that the high domain is affected semi-permanently by tip indentation (see 3.4.1), meaning that the minimum spacing between successive force curves has to be at least on the order of the tip radius to avoid subsequent force curves being influenced by the previous ones. Thus the tip radius is the crucial factor in determining the lateral resolution that can be achieved, and the modified probes presented in chapter 2 serve as a very useful tool to carry out these experiments.

As is to be expected, the force required to penetrate the bilayer using a sharp tip is significantly lower than it is for commercial probes. The breakthrough force is reduced by a factor of about 6, which is commensurate with the decrease in the radius of the tip. Qualitatively, the force curves exhibit similar characteristics to their counterparts captured with commercial probes: The high domain is penetrated in two distinct stages, leading to the initial kink described in section 3.4.1, while the low domain force curves display a relatively smooth curve followed by a single breakthrough event. In measurements on bulk HD (i.e. away from the boundary) it was found that the increase in modulus going from 0% cholesterol to 5% cholesterol observed in section 3.4.1 persists when using sharp probes and is of a similar magnitude.

Qualitatively speaking, the force curves captured on the boundary between HD and LD seemed to be an amalgamation of high and low domain force curves: they display the low breakthrough force of the LD, but with the double kink structure

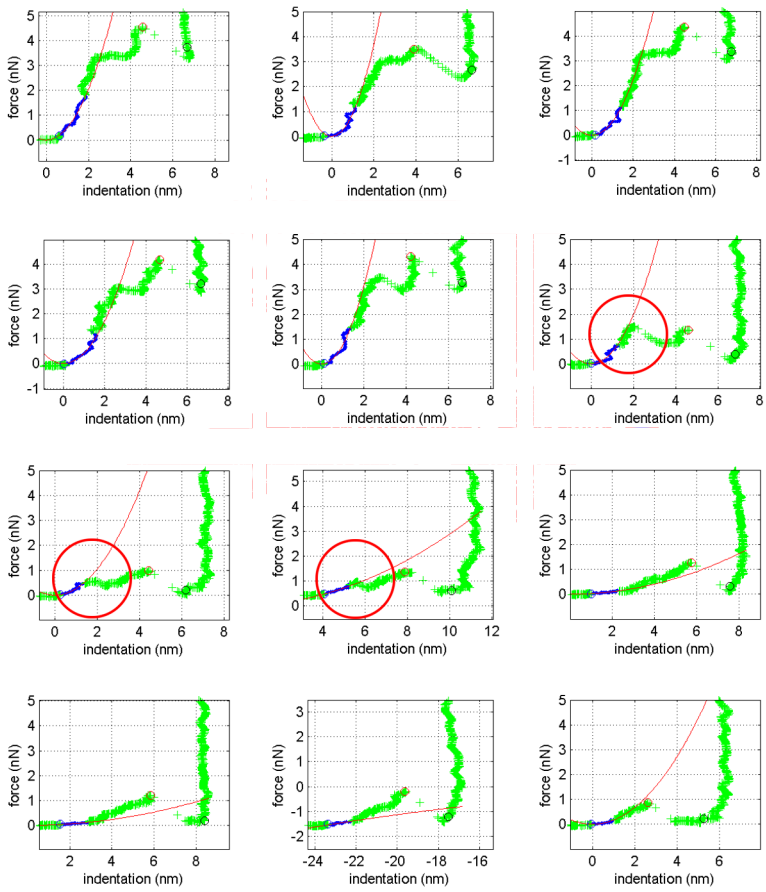

Figure 3.21: A series of force curves captured in a line across the HD/LD boundary of a DSPC/DOPC sample without cholesterol, starting on the high domain (top left) and finishing on the low domain (bottom right). Force curves captured in the transition region exhibit a low breakthrough force akin to low domain force curves, yet maintain the double-kink structure found in high domain force curves. The kinks are marked by the red circles.

found on the HD. An example of a series of force curves taken across the boundary of a sample without cholesterol is shown in fig. 3.21. The lateral distance between each force perpendicular to the boundary is approximately 3.7 nm. The inevitable time delay between imaging and capture of force curves, in combination with the lateral drift of the sample with respect to the tip and the changes in domain shapes due to lipid mobility, results in some uncertainty in the distance perpendicular to the boundary.

Figure 3.22 shows graphs of the breakthrough force (F_{bt}) and the height (h) values derived from individual force curves captured across the HD/LD boundary in DOPC/DSPC/cholesterol bilayers and plotted as a function of lateral distance perpendicular to the boundary. Graphs like these allow an estimation of the length scale over which the transition from one domain to the other occurs. In general, the lateral distance between the last force curve with a breakthrough force characteristic of the low domain and the first force curve with a breakthrough force characteristic of the high domain is 14 $\pm$ 4 nm. This corresponds to $\sim$15 lipid molecules, assuming approximately circular head group areas of 0.6 nm^2 [5].

An interesting feature of the height profile across the boundary as determined by force curves is that the height measured near the high domain side of the boundary seems to be consistently higher than the height that is in evidence in the high domain itself. Nine data sets in which this phenomenon was encountered give an average height increase at the boundary of 0.64 $\pm$ 0.10 nm (N = 9) over bulk high domain. The difference in height between the high and low domains themselves, measured from the same data sets to be 1.02 $\pm$ 0.17 nm. This finding is in clear contrast to data gathered in AFM scanning; there is no "lip" visible at the boundary between high and low domains in AFM height images.

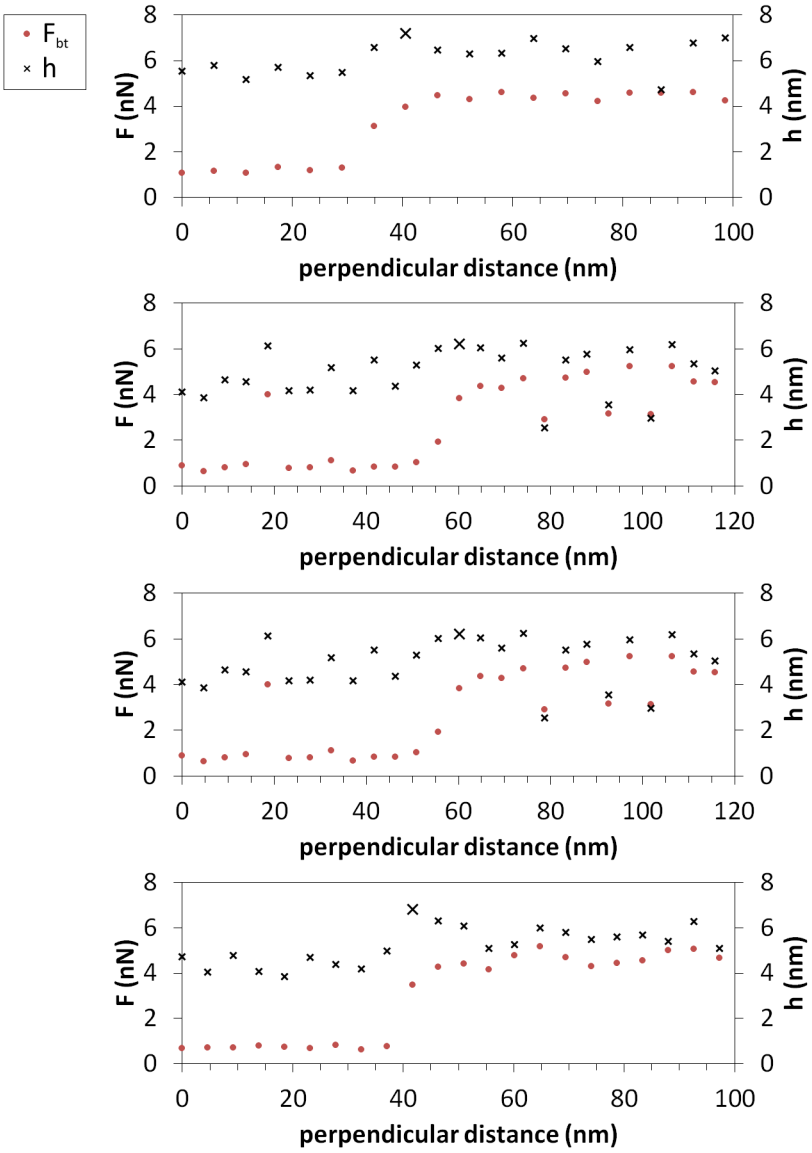

Figure 3.22: Graphs showing the breakthrough force (F_{bt}) and height (h) values of individual force curves as a function of lateral distance perpendicular to the boundary. The top graph is a data set from a 5 mol% cholesterol DOPC/DSPC bilayer; the bottom three are from a 20 mol% cholesterol DOPC/DSPC bilayer. Red circles denote force values, while black crosses are height values. The height value measured on the high-domain side of the boundary region is consistently higher than the average high domain height, and is denoted by a larger cross in the graphs.

3.7 Discussion

3.7.1 Imaging on DOPC/DSPC/cholesterol bilayers

AFM tapping mode imaging provides a wealth of information about lipid bilayers. Here it was used to assess the size, shape, and distribution of the domains found in DOPC/DSPC bilayers with varying cholesterol content. It was also used to study the height difference between said domains and their fractional areas. The results point to significant changes in the composition of each domain as the cholesterol concentration is increased. There are several structural changes in the domains as cholesterol content is increased in this system. The first is the change from high domain islands in a "sea" of low domain to the inverse conformation of low domain islands in a high domain sea at 10 to 15 mol% cholesterol. This conformation seems to reverse once more at 20 mol% cholesterol content, albeit with high domain islands that are significantly smaller in size (as well as total fractional area) than their low cholesterol counterparts. Finally, at 30 mol% cholesterol the fractional area of the high domain radically increases to close to 50% once more.

At 0 mol% cholesterol the bilayer consists of a DOPC-rich low domain and DSPC-rich high domain. It is proposed that when a small amount of cholesterol ($\sim$5 mol%) is introduced the solubility of DOPC in the HD is reduced. The result would be an increase in the area of the LD compared to HD. This hypothesis would also account for the initial increase of the modulus and breakthrough force of the HD in that the "purer" HD at low cholesterol is harder than the more mixed HD at 0 mol% cholesterol. This is supported by the fact that the change in HD modulus going from 0 mol% to 5 mol% cholesterol is almost identical to the difference between 0 mol% cholesterol (mixed) HD to 0 mol% cholesterol pure DSPC. The former difference is slightly smaller at a 19% increase compared to 23% for the latter. This makes sense, as one would not expect a completely pure DSPC phase in the former case.

The change in modulus of the low domain provides further support for this idea: It was found that addition of 5 mol% cholesterol reduced the modulus of the low domain by ∼25%. Pure DOPC was found to have a modulus ∼40% lower than the low domain in the mixed system (at 0 mol% cholesterol). Thus a migration of DOPC from the HD into the LD (caused by the addition of cholesterol) would explain the apparent softening of the low domain.

This hypothesis may also account for the initial increase in Δh: The "purer" HD may be more closely packed, reducing the area per lipid and consequently increasing its height. The height information from the force curves on the HD seems to reproduce almost perfectly the shape of the Δh between the phases garnered from images. That is to say, it seems that the changes in Δh can be fully or almost fully accounted for by changes in the height of the HD. Another possibility seems to be that the inclusion of cholesterol in the high domain increases its height. This is supported by the fact that in patches with three distinct domains (see fig. 3.11) the liquid ordered domain appears to be higher than the gel domain. It is worth noting that molecular dynamics simulations of bilayers containing DOPC, the saturated lipid dipalmitoylphosphatidylcholine (16:0, DPPC), and cholesterol indicate that cholesterol preferentially interacts with DPPC over DOPC [250].

As the cholesterol is further increased to 20 mol%, the height of the HD seems to further increase, while its modulus and breakthrough force drop precipitously. The decrease in these mechanical properties seems indicative of the phase transition from gel to liquid ordered, which is reported to occur between 10 and 20 mol% cholesterol in this system [251].

The reduction in the fractional area of the HD as cholesterol is increased from 0 to 20 mol% cholesterol indicates that a net migration of lipids from the HD into the LD. It appears as though the energetics of the system shift in such a way as to increase the solubility of DSPC in the low domain. Molecular dynamics simulations of the

interactions between cholesterol and lipids indicate that the free energy of DPPC is increased as cholesterol content rises [252], supporting the idea that an increase in cholesterol may serve to drive DSPC into the low domain.

A potential theoretical justification for this hypothesis is that cholesterol, occupying the interstitial spaces between lipid molecules, reduces the steric freedom of DOPC molecules in the HD, making this phase energetically less favourable for them and leading to the initial decrease in HD area. As cholesterol concentration is further increased, DSPC ordering is inhibited more and more, reducing the free energy gap between DSPC in the HD and DSPC in the LD, leading to solubilisation of DSPC and a further reduction of HD area. An increased incorporation of DSPC in the low domain may also account for the rise in the modulus of that domain in the range 10 - 15 mol% cholesterol.

At around 30 mol% cholesterol another transition takes place, causing the sudden increase in the area fraction of the HD. It seems that at this tipping point the energetics of the system shift once more, causing a return of material into the high domain. Increased fractional incorporation of DOPC in the HD would serve to explain the reduction in the height of that domain, as well as the increase in fractional area. Details of the mechanism of such a change in the miscibility of the components of the bilayer cannot be deduced from the data.

It is worth noting that no phase transition is reported in the literature for this system around 30 mol% cholesterol. The change in HD area (and height) must therefore be a more subtle change in the energetics of the system, rather than a significant upheaval in its structure.

The data do not offer an obvious explanation for the changes in appearance of the HD as cholesterol is increased (from big islands to stringy borders to small islands to big continents). The fact that the circumference-to-area ratio varies so much bespeaks changes in the energetic importance of line tension. The fact that the high domain

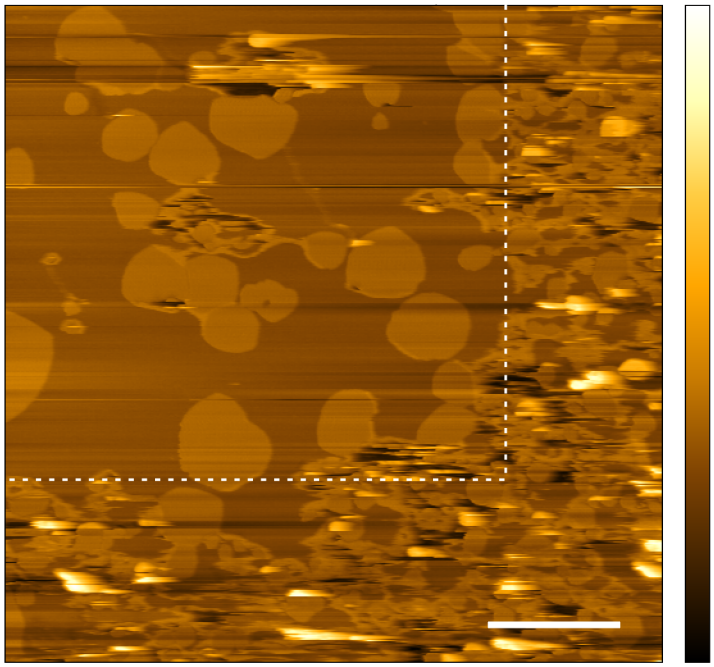

Figure 3.23: AFM height image of a DOPC/DSPC bilayer with 5 mol% cholesterol displaying effects of tip-sample interaction. The area enclosed by the dashed line was repeatedly scanned prior to the capture of this image. The scan area was then moved and a single scan was performed. The scale bar represents 1 µm and the colour scale is 23 nm.

regions seem to preferentially localise near the edges of lipid patches at cholesterol concentrations of 10 - 15 mol% seems further evidence for this notion. A detailed study of the boundary region at different cholesterol concentrations may reveal the underlying causes for this behaviour.

A caveat to the above conclusions is that the reliability of AFM imaging data drawn into question by tip-sample interactions. An example of the severity of such interactions is shown in fig. 3.23. An area of 5 mol% cholesterol DOPC/DSPC bilayer was scanned a number of times. The scan area was then shifted down and to the right to capture the image seen in the figure. The change in the sample surface is very apparent: In the area scanned previously the HD patches area significantly larger and the overall appearance of the bilayer is "cleaner". It seems that the tip interaction causes the small high domains that are initially present to coalesce into larger domains,

as well as sweeping away most of the contaminating lipid globules that do not form part of the bilayer. The presence of these globules make measurements in the more "pristine" regions difficult, but a small sample of measurements was collected and compared to the data obtained on the pre-scanned area. The results indicate that while the appearance of the bilayer is changed greatly, the area fractions of the two domains remains the same.

3.7.2 Force curves on DSPC/DOPC/cholesterol bilayers

It was found that below a cholesterol concentration of ∼20 mol%, high domain force curves exhibit a "double-kink" shape. There are several possible explanations for this phenomenon. At first glance it may seem plausible that each kink corresponds to the tip breaking through one leaflet; first the distal leaflet to produce the first kink, then the proximal leaflet for the second kink. This mechanism is problematic due to the exposure of the hydrophobic tails of the proximal leaflet to the aqueous environment after the first breakthrough event, a conformation that can be presumed to carry a large energetic penalty. Another possible explanation would be to posit a phase transition from the initial gel phase to another phase that is significantly thinner. The change from gel phase to liquid disordered phase is associated with a decrease in bilayer height, but this cannot be the explanation as a liquid disordered bilayer also has a significantly lowered breakthrough force – the tip would instantly penetrate through to the mica instead of encountering renewed resistance and tracing out a second kink. A more exotic phase may fit the observed data more satisfactorily: the interdigitated phase. This bilayer structure is formed when the leaflets are pushed into one another, causing their hydrocarbon tails to overlap. This phase can be induced by the application of hydrostatic pressure [253, 254].

It is possible to extract a value for the height of the layer that is formed in the first breakthrough event from force curve data by calculating the difference in

indentation depth between the endpoint of the indentation and the endpoint of the first kink. The result of this analysis is similar for pure DSPC and the DSPC-rich high domain of the mixed DOPC/DSPC system. For pure DSPC the height of the layer is 3.15 ± 0.08 nm, while for the mixed high domain it is 3.20 ± 0.08 nm. AFM height images of halothane-induced interdigitated DPPC (16:0) bilayers indicate that they are 3.5 nm thick [255]. While the hydrocarbon chains of DPPC are shorter by two carbon links than their DSPC counterparts, it is important to remember that the heights derived from the force curves come from bilayers that are under considerable pressure from the tip. The force at which interdigitation occurs in pure DSPC bilayers is 21.6 ± 0.2 nN. This value is slightly lower at 19.2 ± 0.3 nN for the high domain in DOPC/DSPC bilayers, but in both instances this force is significantly higher than it would be in AFM imaging. It seems reasonable to conclude that the first kink in DSPC and high domain force curves is indeed caused by a phase transition from the gel phase to an interdigitated phase.

The proposed mechanism for tip penetration through the low and high domains of a DOPC/DSPC bilayer can be seen in fig. 3.24. The process shown in fig. 3.24A describes the mechanism for penetration through liquid disordered or liquid ordered phases, where there is only one kink. This mechanism has been proposed elsewhere for dioleoylphosphatidylserine (DOPS) and 1,2-dioleoyl-3-trimethylammonium-propane (DOTAP) bilayers [58]. Fig 3.24B shows the proposed mechanism for breakthrough on gel phase of the system. Here, the first of the two kinks is caused by a conformational change of the bilayer from a standard gel phase to an interdigitated phase. In both A and B, the pressure exerted by the tip causes an increase in the Gibb's free energy of the bilayer in its initial state. Once the pressure surpasses a certain point, the free energy of the bilayer under pressure is greater than the free energy of the bilayer penetrated by the tip (fig. 3.24A) or the bilayer in an interdigitated phase (fig. 3.24B), and thus the transition occurs.

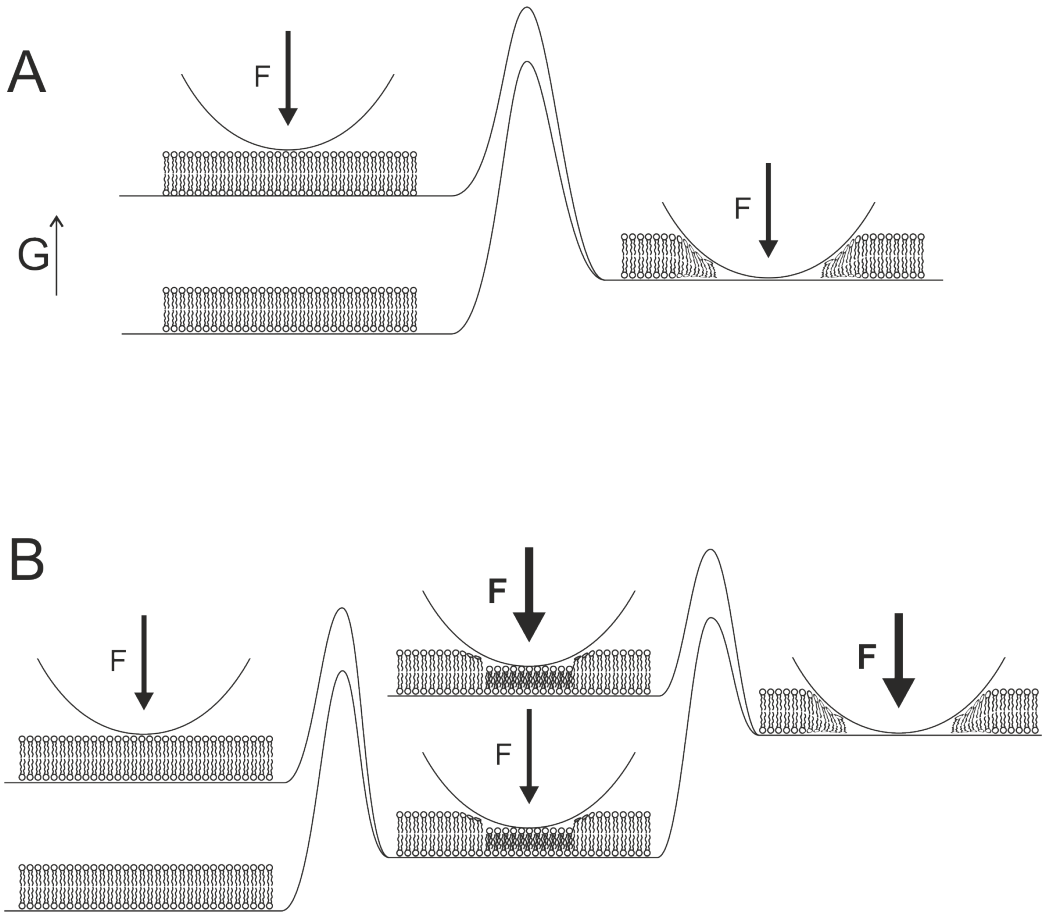

Figure 3.24: Schematic representations of the stages of penetration of an AFM tip through bilayers and their positions in terms of Gibb's free energy (G) and reaction coordinate. These serve as explanations for the shapes of the force curves on the low and high domains. A: Breakthrough on a liquid disordered (low domain) or liquid ordered bilayer (high domain at $\geq$25 mol% cholesterol content). Here, the initial state (the intact bilayer – bottom left schematic) has a lower free energy than the final state (the penetrated bilayer – schematic on right side). In order for breakthrough to happen, the free energy of the initial state has to be raised, which occurs as the tip exerts a force on the bilayer. A pressure-volume term that increases with tip force is added to the free energy of the system. Once the free energy of the transitional state (tip pressing on intact bilayer - top left schematic) is equal to that of the final state, the breakthrough is energetically feasible and is only prevented by kinetic obstacles. B: Breakthrough on a gel phase bilayer (high domain at <25 mol% cholesterol content). Essentially similar to the above, this case is complicated by an intermediate stage, in which the bilayer under the tip reorganises into an interdigitated phase which is energetically more favourable than the (first) transitional state due to the reduction in the volume being compressed. As the pressure is further increased, the free energy is eventually raised to the point that the interdigitated state becomes less energetically favourable than the penetrated bilayer, and breakthrough occurs.

It has been proposed that the double kink phenomenon may be caused by a double layer of lipid, one supported on the mica, the other adhering to the tip [256]. This seems an unlikely explanation for the data presented here, as double kinks have been observed exclusively on the high domain, while the cited article reports dual kink structure for DOPC bilayers in ionic conditions similar to the ones used in this work. Another reason to doubt the double layer explanation is the fact that the dual kink structure of the DSPC-rich phase was observed using not only tips of differing hydrophobicity (namely gold coated tips and bare silicon nitride tips), but also when using the probes modified with a platinum pillar with a $\sim$4 nm radius of curvature. Such a high curvature is likely to be highly energetically unfavourable for the proposed tip-coating bilayer. Finally, the double bilayer hypothesis does not account for the lasting indentations or "puncture marks" left behind after repeated force curves on the DSPC-rich phase.

A noteworthy caveat to the interdigitation hypothesis is the fact that repeated force curves in the same location on low-cholesterol high domain bilayers resembled those taken on the low domain. The reason for this is not clear at this time, although it may simply be that the structure of the interdigitated bilayer is deteriorated by the initial penetration by the tip, resulting in subsequent force curves that do not resemble the initial one. An alternative explanation involves the difference in area per lipid between the interdigitated phase and the gel phase: There is an increase by a factor of $\sim$2 in the lateral area subtended by each lipid in the interdigitated phase, due to the increased number of (essentially incompressible) hydrocarbon tails per unit area. As the interdigitated area of the bilayer relaxes back into the energetically favourable non-interdigitated state, DOPC molecules are preferentially recruited into that area due to their higher diffusivity. The result would be the formation of a small area of low domain bilayer in the region where the first indentation occurred. Subsequent force curves would then be indenting a small patch of LD, explaining their shape.

3.7.3 Effect of temperature on POPE bilayers

The effects of temperature on the mechanical and structural properties of a supported POPE bilayer were investigated. As seen in fig. 3.19, there is a disparity between the height measurements from AFM images and force curves that increases at higher temperatures. The images suggest that the bilayer height decreases at higher temperatures, while the force curves suggest that the bilayer height first decreases and then increases with temperature. This perplexing observation may be the result of a combination of effects of increased temperature and the conditions of each type of height measurement: At low temperatures, the bilayer is likely more ordered, resulting in closer packing of lipids and a greater layer thickness. It may be that this effect is not seen in images due to the interaction between the tip and the bilayer. At higher temperatures it may be that the thickness of the water layer between the bilayer and the substrate increases, contributing to an increased height as measured using force curves, where the point of contact (i.e. the start of the height measurement) is at near zero applied force. In images on the other hand, which are captured at an average force of several nN, the water layer would likely be compressed and the posited effects of temperature would not be visible.

Calculations of the elastic modulus of POPE bilayers show that increasing the temperature causes a decrease in high domain modulus, while the low domain modulus remains relatively constant, albeit measurement fluctuations increase (fig. 3.20). The high domain modulus values are amenable to analysis using Landau theory of phase transition, indicating that the measurement is not affected by any small scale fluctuation and that a mean field approach is sufficient to describe the data. The low domain modulus seems to be consistent with the value expected from the fit of the Landau model, although the degree of the fluctuations makes a definite conclusion difficult. It is worth noting that the analysis rests on the assumption that the the modulus of the bilayer is directly proportional to its lateral packing density. This

assumption ignores other factors such as hydrophobic and electrostatic interactions as the bilayer is deformed.

The problem associated with the CoolerHeater^{TM}, i.e. noise caused by switching the polarity of the Peltier element could be alleviated by introducing a heat source to the underside of the assembly. This way the temperature region in which polarity switching occurs could be shifted to higher temperatures that are not of interest in these experiments, while not affecting the sample temperature in any way. The easiest way to do this would be by using the coolant pump to deliver warm water to the underside of the module. This solution would need to be implemented if a temperature gradation finer than $\sim$1.5°C was desired in the region between 24 and 27°C.

3.7.4 Modified probes and the HD/LD boundary

The utility of EBID platinum modified probes in the study of the boundary between lipid domains by means of indentation was demonstrated. The modified probes provided a lateral resolution between successive force curves superior to that obtainable with commercial probes. It was possible to routinely capture force curves on the boundary between high and low domains of DOPC/DSPC bilayers. These force curves seemed to exhibit a combination of features from those captured on the high domain and those from the low domain. The fact that the breakthrough force in the boundary region is low promotes the conclusion that this region is mechanically similar to the liquid phase low domain. On the other hand, the fact that the boundary force curves exhibit a "double kink" shape, indicates that the boundary region retains qualities of the high domain.

The hypothesis used to explain the phenomenon of the double kink in section 3.7.1 is that the leaflets interdigitate. The resulting interdigitated phase in the high domain exhibits a higher breakthrough force than the gel phase it originates from. This

does not appear to be the case at the boundary: Here breakthrough occurs at a similar force as the initial interdigitation. This may be the result of an increased prevalence of DOPC molecules (and perhaps also cholesterol) disrupting the order of the interdigitated phase and causing it to fail more readily.

Breakthrough force alone does not provide enough data to distinguish between a model where the tip indents parts of the high and low domain (separated by an abrupt boundary) simultaneously and a model where the phase boundary is composed of a blurry transition with properties of both domains. Given the lateral distance between force curves of less than four nanometres and the transition region of around 14 nm, it appears likely that the boundary is smooth rather than abrupt.

Plotting the breakthrough force and height derived from force curves against lateral distance reveals that the transition region between high and low domains seems to occur on a length scale of ∼5 - 20 nm. Given a tip radius of less than 5 nm, this seems indicative of a non-abrupt transition region. These graphs also seem to indicate that increased cholesterol may act to increase the width of the transition region, although further study would be required to corroborate this conclusion.

The proposal that a "lip" forms at the boundary, supported by the height measurements from force curves, also suggests that the boundary is not simply an abrupt transition from HD to LD. The presence of such a lip, although not supported by imaging data, could form the basis of an explanation for the preferred localisation of reconstituted proteins at the phase boundary based on improved hydrophobic matching. Given the fact that the heights of the high domain (fig. 3.12) match the Δh values measured from images, and given the profound ways in which tip-sample interactions can affect lipid bilayers (see fig. 3.23), it seems plausible that this is not just an artifact.

It would be instructive to conduct a detailed study of the effects on boundary width, height, and structure of such variables as ionic concentration, cholesterol con-

tent, and temperature. The collection of more data would allow statistical analysis of the kind that the preliminary results presented here do not permit. Assessing the effect of varying tip size on apparent boundary width would allow firmer conclusions about the actual width of the boundary to be drawn. As the capabilities of measurement techniques are improved, it might also be possible to probe the dynamic nature of the boundary region.

Chapter 4

Membrane budding

4.1 Introduction

In this chapter we present a novel technique pioneered in 2013 [257] for investigating the mechanical properties of lipid bilayers.[1] We show that the approach has the potential to become a useful tool in the study of biological membranes, their mechanical properties, and potentially their constituent proteins. In these experiments bilayers are used to cover arrays of microwells situated on the surface of a silicon chip, as demonstrated in Sumitomo et al 2010 [177]. This allows the observation of a large number of suspended bilayers simultaneously. Due to the nature of the microfabricated substrate, it is not possible to apply direct pressure as it is in micropipette experiments. Osmotic pressure, induced by confining solute species inside the well and varying outside solute concentration, is applied instead.

By using fluorescent lipids in the bilayer and confining dye inside the wells along with the solutes needed to modulate osmotic pressure, it is possible to observe the changes in the shape of the bilayer spanning the pores using fluorescent microscopy [178]. The behaviour of lipid bilayers of different compositions and in different phases were studied. To shed light on the energetics of the budding process, biotin-avidin linkage was used to modulate the adhesion strength. This led to a marked change in the shape of liquid phase buds. As well as investigating the dynamics of bud formation, the long term stability of suspended bilayers was investigated and comparisons between different phases were drawn. To extract some quantitative information from the data, a mathematical model describing the free energy of the system was designed and evaluated using MatLab.

[1] Since the writing of this chapter Gleisner et a [258] published a paper detailing similar work. They used confocal microscopy to study budding of POPC and DPhPC bilayers. By fitting their data to Young-Laplace's law they were able to deduce the membrane tension and thus the adhesion strength between bilayer and substrate. They also investigated the effect of epsin N-terminal homology domain (ENTH) binding to the receptor lipid phosphatidylinositol 4,5-bisphosphate (PIP_2) on budding.

4.1.1 Osmotic pressure as a physical concept

Osmosis is the spontaneous net migration of solvent molecules across a semi-permeable membrane that leads to the equalisation of concentrations in the two compartments separated by the membrane. Osmotic pressure is the pressure required to nullify osmosis. Osmotic pressure acts to prevent osmosis from occurring indefinitely, and increases as osmosis progresses, eventually amounting to an equal and opposing force at which there is no further net movement across the membrane. The osmotic pressure of an ideal solution with low concentration is given by

$$\Pi = iMRT$$

Where i is the dimensionless van 't Hoff factor (equal to one for fully solubilised species), M is the molarity of the solution, R is the gas constant, and T is the (absolute) temperature [259]. Osmotic pressure is a colligative property, which is to say it depends on the concentration of the solute or solutes, but not on their identity.

Thermodynamically, it can be explained as a consequence of a difference in chemical potential of the solvent in the two regions separated by the semipermeable membrane. The chemical potential of the solvent (usually water) is decreased on the side with a higher solute concentration, due to an increase in entropy. The result of this is that solvent molecules flow down the chemical potential gradient, causing an increase in pressure in the region with higher solute concentration, which in turn raises the chemical potential of that region until equilibrium is reached.

4.1.2 Osmotic pressure and bilayer curvature in biology

Osmotic pressure is the result and trigger of a large number of cellular activities in all types of organisms, both prokaryotic and eukaryotic. If osmotic pressure goes unregulated, changes in ambient concentration may cause the lysis of cells. This

risk is particularly great for bacteria, which may be exposed to significant and sudden changes of their environment. As a consequence, many bacteria have evolved emergency pressure release valves to relieve osmotic pressure and prevent the rupture of their membranes. As an example, E. coli bacteria lose potassium under modest osmotic shock [260] and even small metabolite molecules at major osmotic shock [261, 262] in order to avoid lysis. They do this by means of mechanosensitive channels in their membranes [263]. The best-studied of these channels is probably the "large-conductance mechanosensitive channel" MscL [264], but there are several apparently functionally redundant channels in E. coli that serve as stretch-activated channels [263].

Renal cells in animals are examples of eukaryotic cells that are exposed to a wide range of osmotic conditions. They, along with several other types of cells (including red blood cells [265]), express water-specific channels called aquaporins which serve the purpose of facilitating the transport of water molecules down the osmotic pressure gradient [266–268].

In the experiments detailed in this chapter, water molecules cross the bilayer when the osmolarity of the outside solution is changed, leading to a change in volume inside the well and a concomitant swelling, or budding, of the bilayer. The resulting bud is an area where the bilayer is in a highly curved state. Bilayer curvature is an integral part of many cellular processes, including division, movement, vesicle trafficking, and formation of dendrites, axons, and microvillar extensions to name but a few. In vivo, cellular membranes are supported by a network of structural proteins that influence curvature. The cytoskeleton interacts intimately with the membrane and forms the substructure that gives it its broad shape [269, 270], which is then further modified on a smaller scale by peripheral membrane proteins such as clathrins [271], dynamins [272], and caveolins [273]. The study of such proteins

and the cellular processes they facilitate may benefit greatly from the availability of suspended bilayers with finely tunable curvature [274].

The work presented here is a step towards a new approach to providing new methods for the study of a wide range of systems. For example they may lead to new ways to study mechanosensitive ion channels such as MscL, as well as other proteins sensitive to osmotic pressure such as the aquaporins. Indeed, there is evidence to suggest that most, if not all, membrane channels respond in non-trivial ways to membrane tension [232, 275–277], suggesting the importance of a platform to study these effects. It may also provide a convenient way of forming small unilamellar vesicles containing specific substances or combinations thereof. The "budding off" process that occurs when the bud separates from the suspended bilayer over the well, incorporating some of its contents, is akin to endocytosis in cells. This has implications for liposome-based drug delivery techniques [278–280].

4.1.3 Osmotic pressure as a tool to manipulate membranes

There are many ways to probe the properties of membranes and their constituent proteins. Broadly, these can be categorised as either local techniques such as atomic force microscopy, scanning ion conductance microscopy, etc. and global ones including electrophysiology techniques such as capacitance measurements [281–283] and micropipette aspiration [284–286] (including vesicle aspiration and patch clamp). Mechanical assays such as measurements of the curvature of patches or swelling of vesicles in response to pressure (osmotic or otherwise) also fall into this category [287, 288].

When studying heterogeneous membranes, it is important to be able to probe locally, but when looking at single-phase bilayers for example, there are several reasons why a global technique may be preferable. For instance it is likely that a small probe such as an AFM tip causes significant local distortion in the alignment of lipid molecules, making the interpretation of such data difficult (see chapter 3). It may

also lead to damage to the membrane during measurement. Global techniques are less likely to cause such undesirable effects. They are also less susceptible to the stochastic variations that are intrinsic to AFM measurements, since the average behaviour of a large surface area is being measured.

The easiest way to control the osmotic pressure in these experiments is to vary the solute concentration of the bulk solution with respect to that of the solution confined in the well. At the concentrations used in most of the experiments detailed in this chapter, a theoretical maximum osmotic pressure of over 500 kPa would have been necessary to quell the net flow of water molecules into the well. In practice, as the concentration outside the well is reduced, water migrates across the membrane, increasing the enclosed volume and reducing internal concentration (and vice versa when outside concentration is increased). A small pressure gradient remains, accounting for the elastic deformation of the membrane. On longer timescales (of the order of an hour or so) this pressure gradient relaxes back to true equilibrium—as does the membrane itself—due to the slow migration of solute particles from inside the well to the bulk solution through the space between the bilayer and the substrate (Koji Sumitomo, personal communication, January 2014).

4.2 Experimental

4.2.1 Materials and Instrumentation

All lipids were procured from Avanti (Avanti Polar Lipids, Inc., USA). AFM images and force curves were captured on a Dimension 3100 AFM (Bruker Corporation, USA). Confocal microscopy was carried out using a BX61 microscopy (Olympus, Japan) at 40X magnification in air (NA = 0.65) in conjunction with a Fluoview 1200 laser excitation system at 473 and 559 nm (Olympus, Japan).

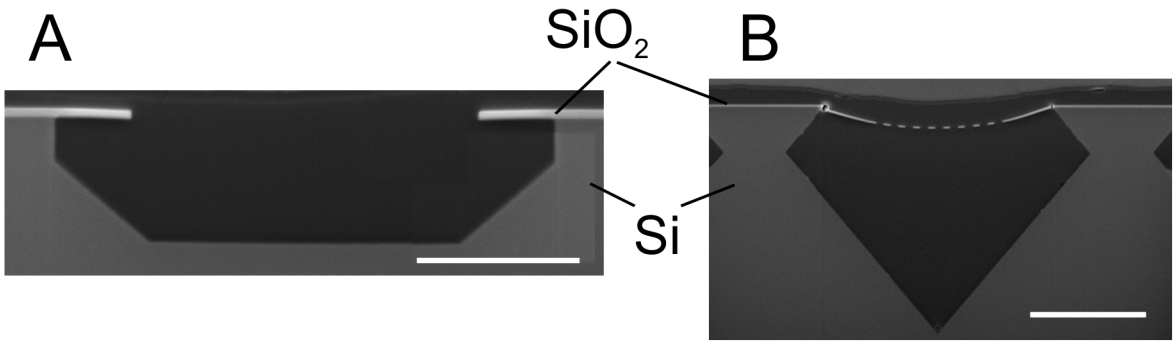

Figure 4.1: SEM images of microwell substrate cross sections. A: 4 μm overhang well. B: Peppershaker substrate. Scale bars: 2 μm. Adapted from reference [178].

4.2.2 The substrates

A significant advantage that comes with using osmotic pressure to probe bilayer mechanics is that it allows parallel measurements on a massive scale, even on relatively simple substrates. It would be an exceedingly complex task to design a substrate that allows equal hydrostatic pressure to be exerted on a large number of compartments spanned by suspended bilayers. The density of the compartments in such a substrate would be necessarily quite low, due to the need for a network of vias and channels. Osmotic pressure makes this task relatively simple: all that is needed is an array of compartments that can be filled with solution and sealed with bilayer. If some compartments end up without a seal, it does not pose a problem, since the compartments are entirely independent of one another.

The substrates used here were of two types: overhang-well substrates and so-called peppershaker substrates. The former consist of arrays of circular holes 1 - 8 μm in diameter in an approximately 100 nm thick silicon dioxide layer over a cavity etched into the silicon beneath, forming an overhanging lip that prevents the bilayer from conforming to the well sides (section 5.4 A). The latter are similar except for the fact that instead of a single circular hole, each cavity is spanned by a silicon dioxide layer with many smaller holes on the order or 100 nm diameter (section 5.4 B).

The fabrication process of overhang substrates is relatively straightforward, in that

it can be achieved using optical lithography techniques. The peppershaker substrates, with their size features, require electron beam lithography. Both types of substrates are etched in a similar fashion after microfabrication. Potassium hydroxide is used to selectively etch the silicon along the <100> plane, leaving the silicon dioxide layer above untouched. The result is a cavity with a trapezoidal cross section underneath the silicon dioxide film. Due to the hydrophobic nature of silicon, it is necessary to oxidise the inner surface of the cavity using piranha solution to enable wetting with aqueous solutions.

4.2.3 GUV formation

There are two main methods used to form giant unilamellar vesicles (GUVs), known as gentle hydration [289] and electroformation [290], respectively. For a recent comprehensive review on these and other methods for GUV formation, see Walde et al [291]. In electroformation, used in this work, lipids in chloroform are transferred to indium tin oxide (ITO) coated glass slides, which serve as the electrodes in the process. Alternately, platinum wires coated in lipid may be used as electrodes. Residual chloroform that may remain after evaporation in air is drawn off by placing the electrodes in a vacuum desiccator for two hours. Subsequently, the lipid-coated electrodes are exposed to a 200 mM sucrose solution and subjected to an AC potential of 1 V at a frequency of 10 Hz for two hours. It is important that the formation chamber be held at a temperature greater than the main transition temperature of the lipid mixture used.

The formation of DSPC GUVs was found to require special care due to the high gel-liquid transition temperature (55° C) of this lipid. Since the lipid is in the rigid gel phase at room temperature, the GUVs were found to be non-spherical in shape unless maintained at more than 55° C. Furthermore, most of the vesicles exhibited a number of small, dark patches with apparently little to no fluorescent lipid (fig. 4.2A).

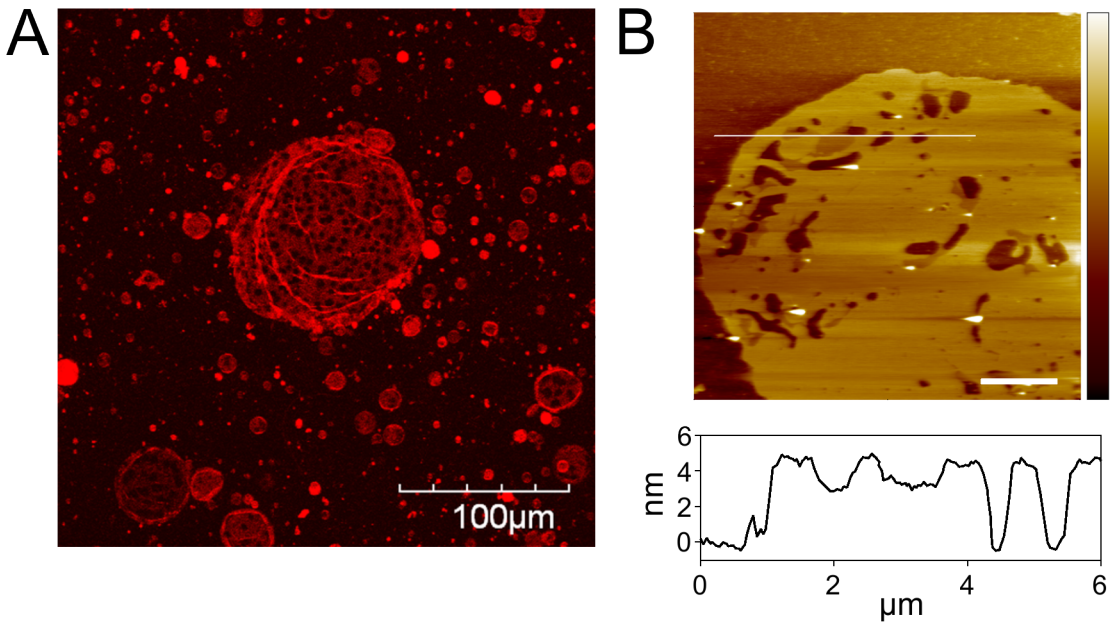

Figure 4.2: The results of DSPC GUV formation at 80° C without cholesterol. GUVs are labelled with 1 mol% rho-DOPE. A: Fluorescence image of DSPC GUV showing the non-spherical shape and the small dark domains characteristic of these GUVs. B: AFM height image of one such GUV ruptured on mica. Two domains are present, as elucidated by the cross section along the white scan line. AFM image colour scale is 15 nm, scale bar is 2 µm.

Investigation with AFM indicates that the GUVs are composed of two height domains: A large area-fraction high domain with small areas of low domain (fig. 4.2B). This suggests that the dark patches observed in the fluorescence images are in fact the low domain. Due to problems involving double layers after rupturing these DSPC GUVs, they were deemed unsuitable for confinement experiments. It was found that cholesterol at concentrations as low as 10 mol% was sufficient to homogenise the DSPC GUVs; consequently we studied DSPC/cholesterol mixtures with between 10 and 40 mol% cholesterol.

No evidence of any domain structure was found in DOPC GUVs. These were homogeneous at all cholesterol concentrations tested (0 – 40 mol%) and on the whole ruptured without forming double layers.

4.2.4 Flow chamber

To allow the osmotic pressure to be varied in a reproducible way, it was deemed necessary to design a flow chamber to conduct the experiments. The chamber had to be well-sealed to avoid changes in osmolarity due to evaporation. A well-sealed chamber also allowed the use of only one syringe, as the liquid would be forced out of the second tube by pressure alone. To make a re-usable, sealable chamber, it was found that silicone sheet (RS components, UK) was the best choice, as it adheres to clean glass surfaces without the use of adhesive and can easily be cleaned and reused. A thickness of three millimetres brings the flow chamber surface close to the focal length of the objective lenses used. To ensure a good seal with the glass slide and coverslip, it is essential that the PTFE tubing does not cause any bulging. That is to say, the hole through the spacer must needs be larger in diameter than the tubing. Sugru® (Formformform, London) proved to be an ideal material for this purpose. The assembled flow chamber with a substrate inserted is shown in fig. 4.3. It is reusable

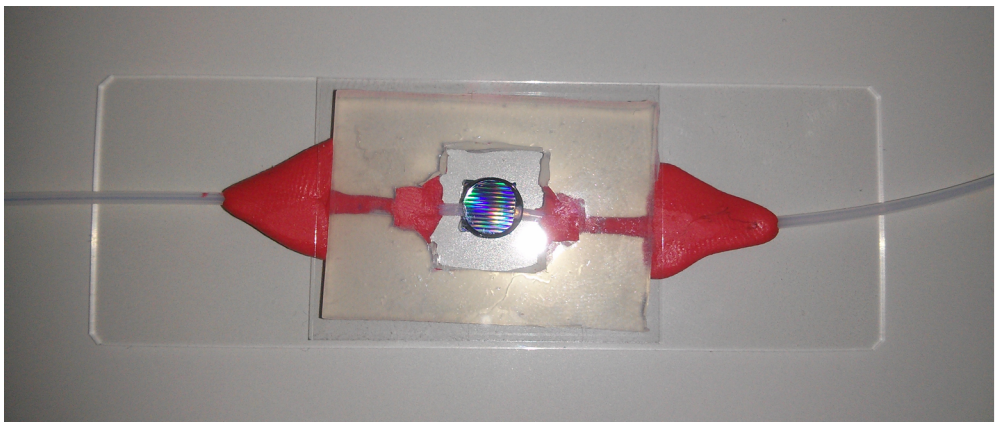

Figure 4.3: The home built flow chamber used to vary osmotic pressure in the experiments. A 3 mm thick silicone spacer separates the microscope slide from the cover glass and creates a chamber in which the substrate sits. PTFE tubing allows the buffer to be exchanged in a controlled manner using a syringe pump (not shown). The tubing is held in place by Sugru®.

provides a seal against evaporation, and allows reproducible rate of dilution of the outside solution and concomitant change in osmotic pressure.

4.2.5 Sample preparation

GUVs rupture spontaneously when in contact with a surface in the presence of divalent ions. 5 mM $CaCl_2$ is sufficient to rupture the GUVs used in these experiments. The maximum osmotic pressure that can be applied outwards is limited by the initially confined solute concentration, so the rupturing solution also contained 200 mM glucose. This has the further benefit of causing the sucrose-containing GUVs to sink to the surface of the substrate more quickly. The fluorescent dye calcein was included at a concentration of 0.1 to 0.5 mM, to allow easy determination of successful confinement.

This rupturing solution was placed on the substrate, followed by a small amount of GUV-containing sucrose solution (at 200 mM). After a brief incubation at room temperature to allow complete rupture to take place, the bulk solution was exchanged in a stepwise manner and replaced with a solution containing no calcein but with the same concentrations of $CaCl_2$ and glucose as the rupturing solution. This ensured

that the sample was kept at osmotic equilibrium during preparation, while removing the fluorescent dye not confined within the wells. After exchanging the bulk solution, the sample was placed in the flow chamber and imaged while osmotic pressure was varied.

4.3 Results

4.3.1 Single phase lipids

Single phase GUVs were used initially. Most of the work was done using DOPC, DSPC, and cholesterol, as this system gives access to the liquid disordered (L_α), liquid ordered (L_o), and gel (L_β) phases. The use of pure DSPC and DOPC was precluded by the inhomogeneity of the GUVs in the case of DSPC and by the instability of the suspended bilayers in the case of DOPC. Mixtures of each type of lipid with cholesterol were used instead.

4.3.1.1 DSPC GUVs

Suspended lipid bilayers composed of DSPC with varying molar fractions of cholesterol were formed and their behaviour when subjected to osmotic pressure was studied. Below approximately 20 mol% cholesterol, no budding is observed (fig. 4.4 A). At these low concentrations of cholesterol, the bilayer is in the gel (L_β) phase [251, 292]. Only very few of the suspended bilayers rupture upon being subjected to osmotic pressure. This indicates that the volume contained in the wells does not change much, which may be the result of the comparatively low permeability of L_β bilayers to water [293–296]. This idea is explored in more detail in section 4.5.

Budding does occur at 40 mol% cholesterol (fig. 4.4 B), i.e. when the bilayer is in the liquid ordered (L_o) phase. The buds on any given sample were of near-uniform

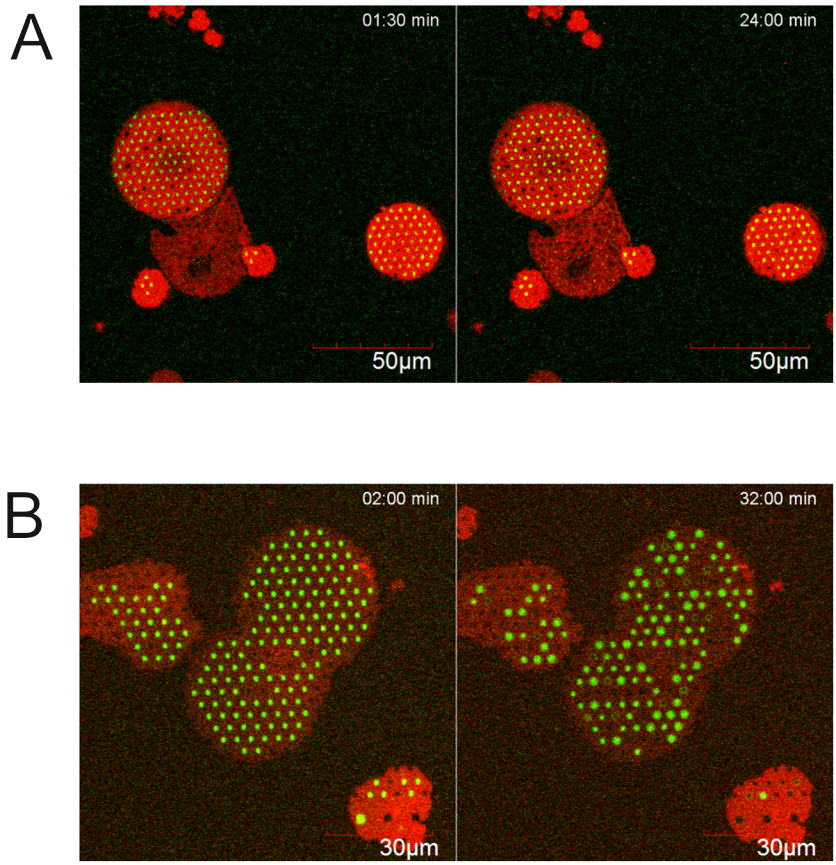

Figure 4.4: Combined rhodamine (red) and calcein (green) fluorescence images before and after dilution of the bulk solution above the suspended bilayers with 20 µl of water per minute. A: DSPC GUVs with 10 mol% cholesterol and 1 mol% rho-DOPE, in the gel phase according to the literature [251, 292]. No budding was observed over the course of the observation. Only a few of the suspended bilayers rupture. B: DSPC GUVs with 40 mol% cholesterol and 1 mol% rho-DOPE, in the L_o phase according to the literature. Budding occurs in suspended bilayers above all the wells. Rupture rate is slightly higher compared to gel phase suspended bilayers.

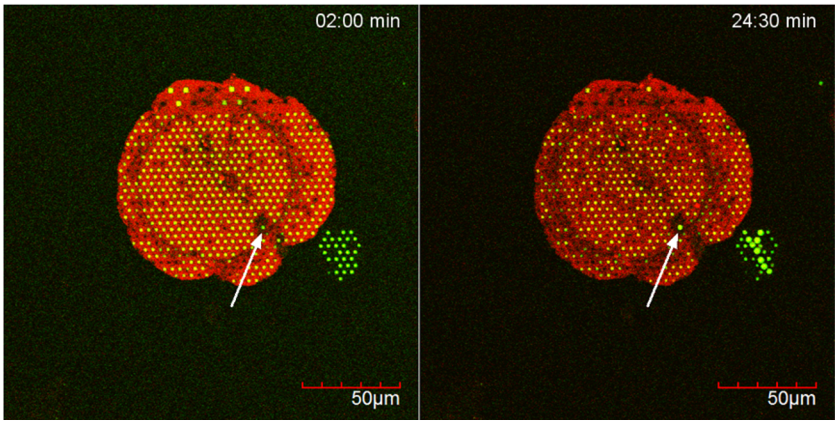

Figure 4.5: Combined rhodamine and calcein fluorescence images of a 20 mol% cholesterol containing DSPC bilayer before and after dilution of the bulk solution above the suspended bilayers with 20 µl of water per minute. There is no budding in the regions with high rhodamine fluorescence. The smaller patch to the bottom right and the well indicated by the white arrow show budding and are presumed to be in the L_o phase. Interestingly, rho-DOPE seems to preferentially localise into the gel phase.

size. Budding can be reversed by increasing solute concentration in the bulk sample volume.

At 20 mol% cholesterol the liquid ordered and gel phases coexist. As expected, budding occurs only in some parts of the membrane (the liquid ordered domains) and not in others (the gel phase domains). Interestingly, the fluorescent rho-DOPE used in these experiments seems to localise preferentially in the gel phase domain as opposed to the liquid ordered domain (fig. 4.5). This is supported by the AFM/confocal observations of pure DSPC bilayers (fig. 4.2).

4.3.1.2 DOPC GUVs

To compare the above findings for gel and liquid ordered phases to the liquid phase (L_α), mixtures of DOPC and cholesterol were investigated in the same ways. It was found that suspended bilayers of DOPC with 0, 5, and 20 mol% cholesterol were very unstable when subjected to osmotic pressure, which caused swift and virtually complete rupture.

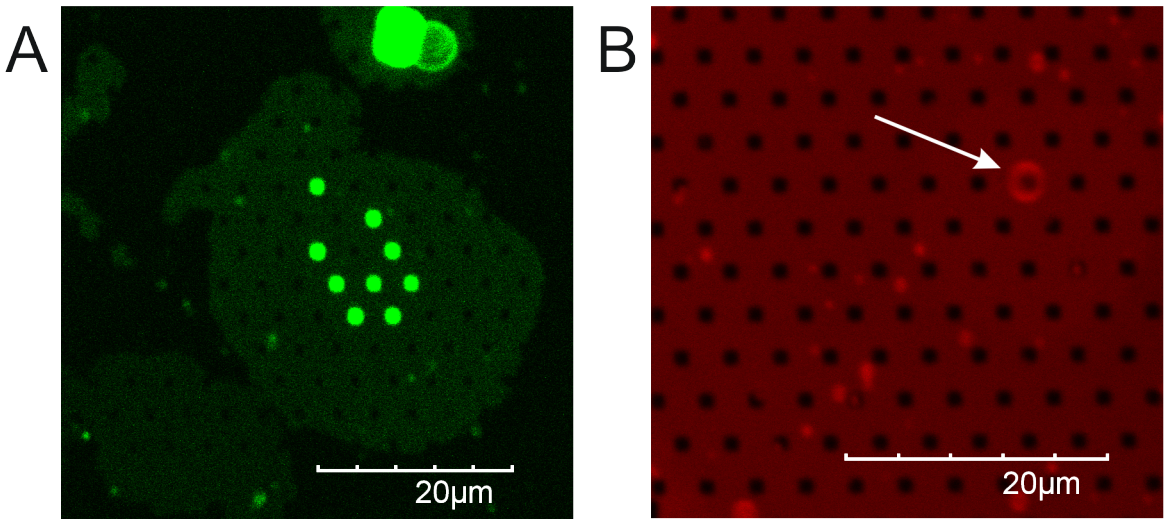

Figure 4.6: Fluorescence images of different phases on the same sample, captured after dilution of the bulk solution. A: DSPC with 40 mol% cholesterol and 1 mol% NBD-DSPE—no budding is apparent. B: DOPC with 40 mol% cholesterol and 1 mol% rho-DOPE—budding has occurred (white arrow). Calcein was confined within the wells to confirm the presence of suspended bilayers and is visible in the green channel (A).

At 40 mol% cholesterol, bilayers were found to be resilient enough to observe budding, although a large number of the suspended bilayers still ruptured during the experiments. The buds that formed in the liquid phase bilayers were significantly larger than the ones seen in the liquid ordered phase. Some were so large that they merged with the ones of neighbouring wells. Barring such merging, the buds were of near-uniform size.

4.3.2 Comparing phases

Initial attempts using multi-phase GUVs failed to yield satisfactory confinement. This may be due to the lack of control of the exact composition of each phase in such vesicles, caused by the migration of species (and in particular of cholesterol) from one phase to the other. If, for instance, the resulting composition of the L_α (DOPC-rich) phase had less than 20 mol% cholesterol, this phase would not result in stable confinement under osmotic pressure, as mentioned in section 4.3.1.2.

Mixing two types of single phase GUVs during sample preparation was found to yield better results. This way, the phases are of known composition, at least until they come into contact on the sample surface. In experiments with both L_o GUVs and L_α GUVs, budding was only observed in the L_α domain (fig. 4.6). This supports the conclusion that budding behaviour is strongly dependent on lipid phase. Since no budding was observed in the liquid ordered domain, it is not possible to quantitatively compare the behaviour of the two phases at this time.

A further finding from such experiments was that rupture occurs at different times in different phases. The graph in fig. 4.7 A shows the normalised number of intact suspended L_α and L_o bilayers as a function of time. By scaling the time values using the relative permeabilities of the two membranes (computed using the theory developed by Nagle et al [296]), the data can be displayed as a function of the increase in the volume of the enclosed well/bud (fig. 4.7 B). It appears as though rupture is caused by an approximately equal increase in volume in both L_α and L_o suspended bilayers.

4.3.3 Biotin avidin modification

Budding is a result of the interplay between the energy required to deform a unit area of bilayer to a given radius of curvature and the binding energy per unit area of the bilayer to the substrate surface. Initially, the membrane is fully bound to the surface of the substrate, and the suspended bilayer is assumed to have zero curvature. As the external concentration is reduced, osmotic pressure will induce some curvature in the suspended bilayer over the well. At a certain point, depending on the stretch modulus and the adhesion, the energy required to induce more curvature in the suspended membrane will equal the energy keeping the membrane at the edge of the well bound to the substrate surface. As more pressure is applied, the dome-shaped bud recedes further and further from the edge of the well as it expands, thus maintaining the

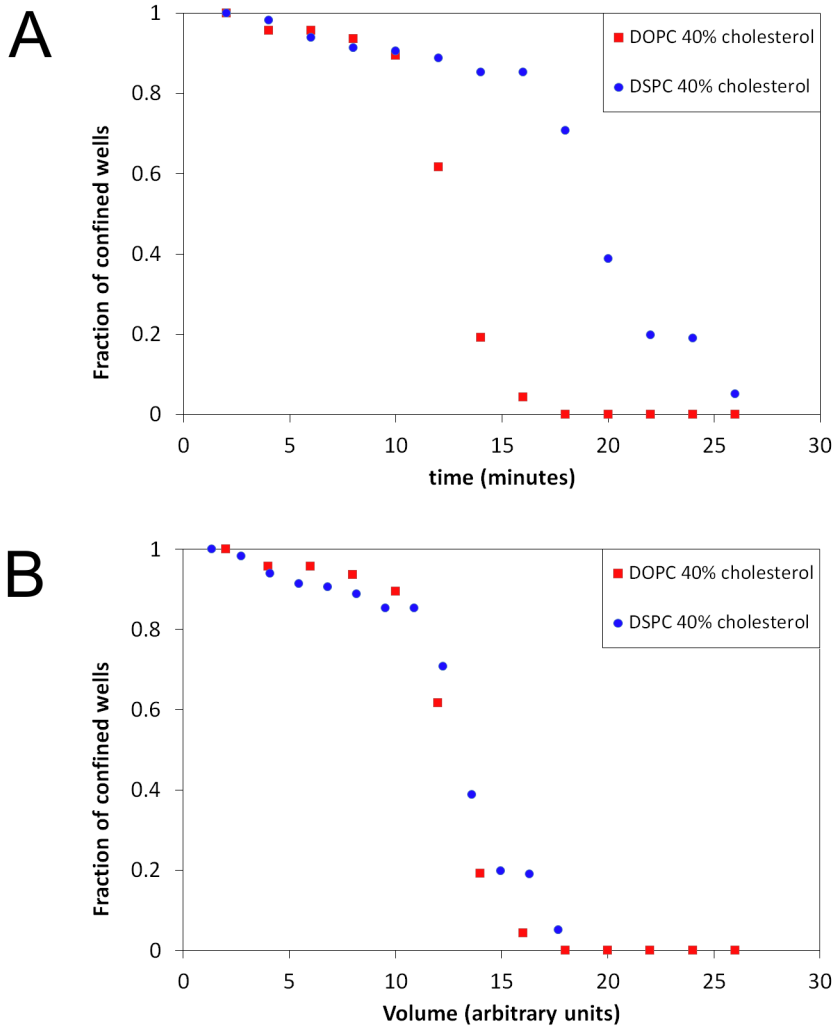

Figure 4.7: Graph showing the fraction of intact suspended bilayers as dilution of the bulk solution with 20 µl of water per minute progresses. A: Fraction of intact bilayers as a function of time. The DOPC membranes rupture first, followed by the DSPC membranes. B: Fraction of intact bilayers as a function of volume. When scaled by their relative permeabilities to water, it becomes clear that rupture occurs at a specific increase in volume, as opposed to a specific osmotic pressure.

equilibrium between the energy stored in the distortion of the membrane and the energy required to unbind the membrane from the surface of the substrate. The behaviour of the different lipid phases can be explained in terms of this energy balance. L_α and L_o bilayers appear to conform to the account given above, albeit with differing points of equilibrium.

To explore the effect of adhesion on bud formation, it was necessary to influence the equilibrium point between binding energy and stretching energy. In particular, it would be interesting to see if budding could be induced in gel phase bilayers if the binding energy between substrate and bilayer could be sufficiently increased. To this end, L_β, L_o, and L_α GUVs containing 1 mol% biotin-DPPE were made. FITC-labelled avidin was found to bind non-specifically to the sample surface. This modification to the experiments was successful in increasing the binding energy of the bilayer to the substrate, as evidenced by budding experiments using L_α DOPC GUVs (fig. 4.8). Instead of forming a dome-shaped bud where the bilayer is lifted off the surface of the sample (fig. 4.8 A), here it takes the shape of a balloon opening out from the well (fig. 4.8 B). The reasons for the differences in the intensity profiles can be deduced from schematic images E and F of the figure: when the bud is dome shaped, fluorescence from only a single bilayer is recorded. Since the bilayer is separated from the SiO_2 substrate (which boosts excitation intensity at this wavelength), the fluorescence intensity in the area of the bud is reduced compared to the rest of the image (fig. 4.8 C). For a balloon shaped bud, on the other hand, fluorescence from three bilayers is recorded, the lowest one of which is bound to the substrate. As a result, fluorescence intensity in the area of the bud is increased compared to the rest of the image (fig. 4.8 D).

DSPC bilayers in the L_o phase with biotin-avidin binding also exhibited budding, but the resolution of the microscope was not good enough to draw firm conclusions

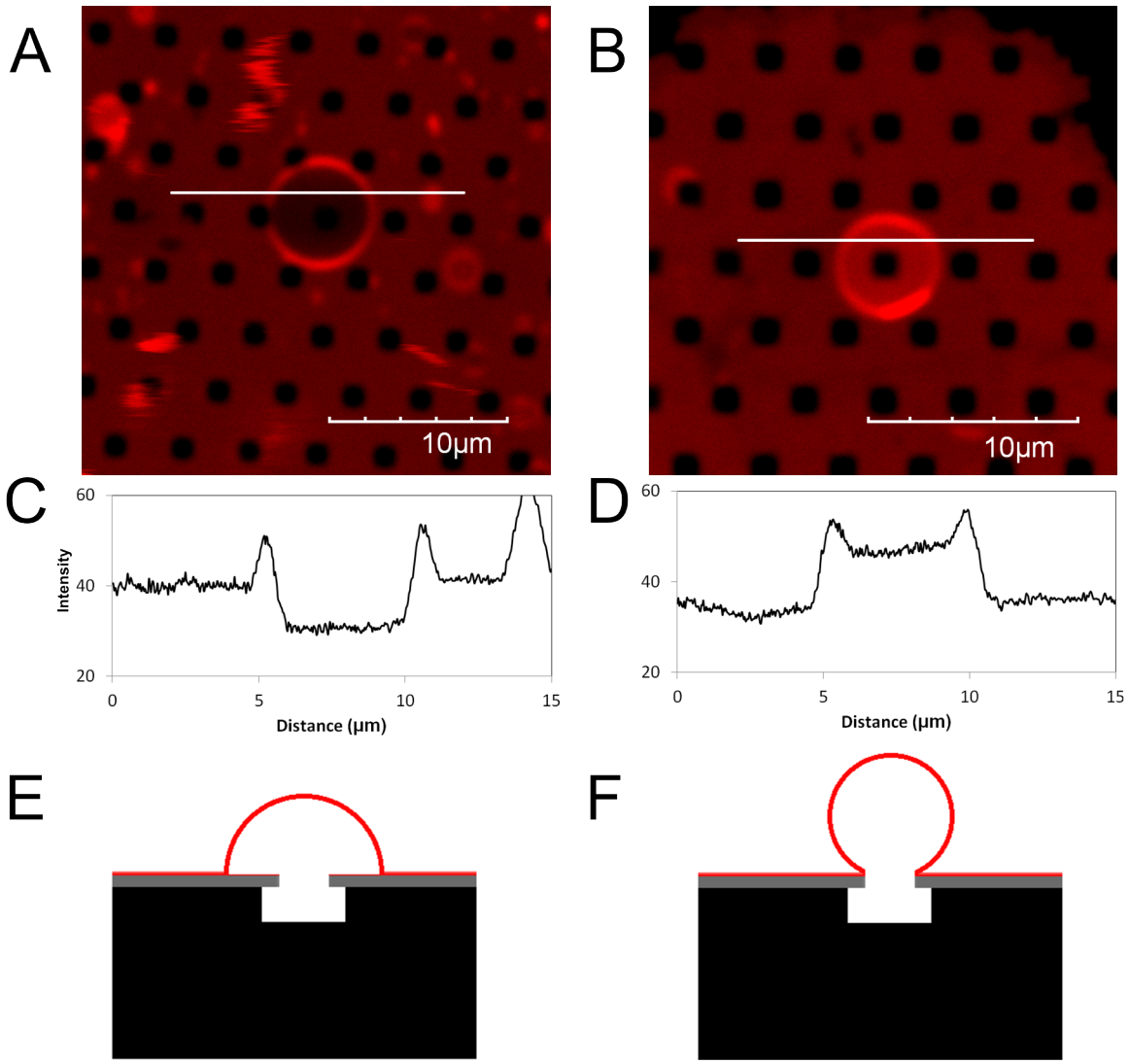

Figure 4.8: Fluorescence images of 40 mol% cholesterol DOPC suspended bilayers containing 1 mol% rho-DOPE. A: No modification made to surface or lipid composition. B: Surface modified with FITC-avidin and bilayer contains 1 mol% biotin-DPPE. C: Fluorescence intensity (arbitrary units) in the region of the bud is reduced in A due to the separation of the bilayer from the SiO_2. D: With biotin/avidin binding fluorescence intensity in the bud region is increased due to the presence of three layers. The schematic images E and F show a side-on view of the bilayer configurations above the wells.

about the nature of these buds, i.e. whether they were dome-shaped or balloon-shaped.

Gel phase suspended bilayers with biotin avidin-binding did not exhibit budding, indicating that it is not the interplay between the stretch modulus and adhesion energy that limits bud formation—an idea that seems to be borne out by the mathematical modelling discussed in section 4.4. This observation lends further support to the hypothesis that it is in fact the permeability of the membrane (which would likely remain low in the presence of biotin-avidin linkage) that prevents budding.

Control experiments with biotin containing GUVs on substrates without avidin showed that the stability of the suspended bilayers is somewhat reduced by the presence of biotin-DPPE. The same applies to GUVs without biotin on avidin coated substrates, where the reduction in stability was even more pronounced. The biotin-containing bilayers seemed more susceptible to formation of aggregates, which may explain their increased rupture rate. Substrates coated with avidin display a significantly more hydrophilic surface, which may be related to the decrease in stability. It may also be a more complicated mechanism relating to specific lipid-avidin interactions. More detailed study is required to answer these questions and deduce the implications for the biotin-avidin binding of lipid bilayers to the substrate surface.

4.3.4 Peppershaker substrates

Budding experiments are largely limited by the tendency of suspended bilayers to rupture as they are subjected to osmotic pressure. In experiments using the more conventional overhang-well substrates, it was found that the size of the well is a critical factor in membrane stability: The smaller the diameter of the opening, the more stable the suspended bilayer seems to be. So-called peppershaker substrates combine the advantage of a relatively large internal volume (necessary to confine a sufficient volume of solution in it for osmotic pressure experiments) with the increased

stability that comes from having only small areas of suspended bilayer. A further advantage of these substrates is that it is possible to observe both outward and inward budding, induced by decreasing and increasing external concentration compared to the concentration inside the well, respectively. The disadvantages of these substrates is the comparatively complex techniques required to fabricate them, as well as the lower density of cavities on the substrate surface. The latter offsets the advantage of increased stability, since it is likely that the absolute number of confined wells will be lower than on the simpler overhang substrates.

4.3.4.1 AFM of substrates

Observation of the peppershaker substrates with AFM in liquid reveals that the SiO_2 film over the cavity is not completely flat. Residual stress in the layer after deposition results in either a convex "dome" shape, or convex depression where the silicon substrate has been etched away. Where the film forms a dome protruding from the sample surface, it is possible by pushing hard enough with the AFM probe, to "flip" it into the concave conformation (fig. 4.9). This process is presumably reversible in principle, but it is not possible to pull on the sample surface with a large enough force using AFM to achieve this.

AFM imaging of the substrates with GUVs ruptured on them confirms the presence of suspended bilayer spanning each pore in the SiO_2 film, and is testament to the robustness of the system. The images themselves are a good indication that bilayer is present, since it would require a very unlikely tip shape to produce such flat-bottomed traces in the absence of a pore-spanning membrane (fig. 4.10 A profiles). To rule out the possibility of such an artifact, force curves were recorded on the suspended parts of the bilayer. Fig. 4.10 C shows examples of force curves with the distinctive breakthrough kink caused by the sudden relaxation of the tip as it ruptures the bilayer. A repeat image scan of the same area shows that the bilayer was indeed ruptured during

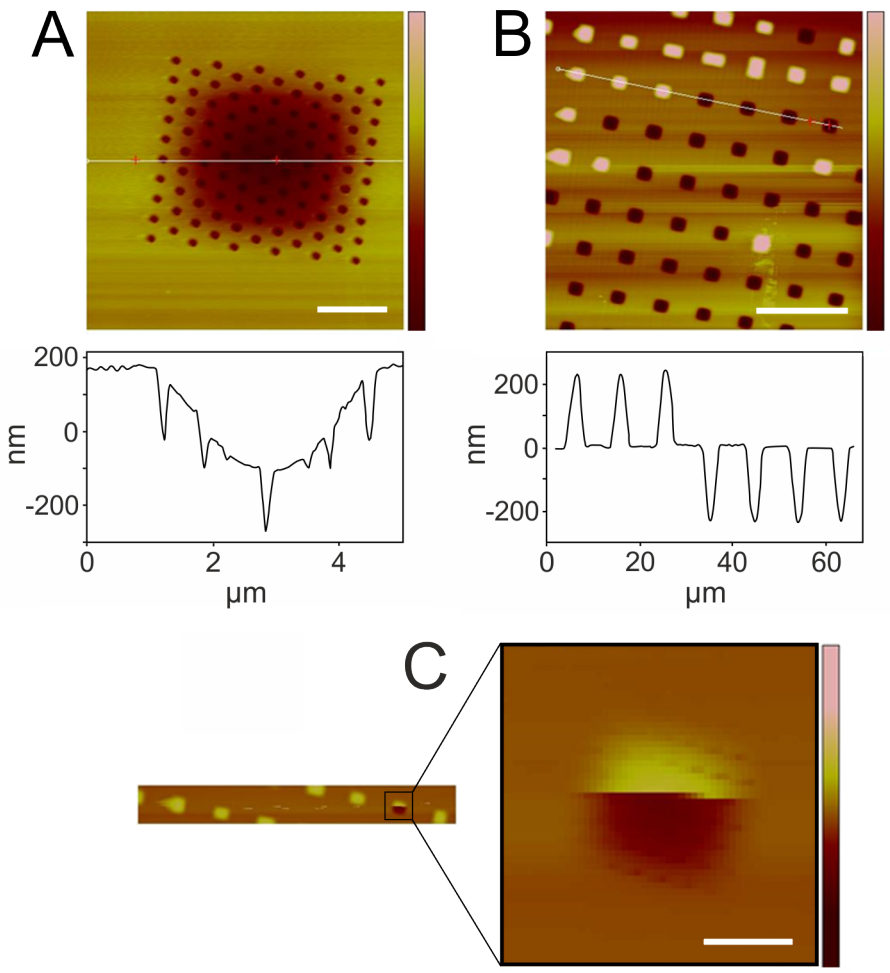

Figure 4.9: AFM height images and cross sections of peppershaker substrates. A: A single peppershaker well, consisting of a cavity spanned by a SiO_2 film with many small pores in it. The film is warped where the underlying silicon has been etched away due to residual stresses after deposition. Colour scale represents 500 nm, scale bar is 1 μm. B: An array of multiple cavities. Residual stresses in the film cause it to become either concave or convex upon etching of the underlying silicon. Colour scale represents 260 nm, scale bar is 20 μm. C: It is possible to "flip" the warped film from outward-facing to inward-facing using the AFM stylus to apply pressure. The scan direction in this example was top to bottom (slow scan direction) and right to left (fast scan direction). Colour scale represents 1.5 μm, scale bar is 2 μm (scale of the left image segment is the same as B).

the force curve measurements and traces spanning this pore now exhibit the expected shape of a pyramidal AFM tip tracking a surface with an essentially infinitely deep hole in it (fig. 4.10 B).

The fact that the AFM images show the suspended bilayer to be recessed inside the pores to a depth of more than 100 nm may be due to the fact that the AFM tip itself is pushing the bilayer into the pores, or it may be that the bilayer naturally conforms to the shape of the pore. Due to the small size of the pores and the limitations of the fabrication process, the lip around the pore entrance is inevitably somewhat rounded. Assuming a reduction in the free energy of lipids that are bound to the SiO_2 surface [297], it is plausible that the bilayer will tend to conform to the inner walls of the pores when at osmotic equilibrium.

4.3.4.2 DPhPC budding

DPhPC bilayers are of interest due to the relative ease with which membrane receptors may be reconstituted into them [6]. They also form membranes that have high electrical resistance, are mechanically durable, and are chemically stable [298], and as such are well suited to electrophysiological measurements. Due to their wide range of applications, understanding the behaviour of this type of lipid molecule is of particular interest.

Experiments with DPhPC were conducted by changing external concentration manually, i.e. by adding water or concentrated solution to the sample. DPhPC suspended bilayers were found to be reasonably robust to these sudden jumps in osmotic pressure. In general, for the case of decreased outside concentration of solutes, budding seems to occur from a small area of each "peppershaker" cavity, usually at or near the edges of the array of pores (fig. 4.11). The decreased brightness of the buds themselves in the red channel indicate that in most cases the bilayer lifts off the

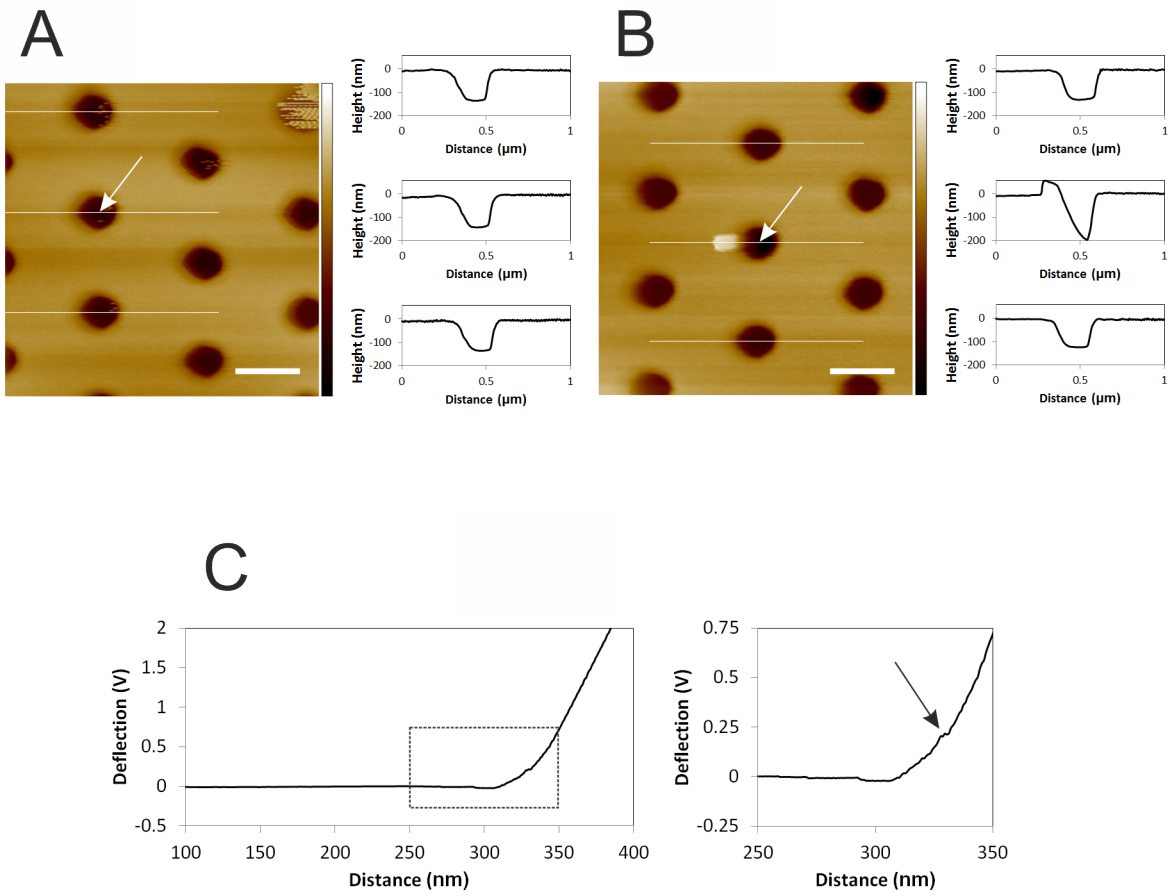

Figure 4.10: AFM height images and force curves of peppershaker substrates with suspended bilayers spanning the pores. Each dark spot in the images represents a pore in the array of pores of a single peppershaker substrate. DPhPC GUVs with 20 mol% cholesterol and 1 mol% rho-DOPE were used. A: Before force curve measurements. The tip traces a flattened section at the bottom of each pore. B: Same region after force curve measurement in the pore indicated by the white arrows. It seems the force curve measurement ruptured the suspended bilayer, depositing some lipid near the edge of the pore. The absence of the suspended bilayer allows the tip to penetrate more deeply into the pore and the profile now shows expected trace of a pyramidal tip tracking a deep hole with steep sides. Colour scales and scale bars both represent 300 nm. C: Force curve showing the characteristic kink caused by the tip breaking through the lipid membrane, captured on the suspended part of the bilayer. The breakthrough kink is indicated by the black arrow in the close up.

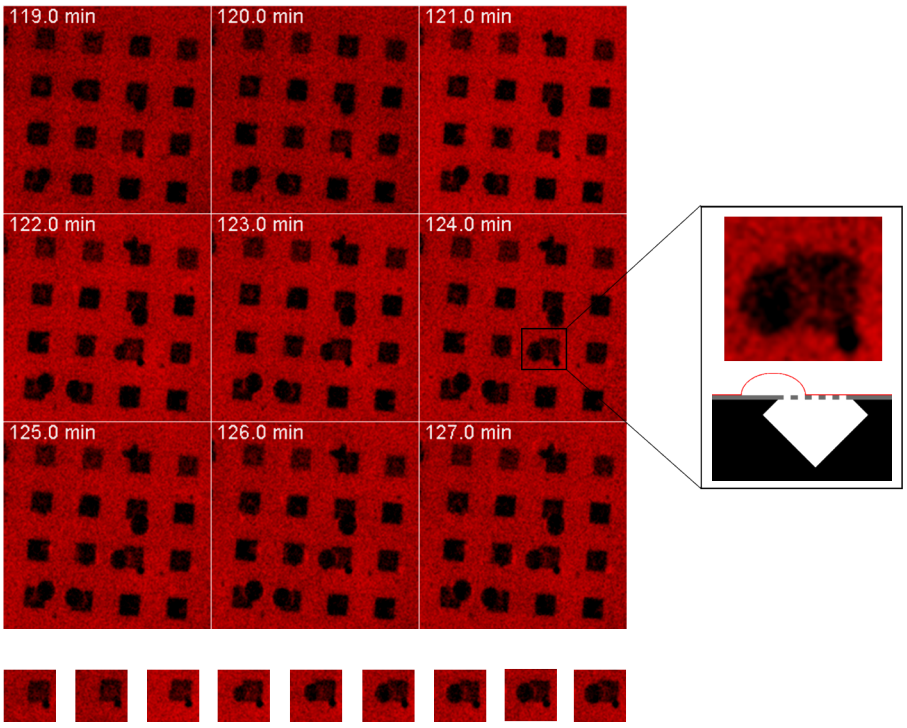

Figure 4.11: Rhodamine fluorescence images of DPhPC GUVs containing 20 mol% cholesterol and 1 mol% rho-DOPE ruptured on a peppershaker substrate in a solution containing 5 mM $CaCl_2$ and 200 mM glucose. Each square is a single cavity of the substrate. Series shows the effect of diluting the effect of changing the outside $CaCl_2$ concentration from 5 mM to 4 mM by manual addition of 200 mM glucose solution. Over the course of a few minutes, dome-shaped buds seem to form from the edges of the peppershaker cavities. A magnified peppershaker cavity with its bud is shown in the box on the right, along with a side-on schematic representation. Each image is 20 by 20 μm. Film strip below shows budding from a single peppershaker cavity at one minute intervals (each frame is 5 by 5 μm).

surface of the substrate, forming dome-shaped buds as opposed to balloon shaped ones (see schematics in fig. 4.8). In a few instances, balloon-shaped buds were observed.

Increasing the outside concentration results in the bilayer budding into the cavity as water molecules escape through the bilayer reducing the enclosed volume. This shows up as an area of reduced calcein fluorescence inside the well (fig. 4.12).

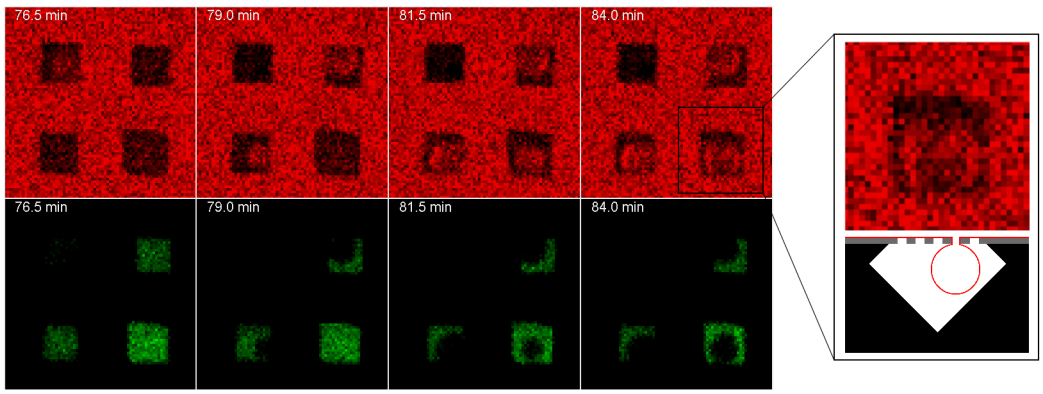

Figure 4.12: Rhodamine fluorescence (red) images of DPhPC GUVs containing 20 mol% cholesterol and 1 mol% rho-DOPE ruptured on a peppershaker substrate in a solution containing 5 mM $CaCl_2$, 200 mM glucose, and 0.1 mM calcein (green fluorescence). Series shows the effect of increasing outside concentration with respect to the confined concentration. The membrane forms a bud inside the cavity, as evidenced by the displacement of calcein in that region. A magnified peppershaker cavity with a side-on schematic of the proposed bilayer conformation inside the bud is shown in the box on the right.

4.3.4.3 Polyacrylamide gel filled cavities

In terms of comparisons to biological membranes, the suspended bilayers used in these experiments lack an important mechanical component: cytoskeletal support. To mimic the structural support of the cytoskeleton—as well as to investigate the potential positive effects on stability—the wells were filled with polyacrylamide gel (PAG). This gel acts as a support for the suspended bilayer when GUVs are ruptured on the substrate. The preliminary work done here indicates the viability of the concept of gel-supported membranes in the context of these types of experiments.

The preparation of gel-filled peppershaker substrates was accomplished by preparing the gel solution and adding it to the substrate while it was still liquid. Once the gel is partially set, it is possible to shear the gel droplet off the substrate by applying a gentle force to one side of it, leaving only the gel inside the cavities.

AFM imaging of gel-filled substrates confirms the presence of PAG in the wells. Changes in setpoint result in large variations of the depth to which the probe tip

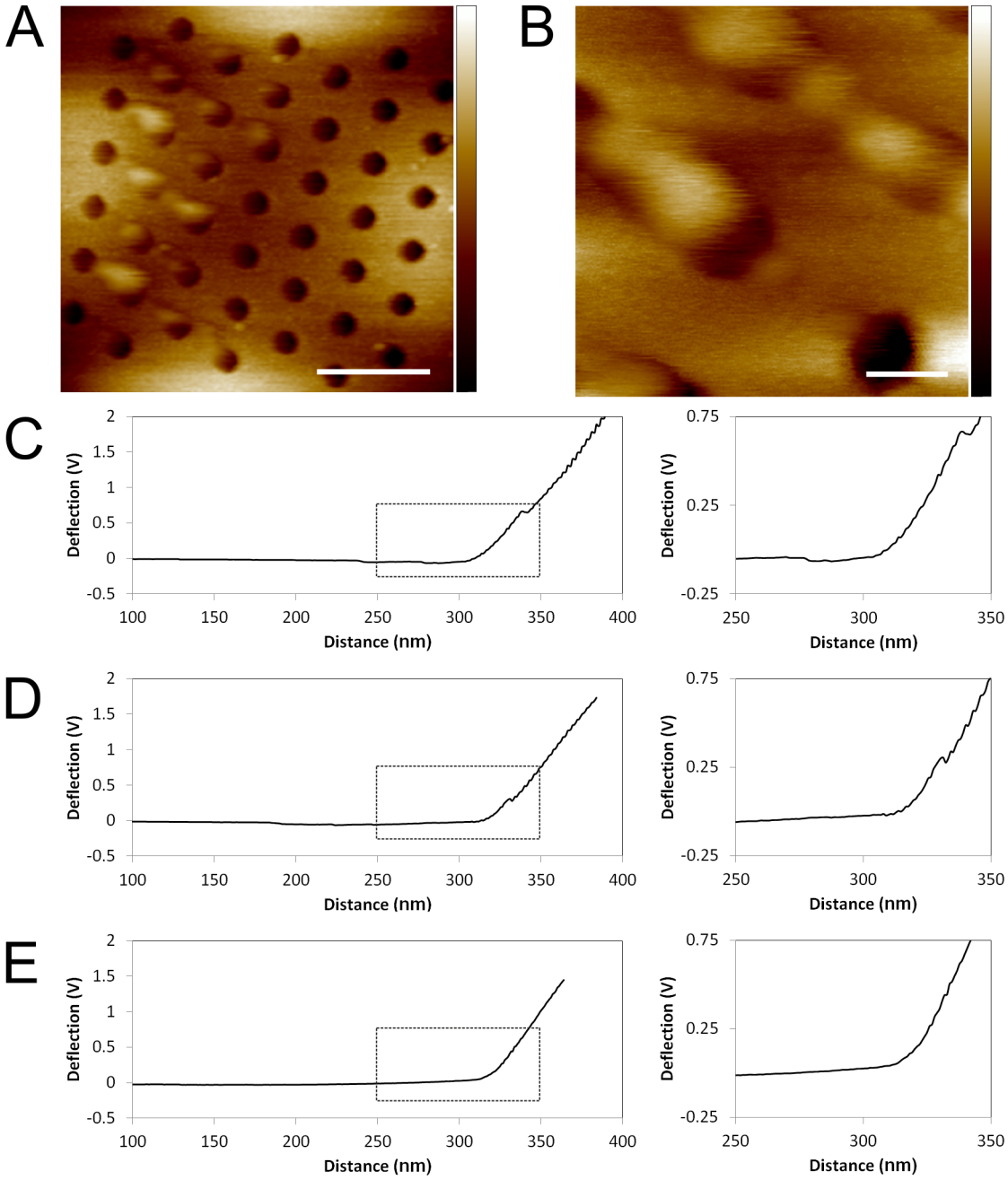

Figure 4.13: AFM height images and force curves on polyacrylamide gel filled peppershaker cavities with DPhPC (20 mol% cholesterol) bilayers. A: Image of a single peppershaker cavity, showing globules of polyacrylamide gel protruding from the pores where it was not cleanly severed. Colour scale represents 250 nm, scale bar is 1 μm. B: Close up of protruding gel globules. Bilayer, while present, is not visible in the topography images. Colour scale represents 200 nm, scale bar is 200 nm. C and D: Force curves captured in the pore regions of bilayer-covered, gel-filled peppershaker substrates. Characteristic lipid breakthrough events confirm the presence of bilayer. Right hand column contains scaled up versions of the regions in the dashed squares. E (control): Typical force curve of gel-filled peppershaker pore with no bilayer present.

penetrates into the pores, affirming the flexible, elastic nature of the gel. These images show that many of the pores retain improperly severed globules of gel (fig. 4.13 A and B). The ability of the gel to support a suspended membrane was confirmed by force curves, which again show the characteristic lipid breakthrough kink (fig. 4.13 C and D).

4.3.5 Lifetime measurements

To assess the stability of suspended bilayers of each phase, samples were observed in osmostatic conditions over a number of days at various points. The number of intact suspended bilayers was counted at each point in time and an exponential decay model was fitted to the data (fig. 4.14). The model was of the form $N(t) = N_0 e^{-\frac{t}{\tau}}$, where $N(t)$ is the number of intact suspended bilayers at t, the time of measurement, N_0 is the initial count, and τ is the characteristic lifetime. The resulting characteristic lifetimes give a measure of the resilience of the suspended bilayer. Due to their high density on the substrate, 1 μm diameter wells were the main focus of these measurements. Data from these indicate that gel phase DSPC bilayers, which proved most stable in conditions of increased osmotic pressure, have the lowest characteristic lifetime of the three phases examined. L_o DSPC bilayers have the longest lifetime, and L_α DOPC and DPhPC bilayers an intermediate one (see table 4.1).

Table 4.1: Characteristic lifetimes of suspended bilayers on 1 μm wells.

Composition	Phase	Characteristic lifetime (h)
DSPC with 10 mol% cholesterol	L_β	11
DSPC with 40 mol% cholesterol	L_o	111
DOPC with 40 mol% cholesterol	L_α	46
DPhPC with 20 mol% cholesterol	N/A	23

DPhPC suspended bilayers on peppershaker substrates exhibited a lifetime of over almost 150 hours—an increase of a factor of more than six from the 1 and

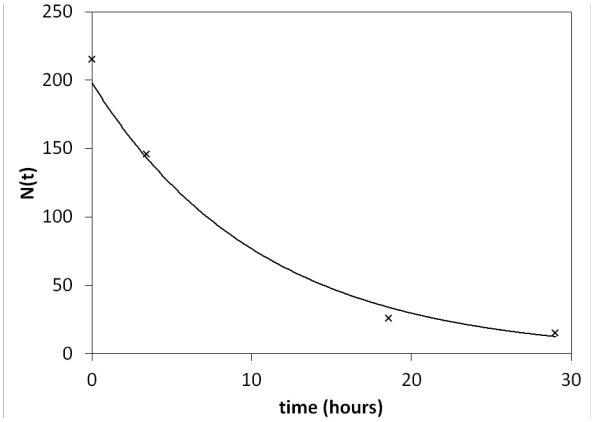

Figure 4.14: An example of the method used to determine the characteristic lifetime of suspended bilayers. Shown is the data for DSPC with 10 mol% cholesterol. The number of intact suspended bilayers is counted at several points in time and an exponential function is fitted to the data.

2 μm overhang wells. The effect of biotin/avidin binding on the lifetime of L_o DSPC bilayers was assessed in the same way. While biotin-containing bilayers seem to be less stable overall than their counterparts without biotin, the binding to avidin nevertheless seems to increase their lifetime compared to unbound biotin-containing bilayers (see table 4.2). Avidin coated substrates seem to significantly reduce the lifetime of bilayers containing no biotin, to the point that by the time of the second measurement after preparation there were no intact suspended bilayers in evidence. This may be related to the increased hydrophilicity of substrates coated with avidin.

Table 4.2: Effect of biotin-avidin binding on lifetime (1 μm wells).

DSPC with 40 mol% cholesterol	Substrate	Characteristic lifetime (h)
with 1 mol% biotin-DPPE	avidin-coated	59
with 1 mol% biotin-DPPE	uncoated	35
without biotin-DPPE	avidin-coated	<2

4.4 Membrane elasticity model of budding

In order to extract quantitative information about the mechanical properties of the membrane, it is necessary to formulate the state of the system mathematically first. The shape of a membrane bud at a given pressure is determined by several factors, each of which can be expressed in terms of a Gibbs free energy. The contributions considered here are from the stretching of the membrane, the adhesion of the membrane on the substrate, and the osmotic pressure term. The minimisation of the total free energy, given by

$$G_{tot} = G_{str} + G_{adh} + G_{osm}$$

determines the equilibrium state of the membrane at that pressure. A similar approach has been used for membranes in glass pipettes to characterise membrane tension [297, 299].

The resulting mathematical model, while not particularly complex, does not admit of an analytical solution. Instead, MatLab was used to find the shape of the free energy surface as a function of bud height and radius at varying ranges of initial conditions and parameters. The resulting surface allows the minimum free energy to be found, along with the equilibrium values of bud height and radius. These values were then interpreted by comparing them to experimental data and, where possible, conclusions were drawn about the mechanical properties of the membrane.

4.4.1 Premise and assumptions

In the calculations that follow, several simplifying assumptions are made about the system. First, it is assumed that the bud takes the shape of a spherical cap and that edge effects at the transition from the flat membrane to the bud itself may be ignored. This is justified by the observation that the contribution to the free energy of bending the membrane is orders of magnitude lower than other contributions. The

second assumption is that the bilayer contains no folds or ripples which may affect the adhesion to the substrate, and that there are no extraneous reservoirs of lipid that may cause changes in bud or patch area. Third, it is assumed that the substrate-bilayer adhesion is reversible and lowers the free energy of the system. The fourth assumption is that the effects of adjacent membrane buds are negligible. Fifth, it is assumed that there is a static friction present that limits the lateral movement of the membrane. Under this assumption, strain increases with tension until the tension reaches a critical point at which it overcomes said static friction, and strain does not increase further. Instead, the membrane starts to slide across the surface of the substrate, while remaining under the maximum (critical) tension. The validity of this assumption is explored in section 4.5.

4.4.2 Applying the model

For the sake of simplicity, we consider only a single well in a substrate, spanned by a bilayer patch of reference area A_0, above which a dome-shaped bud expands. A cross-sectional schematic of this scenario is shown in fig. 4.15. The spherical cap shape of the membrane bud can be described by the radius of the bud and its height. Simple geometric analysis shows that the radius of curvature of the bud, R_c, is given by

$$R_c = \frac{R_b^2 + h^2}{2h}$$

where R_b is the bud radius and h is its height.

The total volume enclosed by the budding suspended bilayer is given by the formula

$$V_{tot} = \frac{\pi h}{6}(3R_b^2 + h^2) + V_0$$

where V_0 is the volume of the well when enclosed by a flat suspended bilayer. A plot showing contours of equal enclosed volume is given in fig. 4.16, along with schematic

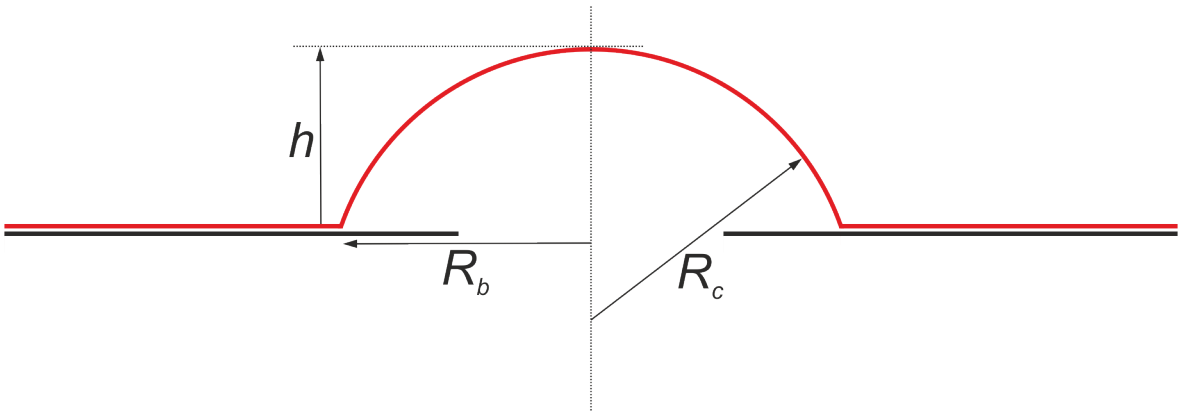

Figure 4.15: Schematic of model geometry. Cavity below well entrance not shown. R_b is the bud radius, h is the bud height, and R_c is the radius of curvature of the bud.

images of possible bud shapes. The bud shape in the model is primarily determined by the strength of the adhesion, while the volume is primarily determined by the pressure. At a constant pressure, membranes with low adhesion will tend to be in the blue region, while membranes with high adhesion will be on the same volume contour in the red region.

In addition to the variables of the model, h and R_b, there are a number of parameters that determine the behaviours of the system. These can be found in table 4.3, along with typical values. Where the parameters did not permit direct measurement, values were taken from the literature.

Table 4.3: Parameters of the model and typical values.

Parameter	Description	Typical value/range
h	Height of the bud	1 - 10 μm
R_b	Radius of the bud	1 - 10 μm
R_w	Radius of the well	0.5 - 4.0 μm
A_0	Unstretched area of the patch	300 - 50 000 μm^2
V_0	Volume of the well (before budding)	8 μm^3
γ	Strength of the adhesion	2 mN/m for SiO_2 [258, 297]
K_A	Area expansion modulus	200 - 3000 mN/m [5]

To understand the model, it is instructive to inspect each contribution to the free

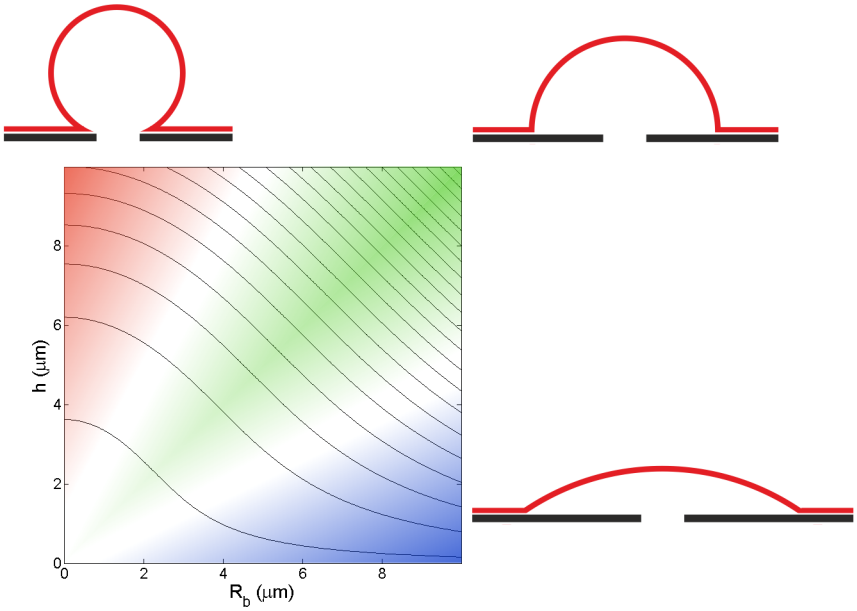

Figure 4.16: The graph shows contours of constant volume as a function of bud height and radius. The shaded regions and the corresponding schematic diagrams give an indication of bud shape (red shading: $R_b < h$; green shading: $R_b \approx h$; blue shading: $R_b > h$.)

energy individually. The contribution made by the stretching of a uniform membrane is of the form

$$G_{str} = \frac{1}{2} A_0 K_A \phi^2$$

where A_0 is the initial area of the bilayer patch, K_A is the stretching modulus or area expansion modulus of the membrane and ϕ is the areal strain. In the case of a spherical cap deviation from a flat membrane, the strain is given by $\phi = \frac{\pi h^2}{A_0}$. It is worth noting that ϕ depends only on h, not on R_b.

The term relating to bilayer adhesion is of the form $G_{adh} = -\gamma A_{adh}$, where A_{adh} is the area of the lipid that is adhered to the surface and γ is a constant denoting the strength of the adhesion per unit area. While the membrane is stretching (rather than slipping), the adhesion area only depends on R_b, yielding

$$G_{adh} = -\gamma(A_0 - \pi R_b^2)$$

but once the areal strain ϕ exceeds a critical value ϕ_{crit}, the adhesion area is no longer independent of h. This is because beyond this point the membrane stops stretching and starts slipping, reducing the area adhered to the substrate as h increases. This results in an adhesion term for $\phi > \phi_{crit}$ of

$$G_{adh} = -\gamma(A_0 - \pi(R_b^2 + h^2 - h_{crit}^2))$$

where h_{crit} is the bud height at which the tension overcomes static friction. A further nuance is that the adhered area is limited for small buds by the size of the well. This can simply be incorporated in the model by limiting the minimum radius of the freestanding region of lipid to be equal to R_w, the radius of the well.

The free energy contribution of the pressure-volume coupling is given by the integral $G_{osm} = -\int \Pi \, dV$, where Π is the osmotic pressure. Since osmotic pressure is proportional to molarity and molarity is inversely proportional to volume, the free energy term is of the form

$$G_{osm} = -nRTln(1 + \frac{\Delta V}{V_0})$$

where n is the number of moles contained within the well/bud, R is the universal gas constant, T the absolute temperature, V_0 the initial volume of the well, and ΔV the change in volume due to osmotic pressure. This form of the free energy assumes pure water on the outside of the well/bud.

$$\Delta V = \frac{\pi h}{6}(3R_b^2 + h^2)$$

for a spherical cap shaped bud.

For completeness, the term that accounts for the bending energy of the membrane

is given by

$$G_{bend} = 8\pi k_b \frac{h^2}{R_b^2 + h^2}$$

where k_b is the bending modulus of the membrane, given by the relation $k_b = K_A d$, where d is the thickness of the membrane. Lipid bilayers have extremely low bending moduli ($k_b \sim 10^{-19}$ J [5]), so the contribution from bending of the membrane is several orders of magnitude lower than the other contributions. Consequently it will be ignored in the following analysis.

How the three relevant components of the free energy (G_{adh}, G_{str}, and G_{osm}) impact the radius and height of the bud, as well as their combined impact, can be seen in fig. 4.17. For buds below a certain height the adhesion term depends quadratically on the radius of the bud and is independent of their height, since the change in patch area is accounted for by the strain in the membrane. Once the strain exceeds a certain value, determined by the interaction between the bilayer and the substrate (as well as the strain, which is affected by patch size), the system transitions to the "slipping" regime, where the increase in area is accounted for by the membrane slipping along the surface towards the location of the bud. This means that the adhesion area, and hence the free energy associated with it, becomes dependent on both radius and height of the bud. The free energy term associated with membrane stretching is independent of bud radius and depends on bud height in a quartic fashion until the critical height is reached. In the slipping regime the strain in the membrane is constant. The pressure term opposes the other two in that G_{osm} becomes more negative for larger buds, while the other two become more positive. The pressure term initially dominates the free energy, but is outweighed by the stretching and adhesion terms as bud size increases, resulting in a stable state: the minimum of the total free energy, G_{tot} gives the radius and height of the bud at a given parameter set.

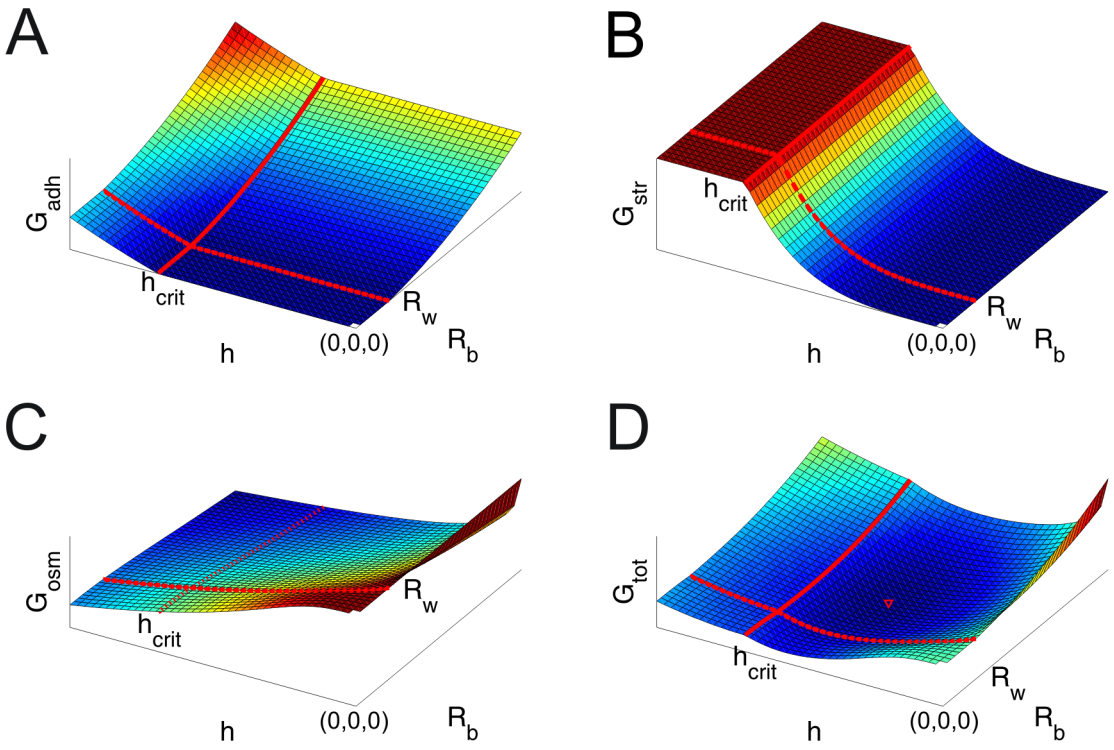

Figure 4.17: Surface plots showing the shape of the free energy contributions from adhesion (A), bilayer stretching (B), osmotic pressure (C), as well as the total free energy (D). R_w denotes the radius of the well, below which the radius of the bud R_b does not influence the adhesion energy. Since bilayer strain only depends on the height of the bud and not the radius, the critical tension at which the bilayer stops stretching and starts slipping corresponds to a critical bud height, h_{crit}. The minimum of the total free energy, located at the red triangle in D, gives the equilibrium bud height and radius. In this example, the minimum is located in the stretching regime ($h < h_{crit}$).

4.4.3 Modelling results

Due to the interdependent nature of the critical strain and the patch area, and the lack of a good measure of the height of the bud, it is at this point only possible to place boundaries on the parameters of the model (e.g. the stretch modulus, K_A; the critical tension, ϕ_{crit}, at a certain patch size; the adhesion strength, γ). These will be detailed here, along with some general findings about the system. It will be assumed that in the absence of biotin and avidin the adhesion strength between bilayer and substrate, γ, has the value 2 mN/m [5, 258, 297]. This value is used in the cited literature as the adhesion between lipids (with the same headgroup: phosphocholine) and glass. It is possible that differences in roughness between glass and deposited SiO_2 has an effect on the adhesion strength, but no data were found to corroborate this.

4.4.3.1 Pressure calibration

The modelling was carried out using a typical parameter set for lipid membranes, in order to explore the parameter space of the model. The first finding of note is that at the maximum theoretical osmotic pressure (resulting from pure water outside the well and 200 mM glucose and 5 mM $CaCl_2$ inside), the equilibrium bud radius and height are approximately 50 μm. This is larger than any buds observed in the experiments, leading to the conclusion that the concerns raised about poor mixing and the escape of solute molecules out of the confined wells are likely legitimate. It seems likely that these issues (in particular the escape of solute molecules) are severely exacerbated by the finite permeability of the suspended bilayers to water: the large discrepancy of theoretical and observed sizes indicates that even in the liquid phase, permeability plays a significant role in the rate of budding. The less permeable the membrane is, the slower budding proceeds, and the more time becomes available for equilibration through escape of confined solute molecules.

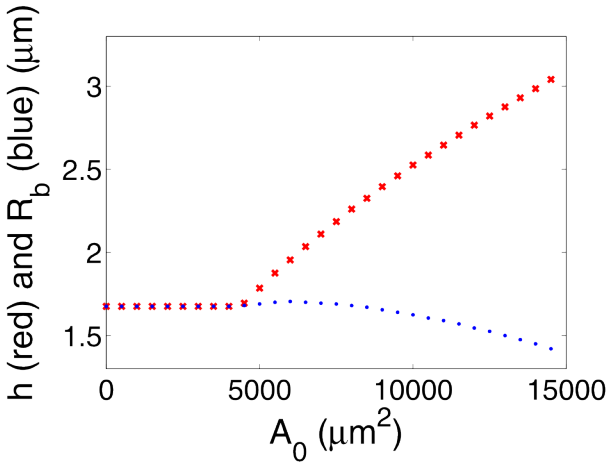

Figure 4.18: Graph showing the dependence of bud height, h (red crosses), and radius, R_b (blue dots), on initial patch area, A_0 at constant pressure. The critical strain ϕ_{crit} is set to 0.2%. In the slipping regime (low A_0) bud height and radius do not depend on patch area. Measurements of radius or, even better, height of buds forming in patches of differing areas would allow the determination of the force required to induce slipping, given knowledge of the stretching modulus of the membrane.

Observations with wells of diameter 8 μm indicate that for this size of aperture the radius of the bud does not exceed the radius of the well measurably. This allows us to put an upper bound on the pressure that was applied in the experiment: for a membrane that is in the slipping regime, the bud radius is independent of patch area, and here the pressure required is 18 kPa, or 3.4% of the maximum theoretical pressure. When the membrane is in the stretching regime, this value depends on patch area. For a large patch area of 30 000 μm^2 (corresponding to a spherical GUV of approximately 100 μm diameter), the pressure at which R_b increases beyond R_w is 26 kPa, or 5.0% of the maximum pressure. From this we can conclude that the pressures applied was rather lower than the maximum theoretical value, likely as a consequence of the finite permeability of the bilayers to water. Further measurements of the behaviour of suspended bilayers on different diameter wells would allow a calibration curve to be fitted and the actual osmotic pressure in the experiments to be determined.

4.4.3.2 Determination of critical strain

The experiments with DOPC/cholesterol mixtures indicate that L_α buds were generally uniform in radius, independent of the size of the patch from which they originate, from which we may conclude that these membranes are in the slipping regime. In the stretching regime, bud radius at a given pressure changes with patch size, while in the slipping regime the radius is independent of patch size (fig. 4.18). Assuming an applied pressure of around 3% of the maximum theoretical pressure, the value of ϕ_{crit} must be less than approximately 0.2% for a membrane such as DOPC (which has a K_A of approximately 235 mN/m [5]).

To obtain a value for the critical tension that causes slipping, buds stemming from patches of a large variety of sizes would need to be measured at low pressure to ensure that some are in the stretching regime. Such a data set could then be used to determine the patch area at which the membrane enters the stretching regime, which, in turn, would give the critical strain ϕ_{crit}. Given knowledge of the stretch modulus, K_A, this would allow a calculation of the tension required to induce slipping of the membrane over the substrate.

4.4.3.3 Effect of biotin avidin binding on adhesion strength

Experimental data such as presented in fig. 4.8 may be used in conjunction with data from the model to infer the value of the adhesion strength, γ. In this particular case, only a limiting value can be found, since in the case of biotin-avidin binding it seems the bud radius is limited by the radius of the well. A plot of the dependence of bud height and radius on adhesion strength is shown in fig. 4.19 A. At low adhesion strength, height and radius are large, such that $h > h_{crit}$ and the system is in the slipping regime. Furthermore, $h = R_b$, meaning that the bud takes the shape of a hemisphere (green shaded region in fig. 4.16). As adhesion strength is increased, the equilibrium size of the bud decreases and eventually crosses the boundary of the

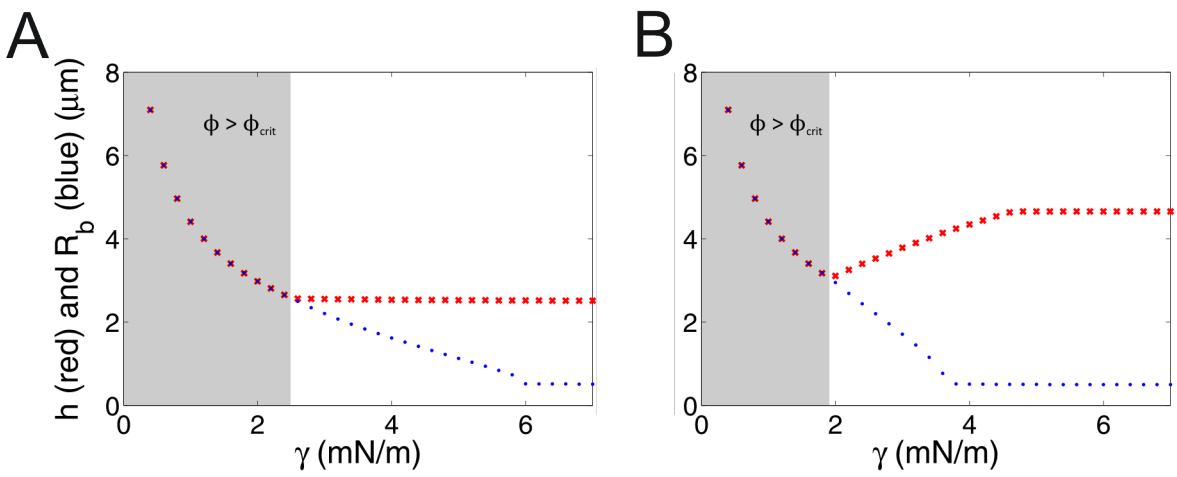

Figure 4.19: Graphs showing the dependence of h (red crosses) and R_b (blue dots) on the adhesion strength, γ. Grey shaded region, where $\phi > \phi_{crit}$, is the slipping regime. Here, bud radius and height are equal, meaning buds are hemispherical (cf green shaded region in fig. 4.16). Outside the grey shaded region the bilayer is in the sticking regime, and bud height is larger than bud radius (cf red shaded region in fig. 4.16). A: ϕ_{crit} assumed to be independent of adhesion strength. B: ϕ_{crit} set to increase linearly with adhesion strength.

stretching and slipping regimes. In the stretching regime, G_{adh} is independent of bud height, and as a consequence increasing the adhesion strength further does not decrease the height of the bud. The radius of the bud keeps decreasing, however, leading to a bud that makes up more than a hemisphere. Eventually, R_b decreases to the size of the well, R_w, below which G_{adh} becomes independent of bud radius, meaning it too stops decreasing further.

A complication comes from the fact that the point at which lateral tension overcomes static friction (i.e. the transition from the stretching to the slipping regime, described by ϕ_{crit}) likely also depends on the adhesion strength. In fig. 4.19 B, ϕ_{crit} was set to increase linearly with adhesion strength. As a result, h_{crit} also increases with adhesion strength, leading to the sloped region in the dependence of h on γ. The flat region occurs, again, when the system transitions from the slipping regime to the stretching regime. The actual relation between the static friction and the adhesion

strength is poorly understood and likely complex: This example is simply given to illustrate how measurements of this sort may allow the study of this interaction.

At the current stage it is possible to say that the adhesion strength of a 1% biotin-DPPE bilayer bound to a surface coated in actin seems to be stronger by a factor of ∼2 - 3, compared to a supported bilayer on silicon dioxide (where γ = 2 mN/m [5, 258, 297]).

4.4.3.4 Behaviour of L_o and L_β phases

Empirically it was found that the radii of buds formed in the L_o phase were smaller by a factor of approximately two compared to those formed in the L_α phase. The L_β phase was not observed to bud at all. As it stands, the model cannot account for these differences in behaviour: The only property included in the membrane that ought to differ significantly between the phases is the stretch modulus, K_A [5]. In the slipping regime, the value of K_A does not affect bud size. Even if the L_o and L_β phases were in the stretching regime (due to their higher stretch modulus), only the bud height would be significantly affected, since G_{str} is independent of bud radius. As mentioned above, the likely explanation for this discrepancy is the difference in permeability of bilayers in each phase. The model currently does not account for permeability, as it focuses on the equilibrium shape of the bud, rather than the dynamics of bud formation.

4.5 Discussion

This chapter explores experiments and mathematical modelling of the novel phenomenon of bilayer budding due to osmotic pressure. Results on the behaviour of the suspended bilayers over microfabricated cavities were presented, and some calculations were performed to deduce information about the physical properties of the

membranes. The conclusions drawn are preliminary, but they provide a starting point for future detailed experiments. Section 4.5.3.2 contains suggestions for potentially fruitful directions in which this work could be extended.

4.5.1 Budding – experimental issues

Bilayer budding was observed in mixtures of DOPC and cholesterol in the L_α phase, as well as mixtures of DSPC and cholesterol in the L_o phase, but not in gel phase DSPC/cholesterol bilayers. The buds in L_o bilayers were consistently smaller than those observed in L_α phase bilayers. In simultaneous measurements with these two phases, budding was observed only in the L_α phase.

Budding experiments were successfully carried out on a variety of substrates, including overhang microwell substrates ranging in pore diameter from 1 to 8 μm and peppershaker substrates with pore sizes ranging from 100 to 300 nm. In experiments using peppershaker substrates, bud formation was observed inside the cavity as well as above the substrate.

In order to allow a valid comparison between lipids of different phases, it was important to observe them in as nearly identical conditions as possible. The rate of dilution in the experiments may vary as a function of position on the substrate surface: due to the design of the flow chamber, the solution in it will not be well-mixed at all times while dilution is taking place. The Reynolds number in the tubing of the flow chamber is of the order of 10^{-7}, indicating that the flow may be presumed to be laminar throughout. It thus seems likely that the rate of dilution will be faster in the centre of the substrate and slower near the edges. Since it is not possible to control where GUVs rupture in the present setup, this is an inevitable source of variability between experiments.

A further complication in drawing a comparison is presented by certain aspects of the experiments that may cause variations in the local conditions on the sample.

These would only be fully controllable by substantial redesigning of the experimental method. The initial volume of liquid on the sample may vary by approximately 10% from one run to the next, since it is imperative that the bilayer be submerged in liquid the whole time. This means there is always a residual amount of liquid left on the sample before it is introduced to the flow chamber, and this amount is not identical each time. The result is that the rate of dilution of the bulk solution above the sample will vary slightly in every run.

For these reasons, observing both L_o and L_α phases in the same experiment and in adjacent locations on the substrate seemed necessary to allow valid comparisons between phases to be drawn. The most prominent downside was the fact that only two colours could be observed on the fluorescent microscope used, meaning that it was not possible to distinctly label both types of lipid and the confined solution in the wells. This problem was not particularly severe, since it was possible to observe for example both a green fluorescent bilayer and green fluorophores inside the wells at the same time (see fig. 4.6A).

Biotin-avidin binding was successfully employed to modulate the energetics of bud formation in L_α phase bilayers. The adhesion strength was increased, changing the bud shape from dome-shaped to balloon shaped. Increasing the adhesion of the bilayer to the substrate did not result in budding on gel bilayers, nor did it measurably increase bud size in liquid ordered bilayers. This indicates that an important factor in bud formation is the permeability of the bilayer to water, and that the lower permeability of gel and L_o phase bilayers inhibits bud formation on the time scale of the experiments. This conclusion is corroborated by the modelling results discussed in section 4.5.3.1.

4.5.2 Lifetime measurements

Measurements indicate that the suspended bilayers formed on microwell substrates are exceptionally long-lived, with characteristic lifetimes of many hours or even days. This is likely due to the small areas involved. Indeed, a correlation between size and rupture rate is found in the data, as described below.

The measurements indicate large differences in the longevity of suspended bilayers in different phases. Rather surprisingly the gel phase DSPC, which showed the greatest robustness against osmotic pressure, seems to be rather short-lived—shorter even than the fragile liquid phase DOPC. Liquid ordered DSPC suspended bilayers were longer lived still, by more than a factor of two than liquid phase bilayers and by a factor of ten longer than gel phase ones. The fact that the liquid phase outlives the gel phase seems to imply that flexibility is an important factor in the longevity of suspended bilayers. The fact that the liquid ordered phase outlives the liquid phase implies that tensile strength of the bilayer still plays a role, albeit a secondary one.

Care was taken to ensure each measurement was taken in the same conditions, and the measurements from the 1 μm wells consisted of several hundred wells from several different patches. Nevertheless, due to the nature of these measurements, it was not feasible to collect data from many different patches, nor from more than one sample per bilayer type. As a result, it is difficult to assess the magnitude of the error stemming from the inherent variability of different lipid preparations (of the same type), or from slight changes in sample preparation. At this time it is not possible to draw firm conclusions about the scaling of the lifetime of suspended bilayers with the size of the well, other than to say that reducing well diameter seems to improve stability. The pronounced differences in the lifetimes of the different phases indicates that perhaps the rupture of membranes has to do with defect propagation. In this view, it may be that fluid membranes are better able to "self-heal" when defects arise.

On the other hand, more ordered membranes may have a lower incidence of defects, explaining the long lifetime of L_o bilayers.

Insights from research on the rupture process of vesicles on substrates [152–155] may be brought to bear on this problem. Even though the geometry in these studies is not the same as for suspended bilayers, the system bears some similarities to a vesicle adsorbed to a surface. There is a portion of the bilayer that is absorbed to a surface, and a connected portion of the bilayer that is not attached to the substrate. The most significant differences seem to be the curvature of the bilayer in an adsorbed vesicle and the presence of an edge in the substrate used in budding experiments.

4.5.3 Mathematical modelling

A model was developed that describes the energetics of membrane budding. It includes free energy terms for the adhesion of the bilayer, the pressure volume coupling, and the stretching of the membrane. The free energy surface is divided into two regimes: an initial stretching regime for low volume increases, and a subsequent slipping regime when buds become larger. The transition from one regime to the other was not empirically observed, but slipping behaviour was seen when patch size was small (fig. 4.20).

The model assumes a static friction that holds the bilayer in place up to a critical tension, after which it is assumed to slide across the surface while remaining under the critical tension. The reality is likely somewhat different. Due to the diffusive nature of lipids in a bilayer, it seems unlikely that such a static friction would be present, holding the bilayer patch in place. It seems more plausible that even small tensions would cause some net motion in the bilayer. The evaluation of the parameter space of the model suggests that the bulk of the results detailed in this chapter took place in the slipping regime, so this inaccuracy should have little effect on the conclusions drawn.

Conclusions about the model parameters were drawn where possible. Most of these are in the form of upper or lower bounds on values, due to the preliminary nature of the experimental data. The following paragraphs detail some of the more promising ways in which refinement of the data could lead to accurate predictions of the properties of this lipid system.

The model leads to several conclusions regarding the experiments described in this chapter. In order to extract information on the mechanical properties of membranes, it is necessary to operate in the correct regime: The effect of the stretching modulus, K_A, will only be apparent in the stretching regime, i.e. when $h < h_{crit}$ and, consequently, $\phi < \phi_{crit}$. It is possible to increase h_{crit} by either increasing A_0 (i.e. studying only large patches) or by increasing the value of ϕ_{crit}—for instance by increasing the interaction between the surface and the bilayer, causing it to be less 'slippery'. Still, as is obvious from the example shown in fig. 4.20, even with the stronger biotin-avidin coupling, it is not difficult to exceed h_{crit} and move to the slipping regime. For this reason, it may be advantageous to study the behaviour of buds at low pressures, where h remains small. To do this would necessitate the ability to measure small heights of buds, which is problematic when using optical microscopy. A potential solution to this problem is explored in section 4.5.3.2.

Of course, it may be informative to study the slipping regime in its own right, as this may provide insights into the nature of the lipid/SiO_2 interaction. To this end, it would be logical to study small patches, where the critical value of the tension would be comparatively smaller, and the effect of membrane stretching would be smaller. The height and radius of the bud at a given pressure, as well as the initial area of the patch, could be measured to allow calculation of the adhesion coefficient γ, given knowledge of the stretching modulus of the membrane used. Since the surface of the samples can be easily modified by sputter coating or spin coating with various materials, and since it is possible to influence the binding between lipids and surface

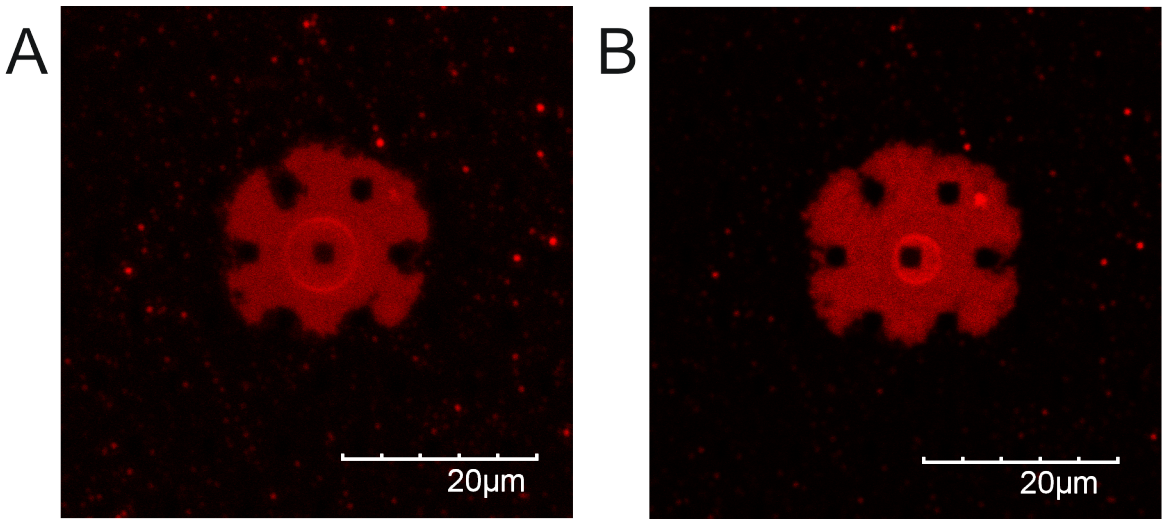

Figure 4.20: Shown are fluorescence images of a bud and the bilayer patch it originates from. The substrate is coated with avidin and the bilayer is composed of DSPC with 40 mol% cholesterol and 1 mol% biotin-DPPE. A: Bud at maximal size. B: Reduced osmotic pressure gradient results in diminished bud size. The excess lipid is incorporated into the supported bilayer patch, resulting in an increase in the adhered area.

using linker molecules such as biotin and avidin, this approach would allow the study of lipid-surface interactions in a wide range of conditions.

The tension in the membrane according to our model follows the simple relation $\phi = \frac{\pi h^2}{A_0}$, meaning that given a measure of the height of the bud and the initial area of the patch it would be a straightforward task to place the membrane under a given tension by applying such a pressure as to form a bud of the desired height. The availability of a membrane with tunable tension has important implications for the study of all membrane ion channels, since the predominant technique in use—patch clamp—introduces a resting tension that is larger by a factor of 10 to 100 than in vivo membrane tensions, even when no pressure is applied [297]. This is a consequence of the geometry of the bilayer in the pipette, where the adhesion of the bilayer itself causes tension in the membrane. In the geometry of membrane budding, the adhesion force is perpendicular to the suspended membrane, so the resting tension ought to

be close to zero. It should therefore be possible to probe a tension regime that is inaccessible to conventional patch clamp measurements using this technique.

4.5.3.1 Behaviour of L_o and L_β phases

It was found that the only way to account for the size difference of buds formed in different phases in the context of the model is to vary the adhesion strength γ or to change the applied pressure p. Changing the stretch modulus does not lead to the behaviour seen in experiments. Results from chapter 3 indicate that the mechanical properties of DSPC and DOPC bilayers converge at cholesterol concentrations of 30 mol% or more. This supports the conclusion that the cause for the differences in budding behaviour of these two lipids is not caused by differences in their mechanical properties.

Different adhesion strengths also seems an unlikely candidate, as in each case the bilayers consisted of phosphatidylcholine headgroup lipids with identical molar fractions of cholesterol. Differences in the applied pressure between the phases seems to be the most likely explanation. The flow cell itself is not a likely cause for such systematic pressure differences but more likely is the different permeabilities of the membranes to water. The permeability of bilayers to water is on the order of 10^{-3} cm/s [300, 301], which is high compared to for instance urea ($\sim 10^{-6}$ cm/s [301, 302]) or ions (($\sim 10^{-12}$ cm/s [303]). Higher ordering of the hydrocarbon region significantly reduces the permeability of the bilayer to small molecules [293–296]. It has been reported that the permeability of gel and liquid phase DPPC bilayers to acetic acid differs by a factor of ~ 500 [294]. This suggests that the rate of transfer of water molecules across gel phase and L_o phase DSPC may be orders of magnitude lower than across L_α DOPC. The result would be a much slower formation of the buds in DSPC as compared to DOPC. Since there is leakage of solutes from inside the well, the equilibrium size of the buds would also be smaller. Thus it may be the difference in membrane

permeability that accounts for the difference in budding behaviour in the different phases studied.

The fact that cholesterol decreases the permeability of a fluid phase bilayers to water [304–307] provides a simple way to test this hypothesis. By observing budding in a single phase bilayer with varying amounts of cholesterol, it might be possible to obtain a relationship between bud size and membrane permeability.

4.5.3.2 Future work

In order to apply the methodologies discussed in this chapter as a way to truly probe the mechanical properties of membranes, several improvements and adjustments will be necessary. The most glaring issue with the presented work is the incomplete knowledge of the pressure applied to the membrane. This is thought to be primarily a consequence of the finite permeability of bilayers to water, coupled with the steady leakage of solutes from inside the cavity. A possible way to reduce leakage would be to apply pressure in the opposite direction and to cause budding into the cavity rather than above it. This may lead to a better seal and reduce leakage. It would also simplify modelling, as the bud radius would be fixed by the radius of the well at all pressures. Downsides to this approach would be the limited size of the bud (due to the finite size of the cavity) as well as potential interactions between the walls of the cavity and the budding bilayer. For these reasons, only the initial stages of budding would lend themselves to this approach, necessitating good z-resolution—an issue that is discussed below.

A further problem in determining the exact pressure is the design of the flow chamber, which likely results in a poorly mixed solution above the well. A more intricately designed chamber that ensures better mixing may be all that is required in order to alleviate this problem. Should the problem persist, there are several other possible solutions that may be worth attempting. A rather inelegant and cumbersome solu-

tion would be to simply measure the osmolarity of the solution above the well using an osmometer. Perhaps a better approach would be to calibrate the actual pressure using wells of a range of diameters in a similar fashion as described in section 4.4.3.1.

The work presented here relies on being able to measure budding with confocal microscopy imaging. As a result, the buds have to be rather large before any quantitative data can be extracted from them. The z-resolution of confocal microscopy in the current setup is, at $\sim$1 µm, not good enough to observe the early stages of budding. Even optimising the z-resolution by using a high NA oil immersion lens and a smaller pinhole would likely be insufficient to observe the suspended bilayer beginning to bulge under osmotic pressure. There are several reasons why this stage is of particular interest, including the fact that suspended bilayers—especially the physiologically most relevant liquid phase ones—are rather fragile and tend to rupture at the high osmotic pressures required to form large buds. Reducing the size of buds and the incidence of ruptures will ensure that the effect of adjacent buds (assumed in the model to be negligible) will be kept to a minimum. Another reason to investigate the early stages of budding is that in the stretching regime (i.e. at low pressure), the adhesion energy is independent of the height of the bud. Conversely, the stretching component of the free energy is independent of the radius of the bud. By measuring the equilibrium height and radius of the bud in the stretching regime, it is therefore possible to extract information about both the adhesion and the stretching of the membrane independently and simultaneously. The early stages of budding may also provide a window into the behaviour of membrane channels in the low-tension regime that is inaccessible to standard patch-clamp techniques [297, 299]. Finally, as mentioned above, the early stages of budding, except for very large patches, are the only option for studying certain mechanical properties of membranes such as the stretching modulus.

A promising potential solution to the problem of the low z-resolution of optical

microscopy is the use of interference fringes as a measure of depth. In the case of a perfectly flat suspended bilayer, there will be some amount of interference in the laser illumination intensity owing to the difference in path-length of the light reflected off the bilayer and that reflected off the bottom of the well. The sign and magnitude of the interference will vary with radial distance from the centre of the bud if the bilayer is curved, leading to interference fringes akin to Newton's rings. This phenomenon has been observed in suspended bilayers spanning microwell substrates (Koji Sumitomo, personal communication, January 2014). The number and spacing of these fringes gives a measure of the height of the dome shape made by the bilayer, given the knowledge of the wavelength of the illuminating laser. This information, in conjunction with the easily measured radius of the bud, would allow computation of, for instance, the stretching modulus of the bilayer. To obtain the stretching modulus, one could simply find the input parameter for K_A that leads to the equilibrium values of h and R_b that were measured experimentally.

Preliminary results presented here indicate that the stability of suspended bilayers improves as aperture size diminishes. This observation could be useful in the design of future substrates. It stands to reason that reducing the size of the aperture would lead to increased stability and thus facilitate the study of membrane budding.

One of the conclusions reached is the importance of membrane permeability to bud formation. It may therefore be interesting to incorporate the dynamic nature of bud formation into the model. Dilution of the bulk liquid would lead to an increase in pressure, while leakage of confined solutes would tend to decrease it. Meanwhile the bud forms according to the rate at which water molecules are able to traverse the bilayer. The idea of a static friction is probably also a poor representation of the real picture. It seems more likely that any strain would cause a net movement of the bilayer as the lipid diffusion becomes biased in the direction of the tension. This could also be incorporated in a future model of the system.

Chapter 5

Towards simultaneous electrical and topographic measurements

5.1 Introduction

An important function of biological membranes is to maintain an electrochemical gradient between different compartments. Such gradients and the potential energy stored in them are essential for many biological processes. It is used as a source of energy, which can be converted variously into chemical potential energy (for instance in ATP synthase), or into kinetic energy directly (as, for example, in the bacterial flagellar motor). Migrations of ions across membranes both trigger and sustain nerve impulses travelling along axons, which in turn cause processes dependent on ionic movement across membranes. In the case of the neuromuscular junction, for instance, the nerve impulse triggers the influx of calcium ions through voltage gated channels in the neuron. The calcium ions trigger the release of ligands that themselves activate ion channels in the muscle cells, depolarising them and causing the cascade that leads to muscle contraction.

Electrophysiological methods have been used to study native membranes as well as model membranes (often containing channel proteins). In all electrophysiological techniques, membranes act as capacitors in a circuit, while channels in the membrane may be treated as resistors in parallel with it [308]. Such methods provide no direct structural information about bilayers and their proteins.

There are scanning probe techniques that detect electrical activity. Techniques detecting currents in air such as conductive (or current-sensing) AFM [309, 310] are able to obtain nanometre resolution in terms of both current and topography [311]. Scanning electrochemical microscopy (SECM) [134] is a technique in which an ultramicroelectrode (UME) is scanned over a surface while recording the current generated by redox reactions occurring at the electrode. Insulating materials reduce the current by limiting diffusion to the electrode, while conducting materials enhance the current by regenerating the redox species. Scanning ion conductance microscopy (SICM) is a related technique, using an electrolyte-filled micropipette as a probe [136], allowing

it to detect ionic currents. These two techniques have been applied simultaneously in an attempt to advance our abilities to probe structural and functional changes of cell membranes [312]. SECM has also been combined with AFM to provide simultaneous amperometric and topographic imaging [313, 314]. Efforts to combine SICM with AFM have been made to the same end, and ion currents from solution in the pico-ampere range have been recorded [315]. Probes reported for both SICM-AFM and SECM-AFM have been significantly larger in tip radius than the probes suggested here based on the modification process detailed in chapter 2.

The change in conductivity of ion channels is the result of conformational changes in the protein. To date, no technique has been able to observe simultaneously structural change and electrical activity in a membrane protein. The most promising candidate for such a technique appears to be AFM, which has the spatial resolution to assess membrane structure in situ. If it can be combined with electrophysiological measurement, using an electrically conductive cantilever as one electrode, this would allow the simultaneous determination of channel activity and conformation. The ultimate goal is to be able to detect both current and structural change of a single membrane channel.

The scale of this task is set by the miniscule nature of both the currents produced and the conformational changes that bring them about. Typical currents produced by membrane channels are on the order of 1 to 10 pA. In many channels, conformational changes occur internally and are on the sub-nanometre or even sub-angstrom scale. Such changes are not within the reach of current AFM technology, but it may be possible to observe changes in the ligand-binding domain of some channels (e.g. AMPAR), where the changes are predicted to be on the order of a nanometre [316, 317]. The requirements for an instrument capable of detecting structural change and electrophysiological function of a single membrane channel are noise levels on the order

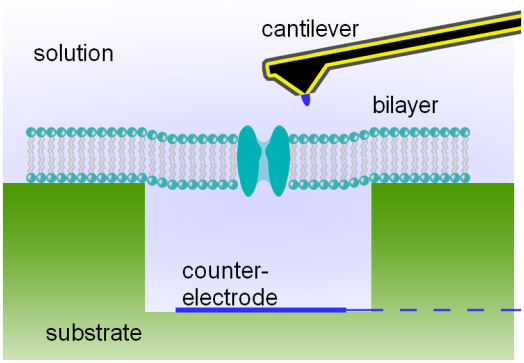

Figure 5.1: Schematic diagram showing a membrane channel incorporated in a suspended bilayer. The AFM tip is used to interrogate both the structure of the channel and its electrical activity with the help of a counter-electrode incorporated in the substrate.

of a pico-ampere and spatial resolution better than a nanometre on a lipid membrane in liquid.

A schematic representation of one conformation of the endeavoured experimental measurements is presented in fig. 5.1. The figure shows a substrate with an electrode in a recessed well, covered by a membrane containing an ion channel. An insulated conductive AFM tip, shown above the membrane, serves both to interrogate the structure of the channel and as another electrode to provide electrical data.

A number of difficulties present themselves in the pursuit of this endeavour. This chapter aims to present solutions to some of these practical difficulties and to propose ways to circumvent others in the future.

5.2 Experimental

Several materials and techniques were explored for their viability in insulating conductive cantilevers. Test coatings were deposited on conductive films of gold on silicon and glass, as well as on cantilevers. Evaporation of gold and silicon was done using an Edwards 306 thermal evaporator (Edwards Ltd, UK), with a TE4 resistive deposition source. Electron beam evaporation coating of silicon dioxide and aluminium oxide

was carried out in a Varian 3120 system (Varian Medical Systems, Inc., USA). A custom built system based on an Ion Tech sputter coater (Ion Tech, Inc., USA) was used for radio frequency sputter coating of silicon dioxide. Plasma enhanced chemical vapour deposition of silicon dioxide and silicon nitride was performed in a Plasmalab 80 Plus (Oxford Instruments plc, UK).

To assess the insulating properties of the coatings, cyclic voltammetry experiments were carried out using a μAutolab II potentiostat/galvanostat (Metrohm Autolab B.V., The Netherlands), in a solution of 100 mM KCl, 1 mM $Fe(CN)_6^{4-}$, and 10 mM HEPES buffer at pH 7. Sweeps were carried out at speeds between 10 and 500 mV/s and using a silver/silver-chloride reference electrode. In order to reduce noise in the measurements, a home-built aluminium box was used to shield the test setup.

Several potential substrates were assessed for their suitability for joint electrical and topographical measurements. Electrode microwell, gold ring microwell, and micropore silicon dioxide membrane substrates were provided by NTT Basic Research Laboratory (Japan). The construction of a prototype sample stage for use in the proposed experiments is detailed in section 5.4.

Modification of substrates and coatings by electrodeposition of silver and copper (respectively), as well as deposition of electrophoretic paint on cantilevers was performed with a TTi QL355TP power supply (Thurlby Thandar Instruments Ltd., UK). SEM images of silver electrodeposition on electrode microwell substrates were captured using a S-4300SE SEM (Hitachi, Ltd., Japan). SEM imaging of copper electrodeposition for pinhole characterisation was carried out in an Inspect S50 SEM (FEI, The Netherlands). FIB milling and subsequent SEM imaging of coatings was performed in an FEI Nova 600 NanoLab (FEI, The Netherlands).

Electrochemistry experiments were carried out using an Axopatch 200B amplifier in conjunction with a Digidata 1440A digitizer (Molecular Devices Corporation, USA). Measurements were followed on a DSO5052A Oscilloscope (Agilent Technolo-

gies, Inc., USA) as well as a computer interface. The setup was isolated in a Faraday cage placed on a compressed air anti-vibration system.

AFM images were captured with a Dimension 3100 AFM (Bruker Corporation, USA). The tunnelling AFM (TUNA) extension module was used for the electrical characterisation of insulated probes in air.

5.3 Coatings

The use of electrically conductive cantilevers in liquid results in significant background noise resulting from conductance from the solution to the cantilever and chip. In order to minimise this noise, it is necessary to insulate the cantilever and chip everywhere except at the tip. Various insulation materials and deposition techniques have been used in conjunction with the above techniques. A popular technique is plasma-enhanced chemical vapour deposition (PECVD), which has been used to deposit silicon dioxide [89] and silicon nitride [91, 97, 103]. Other techniques include low pressure chemical vapour deposition (LPCVD), used to deposit silicon nitride [102], atmospheric pressure CVD, for deposition of the polymer parylene [318, 319], and electrophoretically deposited paint (EDP) [95, 320–323]. The latter is a type of paint that coats conductive parts of a substrate when a voltage is applied to it while it is submerged in the paint. The paint is then cured in a subsequent heating step. This process has the advantage that it coats both sides of a cantilever simultaneously, unlike chemical vapour deposition and sputtering techniques.

In the effort to develop a microfabrication process to make insulated conductive AFM probes for simultaneous electrical and topographical measurements, the viability of several coating techniques and materials was assessed. The simplest of these was the thermal evaporation of silicon in a low-vacuum environment. It was proposed that the oxygen remaining in the deposition chamber might be sufficient to turn the

deposited material into an insulating layer of silicon dioxide, but cyclic votammetry experiments indicated that this was not the case. Thermal evaporation of silicon was dismissed as unsuitable for the purpose of cantilever insulation.

Radio frequency (RF) sputter coating of SiO_2 directly on gold surfaces results in delamination of the coating when immersed in water. The poor adhesion of RF sputtered SiO_2 on gold has been reported in the literature [324]. Chromium has good adhesion properties to both gold and SiO_2 [325] and is commonly used as an adhesion layer between these two. It was found that a 5 to 15 nm thick layer of chromium remedies the adhesion problem.

Flat gold surfaces are electrically insulated by a 40 nm layer of SiO_2 [326], but since AFM cantilevers have edges and protruding features which inhibit even coating, a thicker layer needs to be applied to them to ensure electrical insulation. Another reason to increase coating thickness is to decrease the probe's capacitance when it is submerged in liquid. For these reasons it is sensible to coat the probes with as much SiO_2 as possible without compromising their mechanical properties. It was found that probes with insulation layers as thick as 400 nm function satisfactorily in the AFM. The literature provides accounts of insulating coatings as thick as 800 nm having been applied without rendering the probes useless [97, 98]. Coating thickness on the surface of the pyramidal tips of cantilevers was assessed by cross-sectioning using focused ion beam milling.

Coatings were further characterised using electrochemical measurements, chiefy cyclic voltammetry. Fig. 5.2A-C show the effect of a $\sim$300 nm layer of SiO_2 on a cyclic voltammogram in ferricyanide solution on a gold coated glass slide. The ferricyanide redox peaks are clearly visible in fig. 5.2A, the bare gold surface. After application of the chromium adhesion layer, the magnitudes of the faradaic and capacitive currents are significantly reduced, due to the oxide layer on the chromium coating (fig. 5.2B). The position of the redox peaks is also shifted, as a result of the change in electrode

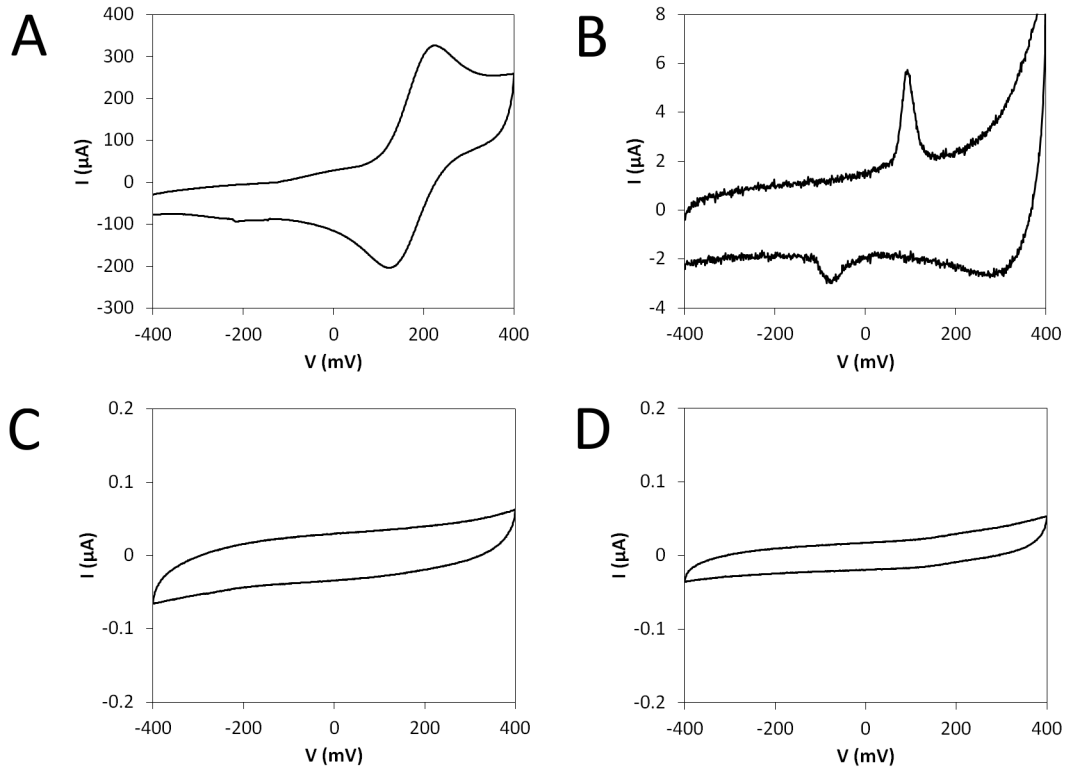

Figure 5.2: Cyclic voltammetry data in a solution of 100 mM KCl, 1 mM $Fe(CN)_6^{4-}$, and 10 mM HEPES buffer at pH 7. A: Bare film of sputtered gold on glass. Redox peaks of ferricyanide clearly visible. B: Sputtered gold film coated in a 10 nm adhesion layer of chromium. Redox peaks shifted due to change in electrode material. Reduction in faradaic and capacitive currents evident. C: As in B, with an added $\sim$300 nm of RF sputtered SiO_2. A significant reduction in capacitive currents. At the sensitivity of the measurement no redox reaction was detected. D: As in C, with surface modified by trichloro(octyl)silane, resulting in further slight reduction of the capacitive currents.

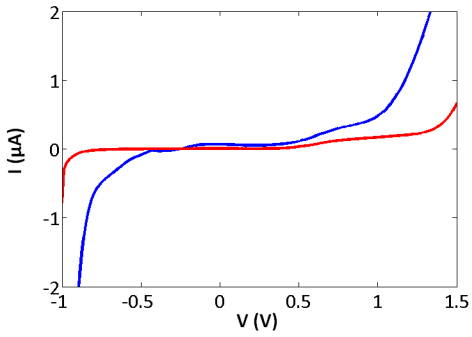

Figure 5.3: Cyclic voltammetry data in a solution of 100 mM KCl, 1 mM $Fe(CN)_6^{4-}$, and 10 mM HEPES buffer at pH 7. Direct comparison between an SiO_2 coated gold slide (blue curve) and a silane-modified SiO_2 coated gold slide (red curve). The direction of the sweeps is negative to positive (return sweeps omitted for clarity). The magnitude of the currents is reduced by silanisation, and the potential window is larger.

material from gold to chromium/chromium-oxide. Once the electrode is coated in the insulating layer of SiO_2, the redox peaks disappear and all that is left is a small amount of capacitive current (fig. 5.2C). The current is reduced by four orders of magnitude by application of the insulating coating. The range over which voltammetry was performed exceeds by a factor of 5 to 10 the range that is expected to be used in AFM experiments based on biologically relevant potentials.

Modification of silicon dioxide coatings with a hydrophobic monolayer is easily achieved through silanisation. In preliminary tests, it was found that current leakage through SiO_2 coatings could be further reduced by incubation at 110° C for 15 minutes with trichloro(octyl)silane in ethanol, which results in the surface being covered by a monolayer of hydrocarbon chains. This also significantly increased the hydrophobicity of the surface, further reduced the currents measured (see fig. 5.2D and fig. 5.3), and extended the potential window over which voltammetry data could be collected (fig. 5.3).

Electron beam evaporation of SiO_2 and Al_2O_3 were compared to RF sputtering. Both types of coatings were characterised with AFM to assess their surface roughness with the result that RF sputter coated SiO_2 has a roughness coefficient R_q about 25

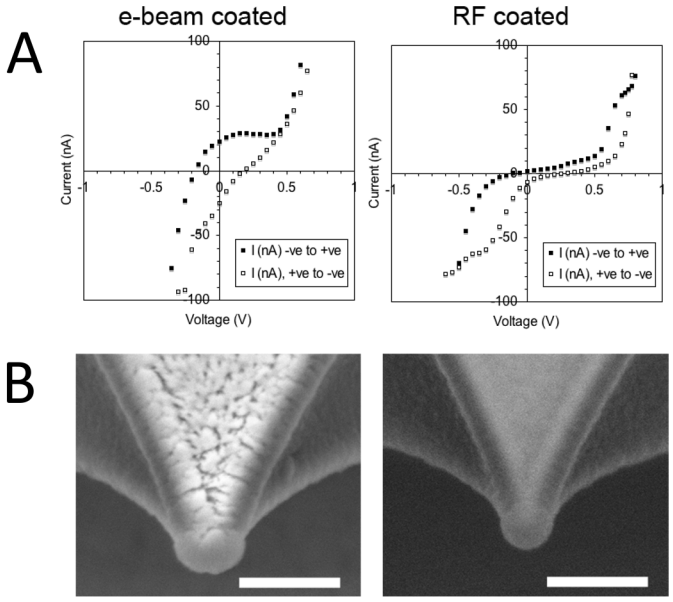

Figure 5.4: Cyclic voltammetry graphs of cantilevers in KCl solution (A) and SEM images of cantilevers (B) coated with electron beam evaporated SiO_2 (left column) and RF sputtered SiO_2. A: Cyclic voltammetry shows that conductance through the e-beam evaporated SiO_2 is significantly higher than through an RF sputtered SiO_2 coating of comparable thickness. B: SEM images of the two types of coating show that the RF coating is smoother than the e-beam coating. Scale bars represent 400 nm.

to 30% lower than that of e-beam evaporation coatings of the same thickness. FIB cross-sectioning and subsequent SEM imaging, as well as SEM imaging of the surface, showed that the e-beam evaporated coatings had numerous defects (fig. 5.4B and C). The latter also registered significantly higher currents in voltammetry experiments (fig. 5.4A) and larger pinhole counts after copper electrodeposition (table 5.1). These results indicate that RF sputtering is the more suitable technique of the two, so e-beam coating was not pursued any further.

FIB milled cross sections of cantilevers on the side facing away from the target during sputter coating indicate that some material is deposited here (fig. 5.5). The thickness of the coating on the back of the cantilever was ∼15% of the coating applied on the front. It is worth noting that the cross section was very close to the edge of the cantilever and that the thickness of the coating likely decreases with distance from the edge.

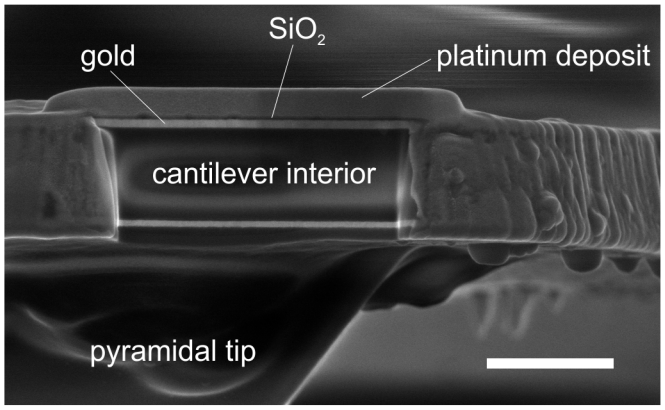

Figure 5.5: SEM image showing the FIB milled cross section at the end of a pyramidal tipped, insulated cantilever. A 100 nm coating of SiO_2 was applied to the tip side of the cantilever. Cross sectioning on the reverse side after deposition of a platinum pad revealed that the coating was approximately 15 nm thick here. Scale bar represents 1 μm.

Plasma enhanced chemical vapour deposition (PECVD) coatings composed of silicon dioxide and silicon nitride were explored as another option. These coatings appeared less granular than the e-beam evaporation coatings and exhibited good insulating performance in cyclic voltammetry tests. These coatings, despite being thinner than the ones deposited using RF sputtering and e-beam evaporation, also exhibited the lowest density of pinholes (see table 5.1).

In order to shed more light on the quality and potential of the coatings, copper was electrodeposited onto insulated gold covered slides and insulated cantilevers from $CuSO_4$ solution. Subsequent imaging with SEM and optical microscopy revealed any pinholes in the insulation coating, as these where the only conductive regions where plating could occur. Examples of SEM images showing electrodeposition of copper are given in fig. 5.6. Table 5.1 shows the density of pinholes detected by copper electrodeposition and subsequent imaging of insulated gold on glass.

In an attempt to forego the cumbersome and time-consuming coating procedures involved in RF sputtering, electrophoretic paint was investigated as an alternative. Electrophoretic deposition describes a process whereby a coating is applied from a

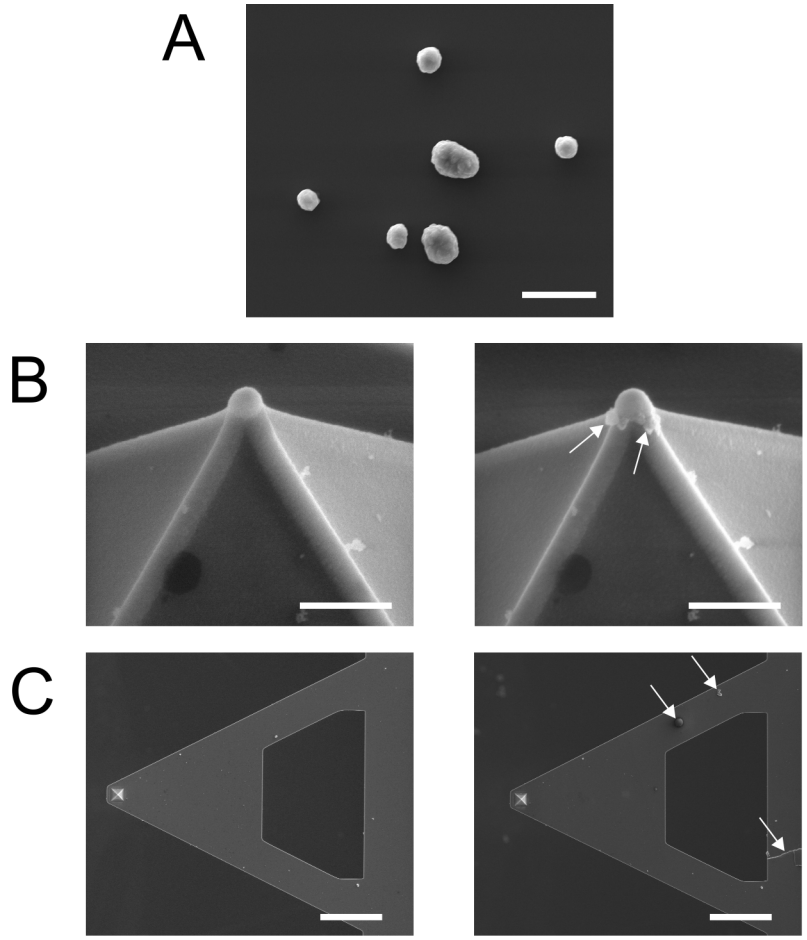

Figure 5.6: SEM images of an insulated gold surface (A), AFM tip (B), and triangular cantilever (C) after copper electrodeposition. A: Copper deposition at pinholes in a silicon dioxide coating on a gold surface. Scale bar is 10 μm. B: Before (left) and after (right) images of copper electrodeposition at the pyramidal tip of a silicon dioxide coated cantilever. Arrows indicate copper deposits. Scale bar is 1 μm. C: Before and after images of copper deposition (indicated by arrows) on a triangular cantilever insulated with silicon dioxide. Scale bar is 25 μm.

Table 5.1: Pinhole densities for various insulating films on gold-coated glass.

Coating	Thickness (nm)	Pinhole density (per mm^2)
E-beam Al_2O_3	100	2100
E-beam SiO_2	100	760
RF sputtered SiO_2	~170	140
PECVD SiO_2	80	72
PECVD Si_xN_y	80	156

solution of colloidal particles to a conductive substrate under the influence of an electric field. ClearClad^{TM}(supplied by LVH-coatings, UK) was used in preliminary tests. The advantages of using such a compound is that both sides of the cantilever can be coated in a single, simple step. It was found in practice that the paint retreats from the edges of the cantilever as it is heated in the curing process. As a result, the coatings performed significantly worse than the silicon dioxide coatings. Further work would be required to assess if the limitations of electrophoretic paint could be satisfactorily overcome by employing multiple coatings. In theory, the process lends itself to such an approach, since in each subsequent coating the colloidal particles would tend to accumulate at the exposed regions of the cantilever.

5.3.1 Tip fabrication

The proposed procedure for fabricating conductive cantilevers insulated everywhere except the tip is as follows:

1. A suitable conductive commercial probe is selected. Olympus OMCL-TR800PB cantilevers were used in this work.

2. The probe is insulated by coating it with SiO_2.

3. FIB milling is used to expose the conductive coating at the apex of the pyramidal tip.

4. A platinum pillar is deposited onto the conductive region to reconstruct a sharp tip.

5. The cantilever chip is electrically connected to a wire using silver paint or conductive epoxy.

6. the connection and wire is insulated using a non-conducting epoxy or other insulating compound such as GE varnish.

The microfabrication steps of the procedure are illustrated in fig. 5.7.

To assess the viability of such probes for electrical measurements, they were used to image conducting samples in a Dimension 3100 AFM while collecting electrical measurements using the TUNA extension module. Highly ordered pyrolytic graphite (HOPG) and evaporated gold on silicon were imaged topographically and electrically. AFM scans showing height and current on a HOPG sample are shown in fig. 5.8. The top two images (A and B) are relatively large scale scans over the layered surface of HOPG. Some of the layers show better conductance than others, as evidenced by the changes in layer colour in fig. 5.8B. It is also evident that certain features visible in the topography image are not reproduced in the current image. This is due to the fact that the steps evident in the height image are not on the surface, but covered beneath other layers, and so they do not affect the conductivity of the sample surface.

Fig. 5.8 C and D show high magnification scans of some HOPG steps. The current image shows multiple layers which are not clearly resolved in the topography image, showcasing the excellent resolution that is possible with conductive tips in air. The lateral resolution in the current image is $\sim$1.5 nm.

AFM height and current images of evaporated gold films on silicon are shown in fig. 5.9. Most of the gold film turned out to be too conductive, resulting in clipping in the TUNA module. This lead to high frequency noise in both current and height images. The film thinned out towards the edge of the sample, and it was found

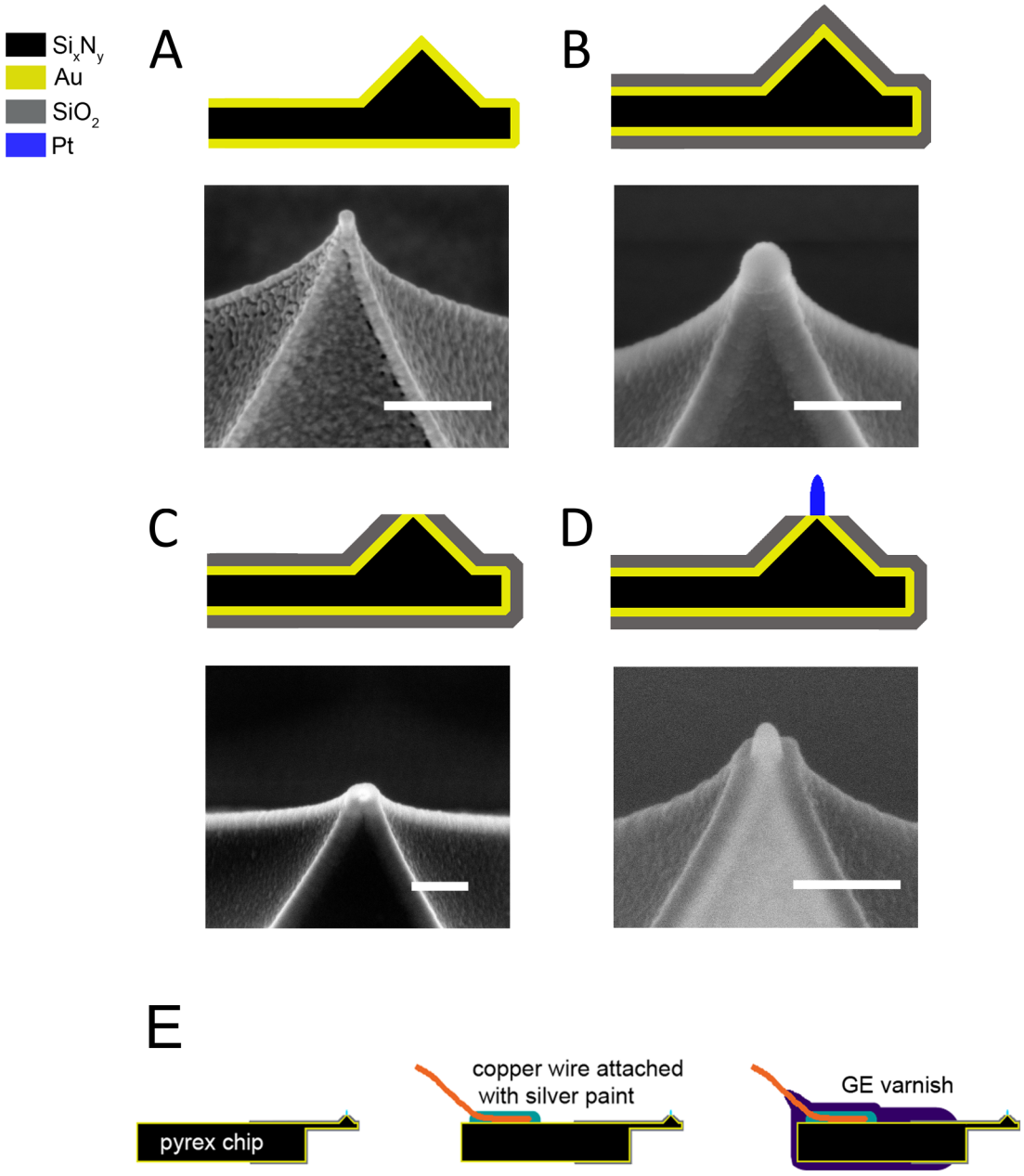

Figure 5.7: Schematic diagrams and corresponding SEM images of the stages in the fabrication of insulated conductive AFM probes. A: Pyramidal tip of a conductive commercial OMCL-TR800PB probe. B: A 150 nm SiO_2 coating was applied to the tip. C: FIB milling was used to ablate the coating at the tip, exposing the underlying gold. D: EBID of platinum to reconstruct a sharp tip in electrical contact with the underlying gold. Scale bars represent 300 nm. E: Schematic diagrams of steps 5 and 6 of the fabrication procedure. From left to right: A modified cantilever chip after EBID reconstruction of probe tip; A wire is connected to the exposed part of the gold coating on the cantilever chip; The assembly is insulated using GE varnish.

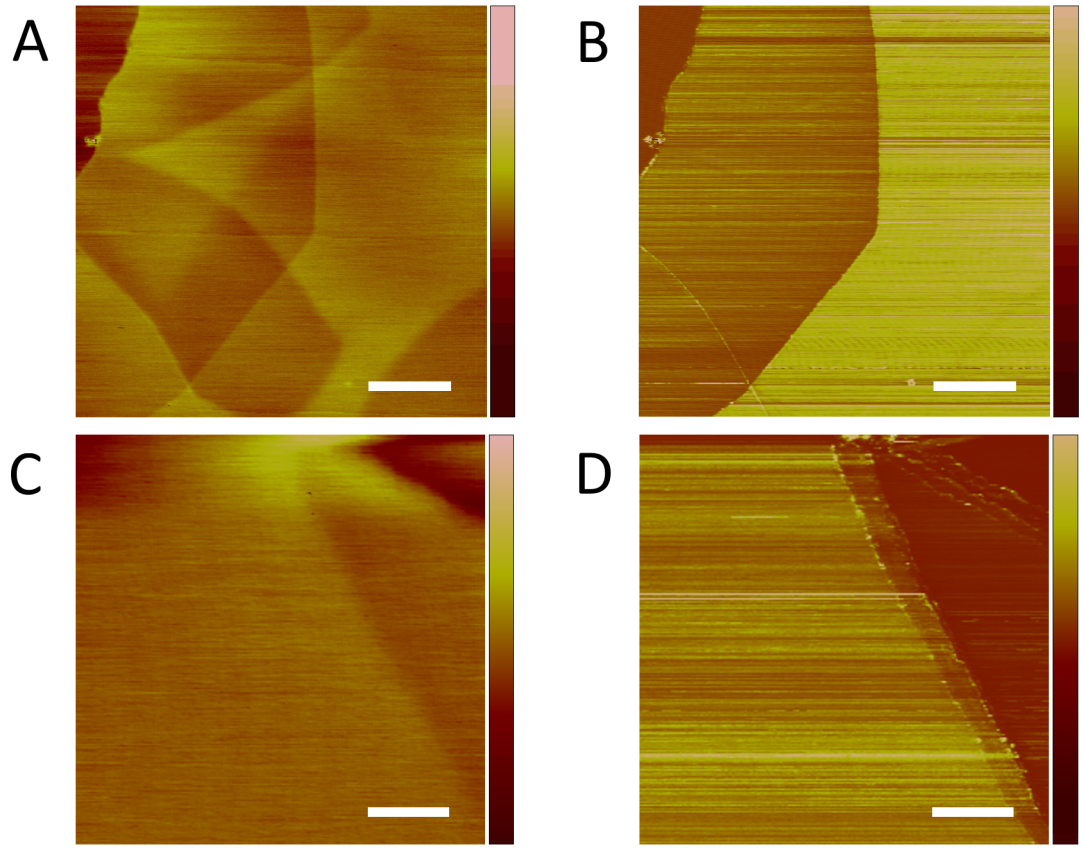

Figure 5.8: AFM height (A and C) and current (B and D) images captured on HOPG in air. A and B: Differential conductivity of HOPG layers is evident. Features beneath the surface are visible in the topography but do not affect current. Scale bars represent 200 nm, colour scales are 5 nm (A) and 3 nA (B). C and D: High magnification images of HOPG layers. Multiple layers that are only visible as a single blurred step are resolved in the current image. Scale bars represent 20 nm, colour scales are 3 nm (C) and 5 nA (D).

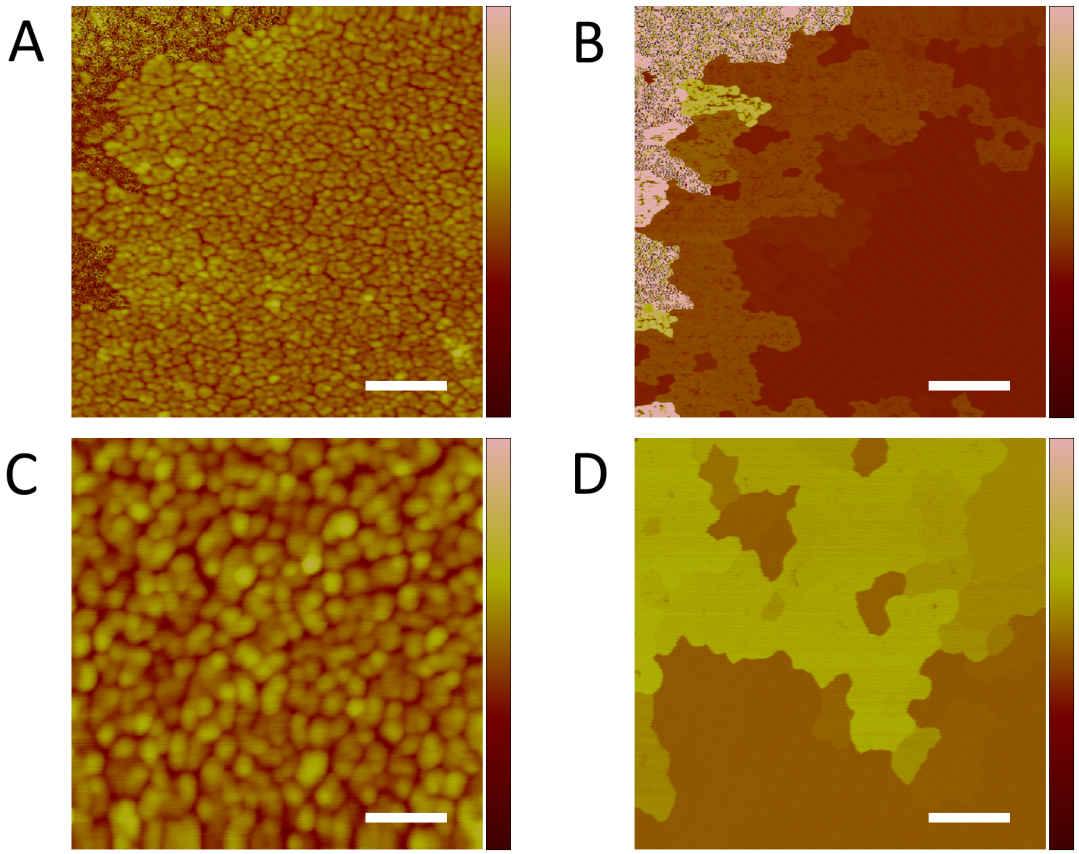

Figure 5.9: AFM height (A and C) and current (B and D) images captured on evaporated gold in air. A and B: Gold layer becomes thinner towards bottom right of image. Domains of decreasing electrical conductivity are evident. In areas of high electrical conductivity, clipping occurs in TUNA module, causing noise in both height and current images (top left). Scale bars represent 200 nm, colour scales are 20 nm (A) and 60 pA (B). C and D: Higher magnification images of evaporated gold, clearly showing regions of gold that are electrically more or less well connected to the rest of the gold layer. Scale bars represent 100 nm, colour scales are 10 nm (C) and 30 pA (D).

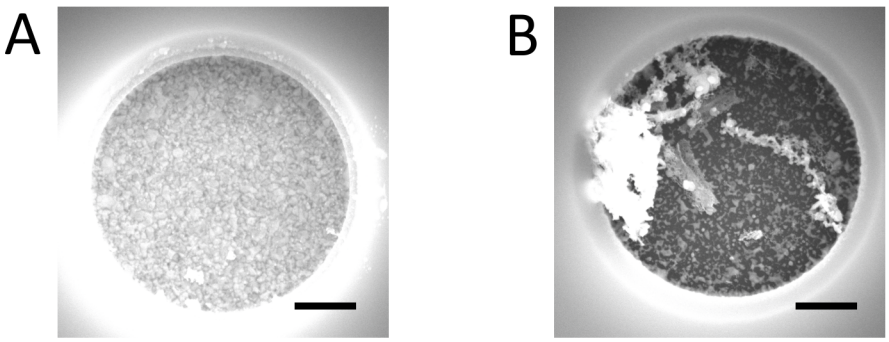

Figure 5.10: SEM images of silver electroplated electrode microwell substrates. A: Coated at 2 nA for 20 seconds. The coating shows little clumping and no gold is left exposed. B: Coated at 3 nA for 10 seconds. Large irregularities were formed and large amounts of the underlying gold is still exposed. Scale bars are 1 μm.

that there was an interfacial region where adjacent gold grains were still in electrical contact with the rest of the film, but displayed significantly lower conductance. This region allowed capture of images that were within the current range of the TUNA module. Fig. 5.9A and B show the interfacial region, with the top left of the image exhibiting the clipping-related noise caused by high conductance. Images C and D show a higher magnification of gold domains in the thinning film. The differences in current visible in image D highlight the changes in conductance of neighbouring gold domains.

5.4 Substrates

In order to function in conjunction with electrophysiological measurements of membrane protein activity the substrates used must allow placement of an electrode on both sides of the membrane. Several types of substrates have been explored for their viability as candidates in joint AFM and electrophysiology experiments.

Modified overhang microwell substrates with an electrode at the bottom of the wells provide a possible geometry that allows for AFM imaging and simultaneous electrophysiological measurements of the sort described in fig. 5.1. The substrates

are fabricated with a gold electrode, which significantly increased voltage drift during electrophysiology experiments. This issue can be resolved by post-fabrication electrodeposition of silver, which can then be further modified to form a silver/silver-chloride electrode. Experiments using Silvrex 50 AG12G/L solution led to the finding that ideal deposition time depends on the diameter of the microwells used. Preliminary tests indicate that good results (meaning fewest irregularities and least amount of gold exposed) can be achieved by applying a constant current of ∼1.5-2 nA for durations ranging from 20 to 60 seconds, depending on well size (longer times for larger sizes). SEM images of silver plated electrode microwell substrates are shown in fig. 5.10. Image A shows the results of successful electroplating, where little to none of the underlying gold is exposed. Image B shows an example of a poor result using a higher current and shorter deposition time. The silver deposit is non-uniform and large parts of the gold are exposed.

Due to the low density of the microwells in the electrode microwell substrates, it is necessary to place GUVs individually over the holes. This can be done using micropipette aspiration and micromanipulators, but the process is cumbersome and time-consuming. In an attempt to develop a method that circumvents the necessity for individual placement, the substrates were modified with exposed gold rings around each microwell. Thiolated lipids bind to gold and in tests with GUVs containing 1 mol% thiolated lipids it was found that the GUVs adhered sufficiently robustly to the gold ring to resist displacement by micropipette expiration.

Using these substrates would allow the spontaneous localisation of GUVs over the holes. It may also provide the additional advantage of improving the seal between the substrate and the membrane, reducing current leakage and reducing one of the sources of noise in electrophysiology experiments. AFM images of gold ring substrates are shown in fig. 5.11. Roughness measurements indicate that the R_q on the gold ring is 5.0 nm, while that on the silicon dioxide surface is 3.6 nm.

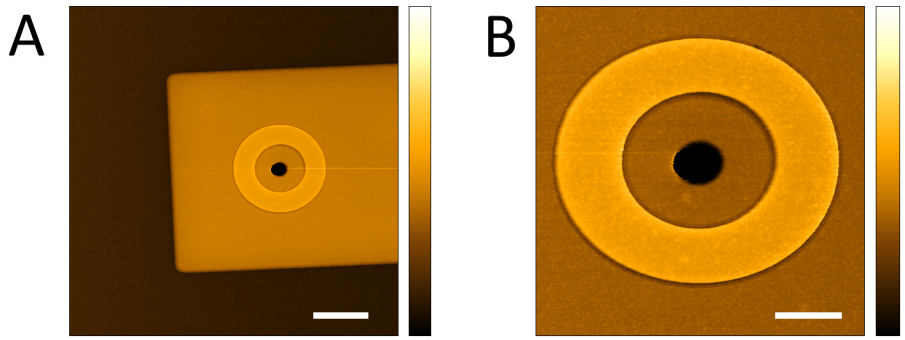

Figure 5.11: AFM height images of gold ring microwell substrates. A: Scan showing gold ring and well aperture in the centre of the underlying electrode pad. Scale bar is 5 µm, colour scale represents 500 nm. B: Magnified view of the gold ring surrounding the well aperture. Scale bar is 2 µm, colour scale represents 250 nm.

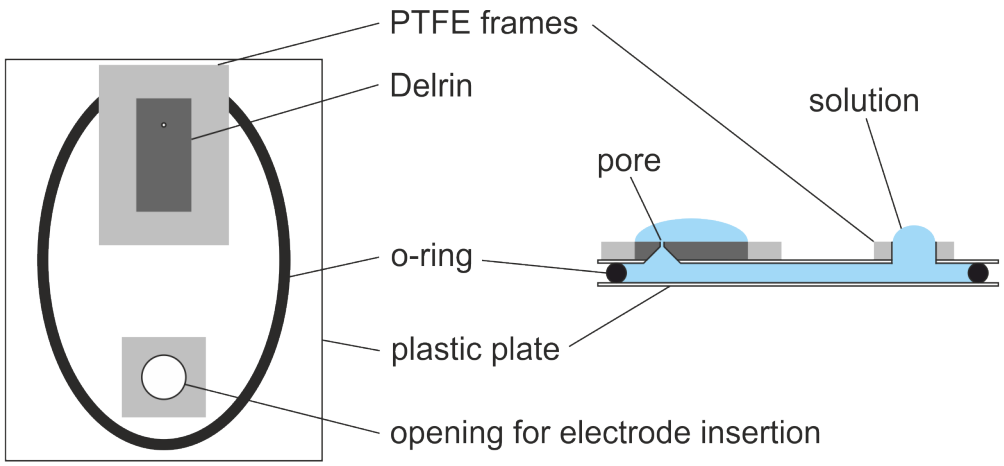

Figure 5.12: Schematic diagram of prototype stage intended for joint AFM and electrophysiological measurements. Top view (left) without solution and cross sectional side view (right) with solution are shown.

Investigations with glass have shown that the roughness of the glass pulled pipettes used for patch clamp is on the order of tens of nanometres [327], and that reducing the roughness by FIB milling to less than five nanometres results in a significantly improved giga-seal [327, 328]. The improvement in the seal in these reports led to a reduction by up to an order of magnitude in noise caused by leakage current. It stands to reason that given the low roughness of the gold ring substrates and the ability to establish chemical link between bilayer and substrate an excellent seal ought to be possible.

A prototype sample stage based on this concept was constructed by cutting the pore section out of a standard electrophysiology polyoxymethylene (POM) cup and setting it horizontally atop a chamber fashioned out of two plastic plates separated by an o-ring (glued in place with epoxy). A polytetrafluoroethylene (PTFE) frame was used to provide a hydrophobic barrier around the pore, allowing a droplet of aqueous solution to be placed there. A second opening into the chamber served as the entry point for a silver/silver-chloride electrode. A schematic of the stage design is shown in fig. 5.12.

AFM imaging on the POM cup surface near the pore revealed that the roughness of the surface was too great to detect the presence of a lipid bilayer on it. Micropore silicon membrane substrates may present a solution to this problem. These substrates consist of a thin silicon dioxide membrane with a single aperture. The diameter of the pore is on the order of a micrometer. Such a substrate could be substituted for the POM cup part of the prototype sample stage and allow AFM measurements to be carried out near or even on the pore.

5.5 Cantilever holder

There are cantilever holders available for the Dimension 3100 AFM that are intended for use in liquid and ones intended for conductive AFM use in air, but none that cater to the needs of conductive AFM in liquid. This section details efforts made to produce a working prototype cantilever that could be used in liquid to measure electrical properties.

In order to determine the geometrical requirements of the holder design, the dimensions of the standard liquid cantilever holder were measured and a computer-aided design (CAD) model was constructed. It is shown in fig. 5.13A. The cantilever is held at an angle of approximately 11° to the horizontal on the quartz glass body of the

holder by means of a metallic spring clip. The holder is affixed to the AFM by means of four pins on the headstage that slot into recessed clips in the holder.

A holder suitable for electrical measurements in liquid needs to fulfill several requirements. It must prevent contact between the solution and the AFM headstage, both to avoid corrosion of the metal parts and to prevent currents from the piezo-controlling elements to be passed to the solution. The holder must also provide stable mechanical support and an electrical connection to the cantilever, while not exposing any part of the measurement circuit to the solution.

Several early designs based on glass were discarded due to difficulties in machining the required shapes out of such a brittle material. An example of such a design is shown in fig. 5.13B. Metal bodies were deemed unsuitable due to the difficulties associated with insulating them from the solution and preventing corrosion in ionic solutions. An example of an early design using a metallic body is shown in fig. 5.13C. Polycarbonate plastic was chosen as the material of the body of the holder, due to its optical transparency, its chemical inertness, and not least due to the fact that it can be machined with relative ease. The design of the prototype holder is shown from three angles in fig. 5.13D. In this design the cantilever is affixed to a metallic stub – an aluminium cylinder beveled so as to angle the cantilever chip at 11° – by means of a conductive adhesive, after which the whole assembly is insulated. The stub itself is attached to the holder by means of a recessed screw on the apposing side of the holder. The screw also serves as the electrical contact on that side of the holder.

5.6 Noise characterisation

Noise characterisation measurements were carried out to assess the feasibility of joint electrophysiological and AFM measurements using the prototype holder and the sample stage presented in section 5.4. Fig. 5.14 summarises some of the findings.

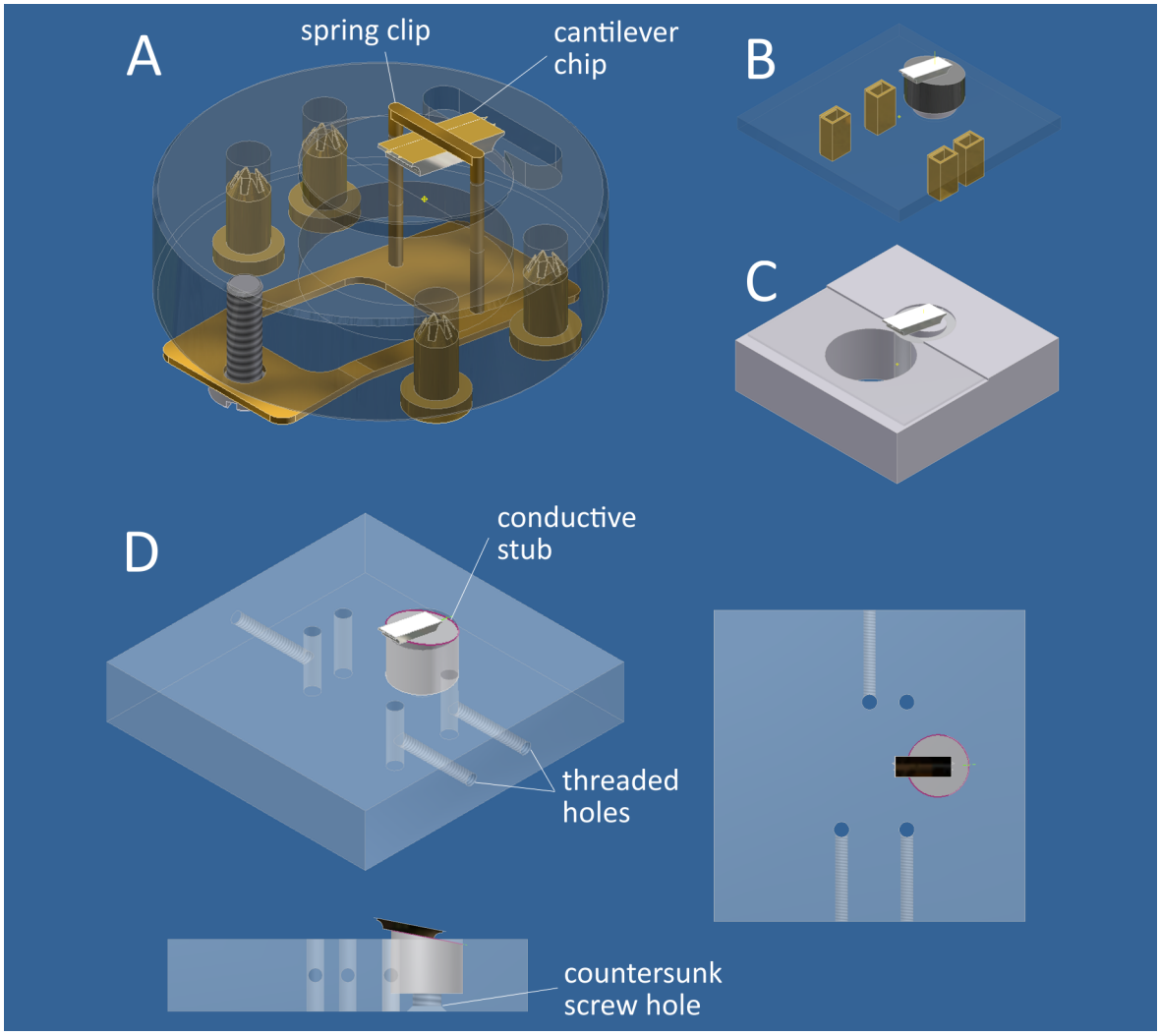

Figure 5.13: Images of the CAD models of cantilever holders. A: Commercial liquid holder for use in a Dimension 3100 AFM. B: Design based on a glass body that proved difficult to machine in practice. C: Design based on a metallic body, discarded due to the difficulties associated with insulation and corrosion. D: Design for the prototype holder constructed from polycarbonate plastic. The cantilever is held at an angle of 11° on a beveled aluminium stub which is secured to the holder by means of a countersunk screw that also serves as the electrical contact to the tip.

The measurements were carried out with two silver/silver-chloride electrodes, one immersed in the droplet atop the sample stage, the other inserted into the compartment beneath the pore. No external voltage was applied, barring voltage drift. Fluctuations in the current reading were recorded in several configurations. The noise levels seem to depend strongly on the presence of the AFM scan head, implicating it as a prominent source of electrical noise in the setup (fig. 5.14A and B). The standard liquid holder appears to massively amplify the noise caused by the scan head when it is immersed in the droplet on the sample stage (fig. 5.14C). Using the prototype holder mitigates this problem, bringing noise levels back to the level they were with no cantilever holder present (fig. 5.14D).

In order to further characterise the effect of the scan head assembly in relation to electrical noise, comparative measurements were taken in the AFM noise-isolation box and the electrophysiology Faraday cage. Using the noise levels in the standard electrophysiology setup as a baseline, it was found that without the scan head of the AFM in place the noise levels in the AFM box were higher by 34%. The noise levels increased by a factor ten when the scan head was replaced, confirming that it acts to amplify electrical noise. Further tests revealed that it was the electrical connection between the scan head and its mounting bracket (which also served as the common ground for the AFM box and electrophysiology equipment) that caused the increase in noise levels. Attempts at preventing electrical contact between the metal mounting bracket and the scan head succeeded in reducing the noise levels significantly, but they were still almost a factor of two higher than when the scan head was removed completely.

These results indicate that the scan head assembly is probably acting as an antenna, amplifying electrical noise generated by the AFM and transmitting it to the electrophysiology circuit ground.

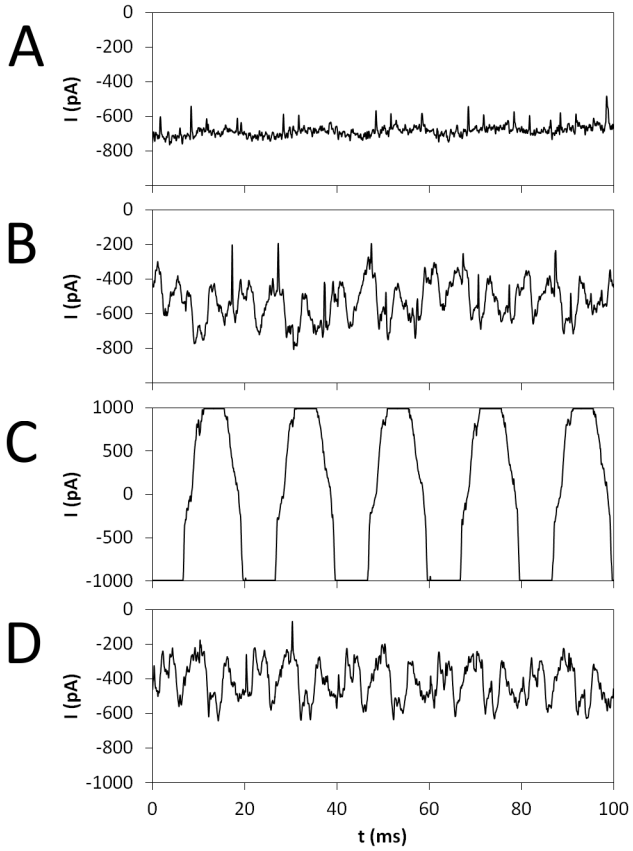

Figure 5.14: Current measurements to characterise electrical noise levels in electrophysiological measurements with in situ AFM. Electrophysiology current measurements taken in prototype sample stage consisting of two compartments of 100 mM KCl solution connected through a 150 µm pore. A: Scan head removed from AFM assembly. B: Scan head in place, without cantilever holder. A marked increase in noise levels is visible. C: Standard liquid holder attached to scan head and immersed in the solution. Noise levels are extreme and current fluctuations exceed the range of the amplifier. D: Standard liquid holder replaced by prototype cantilever holder. Noise levels are similar to B.

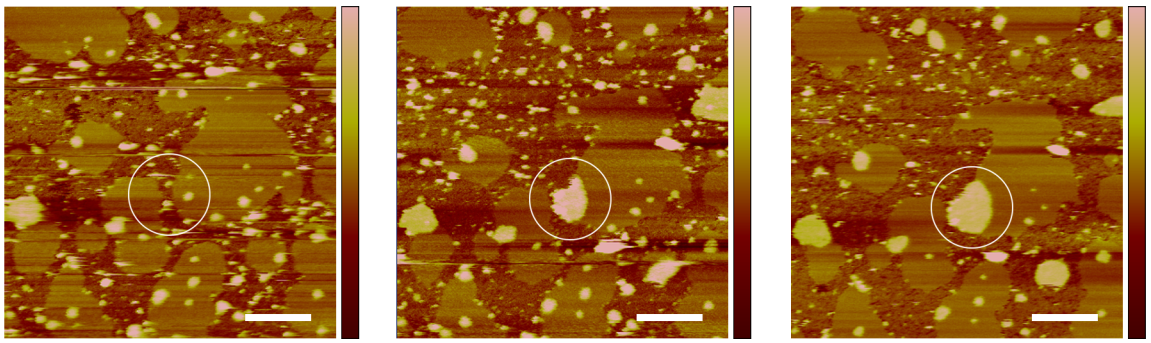

Figure 5.15: A series of height images showing the insertion of α-hemolysin into an egg-PC supported bilayer. Images captured in half hour intervals starting at the time the imaging buffer was exchanged with buffer containing 0.5 mg/ml Hla. Area of interest encircled in each image. Scale bars are 300 nm, colour scales represent 10 nm.

5.7 Towards simultaneous electrical and topography measurements

Preliminary experiments were carried out as a step towards the simultaneous recording of electrical and topographical properties of biological membranes. The membrane channel formed by the bacterial toxin α-hemolysin (Hla) was selected for its ability to spontaneously insert into lipid bilayers from solution, and the comparatively large currents it passes.

AFM images of Hla inserting into a supported egg-PC lipid bilayer are shown in fig. 5.15. Growing domains of inserted proteins are visible in the image series.

Electrophysiology recordings of α-hemolysin using the prototype AFM stage presented in section 5.4, also in an egg-PC bilayer are shown in fig. 5.16. Insertions of Hla channels into the bilayer show up as stepwise increases in the recorded current.

5.8 Discussion and conclusions

This chapter describes preliminary steps toward designing a system capable of the simultaneous measurement of electrical and topographical properties of biological

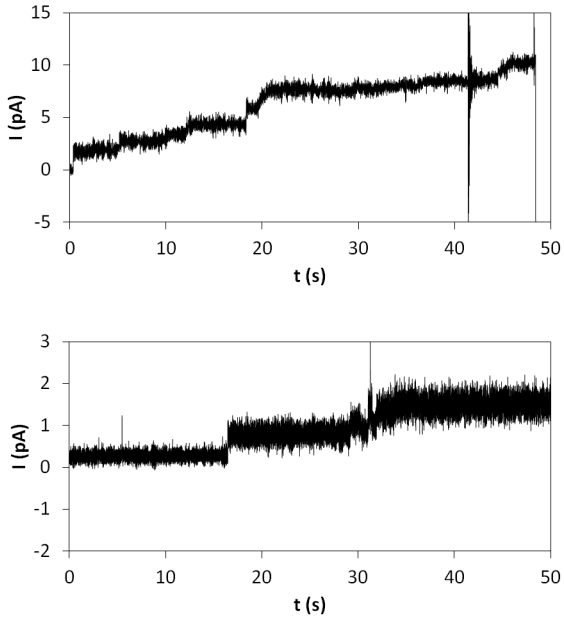

Figure 5.16: Traces showing the stepwise increase in current across an egg-PC bilayer as α-hemolysin self-inserts into it.

systems. The envisioned system is an AFM with electrophysiology capabilities. Ultimately the goal is to use the tip itself as one of the measurement electrodes. This requires a conductive probe that is insulated everywhere except at the tip. To this end, several coating materials – SiO_2, Si_xN_y, Al_2O_3 – were deposited on test samples using a number of different coating techniques, including e-beam evaporation, PECVD, RF sputter coating, and thermal evaporation. Electrophoretic deposition was also assessed, but this technique proved unable to reliably coat edges and recesses of an AFM probe.

Characterisation of coatings using cyclic voltammetry and electrodeposition of copper indicated that the best coatings were produced by PECVD of SiO_2, followed by PECVD Si_xN_y and RF SiO_2. SEM imaging of such coatings applied to cantilevers indicates that they conform well to the surface features. FIB cross sectioning indicates that a small amount of material is deposited on the side facing away from the target. Nevertheless, the cantilever would likely have to be rotated during or between coatings to ensure full insulation.

A fabrication procedure for insulated cantilevers with a fine conductive tip composed of EBID platinum was detailed. The electrical conductivity of cantilevers produced using this procedure was confirmed by scanning conductive surfaces in air.

Substrates with potential for the use in the proposed joint AFM and electrophysiological experiments were explored. The electrical instability of gold electrodes in electrode microwell substrates was addressed by electroplating with silver. Appropriate deposition currents and times were determined.

A prototype AFM holder for use in the proposed experiments was designed and built. The holder succeeded in reducing the electrical noise levels measured using electrophysiology equipment when compared to similar tests with the commercially available liquid holder.

A prototype AFM stage to enable the joint electrophysiological and AFM measurements was designed and built. The viability of electrophysiological measurements using this stage was confirmed in preliminary experiments with α-hemolysin in egg-PC bilayers. AFM experiments with membranes were precluded by the excessive surface roughness of the materials used. Suggestions for improvements using micropore membrane substrates were made.

Individual measurements of the electrophysiological effect of Hla insertion into an egg-PC bilayer and the concomitant topographical changes were measured. Unfortunately the electrical noise caused by the AFM in the current setup precluded the simultaneous measurement of these two phenomena.

Characterisation of the noise led to the conclusion that a significant factor is the amplification of noise through the AFM head stage assembly. Insulating the head stage from its support on the AFM greatly reduced the amount of noise in the measurements. Due to the tight fit of the metal parts involved, significant alterations would need to be made to the stage or its support to enable such an insulation during

AFM imaging. Given the risk of damaging the instrument, such alterations were deemed beyond the scope of this project.

Other approaches to noise reduction carry less risk. It might be possible, for example, to redesign the holder/stage assembly to act as a Faraday cage around the sample. Indium tin oxide could be used as a window for the laser, while more easily machined metal could be used for the rest of the chamber. A gasket made of flexible conductive material [329] would allow relative motion between the tip and the sample. Suitably shielded wires would connect the electrodes to the amplifier.

In conclusion, the current setup is unlikely to achieve the ultimate goal of electrophysiological recording in conjunction with observations of structural changes in single membrane channels. It may not be feasible to achieve this goal without designing a system from the ground up to minimise electrical noise during AFM scanning. Nevertheless, the setup introduced here may serve to observe multi-channel phenomena, where the currents can be orders of magnitude larger. It has been suggested, for example, that AMPA receptor clustering is an important factor in signal potentiation between neurons [330, 331]. Empirical data corroborating or invalidating such claims will likely be within the reach of the current setup in the near future.

Chapter 6

Conclusions

Living cells regulate the area of their plasma membranes through *active* biological mechanisms such as exo- and endocytosis, in which the fusion and fission of lipid vesicles leads to the transport of molecules across the otherwise impenetrable membrane. In this thesis I have studied the elastic properties of model membranes comprising supported or suspended lipid bilayers which provide an understanding of *passively* induced changes in membrane area. The work presented here encompasses:

- the structural characterisation of supported lipid bilayers by means of force curves measured by atomic force microscopy,
- the study of membrane budding as a way to characterise the mechanical properties of suspended bilayers and control their area, and
- the development of experimental methods including the fabrication and characterisation of modified AFM probes, and apparatus to facilitate the simultaneous electrical and topographical properties of membranes and potentially membrane proteins.

6.1 Force curves on lipid bilayers

Mixed-lipid supported bilayers were studied in order to simulate the heterogeneity of native plasma membranes. Although these bilayers comprised only several components we succeeded in elucidating their mechanical properties in response to cholesterol content, temperature, as well as the nature of the phase boundary, all of which are important features of native membranes. AFM force curve data were collected and analysed in conjunction with data obtained from AFM images. Elastic modulus values were determined for DOPC/DSPC bilayers as cholesterol content was varied up to 40%. Tentative conclusions about the compositional changes of the phases as a consequence of increased cholesterol were drawn. In brief, in the absence of cholesterol

distinct domain structure is observed with high and low domains corresponding to gel phase and liquid disordered phases respectively. The inclusion of small amounts (∼5%) of cholesterol appear to lead to a precipitation of DOPC out of the high domain. The result is an increase in the modulus of the high (gel phase) domain and a decrease in the modulus of the low domain. Further increasing cholesterol content of the bilayer leads to a phase change in the high domain from gel to liquid ordered, and a concomitant reduction in modulus. The reduction in the HD area fraction indicates a dissolution of DSPC into the low domain. It is proposed that the increased inclusion of cholesterol causes an increase in the disorder of the HD, the result of which is an increase in the free energy of DSPC in that phase. The reduction in the free energy difference between DSPC in the HD and DSPC in the LD leads to an increased prevalence of DSPC in the LD compared to lower cholesterol concentrations.

A mechanism for the penetration of gel phase bilayers by an AFM tip involving the formation of an interdigitated phase is suggested. Force curves on the gel phase exhibit a characteristic two-step breakthrough. The data is consistent with the formation of an interdigitated bilayer underneath the tip as pressure is applied, followed by the full penetration of the bilayer to the underlying mica. It was noted that subsequent force curves at the same point were reminiscent of low domain force curves. The influx of lipids following the retraction of the tip and relaxation of the bilayer out of the interdigitated state, likely consisted mostly of DOPC (and cholesterol when present), owing to the higher diffusivity of these species. Thus a small area of low domain lipid was formed after the initial indentation, explaining the formation of lasting depressions in the high domain.

Investigations of the LD/HD boundary with EBID modified probes point towards an interfacial region with properties reminiscent of both phases. Force curve height data indicate that the height of the boundary region may exceed that of the high (gel

phase) domain. This observation might explain the frequently observed localisation of reconstituted membrane proteins at membrane phase boundaries.

POPE bilayers were investigated at different temperatures. Imaging data indicate that the main transition temperature of a supported POPE bilayer in 150 mM KCl at pH 7 is 23 ± 1°C. The results from force curve analysis indicate that increasing temperature has the effect of decreasing the modulus of gel phase POPE, while increasing the modulus of liquid phase POPE. A possible cause for this phenomenon is presented. It posits that the highly ordered gel phase of POPE is disrupted when thermal vibrations are increased, while the low domain modulus is enhanced by an increase in the vibrational energy of the bilayer. Height data obtained from force curves suggests that the thickness of the water layer between the membrane and the substrate may increase substantially with temperature, especially above 20°C.

6.2 Membrane budding

Osmotic pressure was used to induce budding in membranes suspended over different kinds of microwell substrates. The budding behaviour of bilayers in the gel, liquid ordered, and liquid disordered phases was studied with confocal microscopy. It was found that liquid disordered bilayers formed large buds, liquid ordered bilayers formed small buds (under similar conditions), while gel phase bilayers were not observed to bud at all. Budding behaviour was modulated by changing in the bilayer-substrate interaction with biotinilated lipid binding to avidin-modified substrates. Using this technique, the shape of buds was changed from hemispherical dome-shaped buds to spherical balloon-shaped buds.

The effects of substrate type, lipid phase, and bilayer-substrate interaction on the lifetimes of suspended bilayers was assessed. It appears that liquid ordered bilayers

are the longest lived, followed by gel phase and then liquid disordered bilayers. Well size is negatively correlated to lifetime.

The viability of polyacrylamide gel as a simulated cytoskeletal support was demonstrated. Preliminary experiments confirmed the inclusion of PAG in peppershaker substrates, as well as proving that it is possible to deposit bilayers onto PAG-containing substrates.

The free energy landscape of bud formation was modelled mathematically and evaluated in MatLab. Two regimes of the model were studied: One in which the bilayer is adherent to the substrate, and one in which the lateral tension causes the bilayer to slide across the substrate. It was concluded that the experiments were likely taking place in the sliding regime. The model was used to calculate upper bounds on the applied osmotic pressure and the adhesion strength of biotin-avidin modified bilayers. Comparative studies between liquid and liquid ordered phase bilayers as well as modelling led to the conclusion that bilayer permeability to water is of critical importance to bud formation. Suggestions for future experiments were made on the basis of knowledge gleaned from modelling. The most promising avenue appears to be the study of the early phase of budding by tracking the interference fringes caused by bilayer curvature.

6.3 EBID modified AFM probes

The main objectives in the work on modified AFM probes was to develop a reliable and efficient procedure to fabricate sharp tips with high aspect ratios. The tip material was to be conductive to allow the technique to be expanded for the manufacture of insulated conductive tips for use in liquid. AFM tips with a radius of curvature of 4.5 nm were fashioned by depositing a platinum pillar at the apex of commercially available AFM probes. Improved performance compared to commercial probes

was registered in characterisation experiments involving gold films and hexagonally close packed arrays of polystyrene latex spheres. Blind tip reconstruction from images of carbon nanotubes confirmed tip radius measurements obtained using SEM. Electrical characterisation revealed that the probes exhibited lower resistance values than expected for EBID platinum, a fact that was concluded to be the consequence of annealing of the deposited material during measurement.

While tips were durable enough to withstand routine AFM imaging and force curve measurements, some tips were damaged when scanning samples with large height variations. The junction between the platinum pillar and the pyramidal tip seems to be the weakest point. In future, tips could be made more resilient by increasing the contact area between the deposited platinum and the gold.

6.4 Towards simultaneous electrical and topographic measurements

Progress in the endeavour to develop a system for the joint measurement of membrane channel activity and structural change was reported. A fabrication method for conductive AFM probes insulated everywhere except at the tip was detailed. Merits and issues of a variety of coating techniques were discussed. PECVD of SiO_2 was found to be the most promising candidate for electrical insulation of cantilevers. Modification with a hydrophobic silane layer was shown to further improve the electrical properties of insulating SiO_2 coatings. Preliminary experiments with insulated cantilevers on highly ordered pyrolytic graphite and evaporated gold films showed that the fabrication technique was successful in maintaining tip conductance.

Electrode microwell substrates show potential for joint electrophysiological and topographical measurements. Two main issues associated with these substrates were identified: Their scarcity on the silicon chip – a consequence of the space taken up

by the underlying electrodes – requires individual placement of GUVs, and the electrode material (gold) is prone to voltage drift in electrophysiological/electrochemical measurements. The proposed solution for the former is the use of gold ring substrates which would allow the passive localisation of GUVs containing thiolated lipids. The second problem was addressed by electroplating the gold electrodes with silver, to then form stable silver/silver-chloride electrodes.

A prototype AFM cantilever holder and a prototype sample stage were designed to meet the requirements for the collection of electrical data in liquid. Preliminary tests using the prototype holder and stage point towards significant electrical noise levels stemming from the AFM. It was found that the head stage of the AFM served to greatly amplify the noise levels, and means to reduce this effect were tested.

Separate measurements of the topography and electrical properties of α-hemolysin were carried out using the prototype equipment. The preliminary results indicate that single channel recordings are likely out of the question using this setup due to the electrical noise, but that it may be possible to study the behaviour of multiple channels in the future.

Bibliography

[1] International Human Genome Sequencing Consortium. Initial sequencing and analysis of the human genome. *Nature*, 409:860–721, 2001.

[2] A. P. Russ and S. Lampel. The druggable genome: an update. *Drug Discov. Today*, 10:1607–1610, 2005.

[3] E. Gouaux and S. H. White. Membranes: Lipids lost, lipids regained. *Current Opinion in Structural Biology*, 11(4):393–396, 2001.

[4] C. Cotman. Lipid composition of synaptic plasma membranes isolated from rat brain by zonal centrifugation. *Biochemistry*, 8(11):4606–4612, 1969.

[5] Derek Marsh. *Handbook of Lipid Bilayers*. CRC Press, 2nd edition edition, 2013.

[6] J. Baranovic. *Structural and funtional characterization of reconstituted* $\alpha - amino - 3 - hydroxy - 5 - methyl - 4isoxazolepropionicacid$ *receptors*. PhD thesis, University of Oxford, Trinity Term 2011.

[7] G. Binnig, C. F. Quate, and C. Gerber. Atomic Force Microscope. *Phys. Rev. Lett.*, 56:930–934, 1986.

[8] G. Binnig and H. Rohrer. Scanning tunneling microscopy, an atomic probe. *Scanning electron microscopy*, 56:930–934, 1983.

[9] G. Binnig and H. Rohrer. Scanning tunneling microscopy—from birth to adolescence. *Reviews of Modern Physics*, 59:615–625, 1987.

[10] G. Meyer and N. M. Amer. Novel optical approach to atomic force microscopy. *Appl. Phys. Lett.*, 53:1045–1047, 1988.

[11] F. J. Giessibl. Piezoresistive cantilevers utilized for scanning tunneling and scanning force microscope in ultrahigh vacuum. *Rev. Sci. Instrum.*, 65:1923–1929, 1994.

[12] F. J. Giessibl. High-speed force sensor for force microscopy and profilometry utilizing a quartz tuning fork. *Appl. Phys. Lett.*, 73:3956–3958, 1998.

[13] D. Rugar, H. J. Mamin, and P. Guethner. Improved fiber-optic interferometer for atomic force microscopy. *Appl. Phys. Lett.*, 55:2588–2590, 1989.

[14] T. Göddenhenrich, H. Lemke, U. Hartmann, and C. Heiden. Force microscope with capacitive displacement detection. *J. Vac. Sci. Technol. A*, 8:383–387, 1990.

[15] F. J. Giessibl. Advances in atomic force microscopy. *Rev. Mod. Phys.*, 75:949–983, 2003.

[16] F. Ohnesorge and G. Binnig. True Atomic Resolution by Atomic Force Microscopy Through Repulsive and Attractive Forces. *Science*, 260:1451–1456, 1993.

[17] D. Fotiadis, S. Scheuring, S. A. Müller, A. Engel, and D. J. Müller. Imaging and manipulation of biological structures with the AFM. *Micron*, 33:385–397, 2002.

[18] A. Engel and D. J. Müller. Observing single biomolecules at work with the atomic force microscope. *Nature Struct. Biol.*, 7:715–718, 2000.

[19] D. J. Müller and Y. F. Dufrêne. Atomic force microscopy as a multifunctional molecular toolbox in nanobiotechnology. *Nature Nanotech.*, 3:261–269, 2008.

[20] E. Meyer, H. Heinzelmann, P. Grütter, T. Jung, H.-R. Hidber, H. Rudin, and H.-J. Güntherodt. Atomic force microscopy for the study of tribology and adhesion. *Thin Solid Films*, 181:527–544, 1989.

[21] Y. Martin, C. C. Williams, and H. K. Wickramasinghe. Atomic force microscope – force mapping and profiling on a sub 100-Å scale. *J. Appl. Phys.*, 61:4723–4729, 1987.

[22] R. Garcìa and R. Pérez. Dynamic atomic force microscopy methods. *Surface Science Reports*, 47:197–301, 2002.

[23] Q. Zhong, D. Imniss, K. Kjoller, and V. B. Elings. Fractured polymer/silica fiber surface studied by tapping mode atomic force microscopy. *Surface Science*, 290:L688–L692, 1993.

[24] T. R. Albrecht, P. Grütter, D. Horne, and D. Rugar. Frequency modulation detection using high-Q cantilevers for enhanced force microscope sensitivity. *J. Appl. Phys.*, 69:668–673, 1991.

[25] N. A. Burnham and R. J. Colton. Measuring the nanomechanical properties and surface forces of materials using an atomic force microscope. *Journal of Vacuum Science and Technology*, 7:2906–2913, 1989.

[26] A. L. Weisenhorn, P. K. Hansma, T. R. Albrecht, and C. F. Quate. Forces in atomic force microscopy in air and water. *Applied Physics Letters*, 54:2651–2563, 1989.

[27] S. R. Cohen. Dynamic atomic force microscopy methodsAn evaluation of the use

of the atomic force microscope for studies in nanomechanics. *Ultramicroscopy*, 42–44:66–72, 1992.

[28] A. L. Weisenhorn, P. Maivald, H.-J. Butt, and P. K. Hansma. Measuring adhesion, attraction, and repulsion between surfaces in liquids with an atomic-force microscope. *Physical Review B*, 45(19):11226–11232, 1992.

[29] M. Radmacher. Measuring the elastic properties of biological samples with the AFM. *IEEE Eng. Med. Biol. Soc.*, 16:47–57, 1997.

[30] J. B. Pethica and W. C. Oliver. Measuring the nanomechanical properties and surface forces of materials using an atomic force microscope. *Journal of Vacuum Science and Technology*, 19:61–66, 1987.

[31] N. A. Burnham, D. D. Dominguez, R. L. Mowery, and R. J. Colton. Probing the surface forces of monolayer films with an atomic-force microscope. *Physical Review Letters*, 64:1931–1934, 1990.

[32] J. H. Hoh and A. Engel. Friction effects on force measurements with an atomic force microscope. *Langmuir*, 9:3310–3312, 1993.

[33] N. J. Tao, S. M. Lindsay, and S. Lees. Measuring the microelastic properties of biological material. *Biophysical Journal*, 63:1165–1169, 1992.

[34] K. Hu, P. Radhakrishnan, R. V. Patel, and J. J. Mao. Regional structural and viscoelastic properties of fibrocartilage upon dynamic nanoindentation of the articular condyle. *Journal of Structural Biology*, 136:46–52, 2001.

[35] A. L. Weisenhorn, M. Khorsandi, S. Kasas, V. Gotzos, and H.-J. Butt. Deformation and height anomaly of soft surfaces studied with the AFM. *Nanotechnology*, 4:106–113, 1993.

[36] M. Fritz, M. Radmacher, and H. E. Gaub. In vitro activation of human platelets triggered and probed by atomic force microscopy. *Exp. Cell Res.*, 205:187–190, 1993.

[37] J. H. Hoh and C.A. Schoenenberger. Surface morphology and mechanical properties of MDCK monolayers by atomic force microscopy. *Journal of Cell Science*, 107:1105–1114, 1994.

[38] A. M. Collinsworth, S. Zhang, W. E. Kraus, and G. A. Truskey. Apparent elastic modulus and hysteresis of skeletal muscle cells throughout differentiation. *Am. J. Physiol.-Cell Physiol.*, 283:C1219–C1227, 2002.

[39] A. Ikai and R. Afrin. Toward mechanical manipulations of cell membranes and membrane proteins using an atomic force microscope: An invited review. *Cell Biochemistry and Biophysics*, 39(3):257–277, 2003.

[40] Y.-B. Lu, K. Franze, G. Seifert, C. Steinhäuser, F. Kirchhoff, H. Wolburg, J. Guck, P. Janmey, E.-Q. Wei, and J. Käs. Viscoelastic properties of individual glial cells and neurons in the CNS. *Proc. Nat. Acad. Sci.*, 103:17759–17764, 2006.

[41] T. Ludwig, R. Kirmse, K. Poole, and U. S. Schwarz. Probing cellular microenvironments and tissue remodeling by atomic force microscopy. *Pflügers Arch.-Eur. J. Physiol.*, 456:29–49, 2008.

[42] S. E. Cross, Y.-S. Jin, J. Tondre, R. Wong, J. Rao, and J. K. Gimzewski. AFM-based analysis of human metastatic cancer cells. *Nanotechnology*, 19:384003, 2008.

[43] C. Rotsch and M. Radmacher. Drug-induced changes of cytoskeletal structure and mechanics in fibroblasts: an atomic force microscopy study. *Biophys. J.*, 78:520–535, 2000.

[44] R. Matzke, K. Jacobson, and M. Radmacher. Direct, high-resolution measurement of furrow stiffening during division of adherent cells. *Nat. Cell Biol.*, 3:607–610, 2001.

[45] A. E. Pelling, D. W. Dawson, D. M. Carreon, J. J. Christiansen, R. R. Shen, M. A. Teitell, and J. K. Ginzewski. Distinct contributions of microtubule subtypes to cell membrane shape and stability. *Nanomed. Nanotechnol. Biol. Med*, 3:43–52, 2007.

[46] M. Rief, M. Gautel, F. Oesterhelt, J. M. Fernandez, and H. E. Gaub. Reversible unfolding of individual titin immunoglobulin domains by afm. *Science*, 276(5315):1109–1112, 1997.

[47] M. Schlierf, H. Li, and J. M. Fernandez. The unfolding kinetics of ubiquitin captured with single-molecule force-clamp techniques. *Proceedings of the National Academy of Sciences of the United States of America*, 101(19):7299–7304, 2004.

[48] K. Voïtchovsky, S. A. Contera, and J. F. Ryan. Electrostatic and steric interactions determine bacteriorhodopsin single-molecule biomechanics. *Biophysical Journal*, 93(6):2024–2037, 2007.

[49] T. Fukuma, M. J. Higgins, and S. P. Jarvis. Direct imaging of lipid-ion network formation under physiological conditions by frequency modulation atomic force microscopy. *Phys. Rev. Lett.*, 98(10):106101–1 – 106101–4, 2007.

[50] G. S. Blackman, C. M. Mate, and M. R. Philpott. Interaction forces of a sharp tungsten tip with molecualr films on silicon surfaces. *Physics Review Letters*, 65:2270–2273, 1990.

[51] J. Domke and M. Radmacher. Measuring the Elastic Properties of Thin Polymer Films with the Atomic Force Microscope. *Langmuir*, 14:3320–3325, 1998.

[52] B. Du, J. Zhang, Q. Zhang, D. Yan, T. He, and O. K. C. Tsui. Nanostructure and Mechanical Measurement of Highly Oriented Lamellae of Melt-Drawn HDPE by Scanning Probe Microscopy. *Macromolecules*, 33:7521–7528, 2000.

[53] H. Shulha, A. Kovalev, N. Myshkin, and V. V. Tsukruk. Some aspects of AFM nanomechanical probing of surface polymer films. *European Polymer Journal*, 40:949–956, 2004.

[54] J. Rädler, M. Radmacher, and H. E. Gaub. Velocity-dependent forces in atomic force microscopy imaging of lipid films. *Langmuir*, 10:3111–3115, 1994.

[55] W. A. Ducker and D. R. Clarke. Controlled modification of silicon nitride interactions in water via zwitterionic surfactant adsorption. *Coll. Surf. A.*, 94:275–292, 1994.

[56] Henning Mueller, Hans-JÃijrgen Butt, and Ernst Bamberg. Force measurements on myelin basic protein adsorbed to mica and lipid bilayer surfaces done with the atomic force microscope. *Biophysical Journal*, 76(2):1072 – 1079, 1999.

[57] J. Schneider, Y. F. Dufrêne, W. R. Barger Jr, and G. U. Lee. Atomic Force Microscope Image Contrast Mechanisms on Supported Lipid Bilayers. *Biophysical Journal*, 79:1107–1118, 2000.

[58] V. Franz, S. Loi, H. Müller, E. Bamberg, and H.-J. Butt. Tip penetration through lipid bilayers in atomic force microscopy. *Colloids and Surfaces B: Biointerfaces*, 23:191–200, 2002.

[59] H. Hertz. Über die berührung fester elastischer Körper (On the contact of rigid elastic solids). *J. reine und angewandte Mathematik*, 92:156, 1896.

[60] J. Boussinesq. *Applications des Potentiels a l'Etude de l'Equilibre et du Mouvement des Solides Elastiques*. Gauthier-Villars, Paris, 1885.

[61] M. T. Kim. Influence of substrates on the elastic reaction of films for the microindentation tests. *Thin Solid Films*, 283(1-2):12–16, 1996.

[62] B. B. Akhremitchev and G. C. Walker. Finite sample thickness effects on elasticity determination using atomic force microscopy. *Langmuir*, 15(17):5630–5634, 1999.

[63] I. N. Sneddon. The Relation between Load and Penetration in the Axisymmetric Boussinesq Problem for a Punch of Arbitrary Profile. *Int. J. Eng. Sci.*, 3:47–57, 1965.

[64] V. M. Aleksandrov. Asymptotic solution of the contact problem for a thin elastic layer. *Prikl. Mat. Mekh.*, 33:61–73, 1969.

[65] R. S. Dhaliwal and I. S. Rau. The axisymmetric boussinesq problem for a thick elastic layer under a punch of arbitrary profile. *International Journal of Engineering Science*, 8(10):843–856, 1970.

[66] W. T. Chen and P. A. Engel. Impact and contact stress analysis in multilayer media. *International Journal of Solids and Structures*, 8(11):1257–1281, 1972.

[67] M. J. Matthewson. Axi-symmetric contact on thin compliant coatings. *Journal of the Mechanics and Physics of Solids*, 29(2):89–113, 1981.

[68] F. Yang. Indentation of an incompressible elastic film. *Mechanics of Materials*, 30(4):275–286, 1998.

[69] R. S. Chadwick. Axisymmetric indentation of a thin incompressible elastic layer. *SIAM J. Appl. Math.*, 62:1520–1530, 2002.

[70] E. K. Dimitriadis, F. Horkay, J. Maresca, B. Kachar, and R. S. Chadwick. Determination of elastic moduli of thin layers of soft material using the atomic force microscope. *Biophysical Journal*, 82(5):2798–2810, 2002.

[71] N. R. Wilson and J. V. Macpherson. Carbon nanotube tips for atomic force microscopy. *Nature Nanotechnology*, 4(8):483–491, 2009.

[72] E. W. Wong, P.l E. Sheehan, and C. M. Lieber. Nanobeam mechanics: Elasticity, strength, and toughness of nanorods and nanotubes. *Science*, 277(5334):1971–1975, 1997.

[73] M.-F. Yu, O. Lourie, M. J. Dyer, K. Moloni, T. F. Kelly, and R. S. Ruoff. Strength and breaking mechanism of multiwalled carbon nanotubes under tensile load. *Science*, 287(5453):637–640, 2000.

[74] D. Qian, G. J. Wagner, W. K. Liu, M.-F. Yu, and R. S. Ruoff. Mechanics of carbon nanotubes. *Appl. Mech. Rev.*, 55:495–533, 2002.

[75] C. Bower, W. Zhu, D. Shalom, D. Lopez, L. H. Chen, P. L. Gammel, and S. Jin. On-chip vacuum microtriode using carbon nanotube field emitters. *Applied Physics Letters*, 80(20):3820, 2002.

[76] A. M. Fennimore, T. D. Yuzvinsky, W.-Q. Han, and A. Zettl. Rotational actuators based on carbon nanotubes. *Nature*, 424(July):25–27, 2003.

[77] M. T. Abramo and L. L. Hahn. The application of advanced techniques for complex focused-ion-beam device modification. *Microelectronics Reliability*, 36(11-12):1775–1778, 1996.

[78] V. V. Aristov, N. A. Kislov, and I. I. Khodos. Direct electron beam-induced formation of nanometer carbon structures in stem. volume 117, pages 775–780, 1991.

[79] Y.K Park, T Nagai, M Takai, C Lehrer, L Frey, and H Ryssel. Comparison of beam-induced deposition using ion microprobe. *Nuclear Instruments and*

Methods in Physics Research Section B: Beam Interactions with Materials and Atoms, 148(1âĂŞ4):25 – 31, 1999.

[80] H. W. P. Koops, R. Weiel, D. P. Kern, and D. P. Baum. High-resolution electron-beam induced deposition. *J. Vac. Sci. Tech. B*, 6:477–481, 1988.

[81] B. Hübner, H. W. P. Koops, H. Pagnia, N. Sotnik, J. Urban, and M. Weber. Tips for scanning tunneling microscopy produced by electron-beam-induced deposition. *Ultramicroscopy*, 42-44, Part 2(0):1519–1525, 1992.

[82] J. Zhao and J. J Davis. Force dependent metalloprotein conductance by conducting atomic force microscopy. *IPP Nanotechnology*, 14:1023–1028, 2003.

[83] J. J. Davis, C. L. Wrathmell, J. Zhao, and J. Fletcher. The tunnelling conductance of molecularly ordered metalloprotein arrays. *Journal of molecular recognition : JMR*, 17(3):167–73, 2004.

[84] A. P. Quist, A. Chand, S. Ramachandran, C. Daraio, S. Jin, and R. Lal. Atomic force microscopy imaging and electrical recording of lipid bilayers supported over microfabricated silicon chip nanopores: lab-on-a-chip system for lipid membranes and ion channels. *Langmuir : the ACS journal of surfaces and colloids*, 23(3):1375–1380, January 2007.

[85] I. Casuso, L. Fumagalli, J. Samitier, E. Padrós, L. Reggiani, V. Akimov, and G. Gomila. Electron transport through supported biomembranes at the nanoscale by conductive atomic force microscopy. *Nanotechnology*, 18(46):465503, November 2007.

[86] P. L. T. M. Frederix, M. R. Gullo, T. Akiyama, A. Tonin, N. F. De Rooij, U. Staufer, and A. Engel. Assessment of insulated conductive cantilevers for biology and electrochemistry. *Nanotechnology*, 16(8):997–1005, August 2005.

[87] P. L. T. M. Frederix, P. D. Bosshart, T. Akiyama, M. Chami, M. R. Gullo, J. J. Blackstock, K. Dooleweerdt, N. F. de Rooij, U. Staufer, and A. Engel. Conductive supports for combined AFM-SECM on biological membranes. *Nanotechnology*, 19(38):384004, September 2008.

[88] J. V. Macpherson and P. R. Unwin. Combined scanning electrochemical-atomic force microscopy. *Analytical chemistry*, 72(2):276–285, January 2000.

[89] B. J. Rodriguez, S. Jesse, K. Seal, A. P. Baddorf, S. V. Kalinin, and P. D. Rack. Fabrication, dynamics, and electrical properties of insulated scanning probe microscopy probes for electrical and electromechanical imaging in liquids. *Applied Physics Letters*, 91(9):093130, 2007.

[90] J. Abbou, C. Demaille, M. Druet, and J. Moiroux. Fabrication of submicrometer-sized gold electrodes of controlled geometry for scanning electrochemical-atomic force microscopy. *Analytical chemistry*, 74(24):6355–6363, December 2002.

[91] R. J. Fasching, Y. Tao, K. Hammerick, and F. B. Prinz. A Pencil Probe System for Electrochemical Analysis and Modification in Nanometer Dimensions ABSTRACT. *Proceedings of SPIE - The International Society for Optical Engineering*, 5116(I):128–135, 2003.

[92] Y. Hirata, S. Yabuki, and F. Mizutani. Application of integrated SECM ultramicro-electrode and AFM force probe to biosensor surfaces. *Bioelectrochemistry (Amsterdam, Netherlands)*, 63(1-2):217–224, June 2004.

[93] D. P. Burt, N. R Wilson, J. M. R. Weaver, P. S. Dobson, and J. V. Macpherson. Nanowire probes for high resolution combined scanning electrochemical microscopy - atomic force microscopy. *Nano letters*, 5(4):639–43, April 2005.

[94] P. S. Dobson, J. M. R. Weaver, D. P. Burt, M. N. Holder, N. R. Wilson, P. R. Unwin, and J. V. Macpherson. Electron beam lithographically-defined scanning electrochemical-atomic force microscopy probes: fabrication method and application to high resolution imaging on heterogeneously active surfaces. *Physical Chemistry Chemical Physics*, 8(33):3909, 2006.

[95] J. Hu, K. B. Holt, and J. S. Foord. Focused ion beam fabrication of boron-doped diamond ultramicroelectrodes. *Analytical Chemistry*, 81(14):5663–5670, July 2009.

[96] M. Salomo, S.E. Pust, G. Wittstock, and E. Oesterschulze. Integrated cantilever probes for SECM/AFM characterization of surfaces. *Microelectronic Engineering*, 87(5-8):1537–1539, May 2010.

[97] C Kranz, G Friedbacher, B Mizaikoff, A Lugstein, J Smoliner, and E Bertagnolli. Integrating an ultramicroelectrode in an AFM cantilever: combined technology for enhanced information. *Analytical Chemistry*, 73(11):2491–500, June 2001.

[98] A. Lugstein, E. Bertagnolli, C. Kranz, A. Kueng, and B. Mizaikoff. Integrating micro- and nanoelectrodes into atomic force microscopy cantilevers using focused ion beam techniques. *Applied Physics Letters*, 81(2):349, 2002.

[99] A. Davoodi, J. Pan, C. Leygraf, and S. Norgren. Probing of local dissolution of Al-alloys in chloride solutions by AFM and SECM. *Applied Surface Science*, 252(15):5499–5503, May 2006.

[100] H. Shin, P.J. Hesketh, B. Mizaikoff, and C. Kranz. Development of wafer-level batch fabrication for combined atomic force-scanning electrochemical microscopy (AFM-SECM) probes. *Sensors and Actuators B: Chemical*, 134(2):488–495, September 2008.

[101] T. Akiyama, M. R. Gullo, N. F. De Rooij, U. Staufer, A. Tonin, A. Engel, and P. L. T. M. Frederix. Insulated Conductive Probes for in situ Experiments in Structural Biology. *AIP Conference Proceedings*, pages 166–171, 2003.

[102] T. Akiyama, . R. Gullo, N. F. De Rooij, A. Tonin, H.-R. Hidber, P. L. T. M. Frederix, A. Engel, and U. Staufer. Development of Insulated Conductive Probes with Platinum Silicide Tips for Atomic Force Microscopy in Cell Biology. *Japanese Journal of Applied Physics*, 43(No. 6B):3865–3867, June 2004.

[103] P. S. Dobson, J. M. R. Weaver, M. N. Holder, P. R. Unwin, and J. V. Macpherson. Characterization of batch-microfabricated scanning electrochemical-atomic force microscopy probes. *Analytical chemistry*, 77(2):424–434, January 2005.

[104] I. Utke, P. Hoffman, Berger R., and L. Scandella. High-resolution magnetic Co supertips grown by a focused electron beam. *Applied Physics Letters*, 80:4792–4794, 2002.

[105] Y. F. Dufrêne and G. U. Lee. Advances in the characterization of supported lipid films with the atomic force microscope. *Biochimica et Biophysica Acta*, 1509:14–41, 2000.

[106] S. Tristram-Nagle and J. F. Nagle. Lipid bilayers: thermodynamics, structure, fluctuations, and interactions. *Chemistry and Physics of Lipids*, 127(1):3–14, 2004.

[107] F. A. Heberle and G. W. Feigenson. Phase separation in lipid membranes. *Cold Spring Harbor Perspectives in Biology*, 3(4):1–13, 2011.

[108] A. Zumbuehl, B. Dobner, and G. Brezesinski. Phase behavior of selected artificial lipids. *Current Opinion in Colloid and Interface Science*, 19(1):17–24, 2014.

[109] K. Simons and E. Ikonen. Functional rafts in cell membranes. *Nature*, 387:569–572, 1997.

[110] K. Jacobson, O. G. Mouritsen, and R. G. W. Anderson. Lipid rafts: At a crossroad between cell biology and physics. *Nature Cell Biology*, 9(1):7–14, 2007.

[111] A. Alessandrini and P. Facci. Phase transitions in supported lipid bilayers studied by afm. *Soft Matter*, 10(33):7145–7164, 2014.

[112] S. Bhattacharya and S. Haldar. Interactions between cholesterol and lipids in bilayer membranes: Role of lipid headgroup and hydrocarbon chain-backbone linkage. *Biochimica et Biophysica Acta*, 1467:39–53, 2000.

[113] D. Boal. *Mechanics of the Cell*. Cambridge University Press, 2002.

[114] J. L. Rubenstein, B. A. Smith, and H. M. McConnell. Lateral diffusion in binary mixtures of cholesterol and phosphatidylcholines. *Proc. Nat. Acad. Sci. USA*, 76:15–18, 1979.

[115] E. L. Elson, E. Fried, J. E. Dolbow, and G. M. Genin. Phase separation in biological membranes: Integration of theory and experiment. *Annual Review of Biophysics*, 39(1):207–226, 2010.

[116] T. Förster. Zwischenmolekulare energiewanderung und fluoreszenz. *Ann. Phys.*, 437:55–75, 1948.

[117] E. H. Synge. A suggested method for extending the microscopic resolution into the ultramicroscopic region. *Phil. Mag.*, 6:356, 1928.

[118] E. Betzig, A. Lewis, A. Harootunian, M. Isaacson, and E. Kratschmer. Near field scanning optical microscopy (nsom): Development and biophysical applications. *Biophysical Journal*, 49(1):269–279, 1986.

[119] D. Magde, E. L. Elson, and W. W. Webb. Thermodynamic fluctuations in a reacting system: Measurement by fluorescence correlation spectroscopy. *Phys. Rev. Lett.*, 29:705–708, 1972.

[120] E. L. Elson and D. Magde. Fluorescence correlation spectroscopy i. conceptual basis and theory. *Biopolymers*, 13:1–27, 1974.

[121] R. Peters, J. Peters, K. H. Tews, and W. Bähr. A microfluorimetric study of translational diffusion in erythrocyte membranes. *Biochimica et Biophysica Acta*, 367(3):282–294, 1974.

[122] S. W. Hell and J. Wichmann. Breaking the diffraction resolution limit by stimulated emission: stimulated-emission-depletion fluorescence microscopy. *Optics Letters*, 19(11):780–782, 1994.

[123] M. J. Rust, M. Bates, and X. Zhuang. Sub-diffraction-limit imaging by stochastic optical reconstruction microscopy (storm). *Nature Methods*, 3(10):793–795, 2006.

[124] S. T. Hess, T. P. K. Girirajan, and M. D. Mason. Ultra-high resolution imaging by fluorescence photoactivation localization microscopy. *Biophysical Journal*, 91(11):4258–4272, 2006.

[125] M. Raab, J. J. Schmied, I. Jusuk, C. Forthmann, and P. Tinnefeld. Fluorescence microscopy with 6 nm resolution on dna origami. *ChemPhysChem*, 15(12):2431–2435, 2014.

[126] F. Bloch. Nuclear induction. *Phys. Rev.*, 70:460–474, 1946.

[127] N. Bloembergen, E. M. Purcell, and R. V. Pound. Relaxation effects in nuclear magnetic resonance absorption. *Phys. Rev.*, 73:679, 1948.

[128] D. Chapman, P. Byrne, and G. G. Shipley. The physical properties of phospholipids. I. Solid state and mesomorphic properties of some 2,3-diacyl-DL-phosphatidylethanolamines. *Proc. Roy. Soc. A*, 290:115, 1966.

[129] D. Chapman and S. A. Penkett. Nuclear magnetic resonance spectroscopic studies of the interaction of phospholipids with cholesterol. *Nature*, 211:1304–1305, 1966.

[130] D. Chapman. Recent studies using nuclear magnetic resonance spectroscopy of lipids and biological membranes. *Biomembranes*, 3:281–292, 1972.

[131] G. Büldt, H. U. Gally, J. Seelig, and G. Zaccai. Neutron diffraction studies on phosphatidylcholine model membranes. I. Head group conformation. *Journal of Molecular Biology*, 134(4):673–691, 1979.

[132] T. J. McIntosh and S. A. Simon. Hydration and bilayer deformation: a reevaluation. *Biochemistry*, 25:4058–4066, 1986.

[133] J. F. Nagle, R. Zhang, S. Tristram-Nagle, W. Sun, H. I. Petrache, and R. M. Suter. X-ray structure determination of fully hydrated L_α phase dipalmitoylphosphatidylcholine bilayers. *Biophysical Journal*, 70(3):1419–1431, 1996.

[134] A. J. Bard, F.-R. F. Fan, J. Kwak, and O. Lev. Scanning electrochemical microscopy. introduction and principles. *Analytical Chemistry*, 61(2):132–138, 1989.

[135] A. J. Bard, F.-R. F. Fan, D. T. Pierce, P. R. Unwin, D. O. Wipf, and F. Zhou. Chemical imaging of surfaces with the scanning electrochemical microscope. *Science*, 254(5028):68–74, 1991.

[136] P.K. Hansma, B. Drake, O. Marti, S. A. C. Gould, and C. B. Prater. The scanning ion-conductance microscope. *Science*, 243(4891):641–643, 1989.

[137] M. Nonnenmacher, M. P. O'Boyle, and H. K. Wickramasinghe. Kelvin probe force microscopy. *Applied Physics Letters*, 58(25):2921–2923, 1991.

[138] E. Drolle, R. M. Gaikwad, and Z. Leonenko. Nanoscale electrostatic domains in cholesterol-laden lipid membranes create a target for amyloid binding. *Biophysical Journal*, 103(4):L27–L29, 2012.

[139] F. Hane, E. Drolle, Y. Choi, S. Attwood, R. Gaikwad, and Z. Leonenko. Atomic force microscopy and Kelvin probe force microscopy to study Alzheimer's disease. volume 4, pages 2817–2824, 2014.

[140] K. M. Merz Jr. Molecular dynamics simulations of lipid bilayers. *Current Opinion in Structural Biology*, 7(4):511–517, 1997.

[141] R. V. Devireddy. Statistical thermodynamics of biomembranes. *Cryobiology*, 60(1):80–90, 2010.

[142] W. F. D. Bennett and D. P. Tieleman. Computer simulations of lipid membrane domains. *Biochimica et Biophysica Acta - Biomembranes*, 1828(8):1765–1776, 2013.

[143] M. C. Rheinstädter and O. G. Mouritsen. Small-scale structure in fluid cholesterol-lipid bilayers. *Current Opinion in Colloid and Interface Science*, 18(5):440–447, 2013.

[144] S. G. Kalko, J. A. Hernández, J. Raúl Grigera, and J. Fischbarg. Osmotic permeability in a molecular dynamics simulation of water transport through a single-occupancy pore. *BBA - Biomembranes*, 1240(2):159–166, 1995.

[145] F. Zhu, E. Tajkhorshid, and K. Schulten. Pressure-induced water transport in membrane channels studied by molecular dynamics. *Biophysical Journal*, 83(1):154–160, 2002.

[146] S. J. Marrink and H. J. C. Berendsen. Permeation process of small molecules across lipid membranes studied by molecular dynamics simulations. *Journal of Physical Chemistry*, 100(41):16729–16738, 1996.

[147] W. Rzepala. *Interactions of carbon nanotubes and lipid bilayers*. PhD thesis, University of Oxford, Trinity Term 2013.

[148] T. Jadidi, H. Seyyed-Allaei, M. R. R. Tabar, and A. Mashaghi. Poisson's ratio and Young's modulus of lipid bilayers in different phases. *Front. Bioeng. Biotechnol.*, 2(8), 2014.

[149] A. Janshoff, H.-J. Galla, and C. Steinem. Piezoelectric mass-sensing devices as biosensors - an alternative to optical biosensors? *Angewandte Chemie - International Edition*, 39(22):4004–4032, 2000.

[150] E. Lüthgens, A. Herrig, K. Kastl, C. Steinem, B. Reiss, J. Wegener, B. Pignataro, and A. Janshoff. Adhesion of liposomes: A quartz crystal microbalance study. *Measurement Science and Technology*, 14(11):1865–1875, 2003.

[151] E. Reimhult, B. Kasemo, and F. Höök. Rupture pathway of phosphatidylcholine liposomes on silicon dioxide. *International Journal of Molecular Sciences*, 10(4):1683–1696, 2009.

[152] I. Reviakine and A. Brisson. Formation of supported phospholipid bilayers from unilamellar vesicles investigated by atomic force microscopy. *Langmuir*, 16(4):1806–1815, 2000.

[153] Z. V. Leonenko, A. Carnini, and D. T. Cramb. Supported planar bilayer formation by vesicle fusion: the interaction of phospholipid vesicles with surfaces and the effect of gramicidin on bilayer properties using atomic force microscopy. *Biochimica et Biophysica Acta (BBA) - Biomembranes*, 1509(1-2):131–147, 2000.

[154] J. Jass, T. Tjärnhage, and G. Puu. From liposomes to supported, planar bilayer structures on hydrophilic and hydrophobic surfaces: An atomic force microscopy study. *Biophysical Journal*, 79(6):3153–3163, 2000.

[155] S. J. Attwood, Y. Choi, and Z. Leonenko. Preparation of DOPC and DPPC supported planar lipid bilayers for atomic force microscopy and atomic force spectroscopy. *International Journal of Molecular Sciences*, 14(2):3514–3539, 2013.

[156] R. Richter, A. Mukhopadhyay, and A. Brisson. Pathways of lipid vesicle deposition on solid surfaces: A combined QCM-D and AFM study. *Biophysical Journal*, 85(5):3035–3047, 2003.

[157] B. Seantier, C. Breffa, O. Félix, and G. Decher. In situ investigations of the formation of mixed supported lipid bilayers close to the phase transition temperature. *Nano Letters*, 4(1):5–10, 2004.

[158] R. P. Richter and A. R. Brisson. Following the formation of supported lipid bilayers on mica: A study combining AFM, QCM-D, and ellipsometry. *Biophysical Journal*, 88(5):3422–3433, 2005.

[159] E. Reimhult, M. Zäch, F. Höök, and B. Kasemo. A multitechnique study of liposome adsorption on Au and lipid bilayer formation on SiO_2. *Langmuir*, 22(7):3313–3319, 2006.

[160] S. Garcia-Manyes, G. Oncins, and F. Sanz. Effect of pH and ionic strength on phospholipid nanomechanics and on deposition process onto hydrophilic surfaces measured by AFM. *Electrochimica Acta*, 51(24):5029–5036, 2006.

[161] S. Garcia-Manyes, G. Oncins, and F. Sanz. Effect of ion-binding and chemical phospholipid structure on the nanomechanics of lipid bilayers studied by force spectroscopy. *Biophysical Journal*, 89(3):1812–1826, 2005.

[162] M.-C. Giocondi, L. Pacheco, P. E. Milhiet, and C. Le Grimellec. Temperature dependence of the topology of supported dimirystoyl-distearoyl phosphatidylcholine bilayers. *Ultramicroscopy*, 86(1-2):151–157, 2001.

[163] F. Tokumasu, A. J. Jin, and J. A. Dvorak. Lipid membrane phase behaviour elucidated in real time by controlled environment atomic force microscopy. *Journal of Electron Microscopy*, 51(1):1–9, 2002.

[164] Z. V. Leonenko, E. Finot, H. Ma, T. E. S. Dahms, and D. T. Cramb. Investigation of temperature-induced phase transitions in DOPC and DPPC phospholipid bilayers using temperature-controlled scanning force microscopy. *Biophysical Journal*, 86(6):3783–3793, 2004.

[165] S. Garcia-Manyes, G. Oncins, and F. Sanz. Effect of temperature on the nanomechanics of lipid bilayers studied by force spectroscopy. *Biophysical Journal*, 89(6):4261–4274, 2005.

[166] C. Rotsch and M. Radmacher. Mapping local electrostatic forces with the atomic force microscope. *Langmuir*, 13(10):2825–2832, 1997.

[167] H. Mueller, H.-J. Butt, and E. Bamberg. Adsorption of membrane-associated proteins to lipid bilayers studied with an atomic force microscope: Myelin basic protein and cytochrome c. *Journal of Physical Chemistry B*, 104(18):4552–4559, 2000.

[168] P. Desmeules, M. Grandbois, V. A. Bondarenko, A. Yamazaki, and C. Salesse. Measurement of membrane binding between recoverin, a calcium-myristoyl switch protein, and lipid bilayers by afm-based force spectroscopy. *Biophysical Journal*, 82(6):3343–3350, 2002.

[169] Y. Kaufman, A. Berman, and V. Freger. Supported lipid bilayer membranes for water purification by reverse osmosis. *Langmuir*, 26(10):7388–7395, 2010.

[170] D. P. Nikolelis, C. G. Siontorou, and V. G. Andreou. Biosensors based on bilayer lipid membranes for automated continuous monitoring or rapid screening of environmental pollutants. *Laboratory Robotics and Automation*, 9(6):285–295, 1997.

[171] D. P. Nikolelis, S.-S. E. Petropoulou, E. Pergel, and K. Toth. Biosensors for the rapid detection of dopamine using bilayer lipid membranes (blms) with incorporated calix[4]resorcinarene receptor. *Electroanalysis*, 14(11):783–789, 2002.

[172] N. Sugao, M. Sugawara, H. Minami, M. Uto, and Y. Umezawa. Na+/d-glucose cotransporter based bilayer lipid membrane sensor for d-glucose. *Analytical Chemistry*, 65(4):363–369, 1993.

[173] T. M. Bayerl and M. Bloom. Physical properties of single phospholipid bilayers adsorbed to micro glass beads. a new vesicular model system studied by 2h-nuclear magnetic resonance. *Biophysical Journal*, 58(2):357–362, 1990.

[174] S. J. Johnson, T. M. Bayerl, D. C. McDermott, G. W. Adam, A. R. Rennie, R. K. Thomas, and E. Sackmann. Structure of an adsorbed dimyristoylphosphatidylcholine bilayer measured with specular reflection of neutrons. *Biophysical Journal*, 59(2 I):289–294, 1991.

[175] R. Northcutt. *Suspended Polypyrrole Films Supporting Alamethicin Reconstituted Bilayer Membranes*. PhD thesis, Virginia Commonwealth University, 2012.

[176] J. J. Kasianowicz, E. Brandin, D. Branton, and D. W. Deamer. Characterization of individual polynucleotide molecules using a membrane channel. *PNAS*, 93(24):13770–13773, 1996.

[177] K. Sumitomo, Y. Tamba, Y. Shinozaki, and K. Torimitsu. Confinement of Fluorescent Probes in Microwells on Si Substrates by Sealing with Lipid Bilayers. *Applied Physics Express*, 3(2):107001–1–107001–3, 2010.

[178] K. Sumitomo, McAllister A., Y. Tamba, Y. Kashimura, A. Tanaka, Y. Shinozaki, and K. Torimitsu. Ca^{2+} ion transport through channels formed by α-hemolysin analyzed using a microwell array on a Si substrate. *Biosensors and Bioelectronics*, 31(1):445–450, 2011.

[179] A Siitonen, K Sumitomo, C Ramanujan, Y Shinozaki, N Kasai, K Furukawa, J Ryan, and K Torimitsu. Elastic modulus of suspended purple membrane measured by atomic force microscopy. *Applied Surface Science*, 254(23):7877–7880, September 2008.

[180] Youichi Shinozaki, Koji Sumitomo, Kazuaki Furukawa, Hidetoshi Miyashita, Yukihiro Tamba, Nahoko Kasai, Hiroshi Nakashima, and Keiichi Torimitsu. Visualization of Single Membrane Protein Structure in Stretched Lipid Bilayer Suspended over Nanowells. *Applied Physics Express*, 3(2):027002, January 2010.

[181] Koji Sumitomo, Youichi Shinozaki, Daisuke Takagi, Hiroshi Nakashima, Yoshihiro Kobayashi, and Keiichi Torimitsu. Atomic Force Microscopy Observation of Membrane Proteins Suspended over Carbon Nanotube Network. *Japanese Journal of Applied Physics*, 48(No. 8):08JB18, August 2009.

[182] T. R. Albrecht, S. Akamine, Carver T. E., and C. F. Quate. Microfabrication of cantilever styli for the atomic force microscope. *J. of Vac. Sci. Tech. A - Vacuum surfaces and Films*, 8:3386–3396, 1990.

[183] R. A. Oliver. Advances in AFM for the electrical characterization of semiconductors. *Reports on Progress in Physics*, 71, 2008.

[184] A. Noy, D. V. Vezenov, and C. M. Lieber. Chemical force microscopy. *Annual Review of Materials Science*, 27:381–421, 1997.

[185] H. Dai, J. H. Hafner, A. G. Rinzler, D. T. Colbert, and R. E. Smalley. Nanotubes as nanoprobes in scanning probe microscopy. *Nature*, 384:147–150, 1996.

[186] S. S. Wong, A. T. Woolley, T. W. Odom, J.-L. Huang, P. Kim, D. V. Vezenov, and C. M. Lieber. Single-walled carbon nanotube probes for high-resolution nanostructure imaging. *Applied Physics Letters*, 73(23):3465–3467, 1998.

[187] M. C. Strus, A. Raman, C.-S. Han, and C. V. Nguyen. Imaging artefacts in atomic force microscopy with carbon nanotube tips. *Nanotechnology*, 16(11):2482–2492, November 2005.

[188] C. V. Nguyen, Q. Ye, and M. Meyyappan. Carbon nanotube tips for scanning probe microscopy: fabrication and high aspect ratio nanometrology. *Meas. Sci. Technol.*, 16:2138–2146, 2005.

[189] J. H. Hafner, C.-L. Cheung, A. T. Woolley, and C. M. Lieber. Structural and functional imaging with carbon nanotube afm probes. *Progress in Biophysics and Molecular Biology*, 77(1):73–110, 2001.

[190] J. Brown, P. Kocher, C. S. Ramanujan, D. N. Sharp, K. Torimitsu, and J. F. Ryan. Electrically conducting, ultra-sharp, high aspect-ratio probes for afm fabricated by electron-beam-induced deposition of platinum. *Ultramicroscopy*, 133:62–66, 2013.

[191] V. Scheuer, H. Koops, and T. Tschudi. Electron beam decomposition of carbonyls on silicon. *Microelectronic Engineering*, 5:423–430, 1986.

[192] D. J. Keller and C. C. Chou. Imaging steep, high structures by scanning force microscopy with electron-beam deposited tips. *Surface Science*, 268:333–339, 1992.

[193] M. Yamaki, T. Miwa, H. Yoshimura, and K. Nagayama. Efficient microtip fabrication with carbon coating and electron–beam deposition for atomic force microscopy. *Journal of Vacuum Science & Technology B*, 10:2447–2450, 1992.

[194] K. I. Schiffman. Investigation of fabrication parameters for the electron-beam-induced deposition of contamination tips used in atomic force microscopy. *Nanotechnology*, 7:163–169, 1993.

[195] F. Zenhausern, M. Adrian, B. Tenheggelerbordier, F. Ardizzoni, and P. Descouts. Enhanced imaging of biomolecules with electron-beam deposited tips for scanning force microscopy. *Journal of Applied Physics*, 73:7232–7237, 1993.

[196] H. Koops, J. Kretz, M. Rudolph, M. Weber, G. Dahm, and K. L. Lee. Characterization and application of materials grown by electron-beam-induced deposition. *Japanese Journal of Applied Physics*, 33:7099–7107, 1994.

[197] M. Wendel, H. Lorenz, and J. P. Kotthaus. Sharpened electron beam deposited tips for high resolution atomic force microscope lithography and imaging. *Applied Physics Letters*, 67:3732–3734, 1995.

[198] J. D. Beard and S. N. Gordeev. Fabrication and buckling dynamics of nanoneedle AFM probes. *Nanotechnology*, 22, 2011.

[199] S. J. Fang, S. Haplepete, W. Chen, C. R. Helms, and H. Edwards. Analyzing atomic force microscopy images using spectral methods. *Journal of Applied Physics*, 82(12):5891, 1997.

[200] C. F. H. Gondran and D. K. Michelson. Effect of probe tip size on atomic force microscopy roughness values for very smooth samples. *Journal of Vacuum Science & Technology A: Vacuum, Surfaces, and Films*, 24(4):1185, 2006.

[201] O. Krause, V. Bouchiat, and A. M. Bonnot. A quantitative comparison of resolution, scanning speed and lifetime behavior of CVD grown Single Wall Carbon Nanotubes and silicon SPM probes using spectral methods. *Journal of Physics: Conference Series*, 61:628–632, March 2007.

[202] C. Oregan, A. Lee, J. D. Holmes, N. Petkov, P. Trompenaars, and H. Mulders. Electrical properties of platinum interconnects deposited by electron beam induced deposition of the carbon-free precursor, $Pt(PF_3)_4$. *J. Vac. Sci. Technol. B*, 31(2), 2013.

[203] M. H. Ervin, D. Chang, B. Nichols, A. Wickenden, J. Barry, and J. Melngailis. Annealing of electron beam induced deposits of platinum from $Pt(PF_3)_4$. *J. Vac. Sci. Technol. B*, 25:2250–2254, 2007.

[204] T. H. Watts, A. A. Brian, J. W. Kappler, P. Marrack, and H. M. McConnell. Antigen presentation by supported planar membranes containing affinity-purified I-Ad. *Proc. Natl. Acad. Sci. USA*, 81:7564–7568, 1984.

[205] T. H. Watts, H. E. Gaub, and H. M. McConnell. T-cell-mediated association of peptide antigen and major histocompatibility complex protein detected by energy transfer in an evanescent wave-field. *Nature*, 320:179–181, 1986.

[206] H. M. McConnell, T. H. Watts, R. M. Weis, and A. A. Brian. Supported planar membranes in studies of cell-cell recognition in the immune system. *Biochimica et Biophysica Acta*, 864:95–106, 1986.

[207] E. Sackmann. Supported membranes: scientific and practical applications. *Science*, 271:43–48, 1996.

[208] J. Salafsky, J. T. Groves, and S. G. Boxer. Architecture and function of membrane proteins in planar supported bilayers: a study with photosynthetic reaction centers. *Biochemistry*, 35:14773–14781, 1996.

[209] I. Reviakine, A. Berksma-Schutter, A. N. Morozov, and A. Brisson. Growth of protein 2-D crystals on supported planar lipid bilayers imaged in situ by AFM. *Journal of Structural Biology*, 121:356–361, 1998.

[210] P. E. Milhiet, M. C. Giocondi, O. Baghdadi, F. Ronzon, B. Roux, and C. le Grimellec. Spontaneous insertion and partitioning of alkaline phosphatase into model lipid rafts. *EMBO Rep.*, 3:485–490, 2002.

[211] C. M. Yip, A. A. Darabie, and J. McLaurin. AB42-peptide assembly on lipid bilayers. *Journal of Molecular Biology*, 318:97–107, 2002.

[212] B. A. Cornell, V. L. Braach-Maksvytis, L. G. King, P. D. Osman, B. Raguse, L. Wieczorek, and R. J. Pace. A biosensor that uses ion-channel switches. *Nature*, 387:580–583, 1997.

[213] C. Bieri, O. P. Ernst, S. Heyse, K. P. Hofmann, and H. Vogel. Micropatterned immobilization of a G protein-coupled receptor and direct detection of G protein activation. *Natural Biotechnology*, 17:1105–1108, 1999.

[214] L. A. Kung, L. Kam, J. S. Hovis, and S. G. Boxer. Patterning hybrid surfaces of proteins and supported lipid bilayers. *Langmuir*, 16:6773–6776, 2000.

[215] S. G. Boxer. Molecular transport and organization in supported lipid membranes. *Current Opinion in Chemical Biology*, 4:704–709, 2000.

[216] I. Reviakine and A. Brisson. Streptavidin 2D crystals on supported phospholipid bilayers: towards constructing anchored phospholipid bilayers. *Lamgmuir*, 17:8293–8299, 2001.

[217] L. Kam and S. G. Boxer. Spatially selective manipulation of supported lipid bilayers by laminar flow: steps toward biomembrane microfluidics. *Langmuir*, 19:1624–1631, 2003.

[218] C. Larsson, M. Rodahl, and F. Höök. Characterization of DNA immobilization and subsequent hybridization on a 2D arrangement of streptavidin on a biotin-modified lipid bilayer supported on SiO_2. *Analytical Chemistry*, 75:5080–5087, 2003.

[219] J. L. Alonso and W. H. Goldmann. Feeling the forces: atomic force microscopy in cell biology. *Life Sciences*, 72:2553–2560, 2003.

[220] J. Yang. AFM as a high-resolution imaging tool and a molecular bond force probe. *Cell Biochem. Biophys.*, 41:435–449, 2004.

[221] Y. F. Dufrêne. Using nanotechniques to explore microbial surfaces. *Nat. Rev. Microbiol.*, 2:451–460, 2004.

[222] A. Alessandrini and P. Facci. AFM: a versatile tool in biophysics. *Meas. Sci. Technol.*, 16:65–92, 2005.

[223] N. Gadegaard. Atomic force microscopy in biology: technology and techniques. *Biotech. Histochem.*, 81:87–97, 2006.

[224] L. J. Johnston. Nanoscale imaging of domains in supported lipid membranes. *Langmuir*, 23:5886–5895, 2007.

[225] T. Ando. High-speed atomic force microscopy coming of age. *Nanotechnology*, 23(6), 2012.

[226] A. Sharma, K. I. Anderson, and D. J. Müller. Actin microridges characterized by laser scanning confocal and atomic force microscopy. *FEBS Lett.*, 579:2001–2008, 2005.

[227] C. M. Franz and D. J. Müller. Analyzing focal adhesion structure by atomic force microscopy. *J. Cell. Sci.*, 118:5315–5323, 2005.

[228] D. J. Frankel, J. R. Pfeiffer, Z. Surviladze, A. E. Johnson, J. M. Oliver, B. S. Wilson, and A. R. Burns. Revealing the topography of cellular membrane domains by combined atomic force microscopy/fluorescence imaging. *Biophysical Journal*, 90:2404–2413, 2006.

[229] M. Murakoshi, T. Gomi, K. Iida, S. Kumano, K. Tsumoto, I. Kumagai, K. Ikeda, T. Kobayashi, and H. Wada. Imaging by atomic force microscopy of the plasma membrane of prestin-transfected Chinese hamster ovary cells. *J. Assoc. Res. Otolaryngol.*, 7:267–278, 2006.

[230] P. Wiggins and R. Phillips. Analytic models for mechanotransduction: Gating a mechanosensitive channel. *Proc. Nat. Acad.Sci. USA*, 101(12):4071–4076, 2004.

[231] C. E. Morris and P. F. Juranka. Nav channel mechanosensitivity: Activation and inactivation accelerate reversibly with stretch. *Biophysical Journal*, 93(3):822–833, 2007.

[232] D. Schmidt and R. MacKinnon. Voltage-dependent K^+ channel gating and voltage sensor toxin sensitivity depend on the mechanical state of the lipid membrane. *Proc. Natl. Acad. Sci. USA*, 105, 2008.

[233] R. Phillips, T. Ursell, P. Wiggins, and P. Sens. Emerging roles for lipids in shaping membrane-protein function. *Nature*, 459(7245):379–385, 2009.

[234] C. E. Morris. Voltage-gated channel mechanosensitivity: Fact or friction? *Frontiers in Physiology*, MAY, 2011.

[235] J. A. Sobek. *Atomic Force Microscopy Studies of Potassium Channels*. PhD thesis, University of Oxford.

[236] J. L. Hutter and J. Bechhoefer. Calibration of atomic-force microscope tips. *Review of Scientific Instruments*, 64:1868–1873, 1993.

[237] R. Garcia and A. San Paulo. Attractive and repulsive tip-sample interaction regimes in tapping-mode atomic force microscopy. *Physical Review B*, 60:4961–4967, 1999.

[238] C. Su, L. Huang, and K. Kjoller. Direct measurement of tapping force with a cantilever deflection force sensor. *Ultramicroscopy*, 100:233–239, 2004.

[239] A. San Paulo and R. Garcia. Tip-surface forces, amplitude, and energy dissipation in amplitude-modulation tapping mode force microscopy. *Physical Review B*, 64:193411, 2000.

[240] S. C. Fain, K. A. Barry, M. G. Bush, B. Pittenger, and R. N. Louie. Measuring average tip-sample forces in intermittent-contact (tapping) force microscopy in air. *Applied Physics Letters*, 76(7), 2000.

[241] B. O. Shcherbin, A. V. Ankudinov, A. V. Kiyuts, and O. S. Loboda. Measurement of the Probe Impact Force of the Atomic Force Microscope Operating in the Amplitude Modulation Mode. *Physics of the Solid State*, 56:531–537, 2014.

[242] M. R. R. de Planque, G. P. Mendes, M. Zagoni, M. E. Sandison, K. H. Fisher, R. M. Berry, A. Watts, and H. Morgan. Controlled delivery of membrane proteins to artificial lipid bilayers by nystatin-ergosterol modulated vesicle fusion. *IEE Proceedings - Nanobiotechnology*, 153:21–30, 2006.

[243] P. M. Brown, J. Steers, S. W. Hui, P. L. Yeagle, and J. R. Silvius. Role of head group structure in the phase behavior of amino phospholipids. 2. Lamellar and nonlamellar phases of unsaturated phosphatidylethanolamine analogues. *Biochemistry*, 25:4259–4267, 1986.

[244] R. M. Epand and R. Bottega. Determination of the phase behaviour of phosphatidylethanolamine admixed with other lipids and the effects of calcium chloride: implications for protein kinase C regulation. *Biochimica et Biophysica Acta*, 994:144–154, 1988.

[245] C. Das, K. H. Sheikh, P. D. Olmsted, and S. D. Connell.

[246] E. Sackmann. *Handbook of Biological Physics, Volume 1.* Elsevier Science B. V., 1995.

[247] P. Atkins, J. de Paula, and R. Friedman. *Quanta, Matter, and Change: A Molecular Approach to Physical Chemistry.* Oxford University Press, 2009.

[248] M. H. Hawton and J. W. Doane. Pretrasitional phenomena in phospholipid/water multilayers. *Biophys. J.*, 52:401–404, 1987.

[249] G. Bryant, J. M. Pope, and J. Wolfe. Motional narrowing of the ^{2}h nmr spectra near the chain melting transition of phospholipid/d_2o mixtures. *European Biophysics Journal*, 21(5):363–367, 1992.

[250] J. De Joannis, P. S. Coppock, F. Yin, M. Mori, A. Zamorano, and J. T. Kindt. Atomistic simulation of cholesterol effects on miscibility of saturated and unsaturated phospholipids: Implications for liquid-ordered/liquid-disordered phase coexistence. *Journal of the American Chemical Society*, 133(10):3625–3634, 2011.

[251] G. W. Feigenson. Phase behavior of lipid mixtures. *Nature Chemical Biology*, 2(11):560–563, 2006.

[252] W. F. D. Bennett, J. L. MacCallum, and P. Tieleman. Thermodynamic analysis of the effect of cholesterol on dipalmitoylphosphatidylcholine lipid membranes. *Journal of the American Chemical Society*, 131(5):1972–1978, 2009.

[253] L. F. Braganza and D. L. Worcester. Hydrostatic pressure induces hydrocarbon chain interdigitation in single-component phospholipid bilayers. *Biochemistry*, 25:2591–2596, 1986.

[254] J. L. Slater and C.-H. Huang. Interdigitated bilayer membranes. *Progress in Lipid Research*, 27:325–359, 1988.

[255] Z. Leonenko, E. Finot, and D. Cramb. AFM study of interaction forces in supported planar DPPC bilayers in the presence of general anesthetic halothane. *Biochimica et Biophysica Acta (BBA) - Biomembranes*, 1758(4):487–492, 2006.

[256] I. Pera, R. Stark, M. Kappl, H.-J. Butt, and F. Benfenati. Using the Atomic Force Microscope to Study the Interaction between Two Solid Supported Lipid Bilayers and the Influence of Synapsin I. *Biophysical Journal*, 87:2446–2455, 2004.

[257] P. Köcher, A. Tanaka, N. Kasai, Y. Kashimura, K. Torimitsu, J. Ryan, and K. Sumitomo. Osmotically induced budding transition in a suspended lipid bilayer. In *60th JSAP Spring Meeting*.

[258] M. Gleisner, I. Mey, M. Barbot, C. Dreker, M. Meinecke, and C. Steinem. Driving a planar model system into the 3rd dimension: Generation and control of curved pore-spanning membrane arrays. *Soft Matter*, 10(33):6228–6236, 2014.

[259] M. Amiji and B. Sandmann. *Applied Physical Pharmacy*. McGraw Hill Professional, 2003.

[260] W. Epstein and S. G. Schultz. Cation Transport in Escherichia coli V . Regulation of cation content. *The Journal of General Physiology*, pages 221–234, 1965.

[261] R. J. Britten, F. T. Mcclure, and F. T. Mcclure. The amino acid pool in escherichia coli. 26(3), 1962.

[262] R. Hagenauer-Tsapis and A. S. D Kepes. Unmasking of an essential thiol during function of the membrane bound enzyme II of the phosphoenolpyruvate. *Biochimica et biophysica acta*, 465:118–130, 1977.

[263] C. E. Berrier, A. Coulombe, I. Szab, M. Zoratt, and A. Ghazi. Gadolinium ion inhibits loss of metabolites induced by osmotic shock and large stretch-activated channels in bacteria. 206:559 – 565, 1992.

[264] B. Martinac, M. Buechner, A. H. Delcour, J. Aidler, and C. Kung. Pressure-sensitive ion channel in Escherichia coli. *Proc. Nat. Acad.Sci. US*, 84, 1987.

[265] R. I. Macey. Transport of water and urea in red blood cells. *Am. J. Physiol.*, 246, 1984.

[266] A. S. Verkman. Mechanisms and regulation of water permeability in renal epithelia. *Am. J. Physiol.*, 257, 1989.

[267] A. S. Verkman. Water channels in cell membranes. *Annu. Rev. Physiol.*, 54:97–108, 1992.

[268] H. Sui, B.-G. Han, J. K. Lee, P. Walian, and B. K. Jap. Structural basis of water-specific transport through the AQP1 water channel. *Nature*, 414(December), 2001.

[269] M. D. Ledesma and C. G. Dotti. Membrane and cytoskeleton dynamics during axonal elongation and stabilization. *Int. Rev. Cytol.*, 227:183–219, 2003.

[270] M. P. Sheetz. Cell control by membrane-cytoskeleton adhesion. *Nat. Rev. Mol. Cell. Biol.*, 2(5), 2001.

[271] R. Nossal. Energetics of clathrin basket assembly. *Traffic*, 2(2):138–147, 2001.

[272] J. E. Hinshaw and S. L. Schmid. Dynamin self-assembles into rings suggesting a mechanism for coated vesicle budding. *Nature*, 374:190–192, 1995.

[273] B. Razani and M. P. Lisanti. Caveolins and caveolae: molecular and functional relationships. *Exp. Cell. Res.*, 271(1):36–44, 2001.

[274] H. T. Mcmahon and J. L. Gallop. Membrane curvature and mechanisms of dynamic cell membrane remodelling. *Nature*, 438, 2005.

[275] C. E. Morris and P. F. Juranka. Lipid stress at play: mechanosensitivity of voltage-gated channels. *Current Topics in Membranes*, 59, 1984.

[276] C. X. Gu, P. F. Juranka, and C. E. Morris. Stretch-activation and stretch-inactivation of Shaker-IR, a voltage-gated K^+ channel. *Biophysical Journal*, 80, 2001.

[277] C. E. Morris and P. F. Juranka. Nav channel mechanosensitivity: activation and inactivation accelerate reversibly with stretch. *Biophysical Journal*, 93, 2007.

[278] G. Gregoriadis and B. E. Ryman. Liposomes as carriers of enzymes or drugs: a new approach to the treatment of storage diseases. *Biochemical Journal*, 124(5):58P, 1971.

[279] G. Gregoriadis. Drug entrapment in liposomes. *FEBS Lett.*, 36(3):292–296, 1973.

[280] T. M. Allen and P. R. Cullis. Liposomal drug delivery systems: From concept to clinical applications. *Advanced Drug Delivery Reviews*, 65(1):36–48, 2013.

[281] J. M. Crowley. Electrical Breakdown of Bimolecular Lipid Membranes as an Electromechanical Instability. *Biophysical Journal*, 13(7):711–724, 1973.

[282] S. H. White. Comments on "electrical breakdown of bimolecular lipid membranes as an electromechanical instability". *Biophysical Journal*, 14(2):155–158, 1974.

[283] O. Alvarez and R. Latorre. Voltage-dependent capacitance in lipid bilayers made from monolayers. *Biophysical Journal*, 21(1):1–17, 1978.

[284] E. A. Evans, R. Waugh, and L. Melnik. Elastic area compressibility modulus of red cell membrane. *Biophysical Journal*, 16(6):585–595, 1976.

[285] R. Kwok and E. Evans. Thermoelasticity of large lecithin bilayer vesicles. *Biophysical Journal*, 65(3):637–652, 1981.

[286] T. H. Haines, W. Li, M. Green, and H. Z. Cummins. The elasticity of uniform, unilamellar vesicles of acidic phospholipids during osmotic swelling is dominated by the ionic strength of the media. *Biochemistry*, 26(17):5439–5447, 1987.

[287] E. Hantz, A. Cao, J. Escaig, and E. Taillandier. The osmotic response of large unilamellar vesicles studied by quasielastic light scattering. *Biochimica et Biophysica Acta*, 862:379–386, 1986.

[288] C. A. Rutkowski, L. M. Williams, T. H. Haines, and H. Z. Cummins. The elasticity of phospholipid vesicles obtained by photon correlation spectroscopy. *Biochemistry*, 30(23):5688–5696, 1991.

[289] J. P. Reeves and R. M. Dowben. Formation and properties of thin-walled phospholipid vesicles. *Journal of Cellular Physiology*, 73:49–60, 1969.

[290] D. S. Dimitrov and M. I. Angelova. Lipid swelling and liposome formation on solid surfaces in external electric fields. *Progress in Colloid & Polymer Science*, 73:48–56, 1987.

[291] P. Walde, K. Cosentino, H. Engel, and P. Stano. Giant Vesicles: Preparations and Applications. *ChemBioChem*, 11:848–865, 2010.

[292] J. Zhao, J. Wu, F. A. Heberle, T. T. Mills, P. Klawitter, G. Huang, G. Costanza, and G. W. Feigenson. Phase Studies of Model Biomembranes: Complex Behavior of DSPC/DOPC/Cholesterol. *Biochimica et Biophysica Acta*, 1768(11):2764–2776, 2007.

[293] L. R. DeYoung and K. A. Dill. Partitioning of nonpolar solutes into bilayers and amorphous n-alkanes. *Journal of Physiological Chemistry*, 96:801–809, 1990.

[294] T. X. Xiang and B. D. Anderson. Permeability of acetic acid across gel and liquid-crystalline lipid bilayers conforms to free-surface-area theory. *Biophysical Journal*, 72:223–237, 1997.

[295] J. C. Mathai, S. Tristram-Nagle, J. F. Nagle, and M. L. Zeidel. Structural determinants of water permeability through the lipid membrane. *The Journal of General Physiology*, 131(1):69–76, 2008.

[296] J. F. Nagle, J. C. Mathai, M. L. Zeidel, and S. Tristram-Nagle. Theory of passive permeability through lipid bilayers. *The Journal of General Physiology*, 131(1):77–85, 2008.

[297] T. Ursell, A. Agrawal, and R. Phillips. Lipid Bilayer Mechanics in a Pipette with Glass-Bilayer Adhesion. *Biophys. J.*, 101(8):1913–1920, 2011.

[298] M. Andersson, J. Jackman, D. Wilson, P Jarvoll, V. Alfredsson, G. Okeyo, and R. Duran. Vesicle and bilayer formation of diphytanoylphosphatidylcholine (DPhPC) and diphytanoylphosphatidylethanolamine (DPhPE) mixtures and their bilayers' electrical stability. *Colloids and Surfaces B: Biointerfaces*, 82(2):550 – 561, 2011.

[299] L. R. Opsahl and W. W. Webb. Lipid-Glass Adhesion in Giga-sealed Patch-clamped Membranes. *Biophysical Journal*, 66(January):75–79, 1994.

[300] R. Fettiplace and D. A. Haydon. Water permeability of lipid membranes. *Physiological reviews*, 60(2):510–550, 1980.

[301] J. Brahm. The permeability of red blood cells to chloride, urea and water. *The Journal of Experimental Biology*, 216:2238–2246, 2013.

[302] A. Finkelstein. Water and nonelectrolyte permeability of lipid bilayer membranes. *Physiological reviews*, 68:127–135, 1976.

[303] F. A. Henn and T. E. Thompson. Synthetic lipid bilayer membranes. *Annual Review of Biochemistry*, 38:241–262, 1969.

[304] D. Needham and R. S. Nunn. Elastic deformation and failure of lipid bilayer membranes containing cholesterol. *Biophysical Journal*, 58(4):997–1009, 1990.

[305] E. Corvera, O. G. Mouritsen, M. A. Singer, and M. J. Zuckermann. The permeability and the effect of acyl-chain length for phospholipid bilayers containing cholesterol: Theory and experiment. *Biochimica et Biophysica Acta - Biomembranes*, 1107(2):261–270, 1992.

[306] M. B. Lande, Donovan J. M., and M. L. Zeidel. The relationship between membrane fluidity and permeabilities to water, solutes, ammonia, and protons. *Journal of general Physiology*, 106(1):67–84, 1995.

[307] A. Finkelstein. *Water Movement through Lipid Bilayers, Pores and Plasma Membranes, Theory and Reality.* J.Wiley and Sons, Inc, 1st edition edition, 1986.

[308] R. Sherman-Gold and H. Maertz Warburton. *The Axon Guide, A guide to electrophysiology and biophysics loboratory techniques, 3rd edition*. MDS Analytical Technologies, 2008.

[309] C. Shafai, D. J. Thomson, M. Simard-Normandin, G. Mattiussi, and P. J. Scanlon. Delineation of semiconductor doping by scanning resistance microscopy. *Applied Physics Letters*, 64(3):342–344, 1994.

[310] P. De Wolf, J. Snauwaert, T. Clarysse, W. Vandervorst, and L. Hellemans. Characterization of a point-contact on silicon using force microscopy-supported resistance measurements. *Applied Physics Letters*, page 1530, 1995.

[311] S. S. Hong, J. J. Cha, and Y. Cui. One nanometer resolution electrical probe via atomic metal filament formation. *Nano Letters*, 11(1):231–235, 2011.

[312] Y. Takahashi, A. I. Shevchuk, P. Novak, Y. Zhang, N. Ebejer, J. V. Macpherson, P. R. Unwin, A. J. Pollard, D. Roy, C. A. Clifford, H. Shiku, T. Matsue, D. Klenerman, and Y. E. Korchev. Multifunctional nanoprobes for nanoscale chemical imaging and localized chemical delivery at surfaces and interfaces. *Angewandte Chemie International Edition*, 50(41):9638–9642, 2011.

[313] C. E. Jones, J. V. MacPherson, Z. H. Barber, R. E. Somekh, and P. R. Unwin. Simultaneous topographical and amperometric imaging of surfaces in air: Towards a combined scanning force-scanning electrochemical microscope (sf-secm). *Electrochemistry Communications*, 1(2):55–60, 1999.

[314] J. V. Macpherson, C. E. Jones, A. L. Barker, and P. R. Unwin. Electrochemical imaging of diffusion through single nanoscale pores. *Analytical Chemistry*, 74(8):1841–1848, 2002.

[315] B. Meckes, F. T. Arce, L. S. Connelly, and R. Lal. Insulated conducting can-

tilevered nanotips and two-chamber recording system for high resolution ion sensing afm. *Scientific Reports*, 4, 2014.

[316] N. Armstrong, J. Jasti, M. Beich-Frandsen, and E. Gouaux. Measurement of conformational changes accompanying desensitization in an ionotropic glutamate receptor. *Cell*, 127(1):85–97, 2006.

[317] A. I. Sobolevsky, M. P. Rosconi, and E. Gouaux. X-ray structure, symmetry and mechanism of ampa-subtype glutamate receptor. *Nature*, 462:745–756, 2009.

[318] A. Kueng, C. Kranz, B. Mizaikoff, A. Lugstein, and E. Bertagnolli. Combined scanning electrochemical atomic force microscopy for tapping mode imaging. *Applied Physics Letters*, 82(10):1592, 2003.

[319] Angelika Kueng, Christine Kranz, Alois Lugstein, Emmerich Bertagnolli, and Boris Mizaikoff. Integrated AFM-SECM in tapping mode: simultaneous topographical and electrochemical imaging of enzyme activity. *Angewandte Chemie (International ed. in English)*, 42(28):3238–40, July 2003.

[320] Claudia E Bach, Richard J Nichols, Heinrich Meyer, and Jurgen Besenhard. An electropainting method for coating STM tips for electrochemical measurements. *Bach*, 67:139–144, 1994.

[321] S. Chen and A. Kucernak. Fabrication of carbon microelectrodes with an effective radius of 1 nm. *Electrochemistry Communications*, 4:80–85, 2002.

[322] Aleix G Güell, Ismael Díez-Pérez, Pau Gorostiza, and Fausto Sanz. Preparation of reliable probes for electrochemical tunneling spectroscopy. *Analytical chemistry*, 76(17):5218–22, September 2004.

[323] Scott N Thorgaard and Philippe Bühlmann. Cathodic electropaint insulated

tips for electrochemical scanning tunneling microscopy. *Analytical chemistry*, 79(23):9224–8, December 2007.

[324] S Szunerits and R Boukherroub. Electrochemical investigation of gold/silica thin film interfaces for electrochemical surface plasmon resonance studies. *Electrochemistry Communications*, 8(3):439–444, March 2006.

[325] M Schneider and H Mohwald. Quantitative measurement of chromiums ability to promote adhesion. *Journal of Adhesion*, 79:597–607, 2003.

[326] S Szunerits, C Kirchner, G Wittstock, R Boukherroub, and C Gondran. Electrochemical investigation of the influence of thin SiO_2 films deposited on gold on charge transfer characteristics. *Electrochimica Acta*, 53(27):7908–7914, November 2008.

[327] M. Malboubi, H. Ostadi, S. Wang, Y. Gu, and K. Jiang. The effect of pipette tip roughness on giga-seal formation. *Proc. World Cong. Eng.*, 2, 2009.

[328] M. Malboubi, Y. Gu, and K. Jiang. Surface properties of glass micropipettes and their effect on biological studies. *Nanoscale Res Lett.*, 6(1), 2011.

[329] Y. Kim, J. Zhu, B. Yeom, M. Di Prima, X. Su, J.-G. Kim, S. J. Yoo, C. Uher, and N. A. Kotov. Stretchable nanoparticle conductors with self-organized conductive pathways. *Nature*, 500(7460):59–63, 2013.

[330] J. Xia, X. Zhang, J. Staudinger, and R. L. Huganir. Clustering of AMPA receptors by the synaptic PDZ domain-containing protein PICK1. *Neuron*, 22(1):179–187, 1999.

[331] L. P. Savtchenko and D. A. Rusakov. Moderate ampa receptor clustering on the nanoscale can efficiently potentiate synaptic current. *Phil. Trans. R. Soc. B*, 369(0167), 2013.

Appendix A - Force curve analysis software

The software was written in MatLab and carries out the entire analysis process, loading the selected directory containing text files with force curve data into memory, extracting and normalising the relevant information (force and indentation of the extend portion of the force curve) from each file, and fitting the model to the data. The force curves inevitably contain some noise, which makes it difficult to detect the breakthrough point(s) (i.e. where the tip penetrates the bilayer to the mica below) algorithmically. This issue was satisfactorily resolved by calculating moving averages with a range of window sizes of the first derivative of the force curve. The contact point of the force curve is detected by comparing this derivative to an appropriate tolerance value. Breakthrough events are detected by applying a peak-finding algorithm to the derivative. The desired contact mechanics model is then fitted to the data and the desired parameters (eg elastic modulus) are extracted.

In addition to visual inspection of each force curve, the software implements several checks on the goodness of the fit: Standard measures such as R^2 values are used, as well as more specific metrics such as the divergence between the contact point found in the data and the contact point of the fitted curve. If the discrepancy is larger than a predefined maximum value, it indicates that something went wrong in either the contact point detection or the fitting of the model, and the data point is discarded as an outlier. In rare cases the best fit parabola was inverted, which would result in a negative modulus, so these cases were also excluded. On the whole, approximately 15% of force curves were eliminated for one or several of these reasons.

After determining the contact point, the program fits the desired model to a predefined portion of the total indentation (the "fit range"). The selection of an appropriate tolerance and fit range is crucial in ensuring a good fit and avoiding systematic errors. If the tolerance is set too high, the early parts of the indentation will be ignored, meaning that relevant data would be ignored in the fitting. On the other hand, if the tolerance is set too low, parts of the force curve where the tip is not yet in contact with the sample will be included in the fitting, resulting in spuriously low modulus values. The fit range is similarly important in producing a good fit: too small a region is undesirable as useful data would be ignored, but too large a region means the assumption of a small indentation would be violated and the model would not hold.

A binary search method was used to determine the optimal tolerance and fit range values, as determined by the magnitude of the contact point offset. Since

the high and low domain force curves are qualitatively different, this process was done for each domain in turn. While an argument could be made for the individual determination of the optimal tolerance and fit range for each experimental run, this approach was rejected for two reasons. Firstly it would have complicated the analysis of the results and made the process more computationally intensive. Secondly, it would have made the comparison between experiments difficult. Instead, the fit quality was optimised for force curves at 0% cholesterol by minimising the offset between the contact point determined by the tolerance and the minimum of the parabola (i.e. the contact point determined by the fit algorithm). The optimal values determined in this way for the low and high domains were then used for these domains at all cholesterol concentrations. The relationship between the fit range, the tolerance, and the aforementioned offset is complex in nature—changing the tolerance affects the fit range since it moves the contact point, which in turn affects the position of the minimum of the parabola. Because of this interaction, an iterative approach was employed whereby an arbitrary fit range was chosen and the offset was calculated for a range of tolerances. The optimal tolerance (the one which gave the lowest offset) was then used while the fit range was varied. This process was repeated until no more significant reductions in the contact point offset were achieved.

The optimal values for the tolerance were found to be 0.0228 for the high domain and 0.0180 for the low domain. This essentially means that for optimal fitting, the contact point of the high domain force curve data is (relatively) nearer the end point of the indentation (the mica surface) than it is for the low domain data. This may be a result of the softer nature of the low domain, where the early, shallow slope of the indentation data is important for the fitting, while on the stiffer high domain, the early part of the indentation may be caused by residual electrostatic effects or the ordering of water layers above the surface.

The optimal values of the fit range were found to be 20.2% of the total indentation depth for the high domain and 15.0% for the low domain. This may be a consequence of the fact that the low domain is significantly thinner than the high domain, potentially leading to the effects of the hard underlying substrate being "felt" through the bilayer earlier for the low domain than the high domain. Both values are consistent with the small deformation assumption of the model, which assumes a maximum indentation depth of around 20% [69].

The MatLab program written for force curve analysis is given below.

```
clc
clear all
close all

basefolder = 'H:\Matlab\force_curves\'
d = dir(basefolder);
isub = [d(:).isdir]; %# returns logical vector
namefolds = {d(isub).name}';
namefolds(ismember(namefolds,{'.','..'})) = [];
foldercounter = 1;
subfoldercounter = 0;
f=1;
for foldindex = 3:length(namefolds)
    d2 = dir(strcat(basefolder,namefolds{foldindex}));
    isub2 = [d2(:).isdir]; %# returns logical vector
    subfolds = {d2(isub2).name}';
    subfolds(ismember(subfolds,{'.','..'})) = [];
for subfoldindex = 1:length(subfolds)
%     tolerancetesting = tolerances(tolindex);
    namefolds(foldindex)
    subfolds(subfoldindex)
    domaincheck = strfndw(subfolds(subfoldindex), '*HD*');
    if domaincheck == 1
        fitrangefactor = 0.2019
        tolerancetesting = 0.0228
    else
        fitrangefactor = 0.1500
        tolerancetesting = 0.0180
    end
%% Loading files
filelist = getAllFiles(strcat(basefolder,namefolds{foldindex
  },'\',subfolds{subfoldindex}));   %got this function off
  the internet to load files from folders and subfolders:
  http://stackoverflow.com/questions/2652630/how-to-get-all-
  files-under-a-specific-directory-in-matlab
```

```
32 filenumber = size(filelist);
33
34 %preallocating for speed:
35 breakthroughforce = zeros([1,filenumber(1)]);
36 breakthroughforcepostkink = zeros([1,filenumber(1)]);
37 contactpoint = zeros([1,filenumber(1)]);
38 contactpointoffset = zeros([1,filenumber(1)]);
39 indentationoffset = zeros([1,filenumber(1)]);
40 E = zeros([1,filenumber(1)]);
41 Rsquare = zeros([1,filenumber(1)]);
42 Epostkink = zeros([1,filenumber(1)]);
43 Eprekink = zeros([1,filenumber(1)]);
44 Rsquarepostkink = zeros([1,filenumber(1)]);
45 Rsquareprekink = zeros([1,filenumber(1)]);
46 h = zeros([1,filenumber(1)]);
47 hprekink = zeros([1,filenumber(1)]);
48 hpostkink = zeros([1,filenumber(1)]);
49 chopoff = zeros([1,filenumber(1)]);
50 clear hthinlayer fthinlayer
51
52 for m = 1:filenumber(1)
53     figurefilename = strcat('edgeseries',num2str(3),'_',
        num2str(m),'.png');
54     file = importdata(filelist{m});
55     data = file.data;
56     indposition = strmatch('Ind', file.textdata); %find the
        columns with Ind and Force in them, since they vary.
57     forceposition = strmatch('Force', file.textdata);
58     FC = [data(:,indposition),data(:,forceposition)]; %FC is
        the extend part of the data for indentation(=11) and
        Force(=7, sometimes =8 or 4 apparently)
59     [~,I]=max(FC(:,2)); %finding the max of the data, so I
        can save only the extend part of the FC
60     FC = FC(1:I,:);
61     force = FC(:,2)*1e9;
62     ind = FC(:,1)*1e9;
```

```
63
64      %% calculating averages and derivatives
65      for l = 20:70 %set this loop up for analysis purposes -
          turns out it's kinda useful in picking out second
          derivative trends!
66          j=0;   %setting up parameters for the contact point
              determination using moving averages - now trying
              to use 2nd derivative of the moving averages to
              find the elbow of the FC
67          tol = .75;
68          window = l;
69          shift = window;
70          movingavg = 0;
71          movingavgold = 0;
72          movingavgold2 = 0;
73          while j < length(force)
74              k=1;
75              Sum = 0;
76              while k <= window && j+k <= length(force)
77                  Sum = Sum + force(j+k);
78                  k=k+1;
79              end
80              j=j+shift;
81              movingavg = Sum/window;
82              firstdev(j,l) = movingavg-movingavgold;
83              movingavgold2 = movingavgold;
84              movingavgold = movingavg;
85          end
86      end
87
88      %% finding contact- and kinkpoint(s)
89      tolerance = .2; %this sets where on the first derivative
          it stops, i.e. has to be high enough to skip over all
          the noise
90      tolerance2 = tolerancetesting%(f); %this sets how far it
          backtracks to the baseline to find the actual contact
```

```
        point, i.e. has to be low enough to go back all the
        way to the contact point
91      firstdev(1:100,:) = 0;
92      hit=0; %to break out of both loops... whatevs.
93      for i = 1:length(firstdev(:,1))
94          for j = 1:length(firstdev(1,:))
95              if firstdev(i,j) > tolerance
96                  hit = 1;
97                  break
98              end
99
100         end
101         if hit == 1;
102             break
103         end
104     end
105     hit=0;
106     while i > 0
107         for j = 1:length(firstdev(1,:))
108             if firstdev(i,j) < tolerance2 && firstdev(i,j)
                  ~= 0;
109                 contactpoint = i;
110                 hit=1;
111                 break
112             end
113             if hit == 1;
114                 break
115             end
116         end
117         i = i-1;
118     end
119
120 %     10/09/13 going for a new technique to find the
    kinkpoints, namely to invert a flattened version of
    firstdev and then using the "fpeak" function by geng jun (
    downloaded) to try and identify peaks.
```

```
121     [crazybitstart,~] = find(abs(firstdev) > 0.8*max(max(abs
          (firstdev))));
122     chopoff(m) = 150 + length(firstdev) - min(crazybitstart)
          ; %this should ensure that the crazy end bits of
          firstdev don't get included in the peakfinding stuff
123     buffron = 150;
124     flatfd=sum(-firstdev(contactpoint+buffron:end-chopoff(m)
          ,:),2); %this reduces firstdev to a single vector
125
126     for p = 1:length(flatfd)
127         if flatfd(p)==0; %this is to move the zero-value
              bits of flatfd out of the way for findpeaks to do
              its job.
128             flatfd(p) = -100;
129         end
130     end
131     clear bigkink* smallkink*
132     s = 150; % sensitivity of the fpeak function
133     peaksfound = fpeak(1:length(flatfd),flatfd,s);
134     [Y,I] = sort(peaksfound(:,2),1,'descend');
135     sortedpeaks = peaksfound(I);
136     bigkink = sortedpeaks(1,1) + contactpoint + buffron - 1;
137     % this is to find the actual max and min points of the
          kink:
138     [~, bigkinkmax] = findpeaks(force(bigkink-120:bigkink-1)
          ,'minpeakdistance',119);
139     bigkinkmax = bigkink-120+bigkinkmax-1;
140     [~, bigkinkmin] = findpeaks(-force(bigkink-30:bigkink
          +90),'minpeakdistance',120);
141     bigkinkmin = bigkink-30+bigkinkmin-1;
142 %     to see if there's more than one legit kink i'm going
    to compare the difference between the value of flatfd at
    the second alleged kink vs the values of flatfd at the
    other kinks (which should bee similar to one another).
143 if numel(Y) > 1
```

```
144         if abs(Y(2)-mean(Y(3:end))) > abs(Y(1)-mean(Y(3:end)
              ))/25
145             smallkink = sortedpeaks(2,1) + contactpoint +
                  buffron - 1;
146             [~, smallkinkmax] = findpeaks(force(smallkink
                  -120:smallkink-30),'minpeakdistance',90);
147             smallkinkmax = smallkink-120+smallkinkmax-1;
148             [~, smallkinkmin] = findpeaks(-force(smallkink
                  -40:smallkink+30),'minpeakdistance',70);
149             smallkinkmin = smallkink-40+smallkinkmin-1;
150             fprintf('two legit kinks found')
151         else
152             smallkink = 1;
153             smallkinkmax = 1;
154             smallkinkmin = 1;
155         end
156     else
157         smallkink = 1;
158         smallkinkmax = 1;
159         smallkinkmin = 1;
160     end
161     %here i am calculating the height of the bilayer from
          the contactpoints and kinkpoints. Alternately I have
          measured the bilayer height as 5.74nm and 3.92nm in
          images taken in the same experiment.
162     if bigkink > smallkink
163         h(m) = ind(bigkinkmin)-ind(contactpoint);
164         hprekink(m) = ind(smallkinkmin)-ind(contactpoint);
165         hthinlayer(m) = ind(bigkinkmin)-ind(smallkinkmin);
166         if hthinlayer(m) > 5
167             hthinlayer(m) = 0
168         end
169         fthinlayer(m) = force(smallkinkmax)-force(
              contactpoint);
170         ftotal(m) = force(bigkinkmax)-force(contactpoint);
```

```
171         hpostkink(m) = ind(bigkinkmin)-ind(smallkinkmin)+ind
              (smallkinkmax)-ind(contactpoint);
172     else
173         h(m) = ind(smallkinkmin)-ind(contactpoint);
174         hprekink(m) = ind(smallkinkmin)-ind(contactpoint);
175         hthinlayer(m) = 0;
176         fthinlayer(m) = 0;
177     end
178     layerheight = ind(bigkinkmin)-ind;
179     [~,tappingforceindexmin] = min(abs(layerheight - 3.59));
180     [~,tappingforceindexmax] = min(abs(layerheight - 3.77));
181     ftappingmin(m) = ind(bigkinkmin)-ind(
          tappingforceindexmin);
182     ftappingmax(m) = ind(bigkinkmin)-ind(
          tappingforceindexmax);
183
184     %% Fitting:
185     %createFit130805.m is a (slightly modified) function
          generated using the curve fitting toolbox. It spits
          out a plot and also all the coefficients in the form
          of a cfit
186     [fitresultprekink, gofprekink, fitresult, gof, indshift,
           forceshift, ind, force,contactpointoffset(m),
          indentationoffset(m)] = createFit130902(ind, force,
          fitrangefactor, contactpoint, smallkink, bigkink,
          smallkinkmin, smallkinkmax,bigkinkmin,bigkinkmax, h(m)
          ,filelist{m});
187     %% Calculating E from the p1 coefficient using the
          Chadwick model:
188     R = 30e-9;
189     Rsquare(m)=gof.rsquare;
190     E(m) = fitresult.p1*3*h(m)/2/pi/R;
191     Eprekink(m) = fitresultprekink.p1*3*hprekink(m)/2/pi/R;
192     Rsquareprekink(m)=gofprekink.rsquare;
193     breakthroughforce(m)=force(max(bigkinkmax,smallkinkmax))
          -force(contactpoint);
```

```
194         clear force firstdev
195 end
196 Summary = [E', h', contactpointoffset', indentationoffset',
        Rsquare', breakthroughforce'];
197
198 outliers = find(abs(Summary(:,4)) >= 1);
199 Summarysansoutliers = Summary;
200 Summarysansoutliers(outliers,:) = [];
201 filelistsansoutliers = filelist;
202 filelistsansoutliers(outliers) = [];
203 rsquarelimited = find(Summarysansoutliers(:,5) < 0.9);
204 Summaryrsquarelimited = Summarysansoutliers;
205 Summaryrsquarelimited(rsquarelimited,:) = [];
206 filelistrsquarelimited = filelistsansoutliers;
207 filelistrsquarelimited(rsquarelimited) = [];
208 Summaryaverages = mean(Summarysansoutliers,1);
209 Summaryerrors = std(Summarysansoutliers)/sqrt(length(
        Summarysansoutliers(:,1)));
210 Summaryaveragesanderrors = [Summaryaverages ; Summaryerrors];
211
212 hthinlayeravg = mean(hthinlayer(find(hthinlayer ~= 0)));
213 fthinlayeravg = mean(fthinlayer(find(fthinlayer ~= 0)));
214 hthinlayererr = hthinlayeravg/sqrt(length(find(hthinlayer ~=
        0)));
215 fthinlayererr = fthinlayeravg/sqrt(length(find(fthinlayer ~=
        0)));
```

The function called in the fitting of the data

`createFit130902.m`

is given below.

```
function [fitresultprekink, gofprekink, fitresult, gof,
    indshift,forceshift,xData,yData,contactpointoffset,
    indentationoffset] = createFit131007(ind, force,
    fitrangefactor, contactpoint, kinkpoint, kinkpoint2,
    kinkmin, kinkmax,kinkmin2,kinkmax2,h,filename)
%CREATEFIT(IND,FORCE)
%% Fit:
[xData, yData] = prepareCurveData( ind, force );
% Set up fittype and options.
ft = fittype( 'poly2' );
opts = fitoptions( ft );
opts.Lower = [-inf -inf -inf];
opts.Robust = 'Bisquare';
opts.Upper = [Inf inf inf];
%this one selects between kinkpoint and kinkpoint2:::: ex =
    excludedata( xData, yData, 'indices', [1:contactpoint,
    round(contactpoint+fitrangefactor*(max(kinkpoint,
    kinkpoint2)-contactpoint)):length(ind)] ); %this excludes
    everything up to contactpoint, and everything from e.g.
    15% (=fitrangefactor) up to breakthrough force.
[c excludypoint] = min(abs(xData-xData(contactpoint)-
    fitrangefactor*h));
ex = excludedata( xData, yData, 'indices', [1:contactpoint,
    excludypoint:length(ind)] ); %this excludes everything up
    to contactpoint, and everything from an indentation
    greater than eg 20% (=fitrangefactor) of the height of the
     bilayer h.
opts.Exclude = ex;
[fitresult, gof] = fit( xData, yData, ft, opts ); % Fit
    model to data.
%shift data to vertex of parabola:
x0 = -fitresult.p2/2/fitresult.p1;
```

```
18 y0 = fitresult.p3 - fitresult.p2^2/4/fitresult.p1;
19 xData=xData-x0;
20 yData=yData-y0;
21 % calculate offsets between fit and contactpoint:
22 contactpointoffset = sqrt(yData(contactpoint)^2+xData(
     contactpoint)^2);
23 indentationoffset = xData(contactpoint);
24 % Fit model to data just before first kink (IF THERE ARE TWO
     KINKS! else it fits it just before the kink). Have to do
     this before shifting the rest of the kink distance, since
     the vertex of this parabola wouldn't be at (0,0) otherwise
     .
25 if kinkmin ~= 1;
26     ex2 = excludedata( xData, yData, 'indices', [1:round((
         contactpoint+kinkmax)/2),kinkmax:length(ind)] ); %this
          is to fit from about halfway to kinkpoint (one) to
         kinkmax, to compare with post-kink fit.
27     opts.Exclude = ex2;
28     opts.Lower = [-Inf 0 0];
29     opts.Upper = [Inf 0 0];
30     [fitresultprekink, gofprekink] = fit( xData, yData, ft,
         opts );
31 else
32     ex2 = excludedata( xData, yData, 'indices', [1:round((
         contactpoint+kinkmax2)/2),kinkmax2:length(ind)] ); %
         this is to fit from about halfway to kinkpoint (one)
         to kinkmax, to compare with post-kink fit.
33     opts.Exclude = ex2;
34     opts.Lower = [-Inf 0 0];
35     opts.Upper = [Inf 0 0];
36     [fitresultprekink, gofprekink] = fit( xData, yData, ft,
         opts );
37 end
38 %adding a bit to shift the data so the vertex is at the
     origin minus the width of the first kink, to make the post
```

```
    -kink fitting more pointful - I'm not sure about
    forceshift: I think it might not be necessary
39  indshift=xData(kinkmin)-xData(kinkmax);
40  forceshift=0;%yData(kinkmin)-yData(kinkmax);
41  xData=xData-indshift;
42  yData=yData-forceshift;
43
44  fitresult.p2=fitresult.p2+2*fitresult.p1*(x0);
45  fitresult.p3=fitresult.p3-(y0)-fitresult.p1*(x0)^2;
46  fitresult.p2=fitresult.p2+2*fitresult.p1*(indshift);
47  fitresult.p3=fitresult.p3-(forceshift)+fitresult.p1*(
    indshift)^2;
48  fitresultprekink.p2=fitresultprekink.p2+2*fitresultprekink.
    p1*(indshift);
49  fitresultprekink.p3=fitresultprekink.p3-(forceshift)+
    fitresultprekink.p1*(indshift)^2;
```

Appendix B - List of abbreviations

AFM atomic force microscopy

AMPAR $\alpha-amino-3-hydroxy-5-methyl-4isoxazolepropionicacid$ receptor

CNT carbon nanotube

DOPC 1,2-dioleoyl-sn-glycero-3-phosphocholine

DPhPC 1,2-diphytanoyl-sn-glycero-3-phosphocholine

DPPC 1,2-dipalmitoyl-sn-glycero-3-phosphocholine

DPPE 1,2-dipalmitoleoyl-sn-glycero-3-phosphoethanolami

DSPC 1,2-distearoyl-sn-glycero-3-phosphocholine

EBID electron beam induced deposition

ENTH epsin N-terminal homology domain

EPR electron paramagnetic resonance

FC force curve

FCS fluorescence correlation spectroscopy

FIB focused ion beam

FITC fluorescein isothiocyanate

FRET Förster/fluorescence resonance energy transfer

GUV giant unilamellar vesicle

HD high domain

HOPG highly ordered pyrolytic graphite

IBID ion beam induced deposition

invOLS inverted optical lever sensitivity

ITO indium tin oxide

KPFM kelvin probe force microscopy

LD low domain

MD molecular dynamics

MWNT multi-walled nanotube

NMR nuclear magnetic resonance

NSOM near-field scanning optical microscopy

PAG polyacrylamide gel

PALM photoactivated localization microscopy

POPE 1-palmitoyl-2-oleoyl-sn-glycero-3-phosphoethanolamine

PSD power spectral density

PTFE polytetrafluoroethylene

QCM quartz crystal microbalance

RF radio frequency

SECM scanning electrochemical microscopy

SEM scanning electron microscopy

SICM scanning ion conductance microscopy

SLB supported lipid bilayer

SPM scanning probe microscopy

STED stimulated emission dissipation

STM scanning tunnelling microscopy

STORM stochastic optical reconstruction microscopy

TUNA tunnelling AFM